Modeling and Control for a Class of Tendon-Driven Continuum Mechanisms

Von der Fakultät für Maschinenbau
der Gottfried Wilhelm Leibniz Universität Hannover

zur Erlangung des akademischen Grades
Doktor-Ingenieur (Dr.-Ing.)
genehmigte Dissertation

von

Dipl.-Ing. Bastian Deutschmann

2020

1. Referent: Prof. Dr.-Ing. Jessica Burgner-Kahrs
2. Referent: Prof. Dr.-Ing. Eduard Reithmeier
Tag der Promotion: 10. Oktobor 2019

Preface

This dissertation is based on research undertaken at the Institute of Robotics and Mechatronics of the German Aerospace Center (DLR) in Oberpfaffenhofen, Germany. It took five years (2015 - 2019) to accumulate the results which are reported in this thesis. Nevertheless, this work would have not been possible to be finished without the help of a lot people that gave me support and advice in various ways.

I am very grateful to Prof. Jessica Burgner-Kahrs, my supervisor from the (former) Laboratory for Continuum Robots at the Leibniz University of Hannover, for her support and invaluable advice. Whenever I visited her, she spared much time and provided her undivided attention for discussing my work.

Furthermore, my special thanks go to Dr. Christian Ott, who mentored me throughout my time working on control for continuum mechanism and gave me advice on the corresponding publications.

Moreover, I wish to thank Dr. Simon Eugster from the University of Stuttgart, with whom I collaborated in a very productive way resulting in valuable publications and a DFG Project. Besides this scientific impact, Simon introduced me to the topic of nonlinear beam theory and filled several knowledge gaps in general mechanics and mathematics.

Without the excellent and continuous maintenance of the robot software, communication infrastructure and hardware the numerous experiments in this thesis would not have been possible at all. In particular, I would like to thank Robert Burger, Florian Schmidt, Werner Friedl, Markus Bihler, Thomas Bahls, Dr. Maxime Chalon, Martin Pfanne, Manuel-Maria Bras Pereira Mascarenhas and Jens Reinecke. Especially the latter six persons did help and encourage me by discussing ideas and concepts that contributed largely to findings in this thesis and made my lunch breaks much more entertaining. I would like to thank also my former students David Fehrenbach, Tong Liu and Anton Shu for their contribution on design, modeling and control of tendon-driven continuum mechanisms.

Moreover, I would like to thank my office roommate Julian Klodmann for the mental support and fruitful discussions on nearly any topic throughout the nine years that we sit in an office together. Also, Thomas Bahls deserves special thanks as he supported me and my daily working experience with off topic discussions and good food. It was Julian and Thomas together with Sophie Lantermann, Andreas Tobergte, Dr. Uli Hagn, Jan Tully, Anja Hellings and Dr. Rainer Konietschke, who initially supported my employment at the institute as well as these persons introduced me to building, operating and maintaining robotic systems and also contributed largely to my first publication. Furthermore, I would like to thank Prof. Alin Albu-Schäffer, Head of the Institute of Robotics and Mechatronics, for giving me the possibility to conduct research in the exciting field of robot control.

Special thanks go to Julian Klodmann, Jens Reinecke and Dr. Alexander Dietrich from

whom I learned to write publications and giving scientific presentations. Furthermore, I would like to thank them for proof-reading this thesis.
Several other people outside of the scientific environment largely contributed towards the completion of this thesis and gave me power to push through night and weekend shifts. I would like to thank Jan and Timo for amusing nights at the river, Felix, Doro, Andi and Caro for the enjoyable time on weekend trips or on vacations and my "Stammtisch", Markus, Minh, Christian, Erik, Christian, Markus for pleasant evenings in Munich's gastronomy.
Special thanks and love to my parents Edith and Reinhold who have always encouraged me to pursue my goals in life and to be happy. Last, I thank my Love Catharina. Without her patience, support and motivation, this work would have never been completed.

Abstract

In recent years, the application of continuum robots is constantly growing as they combine high dexterity and a small design space. Commonly, snake-like mechanisms are built to serve as steerable catheters in medical applications or robotic manipulators to entangle unknown objects. "Continuum" describes the slender, continuously deformable structure in these robots which provides the motion capability. More recently, shorter joint modules with larger cross sections, termed tendon-driven continuum mechanism are used in other robotic areas for application as multi-fingered robotic or prosthetic hands, quadrupedal or humanoid necks and spines, or entire manipulators. The advantages of this novel class of mechanisms are their intrinsic self-support, their ability to handle physical contacts and collisions in a robust and safe way, which predestines them for these areas. Due to their application, the overall motion is smaller but more dynamic which limits the approaches for analysis and control developed for regular continuum robots.

This thesis contributes to robotics research by developing dedicated approaches in modeling, state estimation and control for this novel class of tendon-driven continuum mechanisms. For the analysis of their static and dynamic behavior, a nonlinear beam finite element model is adapted to predict the workspace of this class of mechanisms accurately. However, this model cannot be utilized in model-based control due to the large number of degrees of freedom which yields high computational costs. Therefore, a second model is derived that reduces the number of degrees of freedom essentially and a generic calibration procedure is introduced to find the corresponding physical parameters. For the application of common robotic model-based controllers, an exact estimation of the pose and its velocity is crucial, whereas the commonly proposed shape estimation strategies are insufficient. Therefore, this thesis introduces and compares three specifically designed state estimation techniques for the new class of mechanisms using on-board sensors. On this basis, nonlinear model-based control approaches in the configuration space of the continuum mechanism are introduced. The underactuation of these mechanisms is specifically treated in the approaches by a transformation to the input output normal form.

The developed methods in modeling, state estimation and control presented in this work are experimentally validated on a humanoid robot. Due to their promising results, this thesis lays the foundation for the use of tendon-driven continuum mechanisms as generic joint modules for modular robotic systems which may mark the beginning of a new generation of light-weight robots.

Keywords: Continuum Mechanisms, Underactuated Systems, Soft Material Robotic Systems

Kurzfassung

Titel:
Modellierung und Regelung für eine Klasse von seilgetriebenen Kontinuumsmechanismen

Die Anwendung von Kontinuumsrobotern hat in der letzten Jahren stetig zugenommen, da Sie ein hohes Maß an Dexterität bieten und zugleich wenig Platz einnehmen. Überwiegend werden schlangenartige Mechanismen konstruiert, die als aktuierte Katheter in medizinische Anwendungen dienen, oder in Manipulatoren eingesetzt werden die unbekannte Objekte umgreifen können. Der Begriff „Kontinuum“ beschreibt dabei die schlanke, kontinuierlich verformbare Struktur des Roboters die für dessen Bewegungsfähigkeit charakteristisch ist. Jüngst werden auch kürzere Mechanismen mit größerem Querschnitt, sogenannte „seilgetriebene Kontinuumsmechanismen“, für andere robotische Anwendungen genutzt, zum Beispiel für robotische oder prothetische mehrfinger Hände, als Hals oder als Wirbelsäule von Vierbeinern- oder humanoiden Robotern sowie als vollständige Manipulatoren. Die Vorteile dieser neuen Klasse von Mechanismen sind deren intrinsische Eigenstabilität sowie die Fähigkeit mit physischen Kontakten und Kollisionen sicher umzugehen, was sie wiederum für die zuvor genannten Anwendungsgebiete prädestiniert. In ihrer Anwendung ist die Bewegung dieser seilgetriebenen-Kontinuums Mechanismen insgesamt kleiner, jedoch dynamischer, was bekannte Ansätze zur Analyse und Regelung von Kontinuumsrobotern nur bedingt nutzbar macht.

Diese Arbeit entwickelt dedizierte Ansätze in der Modellbildung, Zustandsschätzung und Regelung für diese neue Klasse von seilgetriebenen Kontinuumsmechanismen und leistet damit einen Beitrag zur robotischen Forschung. Zur Analyse des statischen und dynamischen Verhaltens wird ein nichtlineares, Finite Element Model (FEM) adaptiert, um den Arbeitsraum dieser Klasse von Mechanismen genau abzubilden. Dieses Modell kann jedoch nicht zur modellbasierten Regelung verwendet werden, da die große Zahl an Freiheitsgraden immense Rechenkosten verursacht. Daher wird ein zweites Modell entwickelt, das die Zahl der Freiheitsgrade drastisch reduziert. Mit einer generischen Kalibrationsmethode, welche im Rahmen dieser Arbeit entwickelt wurde, werden anschließend die physischen Parameter dieser reduzierten Modelle identifiziert. Für die Anwendung üblicher robotischer modellbasierter Regler, ist die exakte Kenntnis der Pose und der korrespondierenden Geschwindigkeit entscheidend, während die vorgeschlagenen Strategien von Kontinuumsrobotern zur Formschätzung insuffizient sind. Daher stellt diese Arbeit drei spezifisch entworfene Techniken zur Zustandsschätzung dieser neuen Klasse an Mechanismen vor und vergleicht diese, wobei nur „on-board“ Sensoren verwendet werden. Auf dieser Basis werden nichtlineare, modellbasierte Regelungsansätze im Konfigurationsraum der Mechanismen vorgeschlagen und verglichen. Hierbei wird die Unteraktuierung dieser Mechanismen in den Ansätzen durch eine Transformation zur Eingangs-Ausgangs Nor-

malform speziell berücksichtigt.

Die entwickelten Methoden zur Modellgebung, Zustandsschätzung und Regelung, die in dieser Arbeit präsentiert werden, sind experimentell an einem humanoiden Roboter implementiert und validiert. Aufgrund der vielversprechenden Ergebnisse, legt diese Arbeit den Grundstein für die Analyse und Regelung von seilgetriebenen Kontinuumsmechanismen die als generisches Gelenk-Module in modularen robotischen Systemen eingesetzt werden sollen und kann damit den Beginn einer neuen Generation von Leichtbaurobotern einleuten.

Stichwörter: Kontinuums Mechanismen, Unteraktuierte Systemse, Robotische Systeme aus weichen Materialien

Contents

List of symbols

Throughout this thesis scalar quantities are denoted by plain letters. For vector and matrix quantities bold letters are used instead. Dots denote derivatives with respect to the time t (i.e. $\dot{\boldsymbol{r}} := \frac{d}{dt}\boldsymbol{r}$, $\ddot{\boldsymbol{r}} := \frac{d^2}{dt^2}\boldsymbol{r}$). Primes denote derivatives with respect to the configuration parameter ν (i.e. $\boldsymbol{r}' := \frac{d}{d\nu}\boldsymbol{r}$, $\boldsymbol{r}'' := \frac{d^2}{d\nu^2}\boldsymbol{r}$).

Symbols used in Chapter 1 & 2	description
$a_z \in \mathbb{R}$	width of the continuum (squared cross section)
$a_y \in \mathbb{R}$	depth of the continuum (squared cross section)
$d \in \mathbb{R}$	width of the top platform (squared cross section)
$L \in \mathbb{R}$	length of the continuum
$n \in \mathbb{N}$	number of degree of freedom (i.e. number of generalized coordinates)
$r \in \mathbb{N}$	number of tendons (number of inputs)
$r_t \in \mathbb{R}$	radius of the top platform

Symbols used in Chapter 3	description
$A \in \mathbb{R}$	cross sectional area of the continuum
${}_{\mathcal{B}}\boldsymbol{a}_{\mathrm{CoM}} \in \mathbb{R}^3$	linear acceleration vector of the CoM, respecting $\mathcal{B}$
$\boldsymbol{A}_{\mathcal{BN}}(\nu, t)$	material orientation along the centerline, respecting $\mathcal{B}$
$\boldsymbol{A}_{\mathcal{BH}}(\nu, t)$	orientation of the head, respecting $\mathcal{B}$
$\Delta\boldsymbol{A}_i \in \mathbb{R}^{3\times3}$	rotational difference between to matrices $\boldsymbol{A}$ and $\tilde{\boldsymbol{A}}$
$\mathcal{B}$	base frame $\mathcal{B}$ rigidly connected at the base platform of the mechanism, given in $\mathcal{O}$
$\mathcal{C}$	set of candidate poses $\boldsymbol{p}_i$ that fulfill certain constraints
$\boldsymbol{C}_r^e \in \mathbb{R}^{3\times\mathrm{ndof}}$	connector matrix to extract the positions of element e from $\boldsymbol{q}$
$\boldsymbol{C}_\phi^e \in \mathbb{R}^{3\times\mathrm{ndof}}$	connector matrix to extract the orientations of element e from $\boldsymbol{q}$
$\boldsymbol{C}^L \in \mathbb{R}^{\mathrm{ndof}\times6(k_{el}+1)}$	special connector matrix that extracts $\boldsymbol{q}_L$ from $\boldsymbol{q}$
$\mathcal{D}$	set of design poses, $\mathcal{D}$ is a subset of $\mathcal{C}$
$\boldsymbol{D}(\boldsymbol{q}) \in \mathbb{R}^{n\times n}$	nonlinear damping matrix
$E_x \in \mathbb{R}$	Young's modulus along the x-axis of the local coordinate system $\mathcal{N}$

$E_y \in \mathbb{R}$	Young's modulus along the y-axis of the local coordinate system $\mathcal{N}$
$E_z \in \mathbb{R}$	Young's modulus along the z-axis of the local coordinate system $\mathcal{N}$
${}_{\mathcal{B}}\boldsymbol{e}_x^N$, ${}_{\mathcal{B}}\boldsymbol{e}_y^N$, ${}_{\mathcal{B}}\boldsymbol{e}_z^N, \in \mathbb{R}^3$	base vectors of the frame $\mathcal{N}$ representing a material orientation.
${}_{\mathcal{B}}\boldsymbol{e}_{t,i}^H \in \mathbb{R}^3$, for $i = 1 \dots r$	tendon normal vector of the ith tendon.
${}_{\mathcal{B}}\boldsymbol{f}(\nu, t) \in \mathbb{R}^3$	distributed external force along the centerline respecting the coordinate system $\mathcal{N}$
${}_{\mathcal{B}}\boldsymbol{f}_c \in \mathbb{R}^6$	generalized external Cartesian force applied at the tip of the mechanism respecting the coordinate system $\mathcal{B}$
${}_{\mathcal{B}}f_x \in \mathbb{R}$	axial Cartesian force applied at the tip of a continuum, respecting the base frame $\mathcal{B}$
${}_{\mathcal{B}}\boldsymbol{f}_{min} \in \mathbb{R}^6$	lower bound for a feasible generalized Cartesian force applied at the tip of the mechanism
${}_{\mathcal{B}}\boldsymbol{f}_{max} \in \mathbb{R}^6$	upper bound for a feasible generalized Cartesian force applied at the tip of the mechanism
$\mathcal{B}$	
$G_t \in \mathbb{R}$	torsional shear modulus
$G_y \in \mathbb{R}$	shear modulus along the y-axis of the local coordinate system $\mathcal{N}$
$G_z \in \mathbb{R}$	shear modulus along the z-axis of the local coordinate system $\mathcal{N}$
$h_p \in \mathbb{R}$	pulley height with respect to the origin of $\mathcal{B}$ of the planar mechanism
$\mathcal{H}$	head frame rigidly connected at the head platform
$I_x \in \mathbb{R}$	polar moment of area for torsion along the x-axis of the local coordinate system $\mathcal{N}$
$I_y \in \mathbb{R}$	second moment of area for bending along the y-axis of the local coordinate system $\mathcal{N}$
$I_z \in \mathbb{R}$	second moment of area for bending along the z-axis of the local coordinate system $\mathcal{N}$
$\boldsymbol{J} \in \mathbb{R}^{3\times3}$	tensor of the second moment of areas of the continuum structure
${}_{\mathcal{H}}\boldsymbol{I}_H \in \mathbb{R}^3$	inertia tensor of the head
$k_{el} \in \mathbb{N}$	number of elements
$k_y \in \mathbb{R}$	scalar parameter for a kinematic coupling along y
$k_z \in \mathbb{R}$	scalar parameter for a kinematic coupling along z
$\boldsymbol{k}(\boldsymbol{q}, \dot{\boldsymbol{q}}) \in \mathbb{R}^n$	generalized forces of the system
$\boldsymbol{K}_{bt} \in \mathbb{R}^{3\times3}$	local stiffness matrix for bending and torsion
$\boldsymbol{K}(\boldsymbol{q}) \in \mathbb{R}^{n\times n}$	nonlinear stiffness matrix
$l_p \in \mathbb{R}$	pulley distance in z with respect to the origin of $\mathcal{B}$ of the planar mechanism
${}_{\mathcal{B}}\boldsymbol{l}(\nu, t) \in \mathbb{R}^3$	distributed external torque along the centerline respecting the coordinate system $\mathcal{B}$
m_H	head mass

M_x	internal torsional torque along the x-axis of the local coordinate system $\mathcal{N}$
M_y	internal bending torque along the y-axis of the local coordinate system $\mathcal{N}$
M_z	internal bending torque along the z-axis of the local coordinate system $\mathcal{N}$
${}_{\mathcal{N}}\boldsymbol{m}(\nu,t) \in \mathbb{R}^3$	internal torque along the centerline respecting the coordinate system $\mathcal{N}$
${}_{\mathcal{B}}\boldsymbol{m}_w \in \mathbb{R}^3$	external Cartesian torque applied at the tip of the mechanism respecting the coordinate system $\mathcal{B}$
$\boldsymbol{M}(\boldsymbol{q}) \in \mathbb{R}^{n\times n}$	massmatrix, positive definite
$n_m \in \mathbb{N}$	number of data points measured for the parameter identification problem
$n^e \in \mathbb{N}$	node e for $e = \{1, \ldots, k_{el}$
$n_{\text{red}} \in \mathbb{N}$	reduced number of generalized coordinates
$\text{ndof} \in \mathbb{N}$	number of elemental degree of freedom
$N \in \mathbb{R}$	normal force along the x-axis of local coordinate system $\mathcal{N}$
$\mathcal{N}$	beam frame attached to a point and a material orientation along centerline
${}_{\mathcal{N}}\boldsymbol{n}(\nu,t) \in \mathbb{R}^3$	internal force along the centerline respecting the coordinate system $\mathcal{N}$
${}_{\mathcal{B}}\boldsymbol{n}_w \in \mathbb{R}^3$	external Cartesian force applied at the tip of the mechanism respecting the coordinate system $\mathcal{B}$
$\boldsymbol{N}(\nu^e) \in \mathbb{R}^{3\times\text{ndof}}$	linear interpolation matrix for element e
$p \in \mathbb{N}$	number of desired parameters in the parameter identification problem
$\boldsymbol{p}_i \in \mathbb{R}^6$	exemplary pose in a six dimensional space
$\boldsymbol{P}(\boldsymbol{q}) \in \mathbb{R}^{n\times r}$	input coupling matrix
$Q_y \in \mathbb{R}$	shear force along the y-axis of local coordinate system $\mathcal{N}$
$Q_z \in \mathbb{R}$	shear force along the z-axis of local coordinate system $\mathcal{N}$
$\boldsymbol{q} \in \mathbb{R}^n$	vector of generalized coordinates
$\boldsymbol{q}_L \in \mathbb{R}^{\text{ndof}}$	vector that incorporates the elemental degree of freedom of the last node (at $\nu = L$)
$\boldsymbol{q}_{\text{red}} \in \mathbb{R}^{n_{\text{red}}}$	generalized coordinates of a reduced system
$r_{pulley} \in \mathbb{R}$	radius of a tendon pulley
${}_{\mathcal{B}}\boldsymbol{r}(\nu,t) \in \mathbb{R}^3$	position vector any point along the centerline
${}_{\mathcal{B}}\boldsymbol{r}_L = (x,y,z)^T \in \mathbb{R}^3$	position vector of the head
${}_{\mathcal{B}}\boldsymbol{r}^e$	position of the centerline at node e
${}_{\mathcal{B}}\bar{\boldsymbol{r}}(\nu,t)$	variational family of the position of the centerline respecting $\mathcal{B}$
${}_{\mathcal{B}}\boldsymbol{r}^{h,e}$	elemental shape function of element e for the centerline position
${}_{\mathcal{B}}\delta\boldsymbol{r}_{adm} \in \mathbb{R}^3$	admissible virtual displacement that fulfills the principle of virtual work of a system

${}_{\mathcal{B}}\delta\boldsymbol{r}(\nu,t)$	virtual displacement of the position of the centerline respecting $\mathcal{B}$
${}_{\mathcal{H}}\boldsymbol{r}_{t,i} \in \mathbb{R}^3$, for $i = 1 \dots r$	vector to the connection point of the ith tendon, respecting $\mathcal{H}$
${}_{\mathcal{B}}\boldsymbol{r}_{p,l} \in \mathbb{R}^3$	vector of the left pulley center respecting $\mathcal{B}$
${}_{\mathcal{B}}\boldsymbol{r}_{p,r} \in \mathbb{R}^3$	vector of the right pulley center respecting $\mathcal{B}$
${}_{\mathcal{H}}\boldsymbol{s}_{\mathrm{CoM}} \in \mathbb{R}^3$	vector to center of mass (CoM) of the head, respecting $\mathcal{H}$
${}_{\mathcal{B}}\boldsymbol{s}_{\mathrm{CoM}} \in \mathbb{R}^3$	vector to center of mass (CoM) of the head from $\mathcal{B}$, respecting $\mathcal{B}$
$T \in \mathbb{R}$	period of an general linear oscillation
${}^{\mathcal{B}}\boldsymbol{T}_{\mathcal{H}} \in \mathbb{R}^{4\times4}$	homogeneous transformation matrix describing the position and orientation of $\mathcal{H}$ respecting $\mathcal{B}$
${}^{\mathcal{B}}\boldsymbol{T}(\dots) \in \mathbb{R}^{4\times4}$	homogeneous transformation matrix for a translation or rotation depending on the variable used in ...
$\boldsymbol{e} \in \mathbb{R}^6$	pose error
$\boldsymbol{u} \in \mathbb{R}^r$	vector of inputs / vector of tendon tensions
${}_{\mathcal{B}}\boldsymbol{v}_{\mathrm{CoM}} \in \mathbb{R}^3$	linear velocity vector of the CoM, respecting $\mathcal{B}$
$\delta W \in \mathbb{R}$	total virtual work of a system
$\delta W^{stat} \in \mathbb{R}$	virtual work due to static forces and torques
$\delta W^{dyn} \in \mathbb{R}$	virtual work due to dynamic forces and torques
$\delta W^{ext} \in \mathbb{R}$	virtual work due to external forces and torques
$\delta W^{int} \in \mathbb{R}$	virtual work due to internal forces and torques
$\delta W^{tendon} \in \mathbb{R}$	virtual work of the tendon tension forces
$\delta W^{grav} \in \mathbb{R}$	virtual work of the gravitational forces
$\delta W^{w} \in \mathbb{R}$	virtual work of a generalized Cartesian force applied at the tip of the mechanism
$\delta W^{dyn,head} \in \mathbb{R}$	virtual work of the dynamic forces of the head
$\delta W^{dyn,beam} \in \mathbb{R}$	virtual work of the dynamic forces of the beam
x	x-coordinate of the position of the head
y	y-coordinate of the position of the head
z	z-coordinate of the position of the head
$\alpha \in \mathbb{R}$	scaling factor for $\boldsymbol{K}(\boldsymbol{q})$ in the Raleigh-Damping model
$\beta \in \mathbb{R}$	scaling factor for $\boldsymbol{M}(\boldsymbol{q})$ in the Raleigh-Damping model
${}_{\mathcal{B}}\boldsymbol{\gamma}(\nu,t) \in \mathbb{R}^3$	linear strain vector, respecting $\mathcal{B}$, ${}_{\mathcal{B}}\boldsymbol{\gamma}(\nu,t) = (\gamma_x(\nu,t),\, \gamma_y(\nu,t),\, \gamma_z(\nu,t))^T$
$\delta \in \mathbb{R}$	logarithmic decrement
$\epsilon \in \mathbb{R}$	kinematic variable describing a translation
$\zeta \in \mathbb{R}$	damping ration of the linearized system
$\eta \in \mathbb{R}$	kinematic variable describing a rotation along z
θ_x	Euler angle along the x-axis of $\mathcal{H}$
θ_y	Euler angle along the y-axis of $\mathcal{H}$
θ	Euler angle along the y-axis of $\mathcal{H}$, in the planar case
θ_z	Euler angle along the z-axis of $\mathcal{H}$
$\iota \in \mathbb{R}$	kinematic variable describing a rotation along x
${}_{\mathcal{B}}\boldsymbol{\kappa}(\nu,t) \in \mathbb{R}^3$	curvature vector of the material orientation, respecting $\mathcal{B}$
$\nu \in \mathbb{R}$	reference arc length

$\nu^e \in \mathbb{R}$	element coordinate $\nu^e \in [-1, 1]$
$\phi \in \mathbb{R}$	kinematic variable describing a rotation along y
${}_{\mathcal{B}}\boldsymbol{\phi}(\nu, t)$	orientation vector to express the material orientation along the centerline, respecting $\mathcal{B}$
${}_{\mathcal{B}}\hat{\boldsymbol{\phi}}(\nu, t) = -{}_{\mathcal{B}}\hat{\boldsymbol{\phi}}(\nu, t) \in \mathbb{R}^{3\times3}$	skew symmetric representation of the orientation vector, respecting $\mathcal{B}$
${}_{\mathcal{B}}\bar{\boldsymbol{\phi}}(\nu, t) \in \mathbb{R}^3$	variational family of the material orientation along the centerline respecting $\mathcal{B}$
${}_{\mathcal{B}}\delta\boldsymbol{\phi}(\nu, t) \in \mathbb{R}^3$	virtual displacement of the material orientation along the centerline respecting $\mathcal{B}$
${}_{\mathcal{B}}\delta\boldsymbol{\phi}_{adm} \in \mathbb{R}^3$	admissible virtual rotation that fulfills the principle of virtual work of a system
${}_{\mathcal{B}}\boldsymbol{\phi}_L \in \mathbb{R}^3$	orientation vector at $\nu = L$ i.e. the tip of the mechanism
${}_{\mathcal{B}}\boldsymbol{\phi}^e$	material orientation along the centerline at node e
${}_{\mathcal{B}}\boldsymbol{\phi}^{h,e}$	elemental shape function of element e for the material orientation along the centerline
$\Delta\boldsymbol{\phi}_i \in \mathbb{R}^3$	axis angle representation of a delta rotation $\Delta\boldsymbol{A}_i$
$\rho \in \mathbb{R}$	material density of the continuum
$\boldsymbol{\chi} \in \mathbb{R}^p$	desired parameters in the parameter identification problem
$\omega_0 \in \mathbb{R}$	Eigenfrequency of the linearized system
Ω_e	element set $\Omega_e = \{\nu \,\vert\, n^e < \nu < n^{e+1}\}$
${}_{\mathcal{B}}\boldsymbol{\omega}(\nu, t) \in \mathbb{R}^3$	rotational velocity of the material orientation, respecting $\mathcal{B}$

Symbols used in Chapter 4	description
$b \in \mathbb{R}$	threshold used within a principal component regression
$\boldsymbol{B} \in \mathbb{R}^{r\times r}$	motor inertia matrix of the tendon actuation system
$c_i \in \mathbb{R}$	parameter for the smooth static friction model
$d \in \mathbb{N}$	polynomial order
$d_{v,i} \in \mathbb{R}$	scalar parameter for the viscous friction part in the friction model
${}_{\mathcal{B}}\boldsymbol{e}^{\mathcal{H}}_{t,i} \in \mathbb{R}^3$	unitary tendon direction vector of the i th tendon
$\boldsymbol{E} \in \mathbb{R}^{r\times r}$	transmission matrix of the tendon actuation system
$\Delta f_i \in \mathbb{R}$	absolute prediction error of the i th component of $\boldsymbol{f}$
$\mathcal{F}$	set of admissible wrenches
$\boldsymbol{f}(\boldsymbol{q}) \in \mathbb{R}^{n_{\text{red}}}$	generalized nonlinear force resulting from a deformation of the continuum used in the reduced model
$\boldsymbol{J}_{\chi,q} \in \mathbb{R}^{6\times n_{\text{red}}}$	configuration Jacobian that maps generalized velocities $\dot{\boldsymbol{q}}$ to generalized Cartesian velocities $\dot{\boldsymbol{\chi}}$
$k \in \mathbb{N}$	number of polynomial coefficients
$\boldsymbol{K}_s \in \mathbb{R}^{n_{\text{red}}\times n_{\text{red}}}$	symmetric part of the stiffness matrix $\boldsymbol{K}(\boldsymbol{q})$
$\boldsymbol{K}_t \in \mathbb{R}^{r\times r}$	linear stiffness matrix of the tendons
$\boldsymbol{l}(\boldsymbol{q}) \in \mathbb{R}^r$	vector of tendon length
$\boldsymbol{q}_0 \in \mathbb{R}^n$	initial configuration for the generalized coordinates $\boldsymbol{q}$ resembling a straight configuration of the continuum.
$r_{m,i} \in \mathbb{R}$	motor pulley radius of the i th tendon actuator

${}_{\mathcal{H}}\boldsymbol{r}_{t,i} \in \mathbb{R}^3$	position of the i th tendon hinge at the top platform, respecting $\mathcal{H}$
${}_{\mathcal{H}}\boldsymbol{r}_{p,i} \in \mathbb{R}^3$	position of the i th tendon contact point on the pulley at the lower platform, respecting $\mathcal{B}$
$w_i \in \mathbb{R}$	transmission ratio of the i th tendon actuator
$\delta W^s \in \mathbb{R}$	virtual work of the nonlinear spring mechanism in the reduced model
$\boldsymbol{x} \in \mathbb{R}^k$	regressor row used within a polynomial regression
$\boldsymbol{X} \in \mathbb{R}^{n_m \times k}$	regressor matrix used within a polynomial regression
$\boldsymbol{\beta} \in \mathbb{R}^k$	vector containing all polynomial coefficients
$\boldsymbol{\epsilon} \in \mathbb{R}^{n_m}$	vector of residuals which is minimized within a polynomial regression problem
$\boldsymbol{\theta}_m \in \mathbb{R}^r$	vector of tendon actuator positions
$\kappa(\boldsymbol{X}) \in \mathbb{R}$	condition number of the regressor matrix
$\boldsymbol{\Lambda} \in \mathbb{R}^{k \times k}$	information matrix of a regression problem
$\boldsymbol{\tau}_m \in \mathbb{R}^r$	vector of tendon actuator torques
$\boldsymbol{\tau}_{fric} \in \mathbb{R}^r$	vector of frictional torques in the tendon actuation system
$\tau_{c,i} \in \mathbb{R}$	Coulomb friction part of the friction model
$\boldsymbol{\tau}_q \in \mathbb{R}^n$	generalized torques
$\boldsymbol{\Phi} \in \mathbb{R}$	scalar optimality criterion
${}_{\mathcal{B}}\dot{\boldsymbol{\chi}} \in \mathbb{R}^6$	generalized Cartesian velocity respecting $\mathcal{B}$

Symbols used in Chapter 5	description
$a_{i,j}^k \in \mathbb{R}$	distance between the mean column norm i and norm j for sensor configuration k
${}_{\mathcal{S}}\tilde{\boldsymbol{a}} \in \mathbb{R}^3$	acceleration measurement of the IMU, expressed in $\mathcal{S}$
${}_{\mathcal{S}}\boldsymbol{a} \in \mathbb{R}^3$	true acceleration of the IMU, expressed in $\mathcal{S}$
${}_{\mathcal{S}}\boldsymbol{a}_b \in \mathbb{R}^3$	acceleration bias of the IMU, expressed in $\mathcal{S}$
${}_{\mathcal{S}}\boldsymbol{a}_n \in \mathbb{R}^3$	acceleration noise of the IMU, expressed in $\mathcal{S}$
${}_{\mathcal{B}}\boldsymbol{a}_g \in \mathbb{R}^3$	acceleration due to gravity, expressed in $\mathcal{B}$
$\boldsymbol{A}_{\mathcal{BS}} \in \mathbb{R}^{3\times3}$	rotation matrix between sensor frame $\mathcal{S}$ and base frame $\mathcal{B}$
$\boldsymbol{A}d_{\mathcal{TB}} \in \mathbb{R}^{6\times6}$	adjoint matrix to transform wrenches expressed in $\mathcal{T}$ to $\mathcal{B}$
$\boldsymbol{C} \in \mathbb{R}^{z+r\times15}$	partial derivative of the measurement with respect to the augmented state
$\boldsymbol{e}_l(\boldsymbol{q}) \in \mathbb{R}^{z+r}$	error vector between the measured and the model length measurements
$\boldsymbol{K}_{cs} \in \mathbb{R}^{z\times z}$	calibration matrix of the additional length sensors that relates the measured voltage to a relative change in length
$\boldsymbol{K}_{ti} \in \mathbb{R}^{15\times z+r}$	Kalman gain matrix at time instant ti
$\boldsymbol{K}_{luen} \in \mathbb{R}^{z+r\in z+r}$	gain in the Luenberger type observer
$\Delta\boldsymbol{l} \in \mathbb{R}^{z+r}$	relative length measurement
$\Delta\boldsymbol{l}_0 \in \mathbb{R}^{z+r}$	initial relative length measurement
$\tilde{\boldsymbol{l}} \in \mathbb{R}^{z+r}$	length measurement, provided by length sensors

$\Delta \boldsymbol{l}_n \in \mathbb{R}^{z+r}$	sensor noise of the length sensors
$\tilde{\boldsymbol{l}}_t \in \mathbb{R}^r$	length measurements corresponding to the tendon length
$\boldsymbol{l}_{t,0} \in \mathbb{R}^r$	initial tendon length that corresponds to an initial pose $\boldsymbol{q}_0$
$\tilde{\boldsymbol{l}}_s \in \mathbb{R}^z$	relative change in length of the additional length sensor
$\boldsymbol{l}_{s,0} \in \mathbb{R}^z$	initial length of the additional length sensors
$\boldsymbol{L} \in \mathbb{R}^{15\times 12}$	partial derivative of the augmented nonlinear state space with respect to the process noise
$n_i^k \in \mathbb{R}$	current norm of the column $i = \{x, y, z, \theta_x, \theta_y, \theta_z\}$ of the coupling matrix for sensor configuration k
$\bar{n}_i^k \in \mathbb{R}$	mean norm of the column $i = \{x, y, z, \theta_x, \theta_y, \theta_z\}$ of the coupling matrix for sensor configuration k
$\delta n_i^k \in \mathbb{R}$	distribution width of the norm of the column $i\{x, y, z, \theta_x, \theta_y, \theta_z\}$ of the coupling matrix for sensor configuration k
$\boldsymbol{Q} \in \mathbb{R}^{z+r\times z+r}$	measurement covariance
$\mathcal{S}$	coordinate system of the inertial measurement unit (IMU)
$\tilde{\boldsymbol{s}} \in \mathbb{R}^z$	measured voltage of the additional length sensor
$\boldsymbol{s}_n \in \mathbb{R}^z$	sensor noise of the additional length sensors
$\boldsymbol{s}_{ti} \in \mathbb{R}^{z+r}$	vector of discrete time process noise at time instant ti
$\boldsymbol{S} \in \mathbb{R}^{6\times 6}$	process covariance matrix
$\mathcal{T}$	force torque sensor coordinate system
$\boldsymbol{T}_{\mathcal{TB}} \in \mathbb{R}^{4\times 4}$	homogeneous transformation of between the base frame $\mathcal{B}$ and the sensor frame $\mathcal{T}$
${}_{\mathcal{T}}\boldsymbol{w}_{\mathrm{FTS}} \in \mathbb{R}^6$	measured wrench (forces and torques) of the force torque sensor expressed in $\mathcal{T}$
${}_{\mathcal{T}}\boldsymbol{w}_{\mathrm{FTS,B}} \in \mathbb{R}^6$	bias of the force torque sensor measurement
${}_{\mathcal{T}}\boldsymbol{w}_{\mathrm{FTS,N}} \in \mathbb{R}^6$	noise of the force torque sensor measurement
${}_{\mathcal{B}}\boldsymbol{w}_{\mathrm{FTS}} \in \mathbb{R}^6$	forces and torques applied at the base and expressed in $\mathcal{B}$
${}_{\mathcal{B}}\boldsymbol{f}_{\mathrm{FTS}} \in \mathbb{R}^3$	forces applied the base and expressed in $\mathcal{B}$
${}_{\mathcal{B}}\boldsymbol{w}_{\mathrm{FTS}}^{\mathcal{H}} \in \mathbb{R}^6$	forces and torques applied at the head frame and expressed in $\mathcal{B}$
$\boldsymbol{u}_{ti} \in \mathbb{R}^6$	discrete time input at time instant ti used in the Extended Kalman Filter
$\boldsymbol{V} \in \mathbb{R}^{z+r\times z+r}$	partial derivative of the measurement with respect to the measurement noise
$\boldsymbol{w}_{ti} \in \mathbb{R}^{z+r}$	vector of measurement noise at time instant ti
$\boldsymbol{y}_{ti} \in \mathbb{R}^{z+r}$	vector of the outputs at time instant ti used in the Extended Kalman Filter
$\tilde{\boldsymbol{\theta}}_m \in \mathbb{R}^r$	measurement of the motor position sensor
$\boldsymbol{\theta}_n \in \mathbb{R}^r$	noise of the motor position sensor
$\boldsymbol{\Sigma} \in \mathbb{R}^{15\times 15}$	partial derivative of the augmented nonlinear state space with respect to the augmented state
$\boldsymbol{\psi}_{ti} \in \mathbb{R}^{15}$	augmented discrete state at time instant ti used in the Extended Kalman Filter

$\boldsymbol{\Psi}_{ti} \in \mathbb{R}^{15\times15}$	state covariance matrix at time instant ti
$\boldsymbol{\Psi}^{q}_{0,0} \in \mathbb{R}^{6\times6}$	Initial state covariance matrix of the pose $\boldsymbol{q}$ part of the state
$\boldsymbol{\Psi}^{v}_{0,0} \in \mathbb{R}^{3\times3}$	Initial state covariance matrix of the linear velocity ${}_{\mathcal{B}}\boldsymbol{v}$ part of the state
$\boldsymbol{\Psi}^{a,\omega}_{0,0} \in \mathbb{R}^{6\times6}$	Initial state covariance matrix of the IMU bias $\boldsymbol{a}_b$, $\boldsymbol{\omega}_b$ part of the state
$\boldsymbol{\varsigma} \in \mathbb{R}^{15}$	augmented nonlinear state-space used in the Extended Kalman Filter
${}_{\mathcal{S}}\tilde{\boldsymbol{\omega}} \in \mathbb{R}^{3}$	measurement of the angular velocity of the IMU, expressed in $\mathcal{S}$
${}_{\mathcal{S}}\boldsymbol{\omega} \in \mathbb{R}^{3}$	true angular rates of the IMU, expressed in $\mathcal{S}$
${}_{\mathcal{S}}\boldsymbol{\omega}_b \in \mathbb{R}^{3}$	bias of the angular rates of the IMU, expressed in $\mathcal{S}$
${}_{\mathcal{S}}\boldsymbol{\omega}_n \in \mathbb{R}^{3}$	noise of the angular rates of the IMU, expressed in $\mathcal{S}$

Symbols used in Chapter 6	description
$\boldsymbol{A} \in \mathbb{R}^{12\times12}$	linear dynamic matrix employed in the $\mathscr{H}_\infty$ controller
$\hat{\boldsymbol{A}}_j \in \mathbb{R}^{12\times12}$	affine dynamic matrices employed in the $\mathscr{H}_\infty$ controller
$\boldsymbol{B} \in \mathbb{R}^{12\times4}$	linear input matrix employed in the $\mathscr{H}_\infty$ controller
$\hat{\boldsymbol{B}}_j \in \mathbb{R}^{12\times4}$	affine input matrices employed in the $\mathscr{H}_\infty$ controller
$\boldsymbol{c}(\boldsymbol{q}) \in \mathbb{R}^{r}$	constraint equation employed in the servo constraint approach
$\bar{\boldsymbol{C}}(\boldsymbol{q}) \in \mathbb{R}^{r\times r}$	matrix of Coriolis and centrifugal terms of the input-output normal form
$\mathbf{e}(s) \in \mathbb{C}^{6}$	control error employed in the $\mathscr{H}_\infty$ controller
$\bar{\boldsymbol{f}}(\boldsymbol{q}) \in \mathbb{R}^{r}$	contribution (generalized forces) of the continuum spring to the input-output normal form
$G(s) \in \mathbb{C}$	transfer function of a linearized plant
$\mathbf{G}_p(s) \in \mathbb{C}^{6+31}$	perturbable system employed in the $\mathscr{H}_\infty$ controller
$\boldsymbol{h}(\boldsymbol{q}) \in \mathbb{R}^{r}$	nonlinear function that describes relationship of the outputs and the generalized coordinates
$\boldsymbol{H}(\boldsymbol{q}) \in \mathbb{R}^{r\times n}$	partial derivative of the output equations $\boldsymbol{h}(\boldsymbol{q})$ with respect to the generalized coordinates
$\mathbf{K}(s) \in \mathbb{C}^{4\times6}$	controller employed in the $\mathscr{H}_\infty$ controller
$\mathbf{K}_\gamma(s) \in \mathbb{C}^{4\times6}$	controller gain tuned using a mixed sensitivity approach employed in the $\mathscr{H}_\infty$ controller
$\mathbf{K}_\mu(s) \in \mathbb{C}^{4\times6}$	controller gain tuned using μ synthesis employed in the $\mathscr{H}_\infty$ controller
$\bar{\boldsymbol{k}}(\boldsymbol{q},\dot{\boldsymbol{q}}) \in \mathbb{R}^{r}$	summary of the nonlinear generalized forces of the input-output normal form
$\boldsymbol{k}_t \in \mathbb{R}^{m}$	part of the static equilibrium along the directions of task variables $\boldsymbol{q}_t$
$\boldsymbol{k}_p \in \mathbb{R}^{n-m}$	part of the static equilibrium along the directions of remaining variables $\boldsymbol{q}_p$
$\tilde{\boldsymbol{k}}(\boldsymbol{u},\boldsymbol{q}) \in \mathbb{R}^{n+r}$	augmented static equilibrium condition that is solved to guarantee positive tendon tensions

$\boldsymbol{K}_{u,p} \in \mathbb{R}^{r\times r}$	linear matrix of the proportional controller applied in the fast control loop
$\boldsymbol{K}_{u,d} \in \mathbb{R}^{r\times r}$	linear matrix of the derivative controller applied in the fast control loop
$\boldsymbol{K}_{p} \in \mathbb{R}^{r\times r}$	positive definite control gain matrix of the proportional control action used in the partial feedback linearization
$\boldsymbol{K}_{d} \in \mathbb{R}^{r\times r}$	positive definite control gain matrix of the derivative control action used in the partial feedback linearization
$\boldsymbol{K}_{c,p} \in \mathbb{R}^{r\times r}$	positive definite control gain matrix of the proportional control action used in the composite control approach
$\boldsymbol{K}_{c,d} \in \mathbb{R}^{r\times r}$	positive definite control gain matrix of the derivative control action used in the composite control approach
$\mathsf{n}(s) \in \mathbb{C}^{6}$	noise signal employed in the $\mathscr{H}_\infty$ controller
$\mathsf{N}(s) \in \mathbb{C}^{16\times 12}$	closed loop transfer function employed in the $\mathscr{H}_\infty$ controller
$m \in \mathbb{N}$	number of task coordinates
$\bar{\boldsymbol{M}}(\boldsymbol{q}) \in \mathbb{R}^{r\times r}$	mass matrix of the input-output normal form
$\boldsymbol{N}_t \in \mathbb{R}^{r\times r}$	Nullspace projector of the task variables
$PD(s) \in \mathbb{C}$	PD controller expressed as a transfer function in the frequency domain
$PD^{\alpha}(s) \in \mathbb{C}$	fractional order PD controller
$\tilde{PD}^{\alpha}(s) \in \mathbb{C}$	integer-order approximation of a fractional order PD controller
$\mathsf{P}(s) \in \mathbb{C}^{51\times 51}$	augmented plant employed in the $\mathscr{H}_\infty$ controller
$\bar{\boldsymbol{P}}(\boldsymbol{q}) \in \mathbb{R}^{r\times r}$	input coupling matrix of the input-output normal form
$\boldsymbol{P}_t \in \mathbb{R}^{m\times r}$	part of the coupling matrix that projects the tendon tension into directions of $\boldsymbol{q}_t$
$\boldsymbol{P}_p \in \mathbb{R}^{n-m\times r}$	part of the coupling matrix that projects the tendon tension into the direction of $\boldsymbol{q}_p$
$\boldsymbol{q}_r \in \mathbb{R}^{n-r}$	vector of remaining coordinates
$\boldsymbol{q}_d \in \mathbb{R}^{n}$	desired generalized coordinates (desired pose)
$\boldsymbol{q}_t \in \mathbb{R}^{n-m}$	task coordinates
$\boldsymbol{q}_p \in \mathbb{R}^{n-m}$	remaining coordinates used in the tendon tension distribution
$\mathsf{r}(s) \in \mathbb{C}^{6}$	control reference signal employed in the $\mathscr{H}_\infty$ controller
$s \in \mathbb{C}$	Laplace variable used to describe the dynamics of linear transfer functions
$\mathsf{u}(s) \in \mathbb{C}^{4}\ u_i > 0\ \forall i$	control inputs (tensile forces) employed in the $\mathscr{H}_\infty$ controller
$\boldsymbol{u}_d \in \mathbb{R}^{r}$	novel control input of the slow control input
$\boldsymbol{u}_{\mathrm{FTS}} \in \mathbb{R}^{r}$	projected force-torque sensor measurement onto the tendon tension forces
$\bar{\boldsymbol{u}}_d \in \mathbb{R}^{r\times r}$	novel control input applied in the feedback linearization approach
$\boldsymbol{u}_{d,ff} \in \mathbb{R}^{r}$	feedforward control action employed in the composite control approach
$\boldsymbol{u}_{d,fb} \in \mathbb{R}^{r}$	feedback control action employed in the composite control approach based on an inverse model

$\boldsymbol{u}_{pre} \in \mathbb{R}^r$	desired pretension forces
$\boldsymbol{u}_{int} \in \mathbb{R}^r$	internal tensions of the systems
$\mathbf{v}(s) \in \mathbb{C}^6$	feedback signal employed in the $\mathscr{H}_\infty$ controller
$\mathbf{w}(s) \in \mathbb{C}^6$	augmented input employed in the $\mathscr{H}_\infty$ controller
$\mathbf{w}_\Delta \in \mathbb{C}^{31}$	uncertainty input employed in the $\mathscr{H}_\infty$ controller
$\mathbf{W}_n \in \mathbb{C}^{6\times6}$	dynamic weight on the noise employed in the $\mathscr{H}_\infty$ controller
$\mathbf{W}_S \in \mathbb{C}^{6\times6}$	sensitivity weight
$\mathbf{W}_T \in \mathbb{C}^{6\times6}$	complementary sensitivity weight employed in the $\mathscr{H}_\infty$ controller
$\mathbf{W}_{KS} \in \mathbb{C}^{4\times4}$	input weight employed in the $\mathscr{H}_\infty$ controller
$\mathbf{y}(s) \in \mathbb{C}^6$	measurable output employed in the $\mathscr{H}_\infty$ controller
$\boldsymbol{y} \in \mathbb{R}^r$	vector of outputs
$\mathbf{z}(s) \in \mathbb{C}^6$	augmented output employed in the $\mathscr{H}_\infty$ controller
$\mathbf{z}_\Delta \in \mathbb{C}^{31}$	uncertain output employed in the $\mathscr{H}_\infty$ controller
$\boldsymbol{\Delta}(s) \in \mathbb{C}^{31\times31}$	uncertainty matrix employed in the $\mathscr{H}_\infty$ controller
$\boldsymbol{\Pi} \in \mathbb{R}^{n\times n}$	permutation matrix employed for the choice of outputs in this thesis
$\boldsymbol{\tau}_{ss} \in \mathbb{R}^r$	control action of the slow control loop
$\boldsymbol{\tau}_{fs} \in \mathbb{R}^r$	control action of the fast control loop
$\tilde{\boldsymbol{\tau}}_{fric} \in \mathbb{R}^r$	model dry friction used in a model-based friction compensation in the fast control loop
$\tau_L \in \mathbb{R}$	control input in the preliminary study of the fractional order controller
$\boldsymbol{\tau}_q \in \mathbb{R}^n$	generalized torques
$\boldsymbol{\phi}(\boldsymbol{q}) \in \mathbb{R}^n$	nonlinear coordinate transformation used in the input-output normal form
$\varphi_m \in \mathbb{R}$	phase margin of the open control loop
$\omega_{cg} \in \mathbb{R}$	desired cross over frequency of the open control loop

CHAPTER 1

Introduction

Robotic research consists of a number of diverse disciplines, for example engineering, mathematics, biology and computer science to name just a few. Comparably diverse are also the robotic hardware systems which originate in rigid-link robotic manipulators with a serial kinematic chain, that were mainly motivated to automate manufacturing lanes, including tasks that demand high accuracy, fast execution cycles, or the handling of heavy objects. As the field of robotics evolved, different robotic operation principles were developed, including robots with a parallel kinematic structure or smaller robots with lightweight links, to mention some examples. Each of these examples is designed based on some advantages over classic rigid-link serial kinematic robots, but also disadvantages arose that originate in their design. For example, the tool center point stiffness and the precision of parallel kinematic robots is superior, compared to a serial kinematic one, in contrast, their workspace volume is comparably small. The smaller design space of lightweight robots enabled them new applications closer to the human but the lower mechanical stiffness, especially in the joints, induces oscillations during motions or interactions that need to be actively controlled.

The commonality of the mentioned systems are rotary joint axes that enable a motion. Structural deformation in these systems is neglected as its amplitude is very small compared with the overall motion. Hence, the computation of the robot's workspace is a purely geometric problem.

Another branch in the field of robot kinematics are redundant robots in which the term "redundant" relates to a number of $n > 6$ joints. If n is slightly bigger than 6, e.g. $n = 7$ the term redundant robots is used, whereas if n is substantially bigger than 6, the term hyper-redundant is used. The first hyper-redundant robotic systems were built by Anderson *et al.* [1] or Chirikjian *et al.* [2]. These robots have been inspired by snakes or tentacles and their targeted applications are manipulation scenarios in which the manipulator tangles around objects or weaves through obstacles, like it cannot be done by classic serial link manipulators.

On a macroscopic scale, so called continuum robots resemble hyper-redundant robots, as both systems possess a snake like shape, however, the motion of a continuum robot is not generated by the actuators with rotary joints serially attached to each other. An early work by Robinson and Davies [3] defined the term "continuum robot" as it follows:

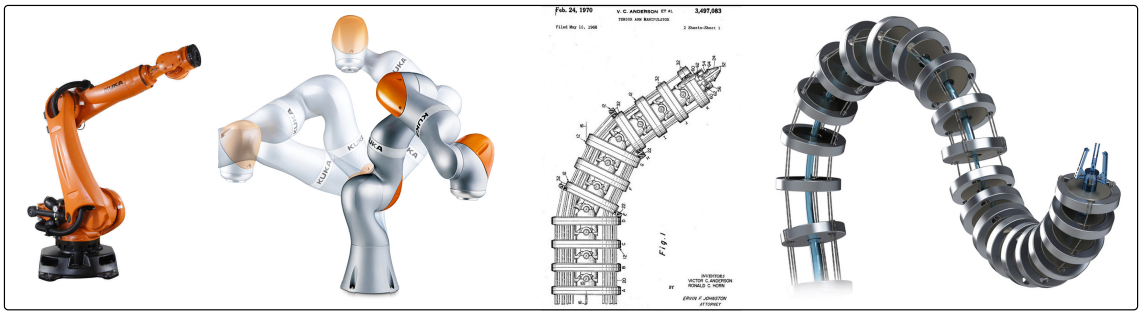

Figure 1.1.: Overview of the classified robotic systems. First image: Rigid link robot with serial kinematic joint arrangement and $n = 6$ joints. Image is taken from [7]. Second image: Kuka LWR-IWA, a light-weight robotic arm with $n = 7$ joint axes. Image is taken from [8].Third image: Tensor arm, a hyper redundant manipulator. Image is taken from [1]. Fourth image: Continuum manipulator, snake-like. Image is taken from [9].

Continuum robots do not contain rigid links and identifiable rotational joints. Instead the structures bend continuously along their length via elastic deformation and produce motion through the generation of smooth curves, similar to the tentacles or tongues of the animal kingdom.

Early systems of that kind are the "Octarm" [4] or the "Clemson Elephant Trunk" [5] which are, similar to hyper-redundant robots, primarily motivated by grasping and manipulation of objects with varying size, inspired by an elephant trunk. From an actuation point of view, continuum robots can be classified into mechanisms with intrinsic actuation, which are based on pneumatic, hydraulic and shape-memory alloys or mechanisms with extrinsic actuation, realized by tendons, multiple push-pulling rods or precurved concentric tubes. Especially tendons with sophisticated tendon routing meet the apparently conflicting requirement of a reduced manipulator diameter with a freely designable workspace, which often appears in medical applications [6]. An overview of the classified robotic systems is given in Fig. 1.1.

In the course of this thesis, a class of tendon-driven continuum mechanisms is analysed. The involved components will be explicitly described in Chapter 2 and the following definition is given for their Characterization:

Definition: *Tendon-Driven Continuum Mechanism.*
In contrast to continuum robots, the terminology continuum mechanism denotes a smaller but thicker, continuously deformable unit and a continuum robot might consist of several, serially attached continuum mechanisms. Even though the structural element is deformed while moving in a continuum mechanism, a snake like profile is not present in a single unit. Furthermore, the investigated mechanism class is tendon-driven and the number of tendons is less compared to the number of degrees of freedom and therefore yields that the mechanisms are underactuated.

This kind of mechanism is applied, for example, as finger joints in robotic [10] or prosthetic [11] multi-fingered hands to enable an adjustment of the grasp to unknown object geometries. They are applied as quadrupedal spines [12] or full manipulators [13, 14] for which several mechanisms are serially attached to each other. Furthermore, parallel continuum robots possess a similar design, with multiple continua in between two rigid platforms [15]. Some of the mentioned robotic systems are illustrated in Fig. 1.2.

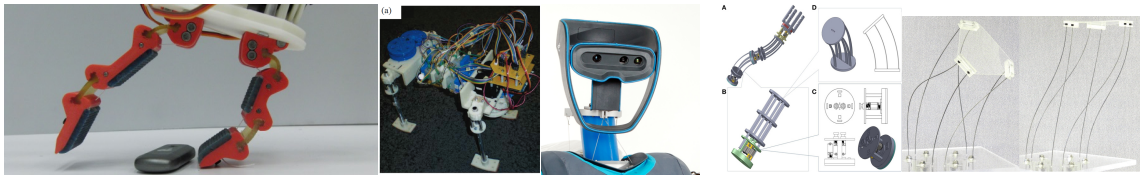

Figure 1.2.: First image: Two-fingered hand from [10]. Second image: Quadropedal spine from [12]. Third image: Robotic neck from [16]. Fourth image: Robotic manipulator Simba from [14]. Fifth image: Parallel continuum robot from [15].

More recently, a tendon-driven elastic continuum mechanism (ECM) was developed for DLR's upper body humanoid robot David (see Fig. 1.3) which is build from passively compliant mechanical elements to enable the robot to dynamically interact with the environment without harming the hardware. The ECM is made out of silicone and the passive compliance of the mechanism features mechanical robustness, which enables the system to handle collisions or shocks with ease, while the elastic structure acts as energy container as it partially compensates for the gravitational forces.

The common properties that qualify a continuum mechanism for the use in previous works [10, 11, 12, 13, 14, 15, 16] are the high dexterity of the continuum, the small design space, the incorporated mechanical robustness and the inherent gravity compensation. Naturally, with these advantages, there are also challenges that need to be overcome. Within the motion of a continuum, an elastic deformation is involved and thus the analysis of the workspace is not a pure geometric problem anymore. Instead, static equilibrium equations need to be solved that depend on the geometry of the structure, the material properties of the structure as well as the loading applied to the structure, including optional masses. In general, a continuum structure reacts to any kind of applied loading with a deformation. Hence, unforeseen collisions can be handled by the structure without damaging the hardware, as the actuators cannot constrain all deformation directions. This is an advantage and is termed "mechanical robustness". On the other hand, this property implies that there are deformations along directions which cannot be actively controlled, yielding an inherent underactuation that needs to be accounted for. For several applications, the continuum needs to be controlled to reach a position, a full pose or even, that the shape conforms to a desired one. Usually, these poses or shapes cannot be described by a finite set of joint axes and therefore a geometric forward and inverse kinematics is generally not applicable to compute task space poses from actuation quantities. As a result, pose or state estimation methods are necessary.

A literature review is presented in the following. On the basis of the challenges from above, the review will consecutively deal with modeling, state estimation and control of continuum mechanisms and whole robots.

1.1. Related work

As outlined in the title and described by the paragraph above, this section aims to present the most relevant literature with respect to the present thesis. Thus, the core area of the presented state of the art will be modeling, state estimation and control of continuum mechanisms used in robotics. Peripheral research areas such as motion planning of continuum robots [17], workspace design and optimization of continuum robots [18] or trajectory generation [19] will not be discussed.

1.1.1. Modeling of continuum mechanisms

A structural deformation is involved in the motion of a continuum mechanism and thus a rigorous model involves methods from the field of continuum mechanics. Depending on the shape, material and geometry of the structure, i.e. the structural properties, different assumptions need to be taken to describe it. Continuum mechanisms are usually slender structures whose extent in length is considerably larger than its diametrical extent. Hence, they are approximated as flexible beams which imply a kinematic arrangement with a centerline along which several material surfaces are ordered. The overall motion is then reduced to a motion of any point and any material surface along the centerline. Furthermore, the structural properties define the amount of shear, axial, bending and torsional deformation which is involved in the motion and thus highly affect the complexity of the model.

A rigorous formulation of an elastic beam undergoing large deformations is discussed in the seminal work of Antmann [20] and is termed "Special Cosserat Beam". Besides the incorporated multi-axial deformation, advanced interaction forces and torques can be modeled, including buoyancy forces acting on the mechanism [21] or actuated tendons which are guided along the mechanism causing external distributed loads [22, 23]. The static workspace design is then tied to the problem of solving a nonlinear ordinary differential equation which describes the configuration of a loaded beam. In the field of continuum robotics, these equations are solved commonly by applying finite difference schemes [21, 22, 24]. Renda *et. al* [21] reports a computation time of 28 min for 1 s simulation time on a desktop computer. The SOFA framework [25] uses another well known discretization method termed "the finite element method" to simulate the deformation of general soft structures under external loading. A volume based discretization is applied here as general bodies can be incorporated. For a beam-like structure with 930 nodes (yielding 2730 DoF), [26] reports 23 ms for a computation cycle. By applying the propagation introduced by Rucker *et al.* [27], the Jacobian matrix of a continuum robot, which relates actuation variables to the position and orientation of the centerline, can be computed and propagated through a geometrically exact model which improves the computation time essentially. A common drawback however remains as these models bring the necessity of carefully identified material parameters whereas commonly, the Young's Modulus alone is not sufficient to describe the deformation properties of the material completely.

A contrary approach to rigorous modeling are reduced models which approximate the deformation characteristic of the mechanism within a limited workspace or under limited loading conditions. The first reported approximations are based on the assumption of a fixed backbone curve of the manipulator and its shape is approximated by a serpenoid [28] or as a circular arc for static [29] and dynamic [30] models. The assumption that the centerline resembles a circular arc implies a constant curvature along the shape. For mechanisms with high axial and shear stiffness with almost negligible operating weight, no external forces and favorable actuators arrangement, the constant curvature assumption is fully justified. Mechanisms of that kind are for instance snake-like nickel-titanium manipulators [31], concentric tube robots [32] from medical robotics, or slender tendon-driven systems as proposed in [33]. The advantage of this approach is a fixed kinematic mapping as the configuration space, i.e. the curvatures can be related to actuation variables and task space variables in real time [34], which is a favorable property in control. Furthermore, the material properties can be easily mapped by a linear stiffness in this configuration space, yielding a simple static model. A major disadvantage of this geo-

metric approach is that zero curvature is not admissible, which often corresponds to the initial (straight) configuration of a mechanism. Approaches that avoid this property are based on approximations of the deformation geometry by multivariate polynomials [35], or a switching logic [36]. Further extensions of the constant curvature kinematics are the integration of gravitational forces [37] and the augmentation of the model to extensible systems [38]. Piecewise constant curvature, to model the kinematics of a segment, is presented by Mahl *et al.* [39]. However authors limit their approach to three degrees of freedom per "piece" and a static model is not addressed, which limits the applicability. Kang *et al.* [40] approximate each segment of their continuum mechanism inspired by an octopus as a parallel mechanism with two rotational and one translational degree of freedom, yielding a known kinematic mapping and a defined workspace. However, a discussion is missing that matches the static properties of the real system onto the parallel structure.

Recent alternatives for a complexity reduction are empirical modeling approaches where an abstract input-output behavior is learned from measured data. The inputs are commonly actuation torques or actuator positions and the corresponding output are the position and orientation of the mechanisms tip. Popular models are based on neural networks [41, 42] to approximate the static characteristics from actuation forces, or a Gaussian mixture model [43] to relate actuator lengths to end positions of the manipulator. The drawback of an empirical model is that the learned behavior is valid only for the trained data. For example, if only reachable configurations of a mechanism are used for training, the resulting empirical model might not be valid if external forces act on the system. Moreover, physical properties like the symmetry of a derived stiffness or compliance matrix may not be taken into account which limit their applicability.

As a result of the presented works, a dynamic modeling approach that incorporates bending, shear, torsion and compression deformations, in combination with nonlinear actuation forces, is missing, especially if computational efficiency is demanded. Therefore, the following question arises:

Q 1 Can we capture the static and dynamic behavior of the system in a uniform, computationally efficient, reduced model without losing accuracy and dynamic effects?

1.1.2. State estimation of continuum mechanisms

In contrast to rigid link robots, the motion of continuum mechanisms cannot be described by a finite set of joint axes and therefore a geometric forward and inverse kinematic is generally not applicable to compute task space poses from actuation quantities. More specifically, a pose along the continuum must be computed by solving a set of equilibrium equations which asks for carefully identified material parameters as outlined in Section 1.1.1.

The full state of a continuum mechanism is relevant, but by no means exhaustive, for a nonlinear dynamic feedback controller in task space. However, the requirement to fully measure the state in a continuum mechanism is hard to fulfill, as even in classical rigid manipulators this is rarely the case because there are usually no velocity sensors present. Additionally, the state of a continuum mechanism usually differs from measurable quantities and asks for state estimation techniques. Mahoney *et al.* [44] define the state of a continuum robot as its shape, which is specified as the position and material orientation along the backbone of the mechanism. The majority of the works presented in the

literature deal with pure shape estimation, as their control approaches are rather kinematic controllers than dynamic ones and thus corresponding temporal derivatives are not needed.

In this work, a primary interest is the estimation of the end pose and velocity of a continuum mechanism for the application in a nonlinear dynamic feedback controller. The pose is contained in the shape and therefore approaches from the literature that discuss shape estimation are of interest. Additionally, pose and velocity estimation approaches from the broader robotic community will be discussed briefly.

Shi *et al.* [45] present a comprehensive overview and classify shape estimation approaches in two categories. The first category includes shape estimations based on external sensors whereas the second category comprises algorithms based on internal sensors. Internal sensors are defined as sensors which are mechanically connected to the mechanism. External sensors are for example a stereo camera system that are inertially fixed and measures the position of markers distributively attached along the shape of the mechanism [46] or single markers attached to the tip [47]. Further approaches are 3D image segmentations to extract the shape [48]. In this thesis however, the target application of continuum mechanisms are mobile systems and thus, shape estimation techniques based on external sensors will not be treated.

A commonly used approach to estimate the shape of a continuum mechanism is a combination of the actuation sensors and a model of the deformation of the mechanism. Herein, the popular assumption of a (segment wise) deformation with constant curvature is applied, using a static model and tendon tension sensors [49], or a kinematic model based on actuation length measurements [38, 50], passive cables along the shape [51] and Fiber Bragg sensors [52]. If tendon length measurements are applied for the shape estimation of multiple segments, the kinematic model might result in a tangled tendon configuration which can be resolved as suggested by [34, 53]. Further approaches include a position sensor on the tip of the mechanism fused in a Kalman Filter for accurate orientation sensing of a tendon-driven constant curvature robot [54]. Another approach is presented by Goldman *et al.* [55] which combines a constant curvature kinematic model to predict the current shape. This prediction is then used in combination with actuation force measurements to predict the real shape in a support vector machine to account for friction and contact forces. Strain sensors based on fabrics are applied by Case *et. al* [56] for shape and stiffness estimation of a cylindrical continuum mechanism in combination with actuator forces/torques. Again, the estimation of the shape is only validated for a constant curvature kinematics without torsion and thus has only limited use.

To overcome the limitations induced by the constant curvature assumption, a piecewise constant curvature is proposed by Kim *et. al* [57] in combination with Fiber-Bragg sensors distributively placed along the mechanism. As they approximate the piecewise constant curvatures by basis functions with constant coefficients, the estimation problem can be formulated as a regression, whereas optimal sensor locations can be found in simulation experiments. Piecewise constant curvature however is only valid for kinematics without torsion and therefore limits the usage. If the material parameters are known with high accuracy, geometrically exact models are applicable. Concurrent shape estimations approaches that rely on rigorous static models apply force-torque sensors or inclinometers [58] in a planar case and Fiber-Bragg-sensors [59] for the spatial case.

As outlined previously, the tip pose of a continuum mechanism and its corresponding velocity, i.e. the state of the tip, is of major interest. This state may be estimated without knowing any properties of the continuum, if a state estimation concept known

from mobile robots is applied. These concepts utilize often an Inertial Measurement Unit (IMU) in combination with length or position measurements fused within an Extended Kalman Filter (EKF), for example in multicopters [60], hand held joysticks [61], tumbling satellites [62] or legged robots [63]. These approaches fuse data with high rates of the IMU and data with lower rates of the length or position measurements. However, some of the reported approaches use the 2D position information of a camera system attached to the mechanism and thus impose a major integration and algorithmic effort. As a result, the following major question for the thesis arises:

Q 2 Which methods are applicable to estimate the relevant states of the system to use them in feedback control?

1.1.3. Control of continuum mechanisms

In the following, control approaches for continuum mechanisms and robots are reviewed. Most recently, Chikhaoui and Burgner-Kahrs [64] outlined that "*Paradoxically, while challenges regarding control of soft continuum robots were identified in the literature . . . , few research is clearly focused on control.*" Indeed, comparably less control approaches are presented that address (unmodeled) nonlinear dynamic effects, actuator limits, actuator dynamics or underactuation.

The majority of the control approaches are kinematic controllers which utilize a model-based Jacobian that relates desired task space positions to desired actuator positions, see e.g. [65]. In these approaches, the controller can therefore be closed locally in each actuator which simplifies the implementation and reduces the effect of model-inaccuracies. On the other hand, dynamic effects from the continuum-like endeffector inertia or the stiffness of the mechanism are neglected, which might effect the closed loop behavior, especially during the transient phase of a motion. For slender, rather stiff continuum manipulators with lightweight endeffectors, the concept might be ideal. In contrast, for mechanisms with considerable mass and compliance, this concept implies a inferior performance. A data-driven approach to derive the Jacobian is presented by Yip *et al.* [66]. Here, the Jacobian is defined by a numerical derivative, which is continuously estimated based on measurements of an external camera and actuator force readings. No assumptions on the kinematic, static or dynamic of the manipulator are necessary and desired tip positions are reached in an real-time optimal control. The approach was extended by Yip *et. al* [67] to include the control of interaction forces at the mechanisms tip. The experimental results cover complex spatial motions which shows that the proposed approach can cope with the nonlinearities present in the mechanism. However, an accurate position-tracking of the robots tip, solved by an external camera, and a three degrees of freedom force-sensor, attached to the tip, are highly demanding and limit the approach to be extended to other mechanisms, which is also the case for [47] were the same sensor information are used in an Extended Kalman Filter to estimate the Jacobian.
A quasistatic control approach is presented by Bosman *et. al* [68] based on a volumetric finite element model of the SOFA framework [25]. The actuator variables are introduced as unilateral constraints and a suitable control action is found by minimizing the difference between the current and the desired tip position, using the static model. The method is tested in simulation on tendon-driven and pneumatic continuum robots. Basically, the method computes the amount of force necessary to deflect the system to a desired pose and therefore resembles a feed forward control scheme whereas disturbances such as unmodeled friction or external contacts, cannot be addressed and deteriorate the approach.

A similar approach is presented by Melingui *et al.* [69] where the static model of a pneumatically driven continuum robot with two sections is learned with a Neural Network and an adaptive controller, again a Neural Network, to translate Cartesian errors into the controllers output. As the approach is time-consuming, fast trajectories cannot be followed. Thus, the authors propose a improvement of the approach in [70] based on a support vector regression for the adaptive part.

Approaches for continuum robots that control the interaction behavior with the environment are also published. Mahvash *et al.* [71] propose such a method for a concentric tube robot with three degrees of freedom. The approach minimizes the error between the measured tip position and the virtual desired position, induced by the desired tip force, computed with a static model. The desired position herein is ensured by a position controller, using a model-based Jacobian to map desired tip positions to desired actuator positions. Another compliant motion controller is developed by Goldman *et al.* [55] and asymptotic stability of the force error is proved by Lyapunov's direct method. With this control architecture, a continuum robot segment can be driven to a configuration that minimizes its interaction with unknown wrenches, acting at unknown locations. The controller uses the difference between the measured and the predicted unperturbed force to move in a direction to minimize the environment interaction.

In the previous approaches, the presented control algorithms are formulated majorly in the actuation space whereas unmodeled effects or disturbances are not accounted for. Furthermore during fast motions, it might be favorable to include more information about the model, for example to compensate gravitational and elastic forces or feed forward inertia forces of the continuum. The first dynamic control approach is presented by Gravagne *et. al* [30] which reflects inertia and viscous friction properties of the actuator to the configuration space of the slender, mass less continuum robot modeled by constant curvature. A setpoint vibration-damping controller is formulated and asymptotic stability can be shown for the linearized system. A configuration-space impedance controller is presented by Toscano *et. al* [72] for a single section of the pneumatically driven bionic handling assistant. The configuration space is defined kinematically by a constant curvature of the backbone. As this assumption implies an inherent singularity in straight configuration (zero curvature), authors report that the controllers gains need to be kept low to avoid instability. A similar approach is reported in [73] which develops a nonlinear controller in the configuration space of the robot with asymptotic tracking error convergence. The controller is developed based on a Lyapunov function in an adaptive control framework. The developments assume full knowledge of the system parameters and planar motions only which highly limits the approach. Furthermore, the singularity in the configuration space is not addressed. A dynamic task space controller is studied Mousa *et al.* [74]. Here, a model-based robust sliding-mode controller for a tendon-driven continuum manipulator is designed, based on a geometrically exact Cosserat Beam, in a planar scenario. The control goal is a translatory position along the shear direction. As it is a slender mechanism, the geometrically exact model is questionable, whereas the underactuation in the task space is not treated at all in the simulation results presented by the authors.

Dynamic controllers are also reported in the actuator space. Braganza *et al.* [75] apply a continuous asymptotic tracking-control strategy for uncertain nonlinear systems with proved asymptotic tracking and without any model of their pneumatically driven Octarm. They make use of an integrated feed forward term, which is designed as a Neural Network based, on back-propagation to meet the boundedness requirement and to compensate for unwanted dynamic effects. Most recently, Falkenhahn *et. al* [50] present and experimen-

Figure 1.3.: Upper body humanoid robot David. Right image is taken from [76]

tally verify model-based dynamic controllers in the actuator space with a cascaded control architecture. The outer MIMO controller uses a feedback linearization to cancel the known dynamics of the model, which are the torques due to inertia, Coriolis and gravitation. The inner controller, locally in each actuator, then ensures that the desired pressures from the outer loop are tracked accurately.

In summary, a control framework in the task-space of a continuum mechanism that accounts for dynamic motions and underactuation is not dealt with so far. Thus, the following research question arises:

Q 3 Which model-based control methods enable set point regulation of an underactuated continuum mechanism with nonlinear tendon-coupling ?

1.2. Contribution

The contribution of the present thesis is to provide answers to the posted research questions for modeling (**Q 1**), state estimation (**Q 2**) and control (**Q 3**). The developments to answer each of the questions will be experimentally tested and discussed on a novel flexible humanoid neck [16], based on an elastic continuum mechanism (ECM), which is made out of silicone. The ECM currently serves a neck joint of DLR's humanoid robot David (see Fig. 1.3). Furthermore, a planar system of the neck has also been developed, which will serve as a second experimental platform. In the following, the contribution is separately highlighted for each of the core areas, modeling, state estimation and control. Table 1.1 summarizes the publications in which cover the contributions described.

1.2.1. Modeling

The contribution of the developed modeling approach is twofold. The first approach is a rigorous model that shall be used majorly for analysis of tendon-driven elastic continuum mechanisms, such as workspace computations or analysis of the transient behavior. Based on a nonlinear Timoshenko beam-formulation, the continuum is approximated as an elastic beam that undergoes large deformations and is located in between two rigid platforms and subjected to nonlinear tendon tension forces and a rigid body on top of the moving platform. In contrast to prior works that assume also beam-like structures (see

paragraph 1.1.1), the static and dynamic analysis of the nonlinear beam is treated with the numerically more robust and mechanical more natural finite element method. Thus it provides equations with a reduced size, compared to a volumetric discretization, and a common structure, which resembles the reduced model of the second modeling approach. As the beam finite element model contains the last property, controllers derived later on can be equally applied to this kind of model.
Two scientific works [77, 78] are already published that discuss the static and dynamic equations for a planar case. This chapter generalizes these works to the spatial case, whereas the static and dynamic equations are given exemplary for two systems with identified material parameters. Furthermore, four use cases are elaborated, which have not been published so far.

The second contribution, regarding modeling, is the derivation of computationally efficient, reduced nonlinear dynamic model based on an abstraction of the tendon-driven elastic continuum mechanism as a rigid body on top of a nonlinear spring system with equilibrium poses, equivalent to the real continuum. An experimental identification procedure is developed to ensure matching equilibrium poses of the nonlinear spring system and the real continuum.
The procedure is presented in the publication [79] and it is applicable to more general identifications of continuum manipulators, patented in [80]. The identification of the nonlinear spring system, introduced in [79], is based on a multivariate polynomial approach. Motivated by the serial kinematic structure of classical robots, an extension is introduced in this thesis, which combines a serial kinematic structure and linear stiffnesses in each of the joints, which heavily simplifies the resulting dynamic equation. The main advantage of the proposed kinematic structure, over approximations known from literature, is that workspace has a simple geometric solution (in contrast to the parallel kinematic structure) and the kinematic mapping is singularity free (in contrast to constant curvature). This extension is also identified experimentally and a discussion is presented, which compares both approaches.

1.2.2. State estimation

The end pose and corresponding velocity are necessary for model-based nonlinear dynamic feedback controllers for this class of mechanisms and are of major interest in this work. Hence, this pose and velocity define the state of the system which is contrary to (longer) continuum robots, where the shape is defined as the state. The temporal evolution of the shape, see paragraph 1.1.2, is of minor interest here.
This thesis contributes to the field of state estimation by implementing and comparing different techniques to estimate the tip position, orientation and corresponding velocities for tendon-driven continuum mechanisms of the defined class, whereas only internal sensors are utilized. Herein, geometric, static and dynamic state estimation approaches are proposed for pose and velocity estimation. In this respect, a novel kinematic mapping is proposed with 4 degrees of freedom, which is singularity free, and is therefore a strong alternative to the common constant curvature approach. To estimate the full six DoF pose geometrically, additional sensors are placed on the system by a proposed placement strategy to improve the estimation quality. Furthermore, a dynamic pose and velocity estimation algorithm is proposed, based on an Extended Kalman Filter, which neglects any knowledge about the deformation of the continuum. Their performance and their applicability w.r.t. real-time control are assessed and discussed in experiments.

The sensor placement strategy in combination with the geometric estimation concept

for a six DoF pose estimation and the dynamic estimation concept based on an Extended Kalman Filter have been submitted for publication in [81].

1.2.3. Control

It is highlighted in paragraph 1.1.3 that comparably less research is focused on motion control for continuum mechanisms. Although a large number of continuum mechanisms have been built for different applications, kinematic controllers based on an static inverse model are suggested. The latter corresponds to a feed forward controller and external disturbances or dynamic effects in the robots transient are not handled by the controller. Model-based approaches which make use of known dynamic properties of the system, to perform fast motions in the task space, are not presented whereas underactution is not specifically treated in case where it is necessary. Hence, the control approaches developed in this thesis present dynamic controllers in the task or configuration space of the robot. The model-based approaches incorporate knowledge of the reduced models, developed in the corresponding chapter. As a first study, well known approach from the field of automatic control is applied, a so called $\mathscr{H}_\infty$ controller. By a structured treatment of the model-nonlinearities, they can be considered in the design of the controller yielding control approach with robust performance. The controller has been published in [82] and is used in this thesis to provide a comprehensive comparison. Thereafter, the underactuation present in the continuum mechanisms of the present class is specifically treated by a transformation to the input-output normal form, which has been neglected in other works, as highlighted in paragraph 1.1.3. A strong feature of the model-based controller is the provision of the control action that deforms the mechanism. In steady-state, this contribution to the control action is high with the result that the feedback gains can be set comparably low, which adds robustness to the system. Furthermore, the linearization by feedback enables control strategies from linear control theory. In this respect, the concept of fractional order control is investigated in [83] which extends a general linear PD controller with an additional coefficient to account for robustness and a fast transient similarly. The control approach involving feedback linearization is published in [84]. Here, an extension is presented that allows to apply the controller onto a beam-finite element model to close the gap towards to the presented rigorous models. Then, a second approach is introduced based on a feed forward term which compensates for static forces and torques of the model. Both approaches are intensively evaluated and compared in experiments.

Table 1.1.: Publications of the present thesis

Reference	Description
Reinecke *et al.* [16]	A structurally flexible humanoid spine based on a tendon-driven elastic continuum." IEEE International Conference on Robotics and Automation, pages 4714-4721, May 2016.
Deutschmann *et al.* [83]	Robust motion control of a soft robotic system using fractional order control. International Conference on Robotics in Alpe-Adria Danube Region. Springer, Cham, 2017.

Deutschmann *et al.* [84]	Position control of an underactuated continuum mechanism using a reduced nonlinear model. 2017 IEEE 56th Annual Conference on Decision and Control, pages 5223-5230, Dez. 2017.
Deutschmann *et al.* [77]	A method to identify the nonlinear stiffness characteristics of an elastic continuum mechanism." IEEE Robotics and Automation Letters (3)3: pages 1450-1457, Jan. 2018.
Deutschmann *et al.* [79]	Reduced Models for the Static Simulation of an Elastic Continuum Mechanism." IFAC-PapersOnLine 51(2), pages 403-408, Mar. 2018.
Eugster and Deutschmann [78]	A nonlinear Timoshenko beam formulation for modeling a tendon-driven compliant neck mechanism." PAMM 18.1 (2018): e201800208.
Shu *et al.* [82]	Robust H-∞ control of a tendon–driven elastic continuum mechanism via a systematic description of nonlinearities." IFAC-PapersOnLine 51(22), pages 386-392, Sept. 2018.
Deutschmann *et al.* [81]	Six DoF pose estimation for a tendon-driven continuum mechanism without a deformation model." IEEE Robotics and Automation Letters (4)4: pages 3425-3432, Jul. 2019.

1.3. Organization of the work

The thesis is structured by six chapters and a graphical illustration of its organization is given in Fig. 1.4. Chapter 2 will define the class of "tendon-driven elastic continuum mechanisms". By the end of this chapter, the reader knows the class of mechanisms and involved components, their properties and arrangement. This is of major importance as the developed models, estimation algorithms and controllers are specifically developed for this class and are not generally applicable to continuum mechanisms. Afterwards, a rigorous model is developed based on the assumption that the system can be approximated by a clamped nonlinear Timoshenko beam with a considerable platform mass at its free end and nonlinear actuation forces acting on this platform. This model is developed in Chapter 3, whereas parameter identification is presented to provide a realistic simulation. In the end, four use-cases are elaborated, each of which embodies a motivation for the chapters "Modeling for control" and "State estimation". A discussion of the amount of computational time necessary for the simulation of static or dynamic equations is also presented. The current implementation is computationally inefficient and therefore not suitable for model-based control. Therefore, the subsequent Chapter 4 develops a reduced dynamic model, based on assumptions which heavily simplify the rigorous model and result in nonlinear rigid body dynamics which are computationally efficient and structurally favorable to be applied in model-based control approaches. The goal of the thesis is to develop dynamic controller for set point regulation of the mechanisms pose. Thus, the state of the system is necessary and different state estimation algorithm are derived and compared in Chapter 5. Several internal sensor information are fused within different techniques that build on kinematic, static or dynamic models. Based on the computationally

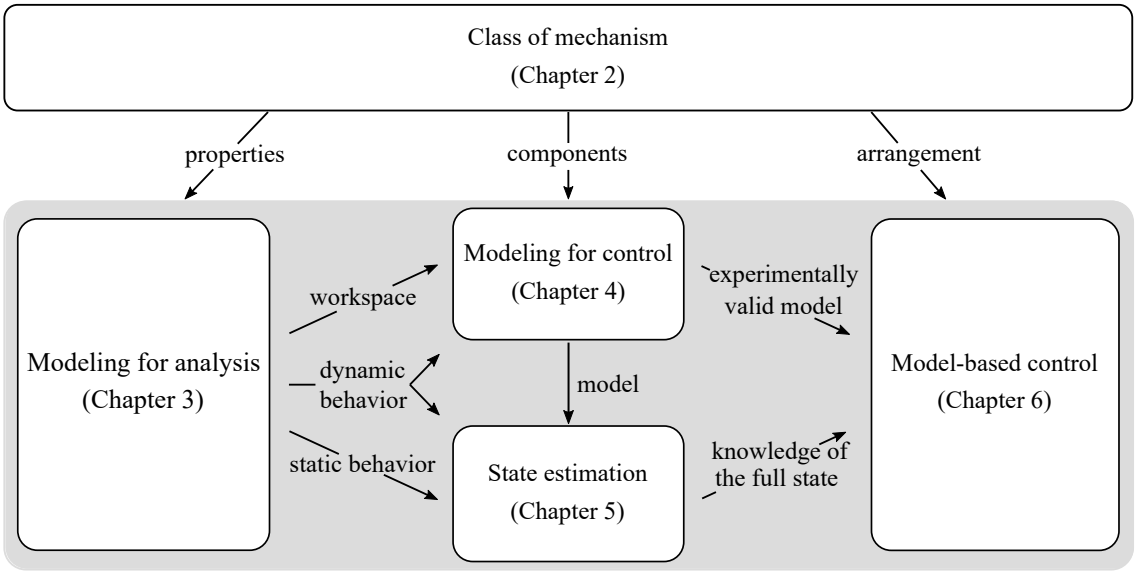

Figure 1.4.: Organization of the subsequent chapters and their interaction.

efficient model and the ability to estimate the full state, dynamic control approaches are derived, discussed and compared in Chapter 6 that enables set point regulation.

CHAPTER 2

Class of mechanism

This chapter will describe the class *tendon-driven elastic continuum mechanism*, which is in focus mechanism of the developed methods for modeling and control of present thesis. The description given in this chapter will start by introducing the different components that constitutes a tendon-driven elastic continuum mechanism. In this respect, the chapter will start by a general description of the different components involved in this system class. Afterward, the two prototypes that are specifically investigated in this thesis will be presented whereas the incorporated hardware will be introduced. In the last part of the chapter, the notation for the mathematical developments of this thesis is presented.

2.1. Components

An overview of the involved components of the class of mechanism is illustrated in Fig. 2.1 which indicates that the main components can be classified to belong either to the *tendon actuation system* or the *Elastic Continuum Mechanism* (ECM) which will be explained separately in the following.

2.1.1. Elastic Continuum Mechanism (ECM)

Generally speaking, the mechanism can be described as a continuum structure in between two rigid platforms, see Fig. 2.1. In this respect, the lower platform is considered to be fixed to the ground whereas the top platform is able to move due to the structural compliance of the continuum. The moving platform on the top is furthermore considered as a rigid-body. The continuum structure on the other hand is considered to possess enough structural compliance to allow for deformations along all axes, i.e. bending and torsion is induced by actuation torques, shear and compression is induced by actuation forces.

Rigid body

The rigid platform and additional masses connected to it, which are for example additional sensors, are summarized to one rigid body. It possesses a considerable mass and inertia and thus cannot be neglected. The tendons are connected to the rigid platform to introduce

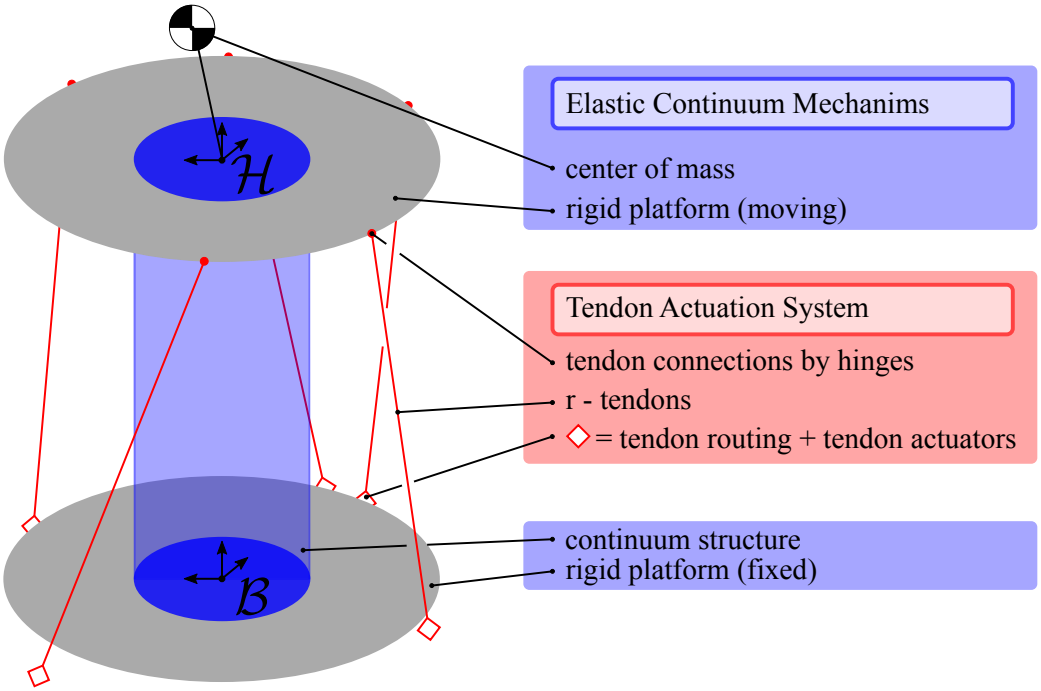

Figure 2.1.: Schematic overview to illustrate the components of a *tendon-driven elastic continuum mechanism.*

a loading that deforms the continuum and to move the rigid body. The interconnections to the tendons are hinges which implies a known loading as a result of a tendon tension. The connection between the rigid body and the continuum structure is rigid as well and it ensures a firm transmission of the introduced loading. The location of the hinges, the center of mass (CoM), the inertia and the mass of the rigid body is considered to be known accurately from their respective CAD-files.
The lower platform of the mechanism is considered to be rigid and not moving, whereas its absolute position and orientation and the location of the tendon pulleys attached to it is considered to be known.

Continuum structure

The continuum structure is made of an elastically deformable material whereas the material properties are chosen to ensure no plastic deformation throughout the desired workspace. Furthermore, the continuum is considered as a beam like structure due its considerable length compared to the dimension of cross section. The purpose of the continuum structure is to provide sufficient elastic deformations which enable a rotational motion of the top rigid platform. In general, a continuum possesses an infinite number of degree of freedom which needs to be actuated by respective loading conditions. The mechanisms in the present class are loaded at the top end only whereas the lower end is clamped to the ground and therefore resemble a cantilever beam which deforms spatially. Due to its structural flexibility brings a kinematic coupling of several deformation directions, for example a rotational motion might induce a translational motion of the top end of the continuum.
The geometric data of the continuum structure is known by the corresponding CAD-files

of the additional molding equipment including the initial length, the cross sectional area and the second moment of inertia. Furthermore, it is assumed that the molding process ensures no air enclosures in the silicone body yielding a homogeneous material with isotropic material parameters. As large deformations are involved in the motion, the material properties especially the stiffness characteristics are not known and thus, need to be identified.

2.1.2. Tendon actuation system

The system is actuated by $r \in \mathbb{N}$ tendons and these tendons are connected to the moving platform by hinges. The goal of the actuation is to move the rigid body on top relative to the lower platform. Thus, the tendons need to be routed by a pulley system which is rigidly connected to the lower platform, illustrated in Fig. 2.1. It can be observed moreover, that the tendons are stretched out from the lower to the top platform without a support or connection to the continuum structure. This implies a nonlinear coupling between the motion of the tendons and the motion of the continuum. In extension of the pulleys in the lower platform, the r tendon actuators are placed which generate tension forces. These actuators are for example rotary motor with a link sided pulley where the tendon is looped around. In this respect, it is assumed that actuator torques can be commanded directly and the actuator position can be measured.
As tendons can transmit pulling forces only, an antagonistic tendon arrangement is ensured and due to the theoretically infinite degree of freedom of the continuum, the r-tendons cannot actuate or constraint every motion direction which yield an underactuated system. Tendons provide the possibility to redirect the actuation force meaning that several pulleys or hinges can be utilized along the lower platform to route the tendon to specific actuator placement. However, it needs to be considered that the friction increases with every pulley-tendon interconnection [85]. For the control strategy later on, it is essential to measure the tendon tensions. This can be done with for example a conventional axial force sensor in the tendon path whereas the system class is considered to provide this possibility.

Summary: Properties of the mechanisms

The involved components described previously yield the following properties for the system class.

Property 1: Due to the compliance of the continuum a deformation along all axes is present as a reaction to any kind of loading applied onto the system.

Property 2: The rigid body possesses a considerable mass and inertia, a low stiffness to inertia ratio is present which yields, when dynamic motions are considered, that the dynamic effects of the complete system cannot be neglected.

Property 3: The utilized tendons are routed without additional tendon channels in the continuum or mountings on the continuum structure which results in a full coupling of the tendon tensions onto all Cartesian deformation directions and a nonlinear coupling of the motion of the rigid body and the motion of the tendons.

Property 4: The system is considered to be underactuated resulting from two characteristics. At first, the continuum structure provides sufficient elastic deformation ability such that the number of strictly positive tendon forces can not achieve

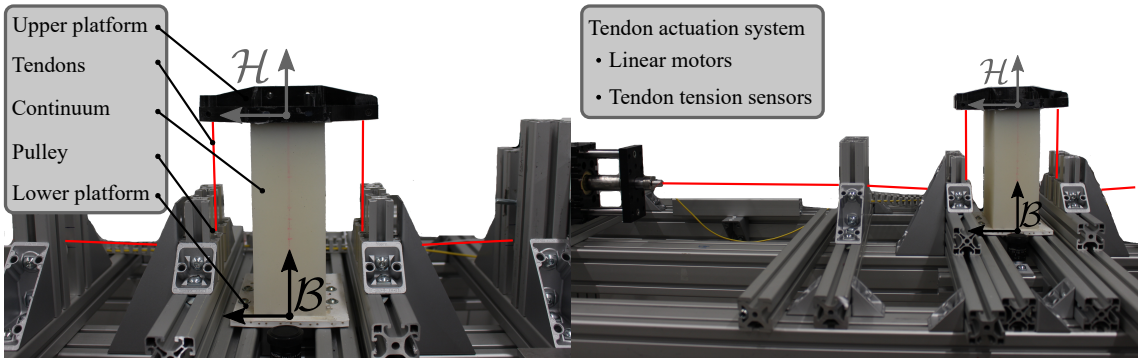

Figure 2.2.: Planar testbed built in the course of the thesis.

full actuation and there are deformation directions and oscillations possible which may not be controlled. Secondly, respecting the control goal which is to control the pose of the rigid body, the system might be underactuted for the control problem as well dependent on the number of tendons connected to the system.

Property 5: The motion of the overall system can not be measured directly by integrated sensors.

2.2. Prototype systems

In the course of the thesis, two specific testbeds have been developed and investigated which are a planar testbed, see paragraph 2.2.1, and a spatial testbed, see paragraph 2.2.2, which will be described briefly in the following. A more detailed description including all aspects involved in the design process of both prototypes can be found in [16].

2.2.1. Planar testbed

The planar testbed is depicted in Fig. 2.2 and it constitutes of an elastic continuum mechanism (ECM) and the tendon actuation system. A more detailed illustration of the ECM is given in Fig. 2.3. The rigid platforms of the ECM in the planar testbed are 3D printed whereas the top platform provides the possibility to mount additional masses and a marker target of a camera for calibration purpose. The continuum structure is molded from silicone whereas Dragon Skin® [86] is chosen as material. It is an addition-curing silicone with a Shore hardness of A30 and a 100% Young's modulus of $E_{100\%} = 600000\text{N/m}^2$. The geometrical shape of the continuum is rectangular and the dimensions of the mechanism are reported in [16] to be $L = 192$ mm, $d = 80$ mm, $a_z = 70$ mm, and $a_y = 123$ mm whereas the explanation of the dimension is given in Fig. 2.3. Since the silicone is highly hydrophobic material, adhesive bonding was not possible [87]. Therefore, form closure and a primer from Wacker was chosen to increase the adhesion. The mechanical design is based on the principle of surface enlargement, which is why anchor points and cavities are included in the base plate and the crossbeam, see Fig. 2.3 on the right. The elastomer is able to flow in and around those structures and achieve a high degree adhesion. The overall testbed is depicted in Fig. 2.2. Dyneema® tendons were chosen, because they are simple to configure and allow high tendon forces [85]. To route the tendons to both sides

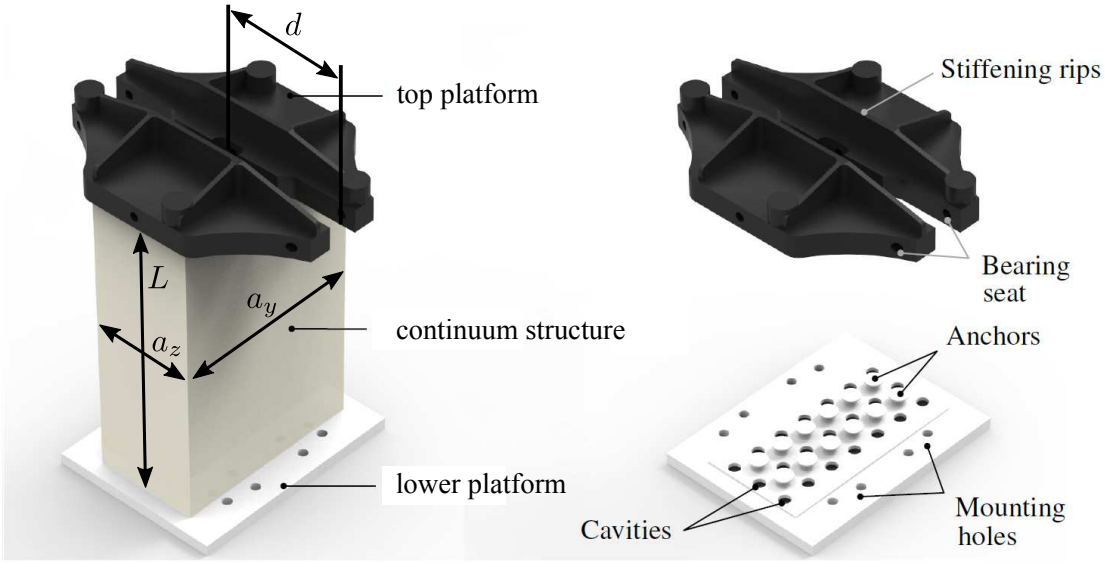

Figure 2.3.: Design of the planar prototype made out of silicone

with low friction, bearing supported pulleys from Carlstahl® are utilized. To connect the tendons properly to the top platform, bearing seats with pulleys are placed, where the tendons are looped around. To generate the tendon tensions, two linear actuators from Linmot® [88] with incorporated position sensors are equipped with an axial force sensor from Omega® [89] to measure position and external force at each slider. The prototype system can be controlled in MATLAB/Simulink® using real time workshop on a QNX-neutrino 6.5 target with which desired actuator forces could be set directly. An EtherCAT bus sends the generated control signals to the current controller of the linear motors and receives sensor information within a control cycle of 1kHz. By applying EtherCAT as an industrial standardized real time communication protocol, a high degree of determinism is ensured. The sensor information are the actuator positions and tendon tension forces. The mean error of the force sensors and the position encoders is ± 0.1 N and ± 0.01 mm respectively.

2.2.2. Spatial testbed

The spatial testbed was specifically designed as a neck of the humanoid robot David of the DLR, see Fig. 2.4 and will be described in the following. Thus, the rigid body of the system is the head of the humanoid and its mass and inertia results from the design of the head, i.e. the arrangement and the selection of the housings, the camera and other sensors as well as the tendon hinges. Additional mounting points on the head provide the possibility to attach a marker target for pose tracking or additional masses on the head to evaluate the model and control algorithms later on. The lower platform and the top platform are manufactured from aluminum to ensure an accurate placement of the head with respect to the rest of the humanoid robot. The same silicone is used to form the continuum structure as in the planar testbed and the surface in between silicone and aluminum is designed comparably including cavities and anchor-points that ensure a firm interconnection. The geometrical shape of the continuum is cylindrical, with a radius of $r_t = 31$ mm and a length of $L = 0.095$ mm, as reported in [16]. The complete

Figure 2.4.: Left: Tendon-driven elastic continuum mechanism as a humanoid robotic neck [16]. This robot is designed to explore concepts for manipulation based on elastic actuation. Right: Picture taken from the newspaper FAZ [76].

setup can be seen in Fig. 2.5. Steal tendons are used for the spatial system which are looped around the hinges of the top platform. For this system, the advantage to use tendon actuation is observable as it provides that the tendon actuators can be located in the back of the mechanism. However, tendon actuation also inherits higher friction and additional designing effort, especially when a tendon has to be fully guided in the different deformation directions of the mechanism. For this purpose a two degree of freedom (2DoF) pulley is utilized, illustrated in Fig. 2.5. Due to the routing through a hollow rotation axis which is supported by bearings, the pulley on the top can turn in two directions. Together with the change of the surrounding angle, it provides a large workspace with low friction. The tendon actuators applied here are rotational brush less permanent magnetic servo motors from RoboDrive® (ILM25) with harmonic drive gears and a transmission ratio of 100:1. FAS tendon force sensors [90] are used in the tendon path to measure the tendon tension. The motors are equipped with encoders to measure the motor angle and thus also the change in tendon length. The system is controlled in 3 kHz control cycle using real time workshop on a real-time-linux target and the implementation of the controllers is done with Matlab/Simulink® which provides an interface to directly command desired motor torques.

2.3. Summary

The previous chapter introduced the components involved in a general *tendon-driven elastic continuum mechanism* as well as the components used in the specific test setups discussed in the present thesis. As a result of this section, the components of the system, their arrangement and characteristics are known which are: The mechanism consists of a continuum structure in between two rigid platforms. The geometric parameters of the mechanism are known, however the material properties of the continuum need identification. The lower platform of the mechanism is considered to be fixed to the ground with known position and orientation. A finite number of r-tendons actuate the system in an antagonistic arrangement and the routing of the tendon is designed without additional tendon-channels or mountings on the continuum structure. The result of this property is

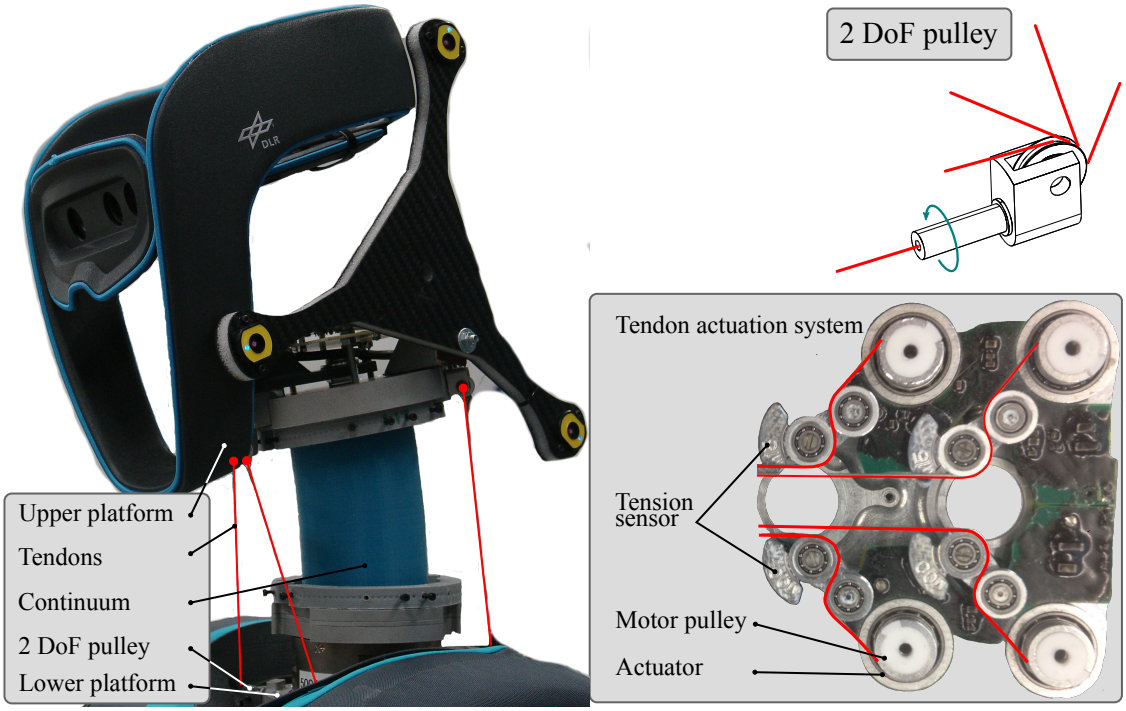

Figure 2.5.: Detailed description of the spatial testbed, i.e. the robotic neck of the humnanoid robot David. Left: Elastic Continuum Mechanism in its stretched out, initial configuration, reference Coordinate systems and the utilized tendon routing. Right, top: Two degree of freedom pulley applied in the top and lower platform to route the tendons spatially. Rigth, bottom: Tendon actuators and tendon force sensors which are utilized in the present system.

a full coupling of the tendon tension forces onto the all Cartesian deformation directions. The control objective is to control the pose of the upper platform. As the continuum structure is elastically deformable, the number of strictly positive tendon forces can not achieve full actuation which implies that there are deformation directions and oscillations which may not be controlled yielding an underactuated system.

CHAPTER 3

Modeling for analysis

The chapter will present a uniform model with which a tendon-driven elastic continuum mechanism (ECM), as described in the last Chapter 2, can be analyzed with respect to the reachable workspace and the static and dynamic characteristic of its deformation. As mentioned, the workspace computation for an ECM requires the solution of a static equilibrium which cannot be solved analytically in general and thus needs a rigorous model. Particularly the computation of the workspace is indispensable for actuator placement or to arrange additional sensors. In addition, knowledge about the static and dynamic deformation characteristic within this space provides the foundation to derive more simplified, reduced models.

Therefore, the goal of the present chapter is to derive the central equations of the thesis which describe the configuration of an elastic continuum mechanism, expressed by the generalized coordinates $\boldsymbol{q} \in \mathbb{R}^n$. The temporal evolution of $\boldsymbol{q}$ is described by the equations of motion which have the following form

$$\boldsymbol{M}(\boldsymbol{q})\ddot{\boldsymbol{q}} + \boldsymbol{k}(\boldsymbol{q}, \dot{\boldsymbol{q}}) = \boldsymbol{P}(\boldsymbol{q})\boldsymbol{u}, \tag{3.1}$$

with the nonlinear mass matrix $\boldsymbol{M}(\boldsymbol{q}) \in \mathbb{R}^{n\times n}$, the vector of generalized forces $\boldsymbol{k}(\boldsymbol{q}, \dot{\boldsymbol{q}}) \in \mathbb{R}^n$, the inputs $\boldsymbol{u} \in \mathbb{R}^r$ i.e. the r-tendon forces, and the input coupling matrix $\boldsymbol{P}(\boldsymbol{q}) \in \mathbb{R}^{n\times r}$. A static configuration for $\boldsymbol{q}$ in contrary is described by the static equilibrium equation,

$$\boldsymbol{k}(\boldsymbol{q}, \boldsymbol{0}) = \boldsymbol{P}(\boldsymbol{q})\boldsymbol{u}. \tag{3.2}$$

The derivation of equations (3.1) and (3.2) is accomplished by a continuum mechanical approach. To motivate this modeling approach, the results presented in [91] are briefly summarized which compares four different, commonly applied modeling techniques for such systems found in robotic literature in simulation. The four approaches, summarized in Tab. 3.1, are used to predict the pose of the tip end of the planar elastic continuum mechanism from Section 2.2.1. The input to the system are the $r = 2$ tendon forces, whereas the output is the position and orientation of the tip end, i.e. the static equilibrium (3.2) is solved. For a comparison, the mean and the maximum absolute prediction error is presented in Tab. 3.1 for each model. The errors of Tab. 3.1 indicate, that the Linear Euler-Bernoulli Beam (LEB) and the Constant-Curvature approach (CC) predict the position

and orientation of the tip end with higher errors, e.g. 5.2 mm mean error in z-direction for the LEB-model. In contrary, more involved models, i.e. the Nonlinear Euler-Bernoulli Beam with Axial deformation (NEBA) reduces this error to 0.6 mm mean error in z-direction which recommends a more complex approach that accounts for deformations in all directions.
However, the numerical solution in this implementation for the NEBA model utilized a spatial discretization by finite-differences and a Newton-Raphson solver which is applicable for this planar case[1]. For orientation representations in three dimensions, this is not valid. Furthermore, to solve the dynamic problem, i.e. solve partial differential equations in general, numerical solvers are available, see e.g. [92]. However, they do not result in equations of the desired form (3.1).

Table 3.1.: Comparison of the absolute prediction error in x, z and θ for the four different modeling approaches based on 89 sampled points of the planar system.

Modeling approach	x [mm]		z [mm]		θ [deg]	
	mean	max	mean	max	mean	max
Linear Euler-Bernoulli Beam (LEB) [93]	4.5651	12.3593	5.2080	21.7339	1.8273	7.6341
Constant Curvature approach (CC) [94]	1.1857	3.6759	4.7075	18.8147	1.8273	7.6341
Nonlinear Euler-Bernoulli Beam (NEB) [95]	1.8704	4.1094	0.7037	1.2612	0.9662	4.7077
Nonlinear Euler-Bernoulli Beam with axial compression (NEBA) [93]	0.2819	0.4666	0.6316	1.8954	1.0336	4.7059

Therefore, the subsequently presented model will provide a solution for this problem and explicitly derive a planar and a spatial model for an elastic continuum mechanism of the form (3.1) and (3.2). As axial, shear, torsional and bending deformations are present, the elastic continuum mechanism is considered as a geometrically nonlinear Timoshenko beam whereas the static and dynamic equations are derived using the principle of virtual work following [96]. The resulting partial differential equations describe the spatial and temporal evolution of the Timoshenko beam. The numerical solution of the equations is gained by a beam finite-element approach which transforms the dynamic equation into (3.1) and the static equation into (3.2).

The kinematic relations and the associated parameterization for a nonlinear Timoshenko beam is setup in Sec. 3.1. Afterward, the equations of motion will be derived in Sec. 3.2 using the principal of virtual work. The beam finite element method is described in Sec. 3.3. Two example systems are explicitly derived in the Appendix A.1 and A.2 following these equations. The material properties, i.e. the material stiffness along and about different axes, are then identified in Sec. 3.4 for the models from A.1 and A.2. The present chapter closes with four application scenarios in Sec. 3.5 which investigates the workspace and the dynamic behavior of two systems.

The content of the following chapter extends the works of the published works [77] and [78] of the author towards a spatial, dynamic model and additionally presents new application scenarios.

3.1. Parametrization & kinematics

For the mathematical development of the equations of motion of the system, we consider a scheme of the tendon-driven elastic continuum mechanism comprising all necessary quantities in Fig. 3.1. A geometrically nonlinear Timoshenko beam model is developed in the

[1] as the rotation can be represented by an angle which can be interpolated linearly.

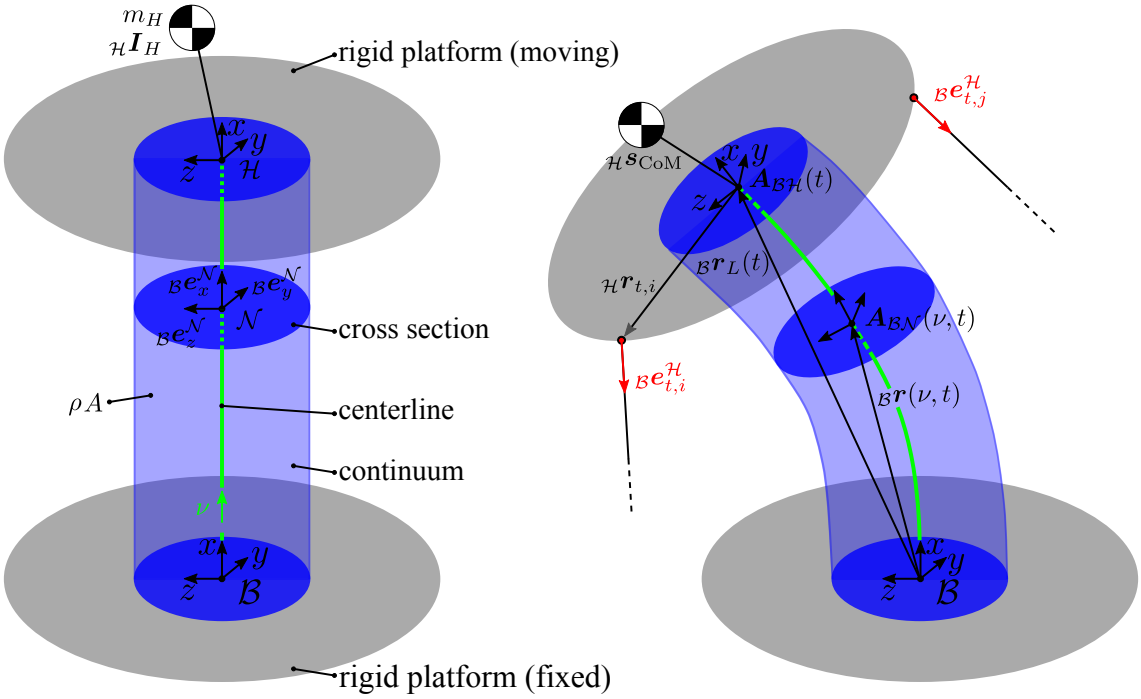

Figure 3.1.: Schematic drawing of the tendon-driven elastic continuum mechanism comprising all necessary quantities for chapter 3.

following that describes the overall motion of the continuum, of material density $\rho \in \mathbb{R}$ and length $L \in \mathbb{R}$, by the temporal and spatial evolution of the beam's centerline. The temporal coordinate is the time t $[s]$ and the centerline is spatially parameterized along its length by the scalar coordinate $\nu \in [0,\ L]$, denoted the reference arc-length. The centerline is furthermore the centroid of all cross sections along ν, with cross sectional area $A \in \mathbb{R}$.
The motion of the centerline is described by the origin of the cross sections fixed coordinate frame $\mathcal{N}$ respecting the spatially fixed frame $\mathcal{B}$, denoted as the position vector ${}_{\mathcal{B}}\boldsymbol{r}(\nu,t) \in \mathbb{R}^3$,

$$ {}_{\mathcal{B}}\boldsymbol{r}(\nu,t) = (x(\nu,t),\ y(\nu,t),\ z(\nu,t))^T. \tag{3.3} $$

The material orientation is described by the orientation of $\mathcal{N}$ respecting $\mathcal{B}$, here the matrix ${}_{\mathcal{B}}\boldsymbol{A}_{\mathcal{BN}}(\nu,t) \in \mathbb{R}^{3\times3}$,

$$ {}_{\mathcal{B}}\boldsymbol{A}_{\mathcal{BN}}(\nu,t) = \left({}_{\mathcal{B}}\boldsymbol{e}^{\mathcal{N}}_x(\nu,t),\ {}_{\mathcal{B}}\boldsymbol{e}^{\mathcal{N}}_y(\nu,t),\ {}_{\mathcal{B}}\boldsymbol{e}^{\mathcal{N}}_z(\nu,t)\right)^T, \tag{3.4} $$

which will be expressed in the following by the rotation vector[2] ${}_{\mathcal{B}}\boldsymbol{\phi}(\nu,t) \in \mathbb{R}^3$ and the corresponding skew symmetric representation,

$$ {}_{\mathcal{B}}\hat{\boldsymbol{\phi}}(\nu,t) = -{}_{\mathcal{B}}\hat{\boldsymbol{\phi}}(\nu,t)^T \in \mathbb{R}^{3\times3}. \tag{3.5} $$

The rigid body is connected to the beam at $\nu = L$ and will be called the head with head mass $m_H \in \mathbb{R}$ and inertia tensor ${}_{\mathcal{H}}\boldsymbol{I}_H \in \mathbb{R}^{3\times3}$. The position and orientation of the head

[2]The equations of motion will be derived explicitly for two example mechanisms in Appendix A.1 and A.2 with a respective orientation representation. Thus, the following equations will be derived for general purpose using ${}_{\mathcal{B}}\boldsymbol{\phi}$

are described by equation (3.3) and (3.4) for $\nu = L$,

$$ {}_{\mathcal{B}}\boldsymbol{r}_L(t) = {}_{\mathcal{B}}\boldsymbol{r}(\nu = L, t), \;\; \boldsymbol{A}_{\mathcal{BH}}(t) = \boldsymbol{A}_{\mathcal{BN}}(\nu = L, t), \tag{3.6} $$

whereas the position of the center of mass (CoM) of the head, ${}_{\mathcal{H}}\boldsymbol{s}_{\mathrm{CoM}} \in \mathbb{R}^3$, can be expressed by

$$ {}_{\mathcal{B}}\boldsymbol{r}_{\mathrm{CoM}}(t) = {}_{\mathcal{B}}\boldsymbol{r}_L(t) + \boldsymbol{A}_{\mathcal{BH}}(t) {}_{\mathcal{H}}\boldsymbol{s}_{\mathrm{CoM}}. \tag{3.7} $$

For the derivation of the virtual work in the next paragraph, virtual displacements are needed. Thus the variational families ${}_{\mathcal{B}}\bar{\boldsymbol{r}}(\nu, t) = {}_{\mathcal{B}}\bar{\boldsymbol{r}}(\nu, t, \varepsilon)$, ${}_{\mathcal{B}}\bar{\boldsymbol{\phi}} = {}_{\mathcal{B}}\bar{\boldsymbol{\phi}}(\nu, t, \varepsilon)$ of the generalized position and orientation functions are introduced, i.e. differentiable parameterizations with respect to a parameter $\varepsilon \in \mathbb{R}$ such that the admissible position and orientation, i.e. the solution of the equations of motion, are embedded in the family and are obtained for $\varepsilon = \varepsilon_0$. The virtual displacement of the centerline ${}_{\mathcal{B}}\delta\boldsymbol{r}(\nu, t)$ and the virtual rotations of the cross-sections ${}_{\mathcal{B}}\delta\hat{\boldsymbol{\phi}}$ are then defined by

$$ {}_{\mathcal{B}}\delta\boldsymbol{r}(\nu, t) = \left.\frac{\partial {}_{\mathcal{B}}\bar{\boldsymbol{r}}(\nu, t)}{\partial \varepsilon}\right|_{\varepsilon=\varepsilon_0}, \; {}_{\mathcal{B}}\delta\hat{\boldsymbol{\phi}}(\nu, t) = \left.\frac{\partial \bar{\boldsymbol{A}}_{\mathcal{BN}}(\nu, t)}{\partial \varepsilon}\right|_{\varepsilon=\varepsilon_0} \boldsymbol{A}^T_{\mathcal{BN}}(\nu, t) \, . \tag{3.8} $$

3.1.1. Beam Kinematics

To establish the kinematic relations for a deformed beam, we consider the evolution of the coordinate frame $\mathcal{N}$ at ν with respect to $\mathcal{B}$. Therefore, we look at the temporal and spatial evolution of the position ${}_{\mathcal{B}}\boldsymbol{r}(\nu, t)$ and orientation ${}_{\mathcal{B}}\boldsymbol{\phi}(\nu, t)$ of the centerline.

Velocities

The temporal evolution of the centerline's position is described by the linear velocity

$$ {}_{\mathcal{B}}\dot{\boldsymbol{r}}(\nu, t) = (\dot{x}(\nu, t), \, \dot{y}(\nu, t), \, \dot{z}(\nu, t))^T \, , \tag{3.9} $$

whereas the temporal evolution of a material surface is described by angular velocity vector ${}_{\mathcal{B}}\boldsymbol{\omega}(\nu, t) \in \mathbb{R}^3$ which is defined to

$$ \begin{aligned} (\boldsymbol{A}_{\mathcal{BN}}(\nu, t))^{\cdot} &= (\boldsymbol{A}_{\mathcal{BN}}(\nu, t) \boldsymbol{A}_{\mathcal{NN}}(\nu, t))^{\cdot} \\ &= \dot{\boldsymbol{A}}_{\mathcal{BN}}(\nu, t) \boldsymbol{A}_{\mathcal{NN}}(\nu, t) \\ &= \underbrace{\dot{\boldsymbol{A}}_{\mathcal{BN}}(\nu, t) \boldsymbol{A}^T_{\mathcal{BN}}(\nu, t)}_{{}_{\mathcal{B}}\hat{\boldsymbol{\omega}}(\nu, t)} \boldsymbol{A}_{\mathcal{BN}}(\nu, t). \end{aligned} \tag{3.10} $$

Here, ${}_{\mathcal{B}}\hat{\boldsymbol{\omega}}(\nu, t) \in \mathbb{R}^{3\times 3}$ is the skew symmetric representation of ${}_{\mathcal{B}}\boldsymbol{\omega}(\nu, t)$.

Strain measures

The linear strain measure is described by the strain vector ${}_{\mathcal{N}}\boldsymbol{\gamma}(\nu, t) \in \mathbb{R}^3$ and can be geometrically explained as the centerline's tangent in the centerline's fixed frame $\mathcal{N}$,

$$ {}_{\mathcal{N}}\boldsymbol{\gamma}(\nu, t) = \boldsymbol{A}^T_{\mathcal{BN}}(\nu, t) {}_{\mathcal{B}}\boldsymbol{r}'(\nu, t). \tag{3.11} $$

The change in orientation along ν is described by the curvature vector ${}_{\mathcal{B}}\boldsymbol{k}(\nu,t) \in \mathbb{R}^3$ expressed in the base frame $\mathcal{B}$ which is defined as

$$\begin{aligned}\left(\boldsymbol{A}_{\mathcal{BN}}(\nu,t)\right)' =&\left(\boldsymbol{A}_{\mathcal{BN}}(\nu,t)\boldsymbol{A}_{\mathcal{N},\mathcal{N}}(\nu,t)\right)'\\ =&\boldsymbol{A}'_{\mathcal{BN}}(\nu,t)\boldsymbol{A}_{\mathcal{N},\mathcal{N}}(\nu,t)\\ =&\underbrace{\boldsymbol{A}'_{\mathcal{BN}}(\nu,t)\boldsymbol{A}^T_{\mathcal{BN}}(\nu,t)}_{{}_{\mathcal{B}}\hat{\boldsymbol{k}}(\nu,t)}\boldsymbol{A}_{\mathcal{B},\mathcal{N}}(\nu,t).\end{aligned} \tag{3.12}$$

Here, the curvature appears in its skew-symmetric representation ${}_{\mathcal{B}}\hat{\boldsymbol{k}}(\nu,t) \in \mathbb{R}^{3\times3}$ which can be extracted using the operation ${}_{\mathcal{B}}\hat{\boldsymbol{k}}(\nu,t)^{\check{}} = {}_{\mathcal{B}}\boldsymbol{k}(\nu,t) \in \mathbb{R}^3$.
In prevision of the following developments, we will need the spatial derivative of the variation of the orientation vector,

$${}_{\mathcal{B}}\delta\boldsymbol{\phi}'(\nu,t) = \delta\left({}_{\mathcal{B}}\boldsymbol{k}(\nu,t)\,{}_{\mathcal{B}}\boldsymbol{\phi}(\nu,t)\right) = {}_{\mathcal{B}}\delta\boldsymbol{k}(\nu,t) - {}_{\mathcal{B}}\delta\boldsymbol{\phi}(\nu,t)\times{}_{\mathcal{B}}\boldsymbol{k}(\nu,t). \tag{3.13}$$

3.1.2. Head Kinematics

As the head is a rigid body, only the temporal evolution and the variation of the position and orientation are of interest. The variations are already defined in (3.8) for $\nu = L$. For the velocity ${}_{\mathcal{B}}\boldsymbol{v}_{\mathrm{CoM}} \in \mathbb{R}^3$ and the acceleration ${}_{\mathcal{B}}\boldsymbol{a}_{\mathrm{CoM}} \in \mathbb{R}^3$ of the CoM, it can be found:

$$\begin{aligned}{}_{\mathcal{B}}\boldsymbol{v}_{\mathrm{CoM}}(t) =&{}_{\mathcal{B}}\dot{\boldsymbol{r}}_{\mathrm{CoM}}(t) = {}_{\mathcal{B}}\dot{\boldsymbol{r}}_L(t) + \dot{\boldsymbol{A}}_{\mathcal{BH}}(t){}_{\mathcal{H}}\boldsymbol{s}_{\mathrm{CoM}},\\ =&{}_{\mathcal{B}}\dot{\boldsymbol{r}}_L(t) + {}_{\mathcal{B}}\hat{\boldsymbol{\omega}}_L(t)\boldsymbol{A}_{\mathcal{BH}}(t){}_{\mathcal{H}}\boldsymbol{s}_{\mathrm{CoM}},\\ {}_{\mathcal{B}}\boldsymbol{a}_{\mathrm{CoM}} =&{}_{\mathcal{B}}\dot{\boldsymbol{v}}_{\mathrm{CoM}}(t) = {}_{\mathcal{B}}\ddot{\boldsymbol{r}}_L(t) + \left({}_{\mathcal{B}}\dot{\hat{\boldsymbol{\omega}}}_L(t) + {}_{\mathcal{B}}\hat{\boldsymbol{\omega}}_L(t){}_{\mathcal{B}}\hat{\boldsymbol{\omega}}_L(t)\right)\boldsymbol{A}_{\mathcal{BH}}(t){}_{\mathcal{H}}\boldsymbol{s}_{\mathrm{CoM}}.\end{aligned} \tag{3.14}$$

Here, the rotational velocity of the head, ${}_{\mathcal{B}}\boldsymbol{\omega}(\nu = L,t) = {}_{\mathcal{B}}\boldsymbol{\omega}_L(t) \in \mathbb{R}^3$ and its temporal derivative ${}_{\mathcal{B}}\dot{\boldsymbol{\omega}}_L(t)$ appears.

3.1.3. Constitutive equations

In the course of the thesis, linear constitutive equations are applied for the internal shear forces, $Q_y \in \mathbb{R}$ and $Q_z \in \mathbb{R}$, in y- and z- direction,

$$Q_y(\nu,t) = G_y A_{\mathcal{N}}\gamma_y(\nu,t),\ Q_z(\nu,t) = G_z A_{\mathcal{N}}\gamma_z(\nu,t), \tag{3.15}$$

with the cross-sectional area A and the shear-modulus in the respective direction G_y, $G_z \in \mathbb{R}$. Furthermore, a linear material law is applied for the internal torques ${}_{\mathcal{N}}\boldsymbol{m} \in \mathbb{R}^3$,

$${}_{\mathcal{N}}\boldsymbol{m}(\nu,t) = \boldsymbol{K}_{bt\mathcal{N}}\boldsymbol{k}(\nu,t) \tag{3.16}$$

with the local stiffness matrix for bending and torsion $\boldsymbol{K}_{bt} \in \mathbb{R}^{3\times3}$,

$$\boldsymbol{K}_{bt} = diag\{G_tI_x,\ E_yI_y,\ E_zI_z\}. \tag{3.17}$$

The introduced quantities are the Young's modulus in y- z-direction E_y, $E_z \in \mathbb{R}$, the shear modulus for torsion $G_t \in \mathbb{R}$, and the second moment of area along the respective axis, I_x, I_y, $I_z \in \mathbb{R}$.
For the axial internal force, a nonlinear Neo-Hookean constitutive equation is applied,

$$N(\nu,t) = \frac{E_xA}{3}\left({}_{\mathcal{N}}\gamma_x(\nu,t) - \frac{1}{{}_{\mathcal{N}}\gamma_x^2(\nu,t)}\right), \tag{3.18}$$

with the Young's modulus $E_x \in \mathbb{R}$ in the x-direction. Note the nonlinear Neo-Hookean material law for the normal force takes into account the experimentally observed stiffening behavior of the material in compression, see paragraph 3.4.2. A linearization around the undeformed configuration, i.e. $\gamma_x^C = 1$, leads directly to Hooke's law,

$$N(\nu, t) = E_x A(_{\mathcal{N}}\gamma_x(\nu, t) - 1). \tag{3.19}$$

Remark on the material parameters

In this paragraph, the Young's modulus and the shear modulus, i.e. the stiffness parameters of the material, have been introduced for each direction separately which is at first contradicting. However, these parameters originate in linear elastic theory for small deformations for which a Young's modulus identified in a tensile or compression test should be applicable to a bending test. As the modeling approach of the present thesis aims for large deformation, this is not the case anymore and thus, axis-specific parameters are used.

3.2. Principle of virtual work

The dynamic equations of the system will be derived using the principle of virtual work, see for example [96, 97]. According to this principle, the virtual work $\delta W \in \mathbb{R}$ of all forces acting on the mechanical system need to be zero for all admissible virtual displacements,

$$\delta W = \delta W^{dyn} + \delta W^{stat} = 0 \; \forall \; {}_{\mathcal{B}}\delta \boldsymbol{r}_{adm}, \, {}_{\mathcal{B}}\delta \boldsymbol{\phi}_{adm}, \tag{3.20}$$

in which $\delta W^{dyn} \in \mathbb{R}$ is the virtual work due to the dynamic forces and $\delta W^{stat} \in \mathbb{R}$ is the virtual work due to the static forces. The latter term contains the gravitational forces, the externally applied force and the internal force due to the deformation of the beam. With the internal forces ${}_{\mathcal{B}}\boldsymbol{n}(\nu, t) \in \mathbb{R}^3$ and the internal moments ${}_{\mathcal{B}}\boldsymbol{m}(\nu, t) \in \mathbb{R}^3$ of the beam structure and the external distributed forces[3] ${}_{\mathcal{B}}\boldsymbol{f}(\nu, t) \in \mathbb{R}^3$ we find after integration by parts [4]

$$\begin{aligned}
\delta W^{stat} &= \int_0^L ({}_{\mathcal{B}}\boldsymbol{n}' + {}_{\mathcal{B}}\boldsymbol{f}) {}_{\mathcal{B}}\delta \boldsymbol{r} + \left({}_{\mathcal{B}}\boldsymbol{m}' + ({}_{\mathcal{B}}\boldsymbol{n} \times {}_{\mathcal{B}}\boldsymbol{r}') \right) {}_{\mathcal{B}}\delta \boldsymbol{\phi} \, d\nu, \\
&= \underbrace{[{}_{\mathcal{B}}\boldsymbol{n}_{\mathcal{B}}\delta \boldsymbol{r} + {}_{\mathcal{B}}\boldsymbol{m}_{\mathcal{B}}\delta \boldsymbol{\phi}]_0^L + \int_0^L {}_{\mathcal{B}}\boldsymbol{f} \delta_{\mathcal{B}}\boldsymbol{r} d\nu}_{\delta W^{ext}} \\
&\quad \underbrace{- \int_0^L {}_{\mathcal{B}}\boldsymbol{n} \left({}_{\mathcal{B}}\delta \boldsymbol{r}' - {}_{\mathcal{B}}\delta \boldsymbol{\phi} \times {}_{\mathcal{B}}\boldsymbol{r}' \right) + {}_{\mathcal{B}}\boldsymbol{m}_{\mathcal{B}}\delta \boldsymbol{\phi}' d\nu}_{\delta W^{int}} .
\end{aligned} \tag{3.21}$$

In the following, the 3 major contributions to the virtual work, δW^{int}, δW^{ext}, and δW^{dyn}, will be derived.

[3] The distributed moments ${}_{\mathcal{B}}\boldsymbol{l}(\nu, t) \in \mathbb{R}^3$ along the beam are assumed to be zero.

[4] For brevity, the explicit dependency on ν and t is left out in the following. They are only stated when quantities are introduced or if it is necessary.

3.2.1. Internal forces

The internal virtual work arises from the internal forces within the continuum when it is deformed. The virtual work of the internal forces for the present case can be found according to (3.21) to

$$\delta W^{int} = -\int_0^L {}_{\mathcal{B}}\boldsymbol{n}\left({}_{\mathcal{B}}\delta\boldsymbol{r}' - {}_{\mathcal{B}}\delta\boldsymbol{\phi}\times{}_{\mathcal{B}}\boldsymbol{r}'\right) + {}_{\mathcal{B}}\boldsymbol{m}_{\mathcal{B}}\delta\boldsymbol{\phi}' d\nu. \tag{3.22}$$

To connect the internal forces and moments to their respective constitutive law, the internal forces are transformed to the cross-sectional fixed frame ${}_{\mathcal{N}}\boldsymbol{n}(\nu,t)\in\mathbb{R}^3$ by

$${}_{\mathcal{N}}\boldsymbol{n} = \begin{pmatrix} N \\ Q_y \\ Q_z \end{pmatrix} = \boldsymbol{A}_{\mathcal{BN}}^T{}_{\mathcal{B}}\boldsymbol{n}, \tag{3.23}$$

with the corresponding normal (3.18) and shear forces (3.15) at a cross section along ν. Similar, the internal moments ${}_{\mathcal{N}}\boldsymbol{m}(\nu,t)\in\mathbb{R}^3$ are projected to the cross section by

$${}_{\mathcal{N}}\boldsymbol{m} = \begin{pmatrix} M_x \\ M_y \\ M_z \end{pmatrix} = \boldsymbol{A}_{\mathcal{BN}}^T{}_{\mathcal{B}}\boldsymbol{m}, \tag{3.24}$$

with the torsional torque $M_x\in\mathbb{R}$ and the two bending torques M_y, $M_z\in\mathbb{R}$. With that, equation (3.22) can be reformulated using (3.8), (3.11), (3.23), (3.24) and the curvature expressed in the cross-sectionnal fixed frame ${}_{\mathcal{N}}\boldsymbol{k} = \boldsymbol{A}_{\mathcal{BN}}^T{}_{\mathcal{B}}\boldsymbol{k}$, to

$$\begin{aligned}
\delta W^{int} =& -\int_0^L {}_{\mathcal{N}}\boldsymbol{n}^T\boldsymbol{A}_{\mathcal{BN}}^T\left(\delta\boldsymbol{A}_{\mathcal{BNN}}\boldsymbol{\gamma} + \boldsymbol{A}_{\mathcal{BNN}}\delta\boldsymbol{\gamma} - {}_{\mathcal{B}}\delta\hat{\boldsymbol{\phi}}\boldsymbol{A}_{\mathcal{BNN}}\boldsymbol{\gamma}\right)\\
&+ {}_{\mathcal{N}}\boldsymbol{m}^T\boldsymbol{A}_{\mathcal{BN}}^T\left((\delta\boldsymbol{A}_{\mathcal{BNN}}\boldsymbol{k} + \boldsymbol{A}_{\mathcal{BNN}}\delta\boldsymbol{k}) - {}_{\mathcal{B}}\delta\hat{\boldsymbol{\phi}}\boldsymbol{A}_{\mathcal{BNN}}\boldsymbol{k}\right)d\nu\\
=& -\int_0^L {}_{\mathcal{N}}\boldsymbol{n}^T\boldsymbol{A}_{\mathcal{BN}}^T\left(\delta\boldsymbol{A}_{\mathcal{BNN}}\boldsymbol{\gamma} + \boldsymbol{A}_{\mathcal{BNN}}\delta\boldsymbol{\gamma} - \delta\boldsymbol{A}_{\mathcal{BN}}\boldsymbol{A}_{\mathcal{BN}}^T\boldsymbol{A}_{\mathcal{BNN}}\boldsymbol{\gamma}\right)\\
&+ {}_{\mathcal{N}}\boldsymbol{m}^T\boldsymbol{A}_{\mathcal{BN}}^T\left((\delta\boldsymbol{A}_{\mathcal{BNN}}\boldsymbol{k} + \boldsymbol{A}_{\mathcal{BNN}}\delta\boldsymbol{k}) - \delta\boldsymbol{A}_{\mathcal{BN}}\boldsymbol{A}_{\mathcal{BN}}^T\boldsymbol{A}_{\mathcal{BNN}}\boldsymbol{k}\right)d\nu.\\
=& -\int_0^L {}_{\mathcal{N}}\boldsymbol{n}^T\,{}_{\mathcal{N}}\delta\boldsymbol{\gamma} + {}_{\mathcal{N}}\boldsymbol{m}^T\,{}_{\mathcal{N}}\delta\boldsymbol{k}\,d\nu
\end{aligned} \tag{3.25}$$

With this formulation of δW^{int} it is possible to connect the virtual work of the internal forces and torques with the respective constitutive equations from paragraph 3.1.3.

3.2.2. External forces

The virtual work of the external forces is derived in (3.21) to

$$\delta W^{ext} = \left[{}_{\mathcal{B}}\boldsymbol{n}_{\mathcal{B}}\delta\boldsymbol{r} + {}_{\mathcal{B}}\boldsymbol{m}_{\mathcal{B}}\delta\boldsymbol{\phi}\right]_0^L + \int_0^L {}_{\mathcal{B}}\boldsymbol{f}\delta{}_{\mathcal{B}}\boldsymbol{r}d\nu. \tag{3.26}$$

For the first part of equation (3.26), the boundary conditions at $\nu = 0$ and $\nu = L$ are necessary. The considered mechanisms are clamped to the ground at $\nu = 0$ whereas at

$\nu = L$ external forces and torques act which resembles a typical cantilever beam. Thus the boundary conditions are

$$\begin{aligned}
{}_{\mathcal{B}}\boldsymbol{r}(\nu = 0) =& \mathbf{0}, \quad {}_{\mathcal{B}}\boldsymbol{\phi}(\nu = 0) = \mathbf{0}, \\
{}_{\mathcal{B}}\boldsymbol{n}(\nu = L) =& \sum_{i=1}^{r} {}_{\mathcal{B}}\boldsymbol{e}_{t,i}^{\mathcal{H}} u_i - m_H g \, {}_{\mathcal{B}}\boldsymbol{e}_x^{\mathcal{H}} + {}_{\mathcal{B}}\boldsymbol{n}_w, \\
{}_{\mathcal{B}}\boldsymbol{m}(\nu = L) =& \sum_{i=1}^{r} \boldsymbol{A}_{\mathcal{B}\mathcal{H}\mathcal{H}} \boldsymbol{r}_{t,i} \times {}_{\mathcal{B}}\boldsymbol{e}_{t,i}^{\mathcal{H}} u_i - {}_{\mathcal{B}}\boldsymbol{s}_{\mathrm{CoM}} \times m_H g \, {}_{\mathcal{B}}\boldsymbol{e}_x^{\mathcal{H}} + {}_{\mathcal{B}}\boldsymbol{m}_w,
\end{aligned} \tag{3.27}$$

with the i-th component of the tendon tension vector $\boldsymbol{u} \in \mathbb{R}^r$, the tendon normal vector ${}_{\mathcal{B}}\boldsymbol{n}_{t,i}^{\mathcal{H}}$ of the i-th tendon, the vector from the rigid platform to the center of mass, transformed in the base ${}_{\mathcal{B}}\boldsymbol{s}_{\mathrm{CoM}}$ and an additional force ${}_{\mathcal{B}}\boldsymbol{n}_w \in \mathbb{R}^3$ and torque ${}_{\mathcal{B}}\boldsymbol{m}_w \in \mathbb{R}^3$, denoted the external Cartesian force $\boldsymbol{f}_c \in \mathbb{R}^6$,

$${}_{\mathcal{B}}\boldsymbol{f}_c = ({}_{\mathcal{B}}\boldsymbol{n}_w^T, \, {}_{\mathcal{B}}\boldsymbol{m}_w^T)^T, \tag{3.28}$$

for calibration purposes[5]. The second part of equation (3.26) is the virtual work of the gravitational force of the continuum,

$${}_{\mathcal{B}}\boldsymbol{f} = -\rho A g \, {}_{\mathcal{B}}\boldsymbol{e}_x^{\mathcal{B}}, \tag{3.29}$$

i.e. a distributed force along the centerline of the beam. By inspection of the boundary conditions (3.27), the virtual work of the external forces can be divided into the virtual work of the tendon actuation, the virtual work of the gravitational force and the virtual work of an arbitrary external wrench δW^w,

$$\delta W^{ext} = \delta W^{tendon} + \delta W^{grav} + \delta W^w. \tag{3.30}$$

Virtual work of the tendon actuation

The virtual work of the tendon actuation can be computed using the boundary conditions (3.27) to

$$\delta W^{tendon} = \left(\sum_{i=1}^{r} {}_{\mathcal{B}}\boldsymbol{e}_{t,i}^{\mathcal{H}} u_i \right) {}_{\mathcal{B}}\delta \boldsymbol{r}_L + \left(\sum_{i=1}^{r} \boldsymbol{A}_{\mathcal{B}\mathcal{H}\mathcal{H}} \boldsymbol{r}_{t,i} \times {}_{\mathcal{B}}\boldsymbol{e}_{t,i}^{\mathcal{H}} u_i \right) {}_{\mathcal{B}}\delta \boldsymbol{\phi}_L, \tag{3.31}$$

which can be essentially simplified by introducing the tendon coupling matrix $\boldsymbol{P}(\boldsymbol{q}) \in \mathbb{R}^{6 \times r}$,

$$\boldsymbol{P}(\boldsymbol{q}) = \begin{pmatrix} {}_{\mathcal{B}}\boldsymbol{e}_{t,1}^{\mathcal{H}} & \dots & {}_{\mathcal{B}}\boldsymbol{e}_{t,r}^{\mathcal{H}} \\ \boldsymbol{A}_{\mathcal{B}\mathcal{H}\mathcal{H}} \boldsymbol{r}_{t,1} \times {}_{\mathcal{B}}\boldsymbol{e}_{t,1}^{\mathcal{H}} & \dots & \boldsymbol{A}_{\mathcal{B}\mathcal{H}\mathcal{H}} \boldsymbol{r}_{t,r} \times {}_{\mathcal{B}}\boldsymbol{e}_{t,r}^{\mathcal{H}} \end{pmatrix}. \tag{3.32}$$

With the coupling matrix, equation (3.31) can be reduced to

$$\delta W^{tendon} = ({}_{\mathcal{B}}\delta \boldsymbol{r}_L^T, \, {}_{\mathcal{B}}\delta \boldsymbol{\phi}_L^T) \, \boldsymbol{P}(\boldsymbol{q}) \boldsymbol{u} \tag{3.33}$$

[5]This arbitrary external wrench will be used later on in an identification procedure to deflect the mechanism to predefined poses.

Virtual work of the gravitational forces

For this part of the virtual work, the gravitational effects of the continuum and the gravitational effect of the head mass are considered. Using the gravitational part of the boundary conditions (3.27) and the gravitational force of the continuum (3.29), the virtual work of the gravitational force can be found to

$$\begin{aligned}\delta W^{grav} = &- \int_0^L \rho A g \delta x(\nu)\, d\nu \\ &- m_H g\, {}_{\mathcal{B}}\delta x_L - \left({}_{\mathcal{B}}\boldsymbol{s}_{\mathrm{CoM}} \times m_H g\, {}_{\mathcal{B}}\boldsymbol{e}_x^{\mathcal{B}}\right) {}_{\mathcal{B}}\delta\boldsymbol{\phi}_L. \end{aligned} \tag{3.34}$$

The first part of equation (3.34) represents the gravitational effect of the beam; the second part the gravitational effects of the rigid body.
Within the identification process in Section 3.4 or to model unmodeled wrenches as disturbances, an external force ${}_{\mathcal{B}}\boldsymbol{n}_w \in \mathbb{R}^3$ and a torque ${}_{\mathcal{B}}\boldsymbol{m}_w \in \mathbb{R}^3$ is exerted at the head, for $\nu = L$, whose virtual work is

$$\delta W^w = {}_{\mathcal{B}}\boldsymbol{n}_w {}_{\mathcal{B}}\delta\boldsymbol{r}_L + {}_{\mathcal{B}}\boldsymbol{m}_w {}_{\mathcal{B}}\delta\boldsymbol{\phi}_L. \tag{3.35}$$

With that, all parts in equation (3.30) are derived.

3.2.3. Dynamic forces

For the virtual work of the dynamic forces, will split up the terms into a part coming from the rigid body dynamics of the head and the continuum dynamics of the beam,

$$\delta W^{dyn} = \delta W^{dyn,head} + \delta W^{dyn,beam}. \tag{3.36}$$

The first part of (3.36) equates to

$$\delta W^{dyn,head} = -m_H {}_{\mathcal{B}}\boldsymbol{a}_{\mathrm{CoM}}\, {}_{\mathcal{B}}\delta\boldsymbol{r}_{\mathrm{CoM}} - {}_{\mathcal{B}}\boldsymbol{I}_H {}_{\mathcal{B}}\dot{\boldsymbol{\omega}}_L\, {}_{\mathcal{B}}\delta\boldsymbol{\phi}_L, \tag{3.37}$$

with the acceleration vector of the head (3.14) and the derivative of angular velocity (3.10). The virtual work from the dynamic forces of the continuum mechanism are found as the following

$$\delta W^{dyn,beam} = -\int_0^L {}_{\mathcal{B}}\delta\boldsymbol{r}\rho A {}_{\mathcal{B}}\ddot{\boldsymbol{r}} + \delta\boldsymbol{\phi}\rho\boldsymbol{J}\, {}_{\mathcal{B}}\dot{\boldsymbol{\omega}} d\nu, \tag{3.38}$$

with the tensor of the second moment of area $\boldsymbol{J} \in \mathbb{R}^{3\times3}$.

3.2.4. Summary

As stated in the beginning of this section, the virtual work of the system (3.20) needs to be zero for all admissible virtual displacements which yields,

$$\begin{aligned}\delta W^{dyn,head} + \delta W^{dyn,beam} + \delta W^{tendon} + \delta W^{grav} + \delta W^w + \delta W^{int} = 0 \\ \forall\, {}_{\mathcal{B}}\delta\boldsymbol{r}_{adm},\, {}_{\mathcal{B}}\delta\boldsymbol{\phi}_{adm}\end{aligned} \tag{3.39}$$

for the equations of motion and

$$\delta W^{tendon} + \delta W^{grav} + \delta W^w + \delta W^{int} = 0 \;\; \forall\, {}_{\mathcal{B}}\delta\boldsymbol{r}_{adm},\, {}_{\mathcal{B}}\delta\boldsymbol{\phi}_{adm} \tag{3.40}$$

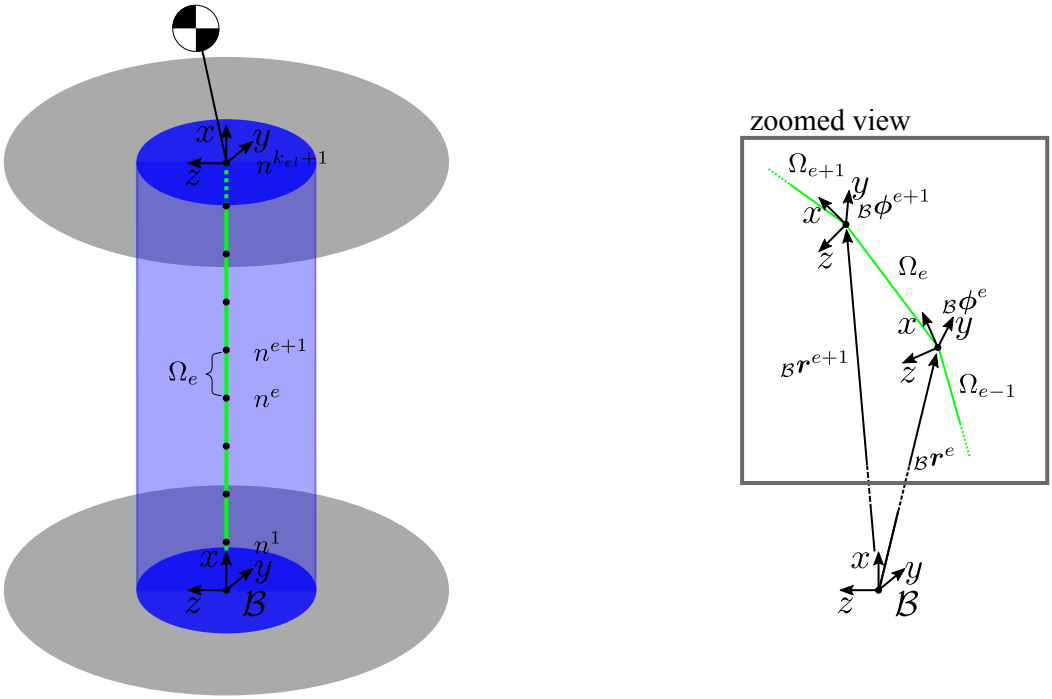

Figure 3.2.: Discretization using the beam finite element method. Left: Graphical illustration of the discretization of the centerline into elements and their corresponding nodes. Right: Element e in a zoomed view and corresponding nodal degrees of freedom of node e and $e+1$.

for the static equilibrium equations. As there is no general analytic solution for the partial differential equation (3.39) nor the ordinary differential equations (3.40), the finite element method will be applied to spatially discretize the beam along its centerline and solve the equations then numerically. By that, the partial differential equation is transformed into a system of nonlinear ordinary differential equations yielding the equations of motion of the form (3.1) and the ordinary differential equation is transformed into a set of nonlinear equations of the form (3.2).

3.3. Discretization: The beam finite element method

For the numerical solution of the partial differential equations, i.e. the equations of motion (3.39), and the ordinary differential equation, i.e. the static equilibrium equation (3.40), a beam finite element method is applied. This method involves a spatial discretization of the beams centerline. Therefore, the parameter space ν of the beams centerline is divided by the nodes $n^1 = 0 < \ldots < n^e < \cdots < n^{k_{el}+1} = L$ into k_{el} element sets $\Omega_e = [n^e, n^{e+1}]$, which is graphically illustrated in Fig. 3.2. Using the relation

$$\nu^e(\nu) = \frac{2}{n^{e+1} - n^e}(\nu - n^e) - 1, \tag{3.41}$$

it is convenient to introduce in every element set Ω_e the element coordinate $\nu^e \in [-1, 1]$. Each element e possesses two nodes, whereas each node has ndof $\in \mathbb{Z}$ nodal degrees of

freedom. The amount of nodal degrees of freedom is in general dependent on the choice of the generalized coordinate function and to the choice of the so called shape-functions which are used to interpolate in between subsequent nodal-degrees of freedom.
In this work, linear shape functions are used and for the general case, ndof = 6 and the nodal degrees of freedom are $({}_{\mathcal{B}}\boldsymbol{r}^{e,T},\, {}_{\mathcal{B}}\boldsymbol{\phi}^{e,T}) \in \mathbb{R}^6$, i.e. the position ${}_{\mathcal{B}}\boldsymbol{r}^e$ of the center-line at e respecting $\mathcal{B}$ and the material orientation ${}_{\mathcal{B}}\boldsymbol{\phi}^e$ at e respecting $\mathcal{B}$, see Fig. 3.2. All nodal degrees of freedom are summarized in the generalized coordinate vector of the approximated system $\boldsymbol{q}(t) \in \mathbb{R}^n$ with $n = \text{ndof}\,(k_{el}+1)$,

$$\boldsymbol{q}(t) = \left({}_{\mathcal{B}}\boldsymbol{r}^{1,T},\, {}_{\mathcal{B}}\boldsymbol{\phi}^{1,T},\, \ldots,\, {}_{\mathcal{B}}\boldsymbol{r}^{e+1,T}, {}_{\mathcal{B}}\boldsymbol{\phi}^{e+1,T},\, \ldots,\, {}_{\mathcal{B}}\boldsymbol{r}^{k_{el}+1,T},\, {}_{\mathcal{B}}\boldsymbol{\phi}^{k_{el}+1,T}\right)^T. \tag{3.42}$$

Now, the aim of the beam finite element method is the approximation of the generalized functions ${}_{\mathcal{B}}\boldsymbol{r}(\nu,t) \approx {}_{\mathcal{B}}\tilde{\boldsymbol{r}}(\nu,t)$, and ${}_{\mathcal{B}}\boldsymbol{\phi}(\nu,t) \approx {}_{\mathcal{B}}\tilde{\boldsymbol{\phi}}(\nu,t)$, via a summation over all k_{el} elements,

$${}_{\mathcal{B}}\tilde{\boldsymbol{r}}(\nu,t) = \sum_{e=1}^{k_{el}} \chi_{\Omega^e}(\nu)\boldsymbol{r}^{h,e}(\nu^e(\nu),\boldsymbol{q}(t)), \tag{3.43}$$

$${}_{\mathcal{B}}\tilde{\boldsymbol{\phi}}(\nu,t) = \sum_{e=1}^{k_{el}} \chi_{\Omega^e}(\nu)\boldsymbol{\phi}^{h,e}(\nu^e(\nu),\boldsymbol{q}(t)). \tag{3.44}$$

In this equations, $\chi_{\Omega^e}(\nu)$ is an operator which ensures that the summation at the nodes is correct, and $\boldsymbol{r}^{h,e} \in \mathbb{R}^3$ and $\boldsymbol{\phi}^{h,e} \in \mathbb{R}^3$ are the shape functions of an element e,

$$\boldsymbol{r}^{h,e} = \boldsymbol{N}(\nu^e)\boldsymbol{C}_r^e\boldsymbol{q}(t) \;\; \boldsymbol{\phi}^{h,e} = \boldsymbol{N}(\nu^e)\boldsymbol{C}_\phi^e\boldsymbol{q}(t). \tag{3.45}$$

In this equation, $\boldsymbol{N}(\nu^e) \in \mathbb{R}^{3\times\text{ndof}}$ ensures the linear interpolation in each element set,

$$\boldsymbol{N}(\nu^e) = 0.5\begin{pmatrix} (\nu^e-1) & 0 & 0 & (\nu^e+1) & 0 & 0 \\ 0 & (\nu^e-1) & 0 & 0 & (\nu^e+1) & 0 \\ 0 & 0 & (\nu^e-1) & 0 & 0 & (\nu^e+1) \end{pmatrix}, \tag{3.46}$$

and $\boldsymbol{C}_r^e \in \mathbb{R}^{6\times 6\,(k_{el}+1)}$, $\boldsymbol{C}_\phi^e \in \mathbb{R}^{6\times 6\,(k_{el}+1)}$ are connector matrices for the translational and rotational part of the generalized coordinates,

$$(\boldsymbol{r}^{e,T},\, \boldsymbol{r}^{e+1,T})^T = \boldsymbol{C}_r^e\boldsymbol{q}(t), \;\; (\boldsymbol{\phi}^{e,T},\, \boldsymbol{\phi}^{e+1,T})^T = \boldsymbol{C}_\phi^e\boldsymbol{q}(t), \tag{3.47}$$

to extract the nodal degrees of freedom of element e.

The dynamics of node $k_{el}+1$ is governed by the rigid body dynamics of the head. Therefore, a special connector matrix $\boldsymbol{C}^L \in \mathbb{R}^{6\times 6(k_{el}+1)}$ is introduced,

$$\boldsymbol{q}_L = (\boldsymbol{r}^{e+1},\, \boldsymbol{\phi}^{e+1})^T = \boldsymbol{C}^L\boldsymbol{q}(t). \tag{3.48}$$

For the subsequent developments, we will need the derivative of the shape functions (3.45) with respect to ν,

$$\begin{aligned} \frac{d}{d\nu}\boldsymbol{r}^{h,e} = \frac{d}{d\nu^e}\boldsymbol{r}^{h,e}\frac{d\nu^e}{d\nu} &= \boldsymbol{N}'\boldsymbol{C}_r^e\boldsymbol{q}(t), \\ \frac{d}{d\nu}\boldsymbol{\phi}^{h,e} &= \boldsymbol{N}'\boldsymbol{C}_\phi^e\boldsymbol{q}(t), \end{aligned} \tag{3.49}$$

with

$$\boldsymbol{N}' = \frac{d\boldsymbol{N}(\nu^e)}{d\nu} = \frac{d\boldsymbol{N}(\nu^e)}{d\nu^e} \underbrace{\frac{d\nu^e}{d\nu}}_{\frac{2}{\Delta L}},$$
$$= \frac{2}{\Delta L} \begin{pmatrix} -0.5 & 0 & 0 & 0.5 & 0 & 0 \\ 0 & -0.5 & 0 & 0 & 0.5 & 0 \\ 0 & 0 & -0.5 & 0 & 0 & 0.5 \end{pmatrix}. \tag{3.50}$$

Furthermore, it is necessary to compute the variation of the shape functions and their derivatives, exemplary shown for $\delta\boldsymbol{r}$,

$$\delta\boldsymbol{r}^{h,e} = \boldsymbol{N}(\nu^e)\boldsymbol{C}_r^e\delta\boldsymbol{q}(t), \quad \frac{d}{d\nu}\delta\boldsymbol{r}^{h,e} = \boldsymbol{N}'\boldsymbol{C}_r^e\delta\boldsymbol{q}(t). \tag{3.51}$$

With the establishment of the shape functions (3.45), their derivatives (3.49) and variations (3.51), we can reformulate the virtual work equations for the internal forces (3.25), the external forces (3.26) and the dynamic forces (3.36). In these expressions, the integral along the beam will be replaced by the following substitution of variables, known from (3.50),

$$\int_0^L d\nu = \sum_{e=1}^{k_{el}} \int_{-1}^{1} \frac{d\nu}{d\nu^e} d\nu^e = \sum_{e=1}^{k_{el}} \int_{-1}^{1} \frac{\Delta L}{2} d\nu^e. \tag{3.52}$$

The developments to derive the virtual work using the shape functions are strongly influenced by the choice of the orientation representation. Therefore, further developments cannot be made in a general manner. Though, two example systems are derived explicitly in the Appendix A.

3.4. Parameter identification

This section covers details about the identification of the elastic parameters and the associated measurements that have been carried out for validation. In the previous section, a geometrically nonlinear Timoshenko Beam has been derived with the assumption of linear elastic material properties. The silicone is known to have nonlinear material properties. In particular relevant for the present case, the material exhibits an increased nonlinear behavior under compression. Thus, it will be investigated in the first paragraph, to which extend the material nonlinearity can be handled with a nonlinear material law while maintaining the assumption of a linear elastic material.
Afterward, elastic parameters for the explicitly derived models i.e. the planar system, see Section A.1, and the spatial system, see Section A.2 are identified.

3.4.1. Identification process

The elastic parameters are incorporated in finite element model describing the statics of a geometrically nonlinear Timoshenko beam which is in general a nonlinear function. Thus, a nonlinear least square optimization is applied for the identification. Within this nonlinear optimization, the error function $\boldsymbol{\Delta}(\boldsymbol{\xi}) \in \mathbb{R}^{n_m}$, is minimized to find the desired parameters $\boldsymbol{\xi} \in \mathbb{R}^p$,

$$\min_{\boldsymbol{\xi}} ||\boldsymbol{\Delta}(\boldsymbol{\xi})||_2^2, \tag{3.53}$$

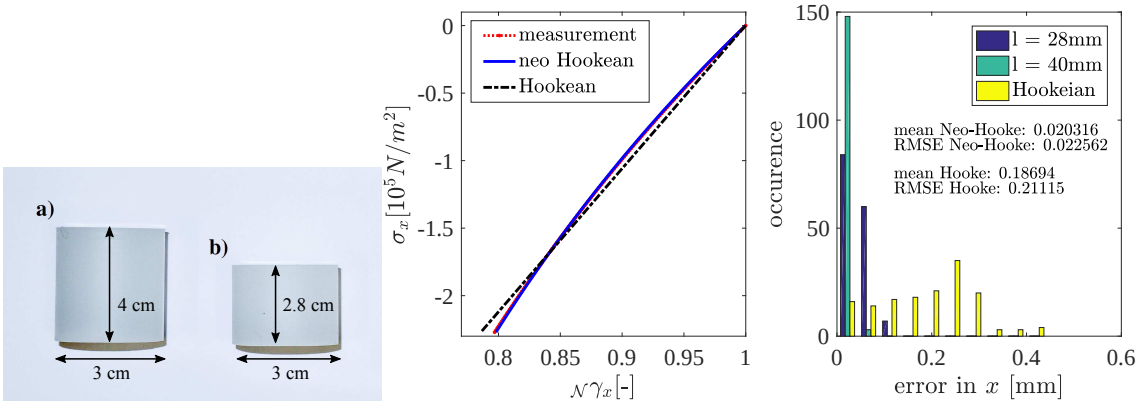

Figure 3.3.: Left: Test specimen for the compression test. a): Long specimen with $L = 40$mm. b): Short specimen with $L = 29$mm. Middle: Identification of the axial stiffness $E_x\,A$ for the two different probes with Neo-Hookean material law. Additionally, the black curve indicates a respective course for a Hookean (linear) material law. Right: Absolute prediction error of the Neo-Hookean and Hookean material law in the compression test.

where $n_m \in \mathbb{N}$ are the number of measurements and $p \in \mathbb{N}$ are the number of to be identified parameters, respectively. The identification process is performed for $k_{el} = 20$ number of elements.

3.4.2. Neo-Hookean compression stiffness

In the compression test, two cylindrical specimens are manufactured of the same silicone as the planar and the spatial testbed [86], see Fig. 3.3. Their diameter is 0.06 m and they are compressed up to 20% of the undeformed length L. The test is conducted for two different lengths $L = [28\text{mm}, 40\text{mm}]$. The measured quantities are the axial force ${}_{\mathcal{B}}f_x \in \mathbb{R}$ [N] and the displacement ΔL [m] which are illustrated in Fig. 3.3 as a stress-strain diagram with the axial stress $\sigma_x = \frac{{}_{\mathcal{B}}f_x}{A}$ and the axial strain ${}_{\mathcal{N}}\gamma_x = \frac{\Delta L}{L}$. For $\boldsymbol{\xi} = E_x\,A$, $p = 1$, the error function used for the identification is

$$\boldsymbol{\Delta}(EA) = (\tilde{x}_1 - x_1(E_x\,A),\, \ldots,\, \tilde{x}_{n_m} - x_{n_m}(E_x\,A))^T, \tag{3.54}$$

where $\tilde{x}_i$ is the measured, $n_m \in \mathbb{N}$ are the number of measurements and $x_i(EA)$ is the computed axial position for an external force (3.28)

$${}_{\mathcal{B}}\boldsymbol{n}^w = ({}_{\mathcal{B}}f_x,\, 0,\, 0)^T,\; {}_{\mathcal{B}}\boldsymbol{m}^w = \boldsymbol{0}, \tag{3.55}$$

with the virtual work contribution (3.35). In the left diagram of Fig. 3.3, a clear non-linearity in the measured stress-strain curve (red curve) can be observed, which can be reproduced by the Neo-Hookean material law (3.18) with a lower mean error of 0.04 mm compared to a linear Hookean law (3.19), with a mean error of 0.18 mm. The histogram of the absolute prediction error, right plot of Fig. 3.3, states further, that the linear material law has a higher standard deviation of 0.6 mm compared to the Neo-Hookean law with 0.02 mm. Furthermore, the identified values for the axial stiffness $E_x\,A$, see Table 3.2, are 20% higher if a linear Hookean is applied, which essentially means that a linear material law overestimates the compression stiffness of the specimens. For the further developments, the nonlinear Timoshenko beam model will be applied only with a Neo-Hookean

Table 3.2.: Left: Identified E for Hookean and Neo-Hookean material laws in a compression test. Right: Identified shear stiffness GA and Young's modulus E for bending.

	compression				shear		
	NeoHooke		Hooke				
L	$(E_x\,A)_{NH}$	$(E_x)_{NH}$	$(E_x\,A)_H$	$(E_x)_H$	$G_z\,A$	$E_y\,I$	E_y
[m]	[N]	[N/m^2]	[N]	[N/m^2]	[N]	[Nm^2]	[N/m^2]
0.028	583.25	866081	688.95	1043000	2929	3.05	867598
0.040	572.06	883012	700.69	1060800	–	–	–

material law as it proved to be more accurate whereas the identified parameter for the Young's modulus in compression will be set to $E_x = 875000[\mathrm{N/m^2}]$.

3.4.3. Identification of the planar system

This section will report on the identification of the remaining elastic parameters, i.e. $G_z\,A$ and $E_y\,I_y$, for the planar model which is explicitly derived in the Appendix A.1. In the following, a shear experiment is discussed with which the experimental data is obtained to identify $G_z\,A$ and $E_y\,I_y$. For the shear test, a force ${}_{\mathcal{B}}f_z \in \mathbb{R}$ in ${}_{\mathcal{B}}\boldsymbol{e}_z^{\mathcal{H}}$-direction is applied at the tip of the ECM as depicted in Fig. 2.2 which leads to a bending deformation about the ${}_{\mathcal{B}}\boldsymbol{e}_y^{\mathcal{H}}$-axis and a shear deformation along the ${}_{\mathcal{B}}\boldsymbol{e}_z^{\mathcal{H}}$-axis. For all displacement increments, the position and orientation are measured by a camera as well as the applied tendon force. The mean value of the identified Young's moduli $E_x = 875000\,N/m^2$ from the compression test is used within the shear test as for the compression stiffness EA and as an initial guess for the Young's modulus in bending. Here, $\boldsymbol{\xi} = (G_z\,A,\ E)^T \in \mathbb{R}^2$, $p = 2$, and the error function for the identification is

$$\Delta(\boldsymbol{\xi}) = (\tilde{z}_1 - z_1(\boldsymbol{\xi}),\, w(\tilde{\theta}_1 - \theta_1(\boldsymbol{\xi})),\, \ldots,\, \tilde{z}_{n_m} - z_m(\boldsymbol{\xi}),\, w(\tilde{\theta}_{n_m} - \theta_m(\boldsymbol{\xi})))^T, \tag{3.56}$$

where $\tilde{z}_i$, $\tilde{\theta}_i$ are the measured, $z_i(\boldsymbol{\xi}), \theta_i(\boldsymbol{\xi})$ are the computed z-position and tip angle for the external force (3.28),

$${}_{\mathcal{B}}\boldsymbol{n}^w = (0,\, 0,\, {}_{\mathcal{B}}f_z)^T,\ {}_{\mathcal{B}}\boldsymbol{m}^w = \boldsymbol{0}, \tag{3.57}$$

and $w = 0.1$ to account for the different units. The results of the identification procedure based on $n_m = 201$ measured poses are depicted in Fig. 3.4 and the associated values can be found in Tab. 3.2. The error plots in Fig. 3.4 confirm that the identified parameters can reproduce the measured behavior with a maximum error in the rotation of 0.7 deg and 1.8 mm (except obvious outliers) in the positions whereas their standard deviations are 0.3 deg and below 0.7 mm respectively.

Validation

For the validation process, the planar system is driven by the antagonistic tendon arrangement, see Fig. 2.2. Again, the tendon actuation forces and the tip pose are measured by external sensors whereas the quality of the identified parameters is evaluated by looking at the error of the planar model and the measured pose. For validation, several different scenarios are executed and in total $n_m = 142$ of measurements are incorporated. At first, only one tendon is pulled at each side. In the second section, the opposing tendon is added with a specified pretension. In the last section, the mechanism is driven with one tendon and an additional mass is added at the top. Herein, an easy to be attached object is applied with a weight of 0.941 kg. The different sections as well as the performed

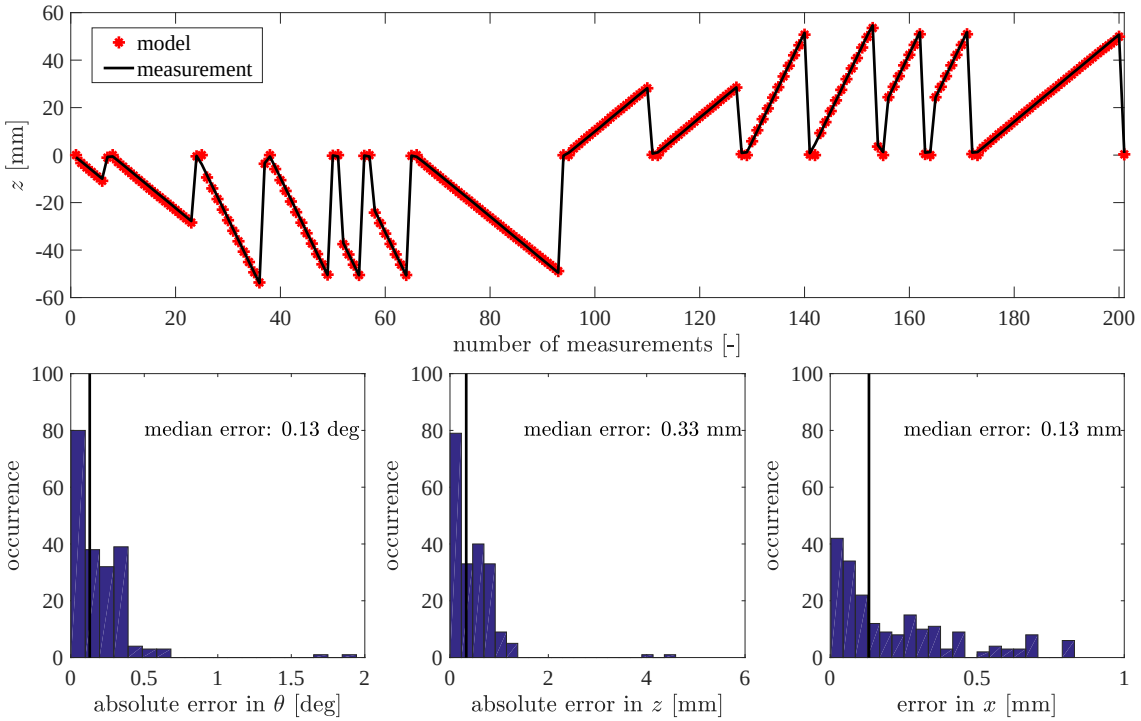

Figure 3.4.: Measurement and model output of the shear experiment. Top: Appended measurement points in z-direction. Bottom: Histogram of the absolute error in θ, z and x between measurement and model with the identified parameters.

measurements points can be observed in the top plot of Fig. 3.5.
The error plots in Fig. 3.5 states that the model with the identified parameters is matching accurately the real system. By examination of Fig. 3.5 it can be concluded, that planar geometrically nonlinear Timoshenko beam of A.1 with the identified parameters of Tab. 3.2 can reproduce the behavior of the real system with a maximum error in the rotation of 1.5 deg (except one outliers) and 1.5 mm in the positions whereas their standard deviations are 0.8 deg and below 0.5 mm respectively.
For comparison, the validation experiment is also evaluated using the a static model of the ECM with a linear (Hookean) material law in the compression direction, see equation (3.19) and its identified axial stiffness from Tab. 3.2. The results are depicted in Fig. 3.5 stating a maximum error in the rotation of 1.5 deg (except one outliers) and 1.6 mm in the positions whereas their standard deviations are 0.8 deg and below 0.5 mm respectively. Thus the achieved accuracy is comparable to the Neo-Hookean material law.

3.4.4. Identification of the spatial system

In the following, the identification process of the spatial system will be reported to identify the elastic parameters, namely the shear stiffness GA in y- and z- direction, their corresponding bending stiffness EI and the torsional stiffness $G_x\, I_x$ along the x-axis. The compression stiffness was already identified in paragraph 3.4.2. For this process, a special test-site is setup which involves a robotic manipulator, and a six-DoF force-torque and a six-DoF pose measurement system. The basic idea for the reported experiments is, that the robot drives the continuum mechanism to several, predefined poses in its workspace. At each pose, the associated deflection wrench ${}_{\mathcal{B}}\boldsymbol{f}_w$, see (3.28) and the pose is measured.

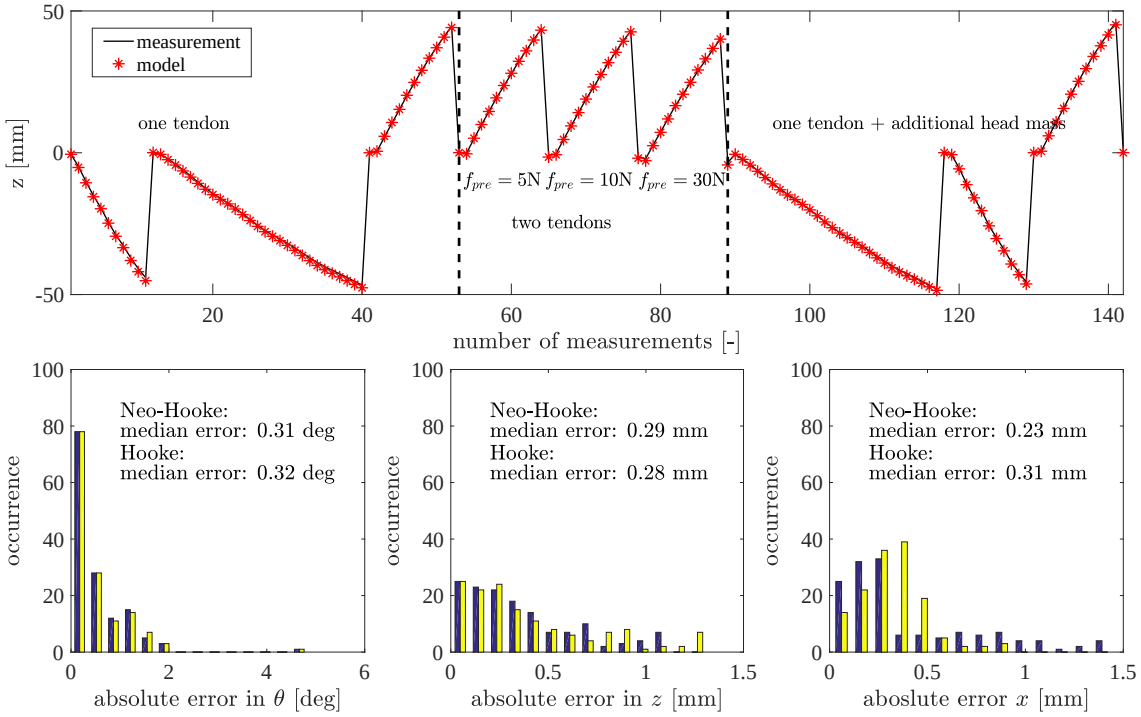

Figure 3.5.: Validation experiments with Neo-Hookean material law (nonlinear material law) and Hookean material law (linear material law) in the compression direction

Based on this data, the identification is carried out. The experimental setup, i.e. the robotic manipulator, the external measurement system and their control interface are explained in the Appendix B.

Uniformly sampled workspace

The idea of this approach is that the elastic parameters contained in the model can be identified if the workspace of the system is uniformly sampled, i.e. every configuration is represented. The workspace is approximated by spatial model from A.2 and identified parameters of the planar model, see Tab. 3.4 are used as an initial guess. This is justified since the same silicone material is used. As the spatial mechanism is cylindrical shaped and thus geometrically symmetric with respect to the $y-$ and $z-$ axis, it is assumed that the shear-stiffness and the bending stiffness along y and z are identical which reduces the problem to the identification of $p = 3$ quantities, i.e. $\boldsymbol{\xi} = (GA, EI, GI)$. For the approximation of the workspace, a feasible wrench region is defined for the components of ${}_{\mathcal{B}}\boldsymbol{f} = ({}_{\mathcal{B}}f_x, {}_{\mathcal{B}}f_y, {}_{\mathcal{B}}f_z, {}_{\mathcal{B}}\tau_x, {}_{\mathcal{B}}\tau_y, {}_{\mathcal{B}}\tau_z)^T$,

$$\mathcal{F} = \{{}_{\mathcal{B}}\boldsymbol{f}_c \in \mathbb{R}^6 | {}_{\mathcal{B}}\boldsymbol{f}_{min} < {}_{\mathcal{B}}\boldsymbol{f}_c < {}_{\mathcal{B}}\boldsymbol{f}_{max}\}, \tag{3.58}$$

with the components of ${}_{\mathcal{B}}\boldsymbol{f}_{max}$ and ${}_{\mathcal{B}}\boldsymbol{f}_{min}$ given in Table 3.3. The maximum and minimum values are chosen to ensure that the corresponding poses covers well the reachable workspace of the continuum mechanism when driven with the tendons. With that, 10000 poses are computed using the spatial model, where the external loading is ${}_{\mathcal{B}}\boldsymbol{f}_c \in \mathbb{R}^6$ (3.28) and the resulting workspace is depicted in the left of Fig. 3.6. In order to sample the generated workspace uniformly and reduce the set to a smaller number of poses to reduce

Table 3.3.: Range of each wrench component ${}_{\mathcal{B}}\boldsymbol{f}_c$

[N]	${}_{\mathcal{B}}f_x$	${}_{\mathcal{B}}f_y$	${}_{\mathcal{B}}f_z$	[Nm]	${}_{\mathcal{B}}\tau_x$	${}_{\mathcal{B}}\tau_y$	${}_{\mathcal{B}}\tau_z$
max	30	60	60	max	3	3	3
min	−66	−60	−60	min	−3	−3	−3

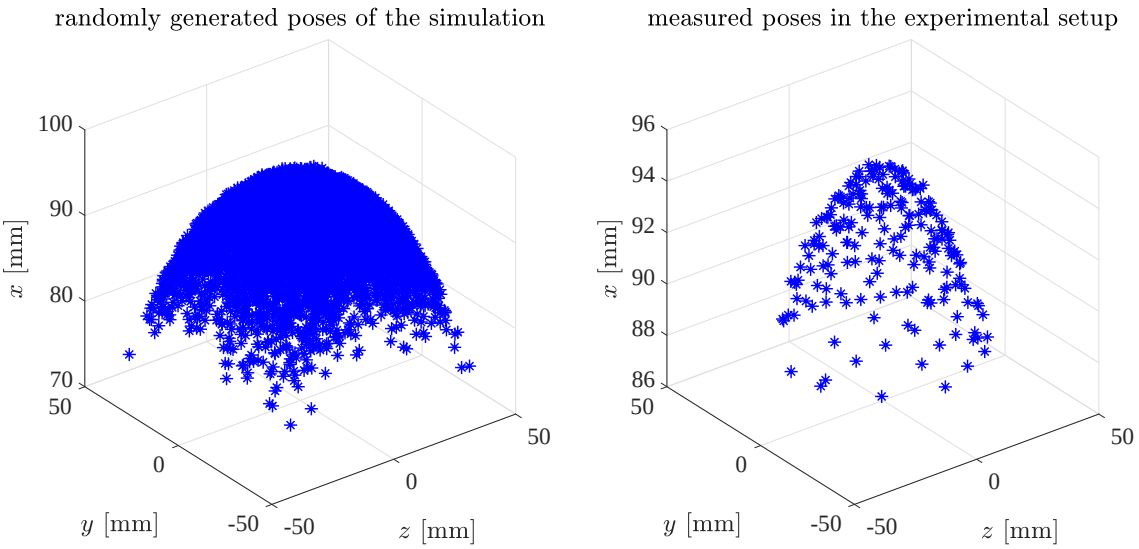

Figure 3.6.: Left: Computed positions with the spatial model and the initial parameters, herein denoted as the candidate set $\mathcal{C}$. Right: Set of sampled poses $\mathcal{D}$ in the experiment using the robotic manipulator.

the computational costs of the identification, the maximin-distance design criteria is introduced [98]. The maximin-distance design aims to select a subset $\mathcal{D}$ from the candidate set $\mathcal{C}$, i.e. our workspace in Fig. 3.6, such that the minimum distance between the design poses is maximized,

$$\max_{\mathcal{D}} \min_{\boldsymbol{p}_1,\boldsymbol{p}_2\in\mathcal{D}} d(\boldsymbol{p}_1,\boldsymbol{p}_2), \tag{3.59}$$

where $\boldsymbol{p}_i \in \mathbb{R}^6$ denotes a certain pose, which is normalized to the range $[-1, 1]$ and $d(\boldsymbol{p}_1,\boldsymbol{p}_2) = \|\boldsymbol{p}_1 - \boldsymbol{p}_2\|^2$ denotes the Euclidean distance between the two poses. Here, the pose $\boldsymbol{p}_i$ of the mechanism consists of the normalized position ${}_{\mathcal{B}}\boldsymbol{r}_L$ whereas the orientation, described by the director triad $\boldsymbol{d}_{i,L}$, is transformed into a corresponding axis-angle representation.
In our case, an analytic solution over the workspace region is not available. In [99] an algorithm is proposed to solve the distance-based optimal design problem for a discrete region which is applied in the following. The basic idea of this algorithm is the following: randomly choose n poses as the initial design set $\mathcal{D}$. Choose a pose $\boldsymbol{p}$ in the candidate set $\mathcal{C}$ and check, if the minimum distance between the poses in the design set can be increased by replacing a certain pose $\boldsymbol{p}_i$ in the design set with $\boldsymbol{p}$.
After sampling the workspace uniformly, the desired poses are subsequently reached by the robot whereas pose and wrench is acquired using the external sensors. The measured translational workspace is seen in the right plot Fig. 3.6.

Identification of the material parameters

The goal is identify $\boldsymbol{\xi} = (GA, EI, GI_x)$ whereas the error function for the identification is

$$\Delta(\boldsymbol{\xi}) = (w_r(\tilde{\boldsymbol{r}}_{L,1} - \boldsymbol{r}_{L,1}(\boldsymbol{\xi})),\, w_\varphi \Delta\boldsymbol{\varphi}_1(\boldsymbol{\xi}),\, \ldots,\, w_r(\tilde{\boldsymbol{r}}_{L,m} - \boldsymbol{r}_{L,m}(\boldsymbol{\xi})),\, w_\varphi \Delta\boldsymbol{\varphi}_m(\boldsymbol{\xi}))^T, \quad (3.60)$$

where $w_r = 1000$ (i.e. scale the error to mm), $w_\varphi = 180/pi$ (i.e. scale the error to deg), $\tilde{\boldsymbol{r}}_L \in \mathbb{R}^3$ is the measured end position, $\boldsymbol{r}_{L,1}(\boldsymbol{\xi})$ is the modeled end position, $\Delta\boldsymbol{\varphi}_i \in \mathbb{R}^3$ is the rotational error of a spatial orientation computed as follows

$$\begin{aligned} \Delta\boldsymbol{A}_i &= \boldsymbol{A}^T_{\mathcal{BH}}(\boldsymbol{\xi})\, \tilde{\boldsymbol{A}}_{\mathcal{BH}}, \\ \Delta\boldsymbol{\varphi}_i &= axisangle(\Delta\boldsymbol{A}_i), \end{aligned} \quad (3.61)$$

where *axisangle* is the operation that computes the axis-angle representation for a given rotation matrix, $\tilde{\boldsymbol{A}}_{\mathcal{BH}} \in \mathbb{R}^{3\times3}$ is the measured and $\boldsymbol{A}^T_{\mathcal{BH}}(\boldsymbol{\xi}) \in \mathbb{R}^{3\times3}$ the modeled orientation of the end of the mechanism.

The identified values of $\boldsymbol{\xi}$ can be found in Tab. 3.4. It can be observed, that the identified values, which are the shear stiffness GA, the bending stiffness EI and the torsional stiffness $G_x\, I_x$. The bending stiffness and torsional stiffness are lower compared the initialized values however the shear-stiffness remains unchanged.
The histogram of the absolute prediction error can be found in Fig. 3.7 of each component direction of (3.60). It can be stated that the error of the identification is bigger, with a maximum of 7 mm in the position and 7 deg in the orientation. This tendency is also reflected by the root-mean-square error (RMSE), shown in the histograms 3.7, which is 1.5 mm in position and 1.7 deg in orientation at maximum. Furthermore, it can be observed that the errors in y and z are not symmetric which indicates systematic errors. For example, a calibration error of the led-target that measured the pose of the continuum might be responsible for the higher translational error z-direction and the rotatory error y-direction (strongly coupled, as shear in z induces bending along y).

Table 3.4.: Initial guess and identified values for the stiffness properties of the spatial mechanism. In the identification process, the stiffness is identified. Next to each stiffness, the projected material parameter, i.e. the Young's and shear modulus are given.

	GA	(Gs)	EI	(E)	GI_x	(G_t)
initialized	368.2	121950	0.617	850000	0.494	340186
identified	368.2	121950	0.606	834770	0.429	295480

The identification of the spatial mechanism with the above results is affected by a strong coupling of the elastic parameters for the given poses, which were chosen based on the decision to cover the workspace uniformly. In contrast, poses that separately excite the different elastic parameters could yield more accurate parameters with which the model matches the real data closer similar to the identification of the planar system. In this case, the identification setup using the robotic manipulator could be applied as well. For a separate excitation, the manipulator could compress the mechanism or introduce a pure torsional torque. Furthermore, poses for which the mechanism needs to be bent could be computed using the constant curvature kinematics. In this way, a pure bending torque is introduced.

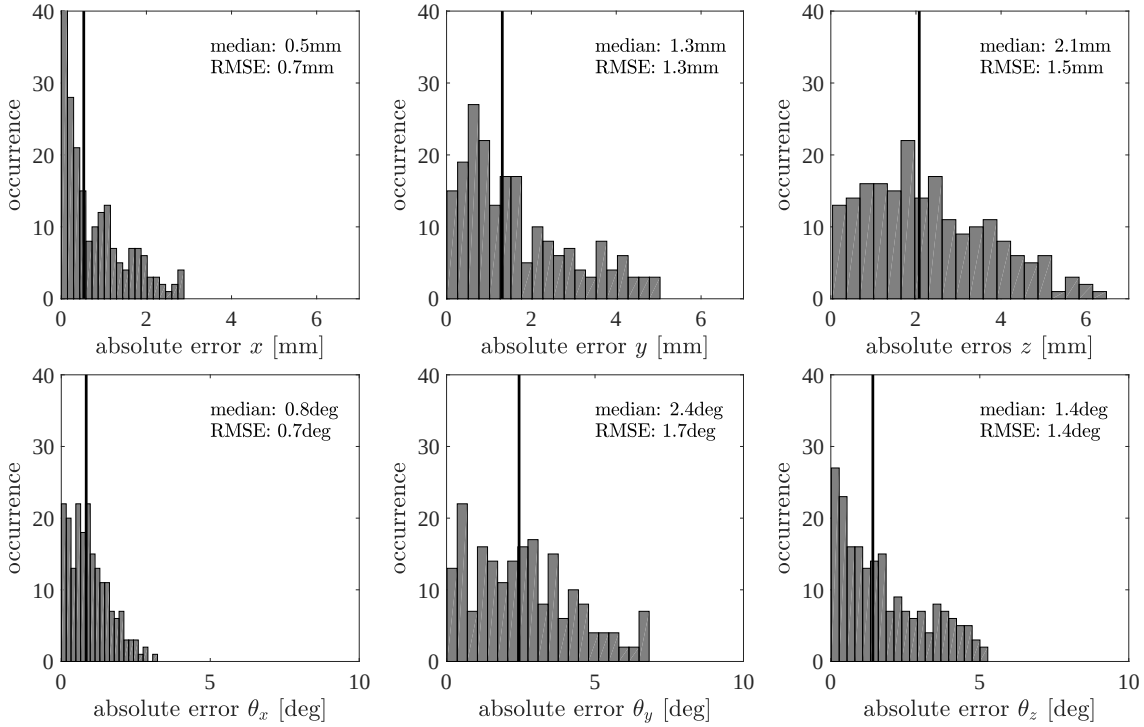

Figure 3.7.: Error histograms of the absolute error for the identification data.

3.5. Applications

The established model of the former section with identified material parameters will be applied in this section to four use cases.
At first, the planar model is investigated. Here, the workspace of the system is computed whereas different arrangements of the pulleys are displayed. Afterwards, the planar dynamic model is treated. Here, a simple damping model is identified to investigate the overall dynamic characteristic. Furthermore, the computational costs are investigated and step responses are simulated with varying head masses to investigate their influence on the overall behavior.
In the third paragraph, the workspace of the spatial system is investigated with respect to different pulley locations and the specific goal will be to find an arrangement with which the torsional workspace can be maximized. In the last paragraph, the workspace of the spatial prototype (see Section 2.2.2) is computed whereas the goal is to find a simpler kinematic representation, i.e. less parameters than 6, which is able to replicate the workspace.

3.5.1. Workspace analysis of the planar system

In the following, the workspace of the planar system is analyzed using the static model of the Appendix. A.1 and its respective stiffness parameters from paragraph 3.4.2 and 3.4.3. The workspace is computed by sampling the input to the model, the tendon forces $\boldsymbol{u} \in \mathbb{R}^2$, randomly within the range $u_i = [10, 170]$ N for $i = 1 \dots 2$. The particular interest of the following investigation is the resulting workspace of such a system w.r.t. the location of the pulleys. For this investigation, the location of the left and the right pulley, described

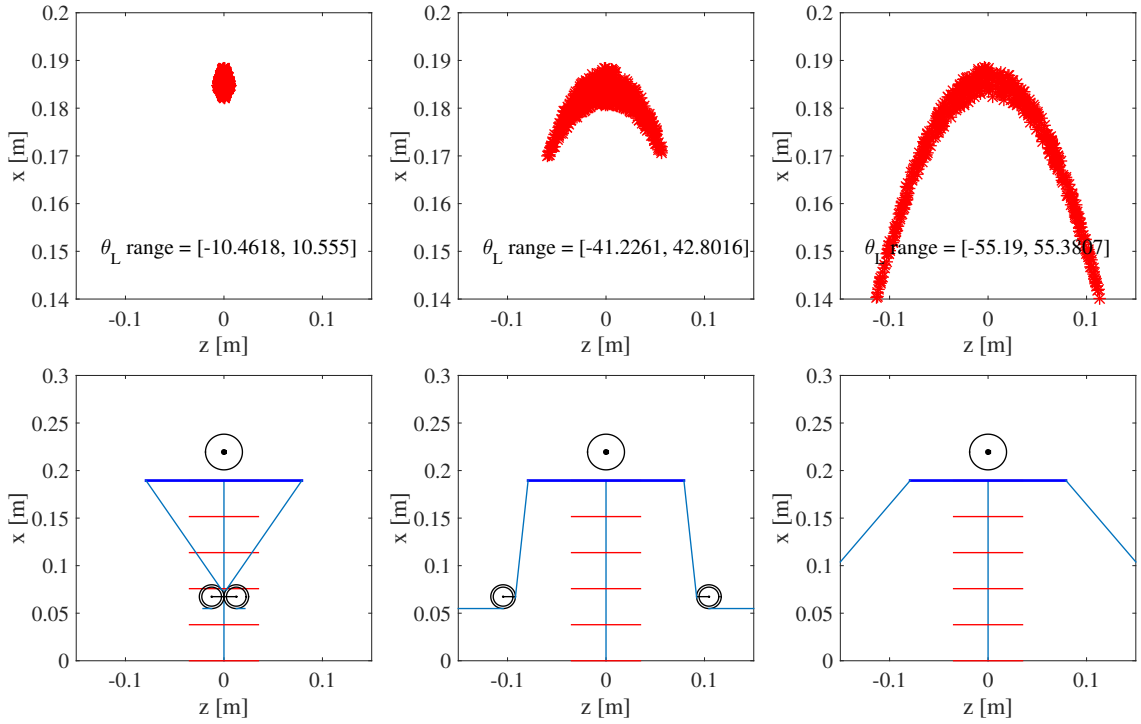

Figure 3.8.: Variation of the pulley location in z-direction (l_p). It can be observed that the workspace increases with increasing l_p.

by

$$ {}_{\mathcal{B}}\boldsymbol{r}_{p,l} = (h_p,\, 0,\, l_p)^T,\ {}_{\mathcal{B}}\boldsymbol{r}_{p,r} = (h_p,\, 0,\, -l_p)^T, \tag{3.62} $$

are altered. At first, the z-component, l_p, of the pulley's is altered starting from $l_p = r_{pulley}$, i.e. where the pulley touches the beam's centerline. The resulting workspace is shown in Fig. 3.8 for three values of l_p stating that the translational and rotational workspace increases with increasing l_p. Second, the x-location, h_p, of the pulley's is altered starting from $h_p = r_{pulley}$, i.e. the case that the pulley touches the ground. The resulting workspace is depicted in Fig. 3.9 for three values of h_p. It can be stated, that the workspace decreases with increasing h_p.

The investigations of this paragraph are only exemplary. However, if a specific design problem is faced for a planar system, the developed model can be helpful for comparing alternatives.

3.5.2. Dynamic characteristic of the planar system

The dynamic characteristic of the present system is directly dependent on the identified material parameters, which are the stiffness parameters of paragraph 3.4.2 and 3.4.3, whereas the damping properties of the ECM is also important. Thus, the subsequent paragraph will discuss a simple damping model and the corresponding identification of the damping parameter. Afterwards the computational time of the dynamic model is investigated. Furthermore, the influence of the top mass onto dynamic characteristic will be discussed.

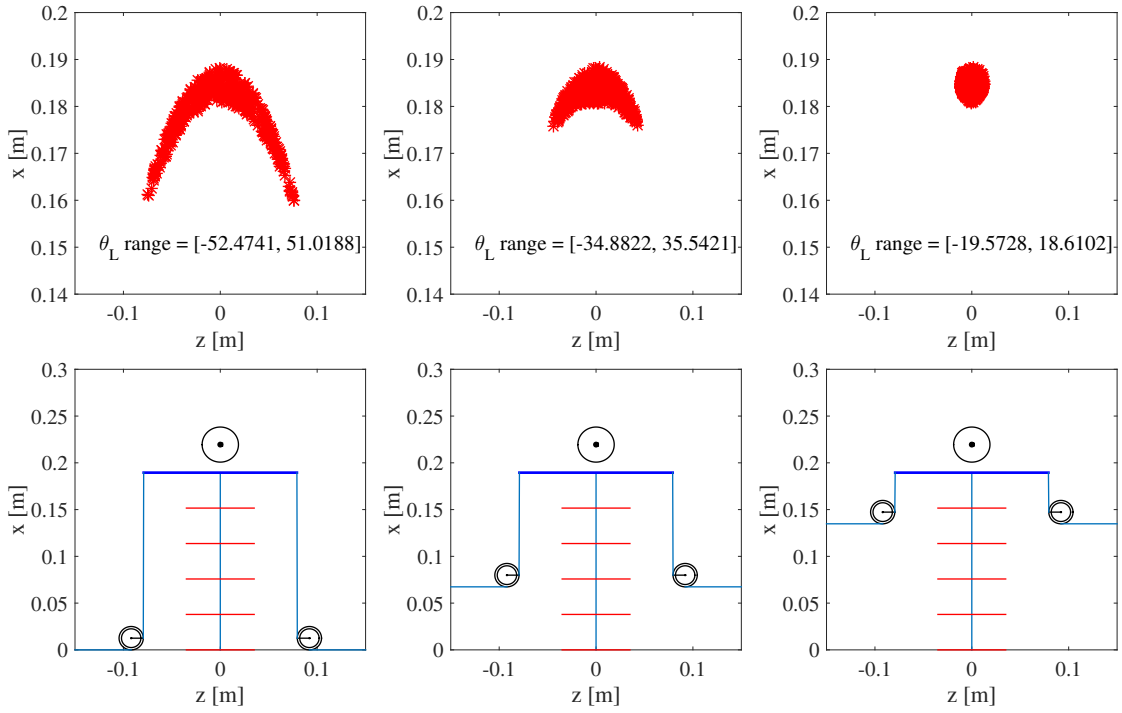

Figure 3.9.: Variation of the pulley location in x-direction (h_p). It can be observed that the workspace decreases with increasing h_p.

Identification of the Damping

This paragraph will discuss a brief identification of the damping characteristic of the planar mechanism based on measured data.
Here, the so called Raleigh-Damping model [100] is applied which consists of a nonlinear damping matrix $\boldsymbol{D}(\boldsymbol{q}) \in \mathbb{R}^{n\times n}$ that constitutes a linearly scaled mass- $\boldsymbol{M}(\boldsymbol{q}) \in \mathbb{R}^{n\times n}$ and stiffness matrix $\boldsymbol{K}(\boldsymbol{q}) \in \mathbb{R}^{n\times n}$,

$$\boldsymbol{D}(\boldsymbol{q}) = \beta \boldsymbol{M}(\boldsymbol{q}) + \alpha \boldsymbol{K}(\boldsymbol{q}), \tag{3.63}$$

with the scaling factors β, $\alpha \in \mathbb{R}$.
The coefficients in (3.63) are fitted based on experimental data which is gained by tracking the tip position of the straight ECM performing a damped oscillation. The oscillation is induced by manually deflecting the mechanism to a given pose from which it freely oscillates back to the initial pose after removing the deflecting force. The recorded response, exemplary shown for the z-component, can be seen in Fig. 3.10. In the left plot, we can see the recorded motion whereas the first 15 detected zero-crossing are plotted for which the identification is carried out. At first, it is observable that the oscillation is almost linear as its period $T = 0.17$ s is almost constant (std= 0.0019 s) similar to the logarithmic-decrement $\delta \in \mathbb{R}$,

$$\delta = \frac{1}{i} \ln \frac{z(t)}{z(t + k\,T)} \tag{3.64}$$

with a mean value of $\delta = 2.0$ and std= 0.1. In equation (3.64), $z(t)$ is the amplitude and $z(t + i\,T)$ is the amplitude i periods away. In terms of a linear dynamic, second order system, an eigenfrequency of $\omega_0 = 5.88$ Hz and damping ration of $\zeta = 0.3$ can be stated

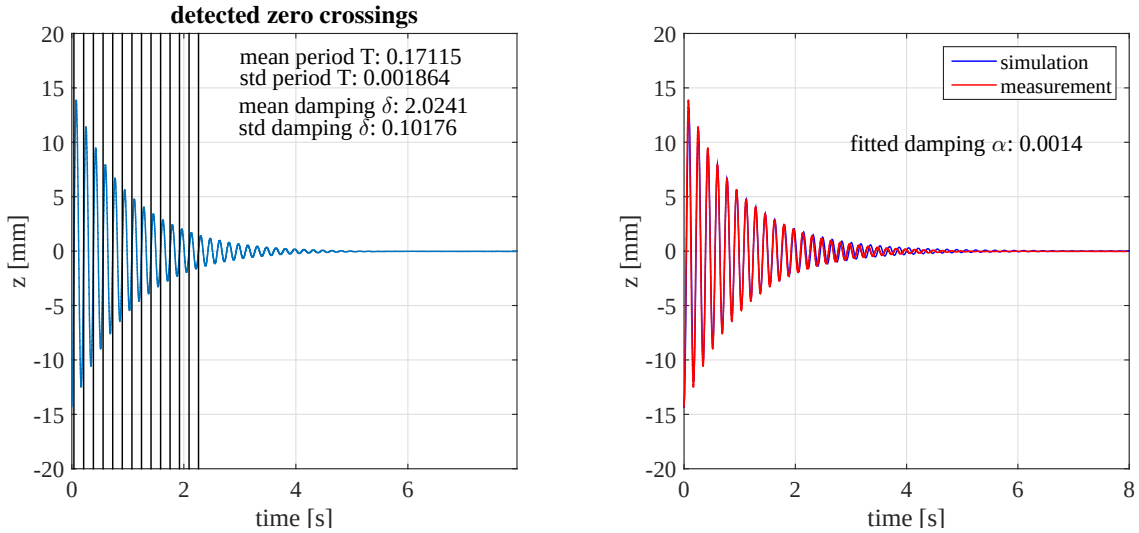

Figure 3.10.: Fitting results for the experimentally identified damping characteristic.

yielding a weakly damped system. The mean values have been computed using the first 15 oscillations.
In the right plot, the fitting accuracy utilizing the Raleigh damping model is stated. For $\beta = 0$ and $\alpha = 1.4e^{-3}$ an almost perfect model match can be reported, investigated for the first 15 oscillations.
Remarks on the damping identification: In general, the identification of the damping properties of such kind of mechanisms is a large research field and thus cannot be treated in all details within this work. The interested reader is referred to [100] for an in dept treatise.

Influence of the top mass

This paragraph will treat the influence of an increasing top mass onto the dynamic characteristic of the elastic continuum mechanism. To do so, the dynamic model of A.1 is simulated with $k_{el} = 4elements$. For the present system with a 1 kg mass on the top, the oscillation introduced by a 100 N step at $t = 2$ s of one tendon force can be observed in the left plot of Fig. 3.11. As expected, the oscillation of the highest node (nd5) is bigger than the lower nodes yielding the typical oscillatory motion of a clamped-free beam. To investigate the influence of higher and lower masses, the right plot of Fig. 3.11 displays the ratio of the maximum amplitudes of the nodes $2-4$ with respect to the maximum amplitude of the highest node 5. As the ratio stays below 1 for all investigated masses, it can be stated that the shape of the oscillatory motion does not change quantitatively.

3.5.3. Torsional workspace of the spatial system

In the following, the workspace of the spatial system is analyzed using the model of the Appendix A.2 and its respective stiffness parameters from paragraph 3.4.4. As the spatial mechanism described in 2.2.2 serves as a robotic neck, it is of interest that the rotational workspace of the system is sufficiently large, e.g. comparable to the human workspace.
The workspace of the present tendon configuration is shown in Fig. 3.12 and it is easily observable that the current tendon configuration limits the orientation workspace along the

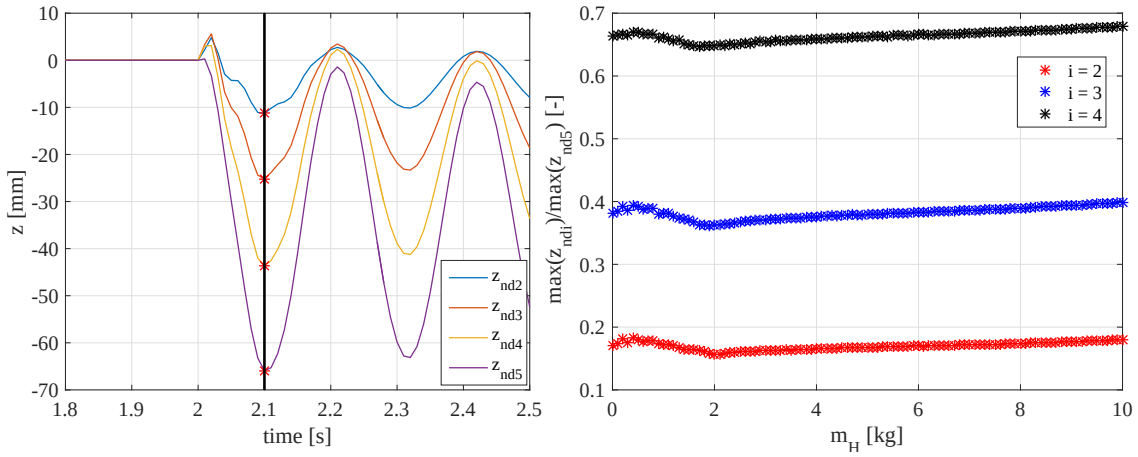

Figure 3.11.: left: Step-response for the planar system with a head mass of 1 kg and a step to 100 N tendon force. The damped oscillation of the z-DoF for all 4 nodes is shown whereas the maximum amplitude of oscillation is highlighted by a red-dot respectively. Right: Ratio of the maximum amplitude of the nodes 2 to 4 with respect to the highest node 5. Again, step responses for a 100 N step are recorded whereas the head-mass was varied from 0.001 to 10 kg.

x-axis with a maximum theoretical rotation of about ±18 deg. To enlarge the workspace around the x-rotation, the tendon configuration is exemplary changed and two novel tendon configurations will be investigated which are displayed in Fig. 3.13.
The symmetric configuration for the test-configurations is chosen to enlarge the rotation along the x-axis. Physically, two opposing tendons, if pulled equally, introduce a torsional torque whereas the bending torques are canceled. With the two test configurations, the maximum rotation along x could be increased to ±25 deg for the first and ±32 deg for the second test configuration.

3.5.4. Kinematic approximation of the spatial workspace

The elastic continuum mechanisms in this thesis are tendon driven whereas the tendons are connected only to the tip end of the continuum. In order to project the effect of the tendons onto the mechanism, the tip pose is necessary and thus has greater importance compared to the whole configuration of the ECM, i.e. any position and material orientation along its centerline.
In general, the end position and orientation of the ECM can be described by a Cartesian pose, i.e. 6 coordinates at minimum. This paragraph discusses briefly the idea to approximate the 6 DoF workspace of the ECM by a reduced number of parameters, $n_{\text{red}} \leq 6$, and will report on the resulting errors that result from the reduction.
In the following, a set of kinematic variables with $n_{\text{red}} = 4$ is discussed,

$$\boldsymbol{q}_{\text{red}} = (\phi,\, \eta\, \iota,\, \epsilon)^T. \tag{3.65}$$

The position and orientation of the head frame $\mathcal{H}$, expressed by the homogeneous transformation matrix ${}^{\mathcal{B}}\boldsymbol{T}_{\mathcal{H}} \in \mathbb{R}^{4\times4}$, can be computed by sequence of homogeneous transformations,

$${}^{\mathcal{B}}\boldsymbol{T}_{\mathcal{H}} = {}^{\mathcal{B}}\boldsymbol{T}(\phi)\, {}^{\mathcal{B}}\boldsymbol{T}(\eta)\, {}^{\mathcal{B}}\boldsymbol{T}(\epsilon)\, {}^{\mathcal{B}}\boldsymbol{T}(k_y\phi)\, {}^{\mathcal{B}}\boldsymbol{T}(k_z\eta)\, {}^{\mathcal{B}}\boldsymbol{T}(\iota) \tag{3.66}$$

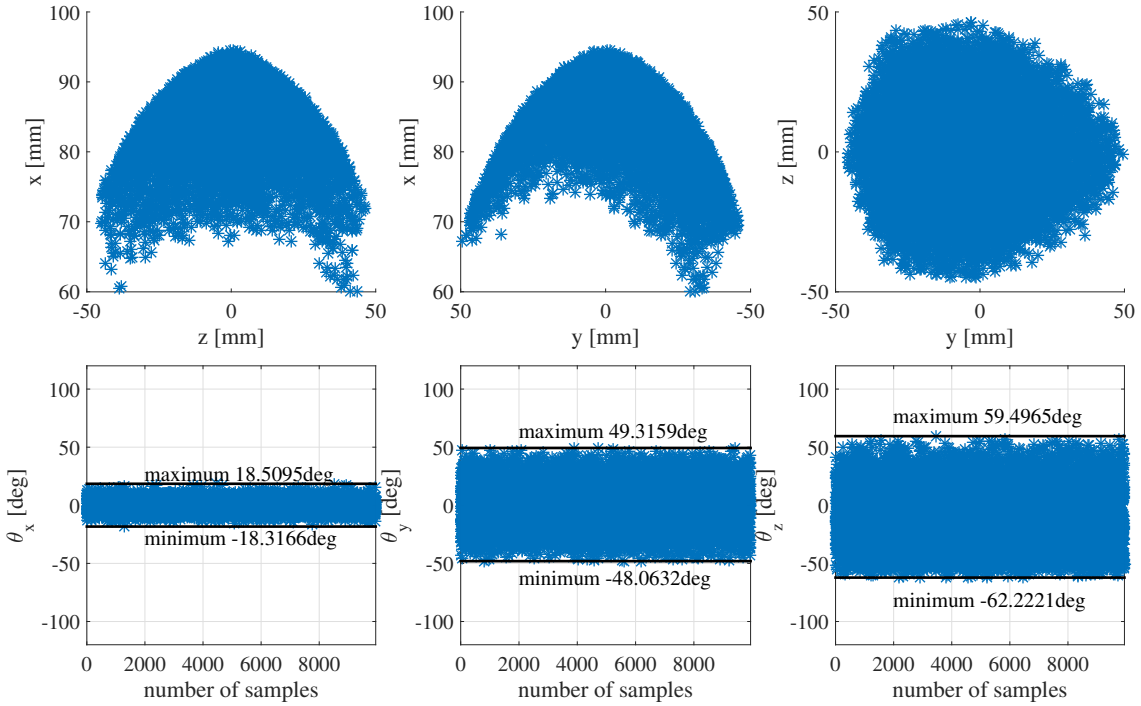

Figure 3.12.: Initial workspace of the spatial testbed. Top row: Projection of the translational workspace onto the x-z, x-y and z-y plane. Bottom row: Orientation workspace, represented by Euler anglers, along all three axis.

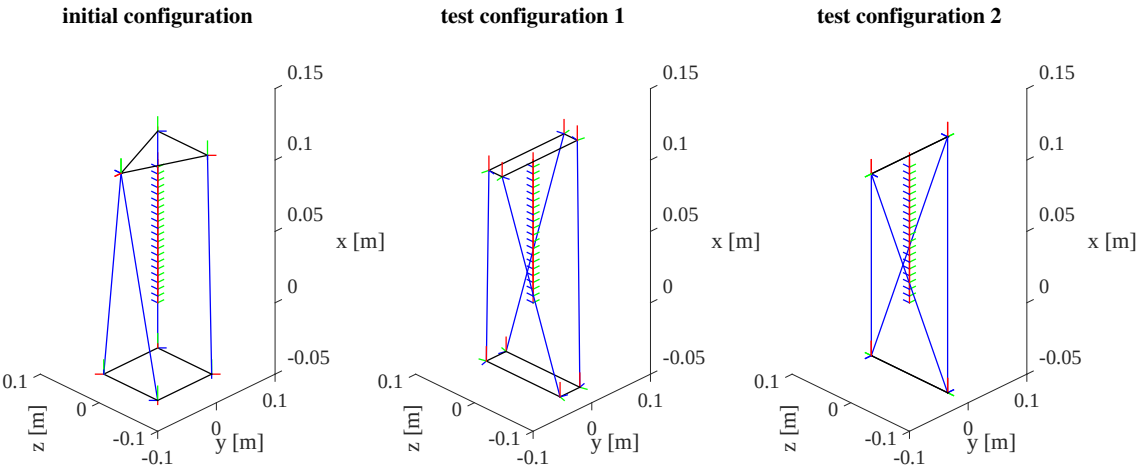

Figure 3.13.: Exemplary tendon configuration which were tested in simulation to increase the rotational workspace. The rotational workspace of the initial configuration is ±18.5 deg which can be increased to ±25.0 deg using test configuration 1 or to ±32.0 deg for test configuration 2.

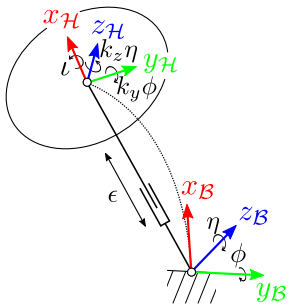

Figure 3.14.: Kinematic structure for the set of reduced kinematic variables. The y- and z-rotation in the base are coupled to the respective rotations in the head frame by two constants, k_y and k_z.

which rotate or translate according to the kinematic structure schematically shown in Fig. 3.14.

To apply the reduced set of kinematic variables, the constant factors $k_y, k_z \in \mathbb{R}$ are exemplary set to two different values. Afterwards, an optimization is carried out using randomly 1000 samples of the workspace (Fig. 3.12), i.e. a set of positions $\boldsymbol{r}_L$ and orientations $\boldsymbol{d}_{1,L}$, $\boldsymbol{d}_{2,L}$, $\boldsymbol{d}_{3,L}$, whereas the pose error $\boldsymbol{e} \in \mathbb{R}^6$ is minimized,

$$\min_{\boldsymbol{q}_{\text{red}}} \; ||\boldsymbol{e}({}^{\mathcal{B}}\boldsymbol{T}_{\mathcal{H}},\, \boldsymbol{r}_L, \boldsymbol{d}_{1,L},\, \boldsymbol{d}_{2,L},\, \boldsymbol{d}_{3,L})||_2, \tag{3.67}$$

to find a suitable set for the reduced kinematic variables. The results are depicted in 3.15 and expressed by the error in position and orientation for two different values for k_y and k_z. It can be stated that the approximation using the reduced kinematic variables fit the simulated data with a maximum mean error in position of ≈ 1.6 mm, (z-direction) and a maximum mean error in orientation of ≈ 1.3 deg (y-direction).

3.5.5. Computation time

This section reports on the computational time of three different beam finite element models subjected to a random input within some bounds. The simulations are implemented in Matlab and performed on the same desktop computer, an Intel Xeon-E5 CPU with 3.50 GHz and 8 Gb RAM. This means, that the recorded times, presented in the following, are comparable with each other. However, the simulation could be run on another target, with higher computational power, and thus might achieve lower times.

Computation time of the planar static model

This paragraphs examines the computational time of the spatial static model derived A.1. In this example, the number of elements is set to $k_{el} = 20$ as it proved to yield a good prediction of the real system, see 3.4.3. A histogram of the simulation time recorded in 1000 simulation runs is given in the left of Fig. 3.16. The input to the simulation model, the $r = 2$ tendon tensions $\boldsymbol{u}$, are randomly chosen within the range [0, 170] which are real limits of the hardware. A mean computational time of ≈ 0.013 s can be reported.

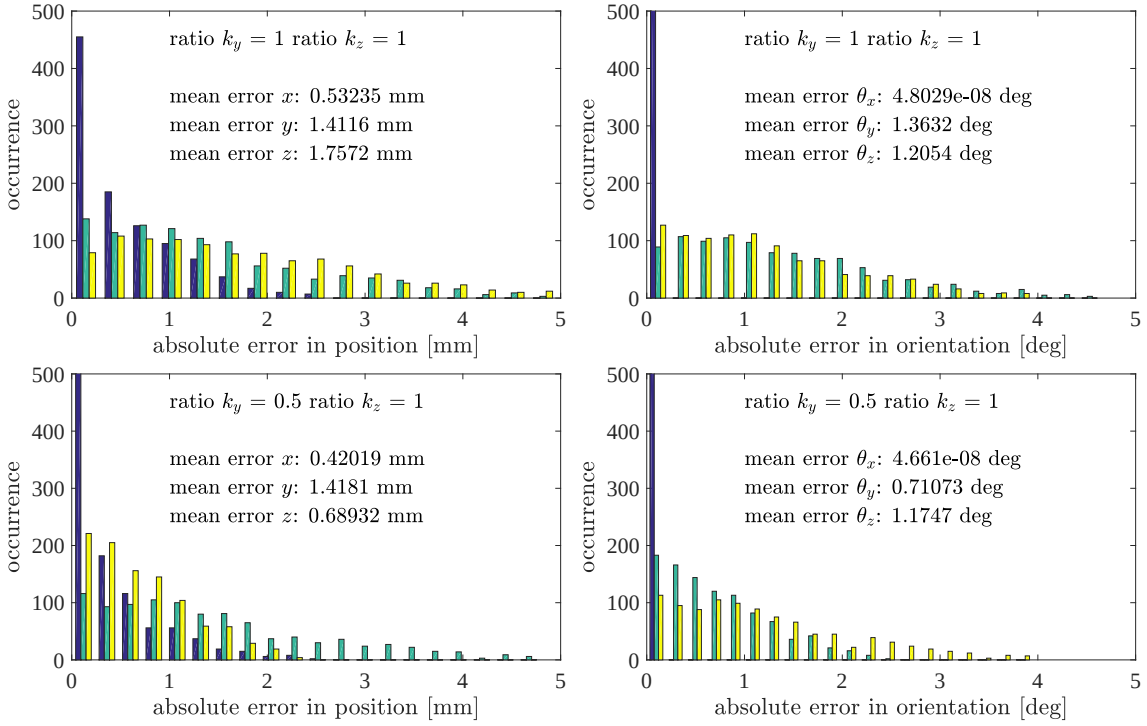

Figure 3.15.: Error histogram for the absolute position and orientation error of 1000 poses of the reduced kinematic mapping for two different constants k_y and k_z.

Computation time of the planar dynamic model

To examine the computational time, random step responses are simulated with a model using $k_{el} = 4$ elements for which one tendon force $u_i \in \mathbb{R}$ is suddenly increased to a random value in the range of [10, 170] N whereas the opposing tendon force is kept constant at 10 N. The total simulated time ranges from 0 to 8 s and the step is executed at $t = 2$ s. The middle plot of Fig. 3.16 displays the histogram of the recorded computational times for 1000 simulations which state a mean computational time of ≈ 9 s.

Computation time of the spatial static model

This paragraphs examines the computational time of the spatial static model derived A.2. In this example, the number of elements is set to $k_{el} = 20$ as it proved to yield a good prediction of the real system, see 3.4.4. A histogram of the simulation time recorded in 1000 simulation runs is given in Fig. 3.16. The input to the simulation model, the $r = 4$ tendon tensions $\boldsymbol{u}$, are randomly chosen within the range [0, 100] which are real limits of the hardware. A mean computational time of ≈ 0.13 s can be reported.

3.6. Summary

This chapter derived the equations of motion for a tendon-driven elastic continuum mechanism using a continuum mechanical approach. The approach utilizes the geometric relations of a nonlinear Timoshenko beam approach to describe the deformation of the continuum with a rigid body at its tip. As a motivation, a planar experimental study is

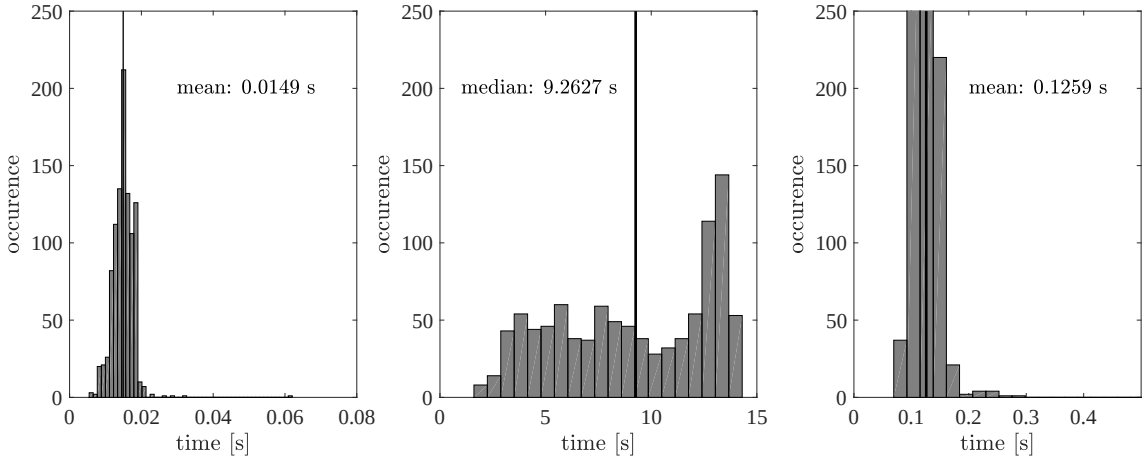

Figure 3.16.: Left: Histogram of the computational time of the planar model subjected to 1000 randomly sampled inputs. Middle: Histogram of the computational time of the planar dynamic model with four elements when simulation randomly generated step responses. Right: Histogram of the computational time of the spatial model subjected to 10000 randomly sampled inputs within the admissible range of tendon forces.

carried out that emphasizes the presence of bending, shear and normal deformation in the real system and thus the Timoshenko beam approach is justified.

Subsequently, the equations of motion as well as the static equilibrium equations for such a system are derived using the principle of virtual work as it is a formalism that can be easily applied for continuous and rigid bodies. To solve the resulting coupled nonlinear partial differential equation of the dynamic case and the coupled nonlinear ordinary differential equation of the static case, a beam finite element approach is utilized which yields the desired structure for the equations of motions (3.1) and for the static equilibrium equation (3.2).

With this framework, the equations of motion and the static equilibrium equations are given for two systems to exemplary guide the interested reader along such involved derivations. Since the motivation of the present chapter has been the computation of the workspace for such mechanisms, the behavior of the material is mandatory. In the present case, the material parameters are the cross sectional stiffness parameters which are identified, again for the two example systems, as they exist in respective test setups. With the identified material parameters, the measured behavior in those real systems could be predicted with a median error in position and orientation of 0.5 mm and 0.8 deg for the planar and a median error in position and orientation of 2.3 mm and 2.6 deg for the spatial system. By comparing the achieved accuracy, it can be stated that the model prediction accuracy is higher for the planar model which seems contradicting as the same silicone material and the same model are used. However, for the planar case, the material parameters have been identified in experiments which solely excite on parameter at a time whereas the spatial model was identified based on measurements that included coupled deformations. This observation lead to the conclusion that the spatial mechanism should be identified based on separately excited material parameters. The second observation is related to the fact, that the material parameters from the planar system provided an accurate initial guess for the spatial system and therefore, it seems that the used silicone

does not vary largely with respect to the manufacturing process.

In the end, the accomplishments of the present chapter, which are essentially fully identified models, are applied in four different use cases that illustrate workspace computations, the static and dynamic deformation characteristics of such systems, and a study on the computational time. The established models are used in the following chapters and lay the foundation for the workspace computations used in this thesis.

CHAPTER 4

Modeling for Control

This chapter treats the derivation of a model which will be used later on in the model-based control approach for tendon-driven elastic continuum mechanism. The rigorous model derived in the former chapter is not suitable for real time control due to the higher computational times, see paragraph 3.5.5, which states a computational efficiency of a spatial model with a mean computational time of ≈ 130 ms. Consequently, this chapter will treat a different, more simplified models which are faster to compute and thus suitable for control. In the course of the chapter, dynamic models are derived which provide the future basis for the control later on.
The necessary assumptions and the respective choice of generalized coordinates to describe the motion of the system are stated and discussed in Section 4.1. These simplification yield, first of all, that the ECM is approximated as a rigid body on top of a multiple degree of freedom spatial spring system. Secondly, the dynamics of the tendon actuators are decoupled from the dynamics of the ECM.
Section 4.2 presents two models which represent the spatial spring system which are based on an experimental identification process. The results presented here have been partially published in [79].

In the second part of this chapter in Section 4.3, the dynamics of the actuation system is discussed. Here, the relationship between desired motor torque and the respective generated tendon force is stated whereas a simple model is derived which will be necessary for the tendon tension control discussed in paragraph 6.2.

4.1. Assumptions & model reduction

The subsequent section presents the relevant assumptions in order to reduce the dynamic equation of the overall system, which is schematically illustrated in Fig. 4.1. The illustration presents a scheme of the complete system on the left hand side and the reduced version on the right hand side. A rigorous model, which describes the system on the left hand side, consists of dynamics of the elastic continuum mechanism, elastically coupled by the tendons, to the dynamics of the r- tendon actuators. Chapter 3 presented a detailed model for the elastic continuum mechanism actuated by r tendon tensions. To design a model-based controller, this model needs to be augmented by the dynamics of

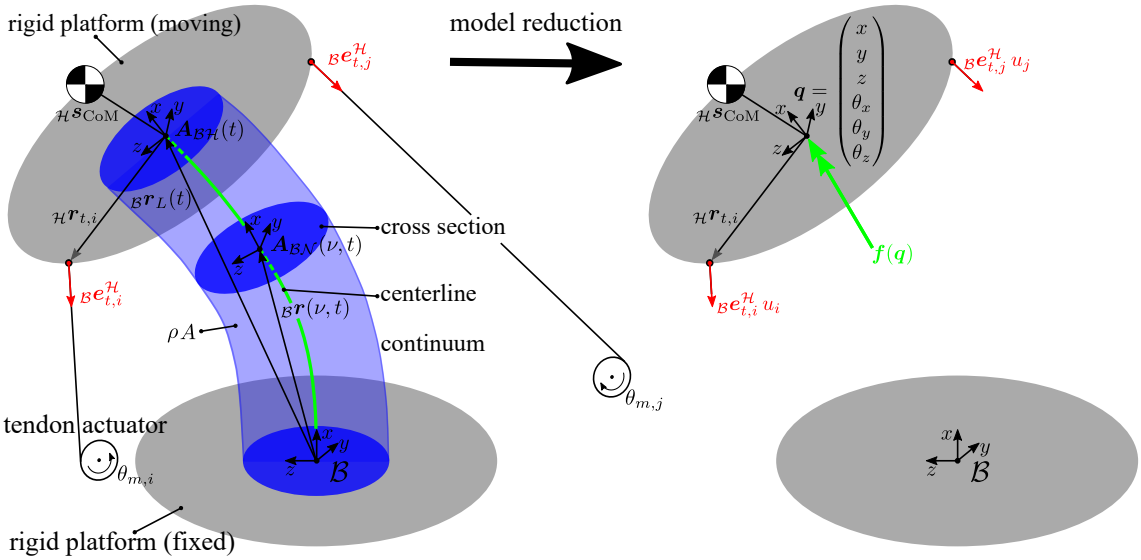

Figure 4.1.: Schematic drawing of the model reduction. The schematic on the left side illustrates a rigorous model that incorporates the dynamics of the continuum and the dynamics of the head, elastically coupled to the dynamics of the actuators. The scheme on the right hand side illustrates the model after the reduction which contains the dynamics of a rigid body coupled to a mass-less nonlinear spring mechanism $\boldsymbol{f}(\boldsymbol{q})$.

the actuators, as illustrated in Fig. 4.1.

To reduce the complexity of the overall model, it is assumed that the stiffness of the tendons is significantly high which enables to neglect the elastic coupling and decouple the dynamics of the actuators, and the dynamics of the continuum mechanism. The assumption is reasonable in the case of steel tendons as they provide a very high stiffness even if a small diameter is used. The dynamics of the tendon actuators is described in Section 4.3, whereas Chapter 3 presented already the dynamics of the tendon-driven ECM, i.e. the beam finite element model of the form (3.1). In this case, a small number of elements already results in a large number of degree of freedom (DoF), e.g. $k_{el} = 5$ elements yields 30 DoF at least. As mentioned already, resulting computational inefficiency presents a challenge for real time use.

To essentially reduce the complexity, it is assumed that the dynamic effects of the continuum structure can be neglected. This assumption is motivated by the investigations of paragraph 3.5.2 which states that the influence of the dynamics of the continuum is not dominant. With this assumption, the density of the continuum is zero, $\rho = 0$, implying that the continuum and the corresponding virtual work of the gravitational forces of the continuum (3.29) and the virtual work of the dynamic forces of the continuum (3.38) vanish. This implies for the total virtual work (3.39)

$$\delta W^{dyn,head} + \underbrace{\delta W^{dyn,beam}}_{=0} + \delta W^{tendon} + \underbrace{\delta W^{grav,head}}_{=0} + \delta W^{grav,beam} + \ldots$$
$$\ldots + \delta W^{w} + \delta W^{int} \; \forall \, {}_{\mathcal{B}}\delta \boldsymbol{r}_{adm}, \, {}_{\mathcal{B}}\delta \boldsymbol{\phi}_{adm}.$$

Furthermore, it is assumed, that the configuration of the continuum can be uniquely described by a set of kinematic parameters, denoted as the reduced generalized coordinates $\boldsymbol{q} \in \mathbb{R}^{n_{\text{red}}}$ in the following. By that, the continuum mechanism is approximated as a mass

less nonlinear spring mechanism ($^{\mathrm{s}}$), with a maximum of 6 DoF ($n_{\mathrm{red}} = 6$) for the spatial case.

By this assumption, the virtual work of the system (3.39) reduces to

$$\delta W^{dyn,head} + \delta W^{tendon} + \delta W^{grav,head} + \delta W^{w} + \underbrace{\delta W^{int}}_{=\delta W^{\mathrm{s}}} = \mathbf{0} \;\; \forall \boldsymbol{q}_{adm} \tag{4.1}$$

with the term for the virtual work of the nonlinear spring system $\delta W^{\mathrm{s}} \in \mathbb{R}$,

$$\delta W^{\mathrm{s}} = \delta \boldsymbol{q}^T \, \boldsymbol{f}(\boldsymbol{q}). \tag{4.2}$$

Here, the introduced nonlinear spring force $\boldsymbol{f}(\boldsymbol{q}) \in \mathbb{R}^{n_{\mathrm{red}}}$, represents a nonlinear, generalized force associated with the stiffness characteristics of the continuum spring. Technically, $\boldsymbol{f}(\boldsymbol{q})$ represents the Cartesian restoring forces and torques, resulting from a deflected continuum mechanism, projected into the generalized directions.

The equation of motion from the reduced system are then derived from (4.1) which yields the desired form of the equation of motion for the elastic continuum mechanism,

$$\boldsymbol{M}(\boldsymbol{q})\ddot{\boldsymbol{q}} + \boldsymbol{c}(\boldsymbol{q}, \dot{\boldsymbol{q}}) + \boldsymbol{d}(\dot{\boldsymbol{q}}) + \boldsymbol{g}(\boldsymbol{q}) + \boldsymbol{f}(\boldsymbol{q}) = \boldsymbol{P}(\boldsymbol{q})\boldsymbol{u}. \tag{4.3}$$

The subsequent section 4.2 will introduce an approach to experimentally identify the generalized force vector $\boldsymbol{f}(\boldsymbol{q})$ to ensure that the deflection characteristic, the equilibrium poses and the workspace of the system coincides to the real system.

4.2. Approximation of the continuum

To approximate the continuum, simple, computationally fast models are proposed in the following and the involved model parameters are identified based on experiments to match equilibrium configurations and the stiffness characteristics of the real system. In the experiment, $\boldsymbol{f}(\boldsymbol{q})$ and the corresponding, deflected position and orientation of the moving platform are measured statically by external sensors and a robotic manipulator is utilized to drive the platform to these static configuration. The three-step process of Fig. 4.2 is proposed, which consists of simulation, experimental design and experiment.
First and foremost, the set of admissible wrenches $\mathcal{F}$ needs to be selected as it serves as the input to the simulation step. An element of $\mathcal{F}$ is a Cartesian wrench ${}_{\mathcal{B}}\boldsymbol{f}_c \in \mathbb{R}^6$ which is applied at the head to deflect the mechanism and expressed in the base frame $\mathcal{B}$. The choice of $\mathcal{F}$ is crucial for the results and is discussed in paragraph 4.2.1.
The first step of the method is treated in paragraph 4.2.2. In this step, each wrench in $\mathcal{F}$ is used to generate a corresponding configuration of the ECM by using the static beam finite element model of chapter 3 including the position and orientation of the moving platform. The set of generalized coordinates to describe the configuration of the ECM, resulting from corresponding wrenches in $\mathcal{F}$, is denoted as the training set $\mathcal{C}$. Basically, each $\boldsymbol{q}$ in $\mathcal{C}$ corresponds to static equilibrium positions and orientations of the moving platform. The overall goal of the approach is to find a nonlinear generalized force function, defined as a mapping

$$\boldsymbol{f} : \mathcal{C} \rightarrow \mathcal{F} \tag{4.4}$$

which maps poses from $\mathcal{C}$ to a corresponding deflection wrench in $\mathcal{F}$. In the simulation step, larger sets for $\{\mathcal{F}, \mathcal{C}\}$ can be handled easily, however, large number of poses which need to be sample experimentally result in long experimental duration and in a high energy consumption which is not feasible. Therefore, the second step of the methodology

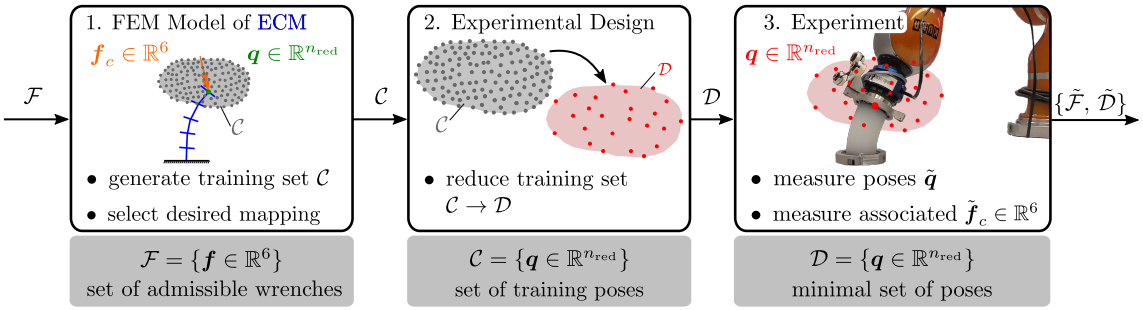

Figure 4.2.: Overview of the three subsequent steps incorporated in the proposed method to identify the stiffness characteristic.

is introduced in paragraph 4.2.3 to reduce the number of poses of the training set $\mathcal{C}$ to a minimum set of informative poses $\mathcal{D}$, called the design poses. The the third step, the experiments, of the described process are discussed in paragraph 4.2.4 and involve the experimental setup described in B. The setup involves a robotic manipulator that enables an automatic execution of the experimental procedure. The experimentally identified model ensures realistic models for $\boldsymbol{f}$ (4.4) although the measured poses $\tilde{\mathcal{D}}$ and the corresponding wrenches $\tilde{\mathcal{F}}$ might deviate from the initially simulated sets, $\{\mathcal{F}, \mathcal{D}\}$. A comparison of $\boldsymbol{f}$ (4.4) which has been identified in simulation and in experiments is therefore treated at the end of the section.

4.2.1. Admissible wrench set

As stated above, the approximation of the continuum is based on the simplification of the continuum structure to a nonlinear spring system (4.2). Technically, a generalized nonlinear force $\boldsymbol{f}(\boldsymbol{q}) \in \mathbb{R}^{n_{red}}$ replaces the continuum and acts on the rigid platform of the head. The incorporated forces and torques are directed along the generalized coordinates $\boldsymbol{q}$.
The set of admissible wrenches $\mathcal{F}$, on the other hand, contains wrenches ${}_{\mathcal{B}}\boldsymbol{f}_c \in \mathbb{R}^6$ which are defined in Cartesian space respecting the base frame $\mathcal{B}$, and possess the component wise formulation

$$ {}_{\mathcal{B}}\boldsymbol{f}_c(\boldsymbol{q}) = \begin{pmatrix} {}_{\mathcal{B}}f_x \\ {}_{\mathcal{B}}f_y \\ {}_{\mathcal{B}}f_z \\ {}_{\mathcal{B}}\tau_x \\ {}_{\mathcal{B}}\tau_y \\ {}_{\mathcal{B}}\tau_z \end{pmatrix}. \tag{4.5} $$

The components in (4.5) act along the Cartesian directions whereas ${}_{\mathcal{B}}\boldsymbol{f}_c$ can be related to the generalized nonlinear force of the continuum using the configuration Jacobian matrix $\boldsymbol{J}_{\chi,q} \in \mathbb{R}^{6\times n_{red}}$,

$$ {}_{\mathcal{B}}\dot{\boldsymbol{\chi}} = \boldsymbol{J}_{\chi,q}\dot{\boldsymbol{q}}, \tag{4.6} $$

with Cartesian velocities of the head respecting the base frame ${}_{\mathcal{B}}\dot{\boldsymbol{\chi}} \in \mathbb{R}^6$. The relationship of $\boldsymbol{f}(\boldsymbol{q})$ and ${}_{\mathcal{B}}\boldsymbol{f}_c$ is then expressed as

$$ \boldsymbol{f}(\boldsymbol{q}) = \boldsymbol{J}_{\chi,q}^T {}_{\mathcal{B}}\boldsymbol{f}_c. \tag{4.7} $$

In the following, the choice and generation of three different sets of admissible wrenches, $\mathcal{F}_i$, $i = \{1 \dots 3\}$ is discussed. As mentioned earlier, the choice of $\mathcal{F}$ is crucial, as it is the

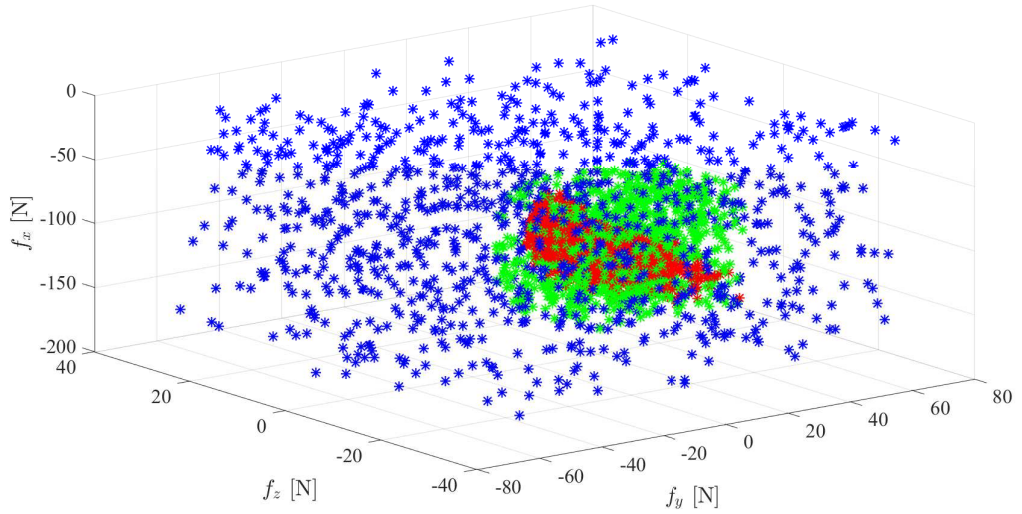

Figure 4.3.: Graphical illustration of the three admissible wrench sets $\mathcal{F}_1$ (blue), $\mathcal{F}_2$ (green) and $\mathcal{F}_3$ (red) used in the simulation step for the specific continuum mechanism, i.e. the spatial testbed of Section 2.2.2. Due to the application, it is expected that the torque-range along z is bigger compared with the y, and consequently the force-range along y is bigger than along z which the specific look of the respective admissible sets.

input to the simulation step and basically decides the generation of the static workspace on which the characteristic of the approximation for the continuum is trained.

Symmetric wrench set $\mathcal{F}_1$

The first wrench set $\mathcal{F}_1$ is generated symmetrically by lower and upper bounds for each wrench component (4.5). The lower bounds for each wrench component are summarized in ${}_{\mathcal{B}}\boldsymbol{f}_{\min} \in \mathbb{R}^6$ and upper bounds for each wrench component are summarized in ${}_{\mathcal{B}}\boldsymbol{f}_{\max} \in \mathbb{R}^6$. A graphical interpretation of the geometrical space generated by $\mathcal{F}_1$ is a six dimensional hyper cube whereas the space generated by the forces only is a 3 dimensional cube and is illustrated in Fig. 4.3 by the blue dots. Thus, the wrench set $\mathcal{F}_1$ is defined as

$$\mathcal{F}_1 = \{{}_{\mathcal{B}}\boldsymbol{f}_c | {}_{\mathcal{B}}\boldsymbol{f}_{\min} < \boldsymbol{f}_c < {}_{\mathcal{B}}\boldsymbol{f}_{\max}\}. \tag{4.8}$$

Wrench sets $\mathcal{F}_2$ & $\mathcal{F}_3$ generated by admissible tendon forces

The second and third set of wrenches are generated by taking admissible tendon forces into account and their implied workspace.
Due to the mechanical properties, tendons can only transmit positive forces (tensions) up until their tensile strength which results in a maximum permissible tendon force per tendon, summarized in the r-dimensional vector of maximum tendon forces $\boldsymbol{u}_{max} \in \mathbb{R}^r$. The Cartesian wrench ${}_{\mathcal{B}}\boldsymbol{f}_c$ is generated by solving the static equilibrium equations of the finite element model (A.94),

$$\boldsymbol{k}(\boldsymbol{q}, \boldsymbol{0}) - \boldsymbol{P}(\boldsymbol{q})\boldsymbol{u} = \boldsymbol{0},$$

for a set of permissible tendon forces

$$\mathcal{U} = \{\boldsymbol{u} \in \mathbb{R}^r |\ \mathbf{0} < \boldsymbol{u} < \boldsymbol{u}_{max}\}, \tag{4.9}$$

resulting in a set of generalized coordinates

$$\mathcal{Q} = \{\boldsymbol{q} \in \mathbb{R}^{n_{\text{red}}} |\ \boldsymbol{k}(\boldsymbol{q}, \mathbf{0}) - \boldsymbol{P}(\boldsymbol{q})\boldsymbol{u} = \mathbf{0} \,\forall\, \boldsymbol{u} \in \mathcal{U}\}. \tag{4.10}$$

Thus, the wrench set $\mathcal{F}_3$ generated by admissible tendon forces is defined to

$$\mathcal{F}_3 = \{{}_{\mathcal{B}}\boldsymbol{f}_c |\ {}_{\mathcal{B}}\boldsymbol{f}_c = \boldsymbol{P}(\boldsymbol{q})\boldsymbol{u},\, \forall \boldsymbol{u} \in \mathcal{U} \wedge \forall \boldsymbol{q} \in \mathcal{Q}\} \tag{4.11}$$

This results in an unsymmetrical set of admissible wrenches, see the illustration in Fig. 4.3, and the resulting set of poses, here denoted as $\mathcal{Q}$ equals the static workspace of the elastic continuum mechanism.

The set $\mathcal{F}_3$ can be augmented to a set of wrenches, denoted as $\mathcal{F}_2$. For the generation of $\mathcal{F}_2$, the component wise maximum and minimum values for ${}_{\mathcal{B}}\boldsymbol{f}_c$ in $\mathcal{F}_3$ are considered, denoted as ${}_{\mathcal{B}}\boldsymbol{f}_{c,min,3} \in \mathbb{R}^6$ and ${}_{\mathcal{B}}\boldsymbol{f}_{c,max,3} \in \mathbb{R}^6$. Then, the set $\mathcal{F}_2$ is generated by

$$\mathcal{F}_2 = \{{}_{\mathcal{B}}\boldsymbol{f}_c |\ {}_{\mathcal{B}}\boldsymbol{f}_{c,min,3} < {}_{\mathcal{B}}\boldsymbol{f}_c < {}_{\mathcal{B}}\boldsymbol{f}_{c,max,3}\}, \tag{4.12}$$

which is geometrically the bounding box on the admissible wrench set $\mathcal{F}_3$, also illustrated in Fig. 4.3 by green dots.

In the following, $\mathcal{F}_1$, $\mathcal{F}_2$ and $\mathcal{F}_3$ are used in the simulation step to produce their corresponding set of head poses $\mathcal{C}_i$ $i = 1, \ldots, 3$ using the static finite element simulation model.

4.2.2. Simulation

Two goals are pursued in the simulation step. The first goal is to generate a training set $\mathcal{C}$ which is defined as the set of poses of the moving platform $\boldsymbol{q}$ that are a solution to the static equilibrium,

$$\mathcal{C} = \{\boldsymbol{q} \in \mathbb{R}^6 |\ \boldsymbol{k}(\mathbf{0}, \boldsymbol{q}) - {}_{\mathcal{B}}\boldsymbol{f}_c = \mathbf{0} \ \forall\ {}_{\mathcal{B}}\boldsymbol{f}_c \in \mathcal{F}\}. \tag{4.13}$$

The second goal is to find a suitable mapping for (4.4) which represents the characteristic of $\boldsymbol{f}(\boldsymbol{q})$ in the workspace $\mathcal{C}$. In the following, two essentially different mappings are introduced and identified, schematically illustrated in Fig. 4.4. For the first mapping, multivariate polynomial (MVP) approach is proposed for each component of $\boldsymbol{f}(\boldsymbol{q})$ whereas the nonlinear spring mechanism acts as a Cartesian spring attached to the origin of the head frame $\mathcal{H}$. Thus, the geometry of the nonlinear deflection and the material properties of the continuum are represented by component wise polynomial functions. The second mapping, denoted as NKLS, on the other hand assumes a known nonlinear kinematics which five rotational and one translational joint, see Fig. 4.4 and a linear spring is introduced along each joint axis to approximate the continuum.

Multivariate Polynomials (MVP)

The first approach assumes that mapping for $\boldsymbol{f}(\boldsymbol{q})$ can be represented by a complex spring mechanism applied at the origin of the head frame $\mathcal{H}$ which is located at the moving platform, as illustrated in Fig. 4.4. The illustrated spring mechanism implies that a

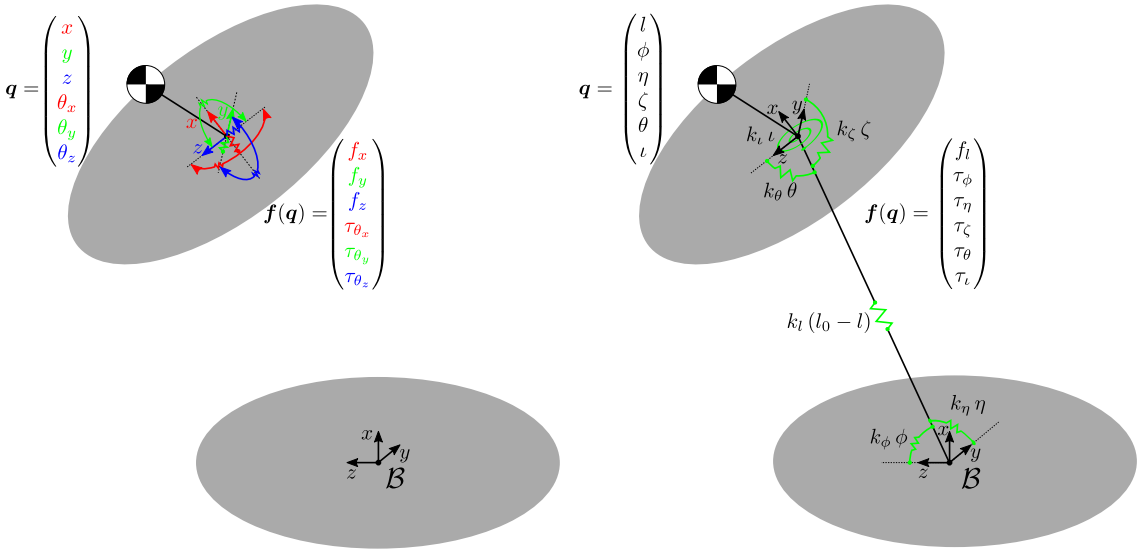

Figure 4.4.: Schematic illustration of the two introduced and trained mappings. Left: A six dimensional spring system is located at the origin of the heap frame and multivariate polynomials model the spring characteristics, which is the mapping from $\boldsymbol{q}$ to $\boldsymbol{f}(\boldsymbol{q})$. Right: Approximation of the continuum mechanism by a serial kinematic arrangement involving five rotational, one prismatic joint, their associated kinematic parameters, as well as linear rotational and translational joint stiffness parameters.

deflection of $\boldsymbol{q}$, containing the (x, y, z) position and the $(\theta_x, \theta_y, \theta_z)$ Euler angles of the head pose,

$$\boldsymbol{q} = (x,\ y,\ z,\ \theta_x,\ \theta_y,\ \theta_z)^T, \tag{4.14}$$

results in coupled restoring forces and torques along the generalized directions,

$$\boldsymbol{f}(\boldsymbol{q}) = (f_x,\ f_y,\ f_z,\ f_{\theta_x},\ f_{\theta_y},\ f_{\theta_z})^T. \tag{4.15}$$

A polynomial mapping will be employed for each component of (4.15) in the following as it increases the computational efficiency. Furthermore, the stiffness matrix $\boldsymbol{K}(\boldsymbol{q}) \in \mathbb{R}^{n_{\text{red}} \times n_{\text{red}}}$ can be derived analytically which is very useful to study the stiffness behavior of the mechanism in the workspace, or the linearization process. Linear, quadratic and cubic relationships between $\boldsymbol{q}$ and each component f_j for $j \in \{x,\ y,\ z,\ \theta_x,\ \theta_y,\ \theta_z\}$ is studied using the polynomial formula

$$f_j^i = (\boldsymbol{x}^i)^T \boldsymbol{\beta}_j + \epsilon_j^i, \tag{4.16}$$

where f_j^i denotes the i-th observation of f_j, $\boldsymbol{\beta}_j \in \mathbb{R}^k$ is a vector containing all polynomial coefficients to be estimated for the j-th component, ϵ_j^i denotes the i-th observation error of the j-th component and $(\boldsymbol{x}^i)^T \in \mathbb{R}^k$ denotes the regressor row containing the information of the i-th observation of the generalized coordinates. Depending on the polynomial order, the dimension k is different and $\boldsymbol{x}^i \in \mathbb{R}^k$ takes different forms. For the linear case, the regressor row constitutes of

$$\boldsymbol{x}^i = (1 \quad x^i \quad y^i \quad z^i \quad \theta_x^i \quad \theta_y^i \quad \theta_z^i)^T \in \mathbb{R}^7, \tag{4.17}$$

for the quadratic case, the regressor row constitutes of

$$\begin{aligned}\boldsymbol{x}^i = (1 \quad x^i \quad y^i \quad \cdots \quad \theta_z^i \quad (x^i)^2 \quad x^i y^i \quad \cdots \quad x^i\theta_z^i \\ \cdots (y^i)^2 \quad y^i z^i \quad \cdots \quad (\theta_z^i)^2)^T \in \mathbb{R}^{28},\end{aligned} \tag{4.18}$$

and for the cubic case, the regressor row constitutes of

$$\begin{aligned}\boldsymbol{x}^i = (1 \quad x^i \quad \cdots \quad \psi^i \quad (x^i)^2 \quad x^i y^i \quad \cdots (\theta_z^i)^2 \\ \cdots (x^i)^3 \quad (x^i)^2 y^i \quad \cdots \quad x^i y^i z^i \quad \cdots \quad (\theta_z^i)^3)^T \in \mathbb{R}^{84}.\end{aligned} \tag{4.19}$$

In general, the regressor row $(\boldsymbol{x}^i)^T$ has dimension $k = \binom{d+n_{\text{red}}}{d} \in \mathbb{R}$ where n_{red} (= 6 in this case) is the number of independent variables and $d \in \mathbb{N}$ is the polynomial degree. Stacking $n_m > k \in \mathbb{N}$ observations (static measurements) of f_j into vector form yields

$$\underbrace{\begin{pmatrix} f_j^1 \\ f_j^2 \\ \vdots \\ f_j^N \end{pmatrix}}_{\boldsymbol{f}_j} = \underbrace{\begin{pmatrix} (\boldsymbol{x}^1)^T \\ (\boldsymbol{x}^2)^T \\ \vdots \\ (\boldsymbol{x}^N)^T \end{pmatrix}}_{\boldsymbol{X}} \boldsymbol{\beta}_j + \underbrace{\begin{pmatrix} \epsilon_j^1 \\ \epsilon_j^2 \\ \vdots \\ \epsilon_j^N \end{pmatrix}}_{\boldsymbol{\epsilon}_j} \tag{4.20}$$

where $\boldsymbol{X} \in \mathbb{R}^{n_m \times k}$ is the regressor matrix and $\boldsymbol{\epsilon}_j \in \mathbb{R}^{n_m}$ is the vector of residuals for the wrench component j. Equation (4.20) represents a general regression problem and the coefficients $\boldsymbol{\beta}_j$ can be computed by minimizing equation (4.20) in the least square sense. In the present case, the polynomial regression suffers from a near collinearity problem, meaning that $(\boldsymbol{x}^i)^T$ are almost linearly dependent and therefore $\boldsymbol{X}$ is badly conditioned. To judge the presence of near collinearity, the condition number $\kappa(\boldsymbol{X}) \in \mathbb{R}$ of the regressor [101] is computed to $\kappa(\boldsymbol{X}) > 5 \times 10^6$, which is problematic. Possible solutions to overcome the problem of collinearity are utilize normalization approaches [102] or orthogonal polynomials [103]. Furthermore, the concept of "Ridge Regression" [104], or the "Principal Component Regression" (PCR) [105] could be applied. The PCR together with the normalization approach proves to be the most effective reduction technique in the present case to reduce $\kappa(\boldsymbol{X})$ essentially. Within the normalization, the data is restricted to [-1, 1]. The polynomial coefficients $\boldsymbol{\beta}_j$ are identified for each wrench component f_i based on $n_m = 1700$ data points. The effect of the polynomial order and the threshold $b \in \mathbb{R}$, utilized by the PCR to detect collinearity, will be evaluated next.

Three different polynomial orders have been assessed for the wrench set $\mathcal{F}_1$ and the corresponding workspace $\mathcal{C}_1$. To evaluate the accuracy of the polynomial model, 300 data pairs from $\mathcal{C}$ are randomly chosen to serve as a test set[1]. The rest is utilized to compute the coefficients $\boldsymbol{\beta}_j$. For comparison, the absolute error $\Delta f_i \in \mathbb{R}$ for the prediction of each component in $\boldsymbol{f}$ is computed as the absolute difference between a prediction $\hat{f}_i \in \mathbb{R}$ and the real component value f_i,

$$\Delta f_i = |\hat{f}_i - f_i|. \tag{4.21}$$

Error histogram will report on the error distribution whereas the root-mean-square error (RMSE) of the prediction is shown in Tab. 4.1 for each component of $\boldsymbol{f}$ and different polynomial orders.

[1] Initially, 2000 data points of $\mathcal{F}_1$ are calculated using the finite element model. 1700 points are chosen for the identification of the polynomial coefficients whereas 300 are chosen for testing.

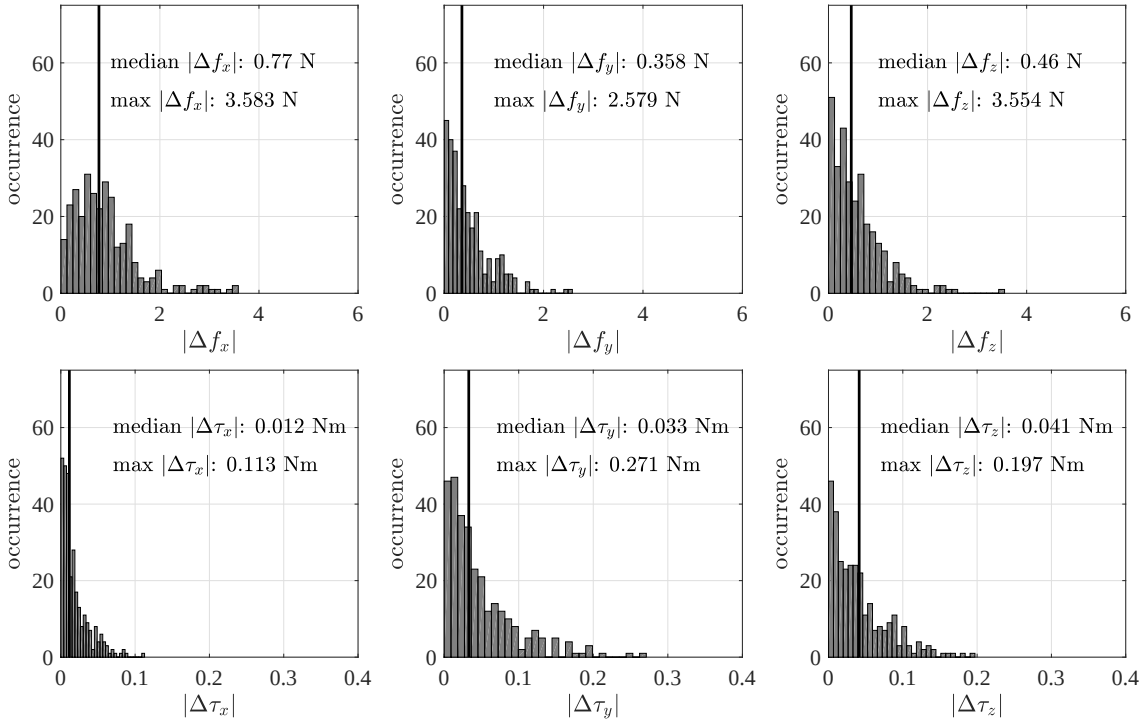

Figure 4.5.: Histogram that shows the distribution of the absolute error of a MVP model applied on the set $\mathcal{F}_1$.

The 1-degree polynomial model (linear regression) and the 2-degree polynomial display large prediction errors whereas the 3-degree polynomial model provides a fit with a very low RMSE, see Table 4.1. The 3-degree polynomial ordinary regression has a condition number of 1067, which can be further reduced by using PCR. In the lower part of Tab. 4.1, three different thresholds b are compared regarding their effect on $\kappa(\boldsymbol{X})$ and the prediction accuracy. An ordinary least square estimation is represented by $b = 0$. As b increases, the prediction error grows but the regression becomes better conditioned.

The absolute error distribution of each f_j by using PCR (with threshold 1.0) onto a 3-degree polynomial regression model is depicted in Fig. 4.5. The vertical axis represents the amount of prediction points referred to a prediction error level. Most of the predicted force components have a absolute error less than 2 N whereas most of the predicted torque components have a absolute error less than 0.2 Nm. The force component in x-direction exhibits the highest absolute error level which can be observed by comparing the RMSE values in Tab. 4.1. To achieve lower condition number, the values in $\mathcal{F}$ and $\mathcal{C}$ have been normalized to the range [-1,1], as explained above. Furthermore, the range of force in x is considerably smaller compared with the other directions. Thus, small changes in $\boldsymbol{q}$, normalized to $[-1, 1]$ might have an higher impact on f_x compared to with other f_i and since it is a least-square problem, result in a decreased fitting accuracy. The prediction RMSE of a MVP model for the three different admissible wrench sets $\mathcal{F}_1$, $\mathcal{F}_2$ and $\mathcal{F}_3$ is given in Tab. 4.2. To achieve comparable results, the PCR threshold has been tuned individually for the approximation of each admissible wrench set in order to achieve a comparable condition number $\kappa(\boldsymbol{X})$.

The RMSE error of the prediction for the wrench sets, $\mathcal{F}_1$,$\mathcal{F}_2$ and $\mathcal{F}_3$, possess a similar trend with the highest error in the force along x. However, the RMSE for the approxima-

Table 4.1.: Comparing the prediction error for $\mathcal{F}_1$ of a MVP model for different polynomial degrees and different thresholds in the applied PCR.

	RMSE [N]			RMSE [Nm]			
degree d	f_x	f_y	f_z	τ_x	τ_y	τ_z	$\kappa(\boldsymbol{X})$
1	22.7	5.1	5.5	0.4	0.2	0.2	18
2	1.9	4.5	4.6	0.1	0.1	0.1	426
3	1.0	0.6	0.7	0.02	0.03	0.02	1067
threshold b (d = 3)	f_x	f_y	f_z	τ_x	τ_y	τ_z	$\kappa(\boldsymbol{X})$
0.0	1.0	0.6	0.7	0.02	0.03	0.02	1067
1.0	1.1	0.8	0.7	0.03	0.03	0.03	184
2.0	1.2	0.8	0.8	0.03	0.07	0.06	45

Table 4.2.: RMSE of a MVP model for three different admissible wrench sets.

	RMSE [N]			RMSE [Nm]			
wrench set	f_x	f_y	f_z	τ_x	τ_y	τ_z	$\kappa(\boldsymbol{X})$
$\mathcal{F}_1$	1.2	0.7	0.8	0.03	0.07	0.06	184
$\mathcal{F}_2$	0.8	0.1	0.1	0.0	0.0	0.0	143
$\mathcal{F}_3$	0.28	0.04	0.01	0.0	0.0	0.0	139

tion of $\mathcal{F}_3$ are considerably lower compared with the RMSE for $\mathcal{F}_1$ which seems reasonable since the space $\mathcal{F}_1$ is considerably larger than $\mathcal{F}_3$ and $\mathcal{F}_1$ covers a lot of configurations of the ECM which are not a equilibrium configuration.

As mentioned earlier, a stiffness matrix $\boldsymbol{K}(\boldsymbol{q}) \in \mathbb{R}^6$ can be derived analytically from the MVP mapping,

$$\boldsymbol{K} = \frac{\partial \boldsymbol{f}(\boldsymbol{q})}{\partial \boldsymbol{q}}. \tag{4.22}$$

From a mechanical point of view, a stiffness matrix needs to be symmetric, $\boldsymbol{K}(\boldsymbol{q}) = \boldsymbol{K}(\boldsymbol{q})^T$, which is not guaranteed due to the data driven approach that identifies $\boldsymbol{f}(\boldsymbol{q})$. To assess the symmetry property of the identified mappings from $\mathcal{F}_1$, $\mathcal{F}_2$ and $\mathcal{F}_3$, the stiffness matrix (4.22) is decomposed into its symmetric and anti-symmetric part,

$$\boldsymbol{K} = \underbrace{\frac{1}{2}\left(\boldsymbol{K} + \boldsymbol{K}^T\right)}_{\text{symmetric part}=\boldsymbol{K}_s} + \underbrace{\frac{1}{2}\left(\boldsymbol{K} - \boldsymbol{K}^T\right)}_{\text{anti symmetric part}=\boldsymbol{K}_a}. \tag{4.23}$$

As a measure of symmetry, the ratio of the maximum singular value of $\boldsymbol{K}_s$ with respect to the maximum singular value $\boldsymbol{K}$ is computed,

$$\frac{||\boldsymbol{K}_s||}{||\boldsymbol{K}||}. \tag{4.24}$$

The maximum value of (4.24) equals one and indicates that the symmetric part of $\boldsymbol{K}$ is equally dominant and thus the matrix $\boldsymbol{K}$ is symmetric. As the value of the metric (4.24) decreases (towards zero), $\boldsymbol{K}$ is less symmetric.
The metric (4.24) is computed for 1000 test configurations for the wrench sets $\mathcal{F}_1$, $\mathcal{F}_2$, $\mathcal{F}_3$ and the boxplot that shows the distribution of the metric is given in Fig. 4.6. It can be observed, that the symmetry property of $\boldsymbol{K}$ is incorporated in the identified mappings as

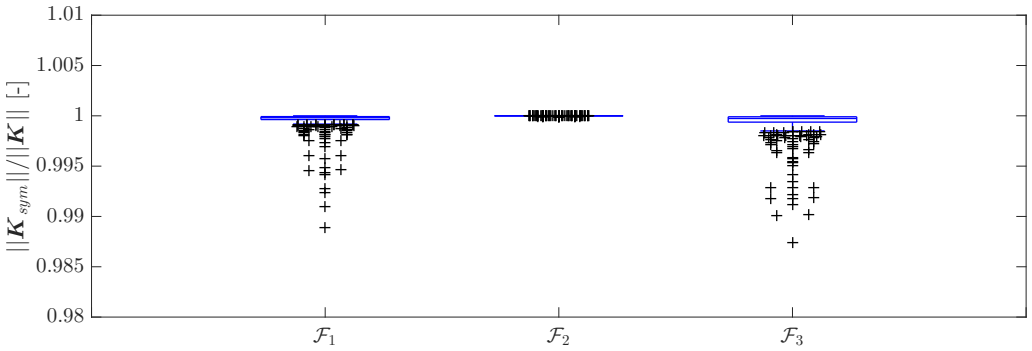

Figure 4.6.: Boxplot of the symmetry ratio (4.24) of the identified stiffness matrices for all investigated wrench ranges

the metric (4.24) ≈ 1 for all wrench sets. Furthermore, the highest symmetry deviation is present for the wrench set $\mathcal{F}_3$ which is indicated by higher distribution > 1. The set $\mathcal{F}_3$ contains only equilibrium configurations of the system. Thus, the sampled pose and wrench space $\{\mathcal{C}_3, \mathcal{F}_3\}$ are subsets of the Cartesian space on which the coefficients for $\boldsymbol{K}$ are identified, which might yield to a higher anti-symmetric nature.

To compare the stiffness characteristics of the identified mappings, the symmetric part of the stiffness matrix for $\mathcal{F}_1$, $\mathcal{F}_2$ and $\mathcal{F}_3$ is assessed in the initial straight configuration, $\boldsymbol{q}_0 = (0.095, 0, 0, 0, 0, 0)^T$. The three stiffness matrices are given in (4.25), (4.26) and (4.27). By comparing the main diagonal elements, it can be observed that the values of $\boldsymbol{K}_{\mathcal{F}_1}$ and $\boldsymbol{K}_{\mathcal{F}_2}$ are matching closely whereas the values in $\boldsymbol{K}_{\mathcal{F}_3}$ are different. However, the signs in $\boldsymbol{K}_{\mathcal{F}_2}$ for $\frac{\partial f_y}{\partial y}$ and $\frac{\partial f_z}{\partial z}$ are different as well compared to $\boldsymbol{K}_{\mathcal{F}_1}$. Furthermore, it seems that the off-diagonal elements, i.e. the cross coupling, is higher in $\boldsymbol{K}_{\mathcal{F}_3}$ compared with the outer two matrices. In conclusion, the stiffness matrix is sensitive with respect to the underlying wrench set i.e. the workspace for which the matrix is valid.

$$\boldsymbol{K}_{\mathcal{F}_1}(\boldsymbol{q}_0)= \begin{pmatrix} 24153 & -19 & -7 & 0 & 0 & 2 \\ -19 & 2379 & 21 & 1 & 1 & -128 \\ -7 & 21 & 2365 & -1 & 127 & -1 \\ 0 & 1 & -1 & 4 & 0 & 0 \\ 0 & 1 & 127 & 0 & 12 & 0 \\ 2 & -128 & -1 & 0 & 0 & 12 \end{pmatrix}. \tag{4.25}$$

$$\boldsymbol{K}_{\mathcal{F}_2}(\boldsymbol{q}_0)= \begin{pmatrix} 27140 & -49 & 2 & 0 & 0 & -2 \\ -49 & 2428 & 0 & 0 & 0 & -136 \\ 2 & 0 & 2400 & 0 & 135 & 0 \\ 0 & 0 & 0 & 4 & 0 & 0 \\ 0 & 0 & 135 & 0 & 12 & 0 \\ -2 & -136 & 0 & 0 & 0 & 12 \end{pmatrix}. \tag{4.26}$$

$$\boldsymbol{K}_{\mathcal{F}_3}(\boldsymbol{q}_0)= \begin{pmatrix} 31697 & -1676 & -87 & -2 & -3 & 80 \\ -1676 & -406 & 0 & 0 & 1 & 23 \\ -87 & 0 & -227 & -43 & -10 & 0 \\ -2 & 0 & -43 & 5 & -3 & 0 \\ -3 & 1 & -10 & -3 & 4 & 0 \\ 80 & 23 & 0 & 0 & 0 & 4 \end{pmatrix}. \tag{4.27}$$

Nonlinear kinematic combined with linear springs (NKLS)

A schematic illustration of the modeling approach of the present paragraph is given in Fig. 4.4 on the right hand side. In contrast to the MVP model were the nonlinear geometry of the deformation and the material properties are hidden within on polynomial mapping, the approach assumes a serial kinematic chain with a linear stiffness in each joint. Therefore, the generalized coordinates for this are reformulated, and consists of the six kinematic variables

$$\boldsymbol{q} = (l,\, \phi,\, \eta,\, \zeta,\, \theta,\, \iota\,)^T \in \mathbb{R}^6 \tag{4.28}$$

which describe five rotational and one translational joint, see Fig. 4.4. The kinematic chain expresses the position and orientation of the head frame ${}^{\mathcal{B}}\boldsymbol{T}_{\mathcal{H}}(\boldsymbol{q})$ which consists of the following multiplication of homogeneous transformations,

$${}^{\mathcal{B}}\boldsymbol{T}_{\mathcal{H}}(\boldsymbol{q}) = \boldsymbol{T}(\phi)\,\boldsymbol{T}(\eta)\,\boldsymbol{T}(l)\,\boldsymbol{T}(\zeta)\,\boldsymbol{T}(\theta)\,\boldsymbol{T}(\iota). \tag{4.29}$$

The idea is supported by the observation made in chapter 3. Paragraph 3.4.3 reported that the position and orientation of the tip of the planar test bed can be predicted with comparable accuracy by the nonlinear Timoshenko beam and linear elastic material laws which implies that the nonlinear behavior of such a system might be approximated by nonlinear geometry combined with a linear elastic stiffness behavior.
As illustrated in Fig. 4.4, linear springs are introduced in each joint and the restoring force of the ECM $\boldsymbol{f}(\boldsymbol{q})$ can therefore represented by

$$\boldsymbol{f}(\boldsymbol{q}) = \begin{pmatrix} f_l \\ \tau_\phi \\ \tau_\eta \\ \tau_\zeta \\ \tau_\theta \\ \tau_\iota \end{pmatrix} = \begin{pmatrix} k_l\,(l_0 - l) \\ k_\phi\,\phi \\ k_\eta\,\eta \\ k_\zeta\,\zeta \\ k_\theta\,\theta \\ k_\iota\,\iota \end{pmatrix} = \boldsymbol{K}_{nkls}(\boldsymbol{q}_0 - \boldsymbol{q}) \tag{4.30}$$

assuming a known initial configuration $\boldsymbol{q}_0 \in \mathbb{R}^6$. The introduced stiffness matrix $\boldsymbol{K}_{nkls} \in \mathbb{R}^{6\times 6}$ is linear and diagonal and can be expressed by

$$\boldsymbol{K}_{nkls} = \mathrm{diag}\{k_l,\, k_\phi,\, k_\eta,\, k_\zeta,\, k_\theta,\, k_\iota\}. \tag{4.31}$$

Similar to the MVP model, the stiffness parameters of the NKLS model (4.31) by solving a linear regression problem. However, the problem is simpler as the identification of each scalar stiffness k_i is dependent only on the respective kinematic variable in $\boldsymbol{q}$, which means that the regression problem is not highly affected by a bad condition number of the regressor due to different scales for the components in $\boldsymbol{q}$.
The linear stiffness parameters (4.31) are identified based on experimental data and for each component of $\boldsymbol{f}(\boldsymbol{q})$, a linear regression problem is solved in which an estimate of the i-th component f_j^i of the j-th observation relates linearly to the i-th generalized coordinate,

$$\underbrace{\begin{pmatrix} f_j^1 \\ f_j^2 \\ \vdots \\ f_j^N \end{pmatrix}}_{\boldsymbol{f}_j} = \underbrace{\begin{pmatrix} q_{0,j} - q_j^1 \\ q_{0,j} - q_j^2 \\ \vdots \\ q_{0,j} - q_j^N \end{pmatrix}}_{\boldsymbol{X}} k_j + \underbrace{\begin{pmatrix} \epsilon_j^1 \\ \epsilon_j^2 \\ \vdots \\ \epsilon_j^N \end{pmatrix}}_{\boldsymbol{\epsilon}_j} \tag{4.32}$$

Table 4.3.: RMSE of a NKLS model for three different admissible wrench sets.

	RMSE [N]			RMSE [Nm]		
wrench set	f_l	τ_ϕ	τ_η	τ_ζ	τ_θ	τ_ι
$\mathcal{F}_1$	16.34	0.03	0.31	0.17	0.22	0.23
$\mathcal{F}_2$	11.16	0.05	0.05	0.08	0.07	0.03
$\mathcal{F}_3$	11.86	0.06	0.06	0.10	0.10	0.03

Table 4.4.: Identified linear stiffness coefficients of the NKLS model

	stiffness [N/m]10^4	stiffness [Nm/rad]				
wrench set	k_l	k_ϕ	k_η	k_ζ	k_θ	k_ι
$\mathcal{F}_1$	12.7	12.0	11.9	12.4	12.5	4.35
$\mathcal{F}_2$	13.2	12.0	12.2	12.15	12.0	4.31
$\mathcal{F}_3$	8.86	10.9	10.5	8.9	8.4	3.9

The RMSE values for the identification of $\boldsymbol{f}(\boldsymbol{q})$ for the NKLS model can be found in Tab. 4.3 for the three different admissible wrench sets $\mathcal{F}_1$, $\mathcal{F}_2$ and $\mathcal{F}_3$. Similar to the MVP approach, the RMSE value in the axial direction f_l is considerably higher compared to the other components and the RMSE values for the identification based on $\mathcal{F}_3$ are lower compared with the respective RMSE values of the other two wrench sets.

In the NKLS approach, six parameters only are used to describe the stiffness characteristics. To assess them, Tab. 4.4 presents the identified stiffness values for the three different admissible wrench sets. Interestingly, the values are comparable throughout the different wrench sets especially for $\mathcal{F}_1$ and $\mathcal{F}_2$ along the rotational stiffness k_ϕ, k_η, k_ζ, k_θ with ≈ 12 [Nm/rad]. As emphasized in Tab. 4.3, the RMSE of the f_l component is large which means that the assumption of a linear stiffness along the translational joint is not feasible. To improve the fitting, a MVP is applied for the l direction only, which means that the force component along in the translational joint $f_l(\boldsymbol{q})$ is a nonlinear function of the other joint variables (4.28). The improvement by this extension of the stiffness for f_l is reported by Tab. 4.5. The former root-mean square error of 16.34 N for $\mathcal{F}_1$, 11.16 N for $\mathcal{F}_2$, and 11.86 N for $\mathcal{F}_3$, can be reduced to 1.9 N, 0.31 N and 0.13 N respectively by applying a nonlinear stiffness model $f_l(\boldsymbol{q})$.

4.2.3. Experimental design

The design of experiments (DoE) is a technique to extract the important information from a set of collected data [106]. If a model of the process that relates the collected data is known, a model-based design can be set up and the important information are selected based on some optimal criteria. For the case that no model is known for the process, a

Table 4.5.: Improvement for the identification of k_l

	RMSE 10^3[N]	RMSE [N]
wrench set	linear stiffness $f_l = k_l(l_0 - l)$	nonlinear stiffness $f_l(\boldsymbol{q})$
$\mathcal{F}_1$	16.34	1.90
$\mathcal{F}_2$	11.16	0.31
$\mathcal{F}_3$	11.86	0.13

model-free design can be used which selects data pairs that span the experimental region as widely as possible with a uniform coverage. The present work studies a two regression problems. Thus, the so called model-based technique is applicable and is discussed in the following. For comparative reasons however, a model-free design method will be studied as well whereas both approaches are compared with respect to their effect on the corresponding fitting accuracy.

Model-based Design

In the following, the regressions models of the prior paragraphs are considered in which the estimation of $\boldsymbol{\beta}$, for the MVP model, and k_j, for the NKLS model, utilizes the least square criterion. The variance of the estimator, here denoted as $Var(\hat{\boldsymbol{\beta}})$, is given by

$$Var(\hat{\boldsymbol{\beta}}) = \sigma^2(\boldsymbol{X}^T\boldsymbol{X})^{-1} \tag{4.33}$$

with

$$\boldsymbol{X} = \begin{pmatrix} \boldsymbol{x}_1^T \\ \boldsymbol{x}_2^T \\ \vdots \\ \boldsymbol{x}_n^T \end{pmatrix} \tag{4.34}$$

where $n \in \mathbb{R}$ stands for the number of observations, $\sigma \in \mathbb{R}$ denotes the variance of the error in equation (4.20) and $\boldsymbol{x}_i$ refers to the i-th row of the regressor matrix $\boldsymbol{X}$ and corresponds to the i-th pose observation in the experiment. The relationship between $\boldsymbol{x}_i$ and the i-th pose $\boldsymbol{q}_i$ is defined in (4.19).
The information matrix [107] is defined as

$$\boldsymbol{\Lambda} = \sum_{i=1}^{k} \boldsymbol{x}_i\boldsymbol{x}_i^T. \tag{4.35}$$

According to (4.33) and (4.35), the relationship between the variance of the estimator and the information matrix is given by

$$Var(\hat{\boldsymbol{\beta}}) = \sigma^2\boldsymbol{\Lambda}^{-1}. \tag{4.36}$$

The n vectors $\boldsymbol{x}_i$ need to be chosen such that a precise estimation of the parameters can be achieved. In other words, the inverse of the information matrix $\boldsymbol{\Lambda}^{-1}$ should be as small as possible, in the sense that a scalar function of $\boldsymbol{\Lambda}^{-1}$ is minimized [108]. A model-based design problem can be formulated as follows:

$$\min_{\boldsymbol{X}} \quad \boldsymbol{\Phi}(\boldsymbol{\Lambda}) \tag{4.37}$$

where $\boldsymbol{\Phi}$ denotes a certain optimality criterion, which reflects the statistical property of the design, whereas different optimality criteria can be found e.g. in [109].
The so called " A-optimality " minimizes the trace of the inverse of the information matrix, indicating the minimization of the enclosing box of the confidence hyper ellipsoid of the parameters [110], and is defined as

$$\text{A-optimality:} \quad \boldsymbol{\Phi}(\boldsymbol{\Lambda}) = \frac{1}{k}\sum_{j=1}^{k} \lambda_j(\boldsymbol{\Lambda}^{-1}). \tag{4.38}$$

where $\lambda_j(\mathbf{\Lambda}^{-1})$ denotes j-th eigenvalue of $\mathbf{\Lambda}^{-1}$ and k denotes the number of coefficients to be estimated. Another very commonly used optimality criterion is D-optimality, defined to

$$\text{D-optimality:} \quad \mathbf{\Phi}(\mathbf{\Lambda}) = (\det(\mathbf{\Lambda}^{-1}))^{1/k}. \tag{4.39}$$

From this definition, it can be concluded that a D-optimal design criteria minimizes the determinant of the inverse of the information matrix and thus minimizes the volume of the confidence hyper ellipsoid of the parameters. According to the relation $\sqrt{\det(\boldsymbol{X}^T\boldsymbol{X})} = \sigma_1\sigma_2...\sigma_k$, where σ_i denotes i-th singular value of $\boldsymbol{X}$, the D-optimality maximizes the product of the length of each principal axis, which represents a maximal volume in the experimental region [111]. Another criterion, the so called E-optimality criterion is formulated as

$$\text{E-optimality:} \quad \mathbf{\Phi}(\mathbf{\Lambda}) = \lambda_{\max}(\mathbf{\Lambda}^{-1}), \tag{4.40}$$

where $\lambda_{\max}(\mathbf{\Lambda}^{-1})$ denotes the largest eigenvalue of $\mathbf{\Lambda}^{-1}$. An E-optimal design has a similar concept as the D-optimal design but it focuses on maximizing the shortest principal axis of the hyper ellipsoid. There are also some other design methods like minimizing the condition number, which makes the hyper ellipsoid closer to a hyper sphere. In the context of robot calibration, the condition number optimality criteria serve as observability index, which helps to choose the proper poses e.g. to calibrate the base inertial parameters [112]. In this work, the D-optimality (4.39) is chosen because of its simple updating formula and less computing effort. In practice, the D-optimality criterion can be further simplified by 'dispensing with the k-th root and one may consider the determinant directly [106]. So the goal of the D-optimal design becomes finding a design set $\mathcal{D}$ consisting of n poses out of the candidate set $\mathcal{C}$, such that the determinant of the inverse of the information matrix is maximized:

$$\mathbf{\Lambda} = \underset{\boldsymbol{X}}{\operatorname{argmax}} \det(\mathbf{\Lambda}). \tag{4.41}$$

To solve the optimal design problem in (4.37), i.e. choosing n points from $\mathcal{C}$, some optimization-based algorithms are proposed. In [113], Gaffke and Heiligers derive the expression of the objective function of the optimal criteria for a full cubic polynomial regression model, like the MVP model (4.20). Based on the assumption of invariance property, see [114], the objective function can be simplified and expressed by a function of a six-dimensional vector $\boldsymbol{\mu}$, whose components are polynomials of the predictors. Then the optimization problem is solved with a gradient method in the convex region defined by $\boldsymbol{\mu}$. After an optimal solution $\boldsymbol{\mu}^*$ is found, the desired design $\boldsymbol{x}_i^*$ is calculated accordingly [114]. The invariance property is an essential condition of the algorithm, which assumes that the regression function and experimental region are invariant with respect to sign changes and coordinate permutations of the predictors. Consider the model (4.20), the equation is invariant under the sign changes of the variables and coordinate permutations. However, the experimental region does not satisfy the invariant property (e.g. z and y are permutable but x and y are not). Furthermore, a continuous experimental region is hard to define in our case, because a certain reachable pose of the ECM is determined through the FEM program. Thus, the workspace of the ECM is a set of discrete poses, making Gaffke's algorithm not applicable here.

To select the a set of informative poses out of the discrete set $\mathcal{C}$ which fulfill the D-optimality criterion, the Fedorov's Exchange Algorithm (FEA) [115] is applied. The basic idea of FEA is repeatedly searching for candidate poses in $\mathcal{C}$, which improves the determinant value by exchanging with certain pose in the design set $\mathcal{D}$. Suppose $\boldsymbol{x}$ is a vector,

which should be exchanged with the row vector $\boldsymbol{x}_i$ in the regressor $\boldsymbol{X}$. The updated determinant of $\boldsymbol{\Lambda}$ is given as

$$\det(\boldsymbol{\Lambda} + \boldsymbol{x}\boldsymbol{x}^T - \boldsymbol{x}_i\boldsymbol{x}_i^T) = \det(\boldsymbol{\Lambda})(1 + \Delta(\boldsymbol{x}_i, \boldsymbol{x})) \tag{4.42}$$

where

$$\begin{aligned}\Delta(\boldsymbol{x}_i, \boldsymbol{x}) =& \boldsymbol{x}^T\boldsymbol{\Lambda}^{-1}\boldsymbol{x} - \boldsymbol{x}_i^T\boldsymbol{\Lambda}^{-1}\boldsymbol{x}_i \\ &+ (\boldsymbol{x}^T\boldsymbol{\Lambda}^{-1}\boldsymbol{x}_i)^2 - \boldsymbol{x}^T\boldsymbol{\Lambda}^{-1}\boldsymbol{x}\boldsymbol{x}_i^T\boldsymbol{\Lambda}^{-1}\boldsymbol{x}_i\end{aligned} \tag{4.43}$$

The Fedorov's EA follows the following steps:

Algorithm 1 Fedorov's Exchange Algorithm

```
specify the number of poses to be chosen n
specify a small value ϵ as threshold
randomly choose n poses from C
compute Λ, Λ^{-1} and det(Λ)
while termination condition not reached do
    for each pose i in D do
        for each pose j in C do
            calculate Δ(x_i, x_j)
        end for
    end for
    find out Δ_max = Δ(x_i, x_j) and [i_m, j_m] = argmax_{i,j} Δ(i, j)
    if Δ_max < ϵ then
        terminate
    end if
    exchange x_im and x_jm
    update Λ^{-1} and det(Λ)
end while
```

Model-free design

In the work of Johnson [98] several distance based design criteria are discussed whereas in the present thesis, the maximin-distance design is introduced in the following. This maximin-distance design aims to select a subset $\mathcal{D}$ from the training set $\mathcal{C}$ such that the minimum distance between design poses are maximized,

$$\max_{\mathcal{D}} \min_{\boldsymbol{q}^1, \boldsymbol{q}^2 \in \mathcal{D}} d(\boldsymbol{q}^1, \boldsymbol{q}^2), \tag{4.44}$$

where $\boldsymbol{q}^i$ denotes a certain pose in $\mathcal{D}$, and $d(\boldsymbol{q}^1, \boldsymbol{q}^2) = \|\boldsymbol{q}^1 - \boldsymbol{q}^2\|$ denotes the Euclidean distance between two poses.
In the present case, an analytic solution over the continuous experimental region is not given and thus not considered here. In [99] an algorithm is proposed to solve the distance-based optimal design problem. The basic idea of this algorithm is similar with the EA: randomly choose n poses as the initial design set $\mathcal{D}$. Choose a pose $\boldsymbol{q}$ in the candidate set $\mathcal{C}$ and check, if the minimum distance between the poses in the design set can be increased by replacing a certain pose $\boldsymbol{q}_i$ in the design set with $\boldsymbol{q}$. The details can be seen as follows:

Algorithm 2 Exchange Algorithm for Distance-based Design

```
specify the number of points to be chosen n
randomly choose n poses from C
while termination condition not reached do
    for each pose q_i in D do
        compute d_i = min_{q∈D, q≠q_i} d(q_i, q)
        for each pose q_j in C do
            calculate d_j = min_q ∈ D, q ≠ q_i d(q_j, q)
            calculate R(i,j) = d_j / d_i
        end for
    end for
    find out the R_max = max R(i,j) and [i_m, j_m] = argmax_{i,j} R(i,j)
    if R_max < 1 then
        terminate
    end if
    exchange q_im and q_jm
end while
```

Comparison of the experimental design methods

For the DoE, a number of poses shall be selected to a set of design poses $\mathcal{D}$ which are sampled in the experiments later on. It is desired that the experimental time does not exceed 30 min excessively. One pose takes about 10 s (see Appendix B) and therefore a total number of $n = 200$ poses are selected. To compactly compare the results for this desired number of poses, this section will focus on the identification of a MVP based on the admissible wrench set $\mathcal{F}_1$.
For both design method, an exchange algorithm is proposed which consecutively selects poses to improve the D-optimality, in the model-based case, and the distance criterion, in the model-free case. Furthermore, both algorithms possess a termination condition, which is reached if the respective criterion is fulfilled by the set of design poses $\mathcal{D}$ to some extent. In order to show the convergence, i.e. the termination condition is reached, of both algorithms, Fig. 4.7 presents the improvement of $\Delta_{\max}$ from (4.43) in the left plot and the improvement of the maximin distance criterion $R_{\max}$.

The RMSE values of the prediction for $\boldsymbol{f}(\boldsymbol{q})$ by a cubic MVP model can be found in Tab. 4.6. In this table, the initial design refers to a model in which the polynomial coefficients are found using the full set of poses $\mathcal{C}_1$ and the corresponding set of wrenches $\mathcal{F}_1$ presented in the simulation step. Accordingly, the model-based (and model-free) design refers to a model in which the polynomial coefficients are found using the reduced set $\mathcal{D}_1$, and corresponding wrenches $\mathcal{F}_{D,1}$ which have been found by the D-optimality criteria (the maximin-distance criterion).

In general, the trend of the RMSE values reported Tab. 4.6 is comparable as reported in the simulation results and the highest prediction error is present in the axial component f_x.
In conclusion, two approaches for the DoE are introduced and compared. The model accuracy resulting in the simulation for both approaches is equally good with a little advantage of the D-optimality which justifies their use for the experimental identification. Furthermore, the no additional error is noticeable due to the usage of a reduced set of poses.

Table 4.6.: RMSE of a MVP model for a pose selection of $\mathcal{F}_1$ based on a Model-free and a Model-based experimental design.

	RMSE [N]			RMSE [Nm]			
design	f_x	f_y	f_z	τ_x	τ_y	τ_z	$\kappa(\boldsymbol{X})$
initial	1.21	0.68	0.78	0.03	0.07	0.06	184
model-based	1.25	0.71	0.80	0.03	0.07	0.06	180
model-free	1.29	0.82	0.91	0.03	0.07	0.07	184

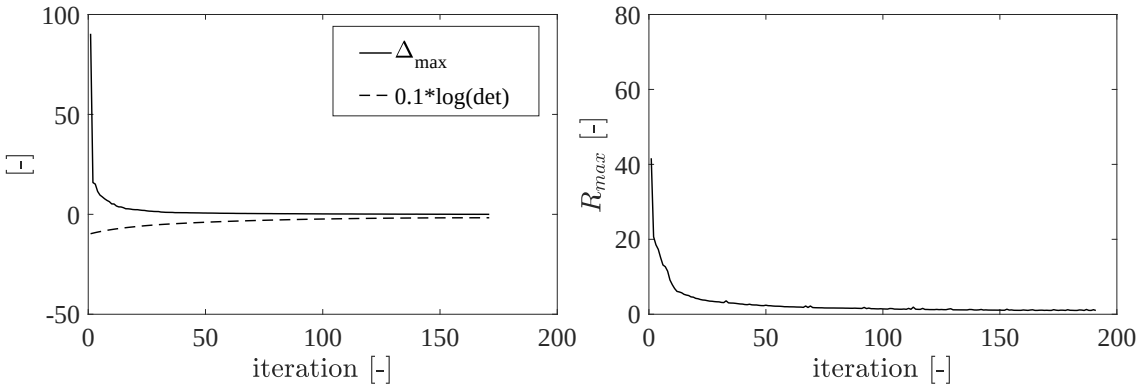

Figure 4.7.: Convergence of the EA algorithms

4.2.4. Experimental results

This section will report on the experimental results gained in two experiments. The first experiment involves the test setup reported in the Appendix B. This setup is basically suitable to identify the respective mappings for each admissible set of wrenches $\mathcal{F}_1$, $\mathcal{F}_2$ or $\mathcal{F}_3$ for both models. Additionally, another option that facilitates the identification setup is discussed in the following. This setup involves the spatial test bed as described in Section 2.2.2 with a tracking target for a camera measurement system mounted at the moving platform of the mechanism. This setup, actuated by the 4 tendons, can be applied for the identification of $\mathcal{F}_3$ as it can measure the head pose w.r.t. to the base of the mechanism as well as the applied forces and torque by a projection of the tendon tensions. To compare the different identification processes, pose-wrench data pairs for $\mathcal{F}_1$ are gained with the robotic manipulator whereas pose-wrench data pairs for $\mathcal{F}_3$ are gained with spatial test bed. The following two paragraphs will now subsequently report on the achieved model accuracy whereas the resulting implication for a dynamic model of the form (4.3) will be discussed afterwards.

Multivariate polynomial model (MVP)

The simulation step reported that a third order MVP model provides a good representation for the mapping $\boldsymbol{f}(\boldsymbol{q})$, thus a third order MVP is trained for $\mathcal{F}_1$ and $\mathcal{F}_3$ with the RMSE values shown in Tab. 4.7. In contrast to the simulation results, the experimentally gained RMSE do not differ largely although the workspace covered by $\mathcal{F}_3$ is considerably smaller than $\mathcal{F}_1$ and thus one would expect that the absolute error to be smaller, which is not the case. One possible explanation for the larger error in $\mathcal{F}_3$ are the tendon tension sensors which are used to measure the wrench. As they are located next to the actuators, the

Table 4.7.: RMSE of a MVP model for the experimentally tested different admissible wrench sets $\mathcal{F}_3$ and $\mathcal{F}_3$.

	RMSE [N]			RMSE [Nm]		
wrench set	f_x	f_y	f_z	τ_x	τ_y	τ_z
$\mathcal{F}_1$	1.57	0.59	0.68	0.04	0.08	0.07
$\mathcal{F}_3$	2.19	0.52	0.48	0.03	0.04	0.12

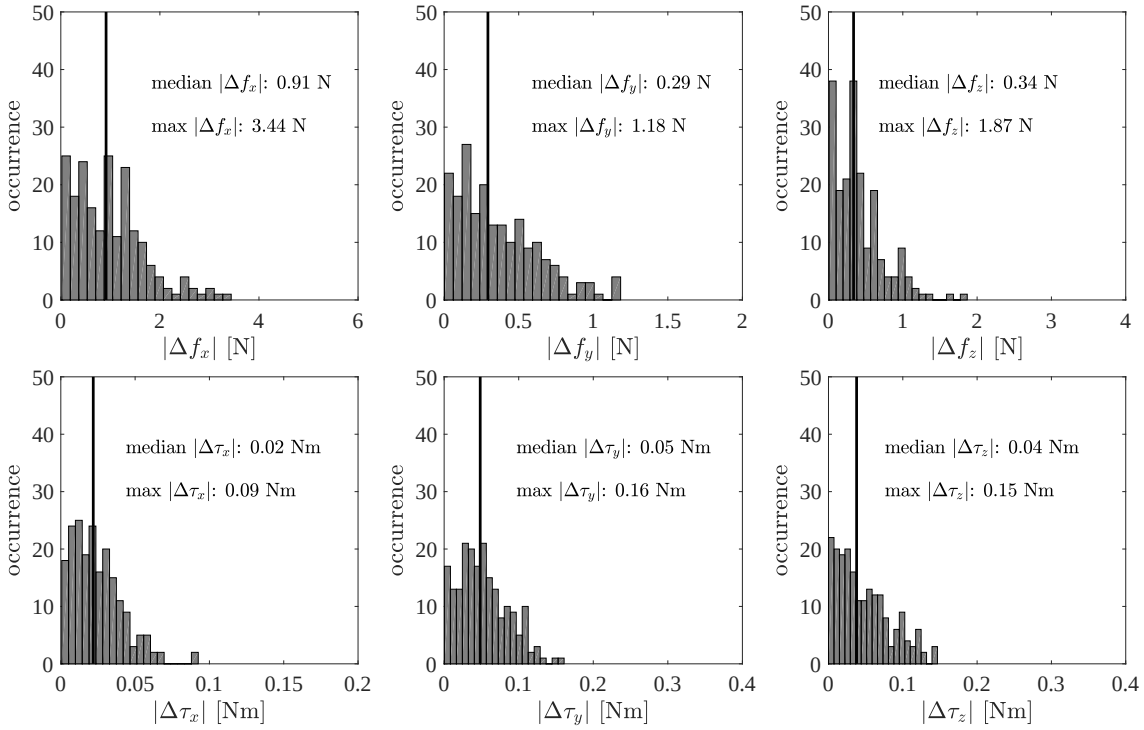

Figure 4.8.: Histogram of the component wise absolute error for a MVP trained on $\mathcal{F}_1$ using the model-based design to reduce the pose set.

measurements are affected by nonlinear friction effects which affect the prediction accuracy. In Fig. 4.8, the histogram of the absolute error is shown for each component of $\boldsymbol{f}(\boldsymbol{q})$, were it can be seen that the maximum error of the force components is 4 N and the maximum error of the torque components 0.2 Nm. Analogously to the simulation step, the stiffness matrix is presented for both identified polynomial mappings. The symmetric property of the stiffness matrix $\boldsymbol{K}(\boldsymbol{q})$ (4.22) is assessed by the metric (4.24) and a corresponding boxplot in Fig. 4.9 depicts the distribution of the metric. As a recall, a metric that $= 1$ indicates a fully symmetric $\boldsymbol{K}$. By assessing Fig. 4.9, it can be observed that both stiffness matrices are symmetric whereas the MVP mapping identified for $\mathcal{F}_3$ provides a $\boldsymbol{K}$ with a higher anti-symmetric part. Furthermore, the stiffness matrices are explicitly given in (4.45) and (4.46). Again, a bigger difference exist between the reported matrices as the diagonal elements are different with different signs, e.g. the values for $\frac{\partial f_{\theta_z}}{\partial \theta_z}$, and the cross

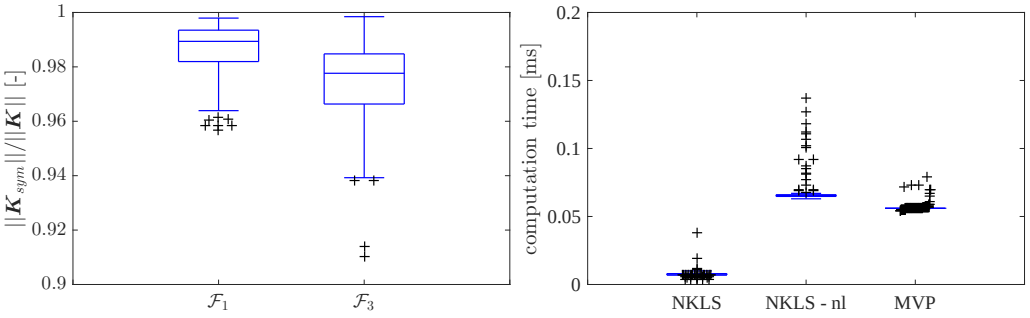

Figure 4.9.: Boxplot of the stiffness metric assessed for the experimentally identified mappings on $\mathcal{F}_1$ and $\mathcal{F}_3$.

coupling is larger for $\boldsymbol{K}_{\mathcal{F}_3}$.

$$\boldsymbol{K}_{\mathcal{F}_1}(\boldsymbol{q}_0)= \begin{pmatrix} 24585 & -778 & 12 & 4 & 49 & -14 \\ -778 & 3461 & 106 & -1 & 28 & 179 \\ 12 & 106 & 3468 & 0 & -178 & 43 \\ 4 & -1 & 0 & 4 & 0 & 0 \\ 49 & 28 & -178 & 0 & 16 & -1 \\ -14 & 179 & 43 & 0 & -1 & 16 \end{pmatrix}. \tag{4.45}$$

$$\boldsymbol{K}_{\mathcal{F}_3}(\boldsymbol{q}_0)= \begin{pmatrix} 29692 & -3723 & -708 & -17 & -22 & 14 \\ -3723 & -3353 & 74 & -40 & 127 & 715 \\ -708 & 74 & -574 & -9 & -9 & -194 \\ -17 & -40 & -9 & 5 & -1 & -3 \\ -22 & 127 & -9 & -1 & 5 & -17 \\ 14 & 715 & -194 & -3 & -17 & -60 \end{pmatrix}. \tag{4.46}$$

Nonlinear kinematics with linear spring

This subsection reports on the identification of the NKLS model, whereas the linear stiffness parameters (4.31) of the NKLS model are found. The simulation step states that the joint stiffness of the linear joint k_l provides a rough approximation only and the achieved accuracy is not sufficient. Therefore a nonlinear approach is proposed for this component additionally, which treats the force in the translational joint $f_l(\boldsymbol{q})$ as a nonlinear function of all kinematic variables $\boldsymbol{q}$. This extension will be also discussed in the following.

The RMSE values for the identification of the NKLS model for the admissible wrench sets $\mathcal{F}_1$ and $\mathcal{F}_3$ are given in Tab. 4.8. Similar to the MVP model of the previous paragraph, the RMSE values differ not largely between a model trained on $\mathcal{F}_1$ and a model trained on $\mathcal{F}_3$. The biggest prediction error is present in the stiffness model of the translational joint with ≈ 5 N. However, by applying a nonlinear model, the RMSE error could be bisected to ≈ 2.5 N. The corresponding error histogram for each component $\boldsymbol{f}$ is given in Fig. 4.10. The identified joint stiffness, see Tab. 4.9 whereas the linear behavior for the torque components is further underlined in Fig. 4.11. where a correlation of the measured static data and the modeled behavior is shown. For the translational joint stiffness, the linear approximation is not sufficient as the measured behavior is not injective, i.e. several values for l can yield to the same value f_l, and thus not linear. Therefore a nonlinear relationship $f_l(\boldsymbol{q})$ is mandatory.

Table 4.8.: RMSE of a NKLS model for the experimentally tested different admissible wrench sets $\mathcal{F}_1$ and $\mathcal{F}_3$.

	RMSE [N]	RMSE [Nm]				
wrench set	f_l, (nonlinear f_l)	τ_ϕ	τ_η	τ_ζ	τ_θ	τ_ι
$\mathcal{F}_1$	3.30 (1.48)	0.19	0.26	0.19	0.21	0.02
$\mathcal{F}_3$	4.92 (2.44)	0.12	0.16	0.16	0.09	0.04

Table 4.9.: Linear stiffnesses of a NKLS model for the experimentally tested different admissible wrench sets $\mathcal{F}_1$ and $\mathcal{F}_3$.

	RMSE 10^3 [N/m]	RMSE [Nm/rad]				
wrench set	k_l	k_ϕ	k_η	k_ζ	k_θ	k_ι
$\mathcal{F}_1$	25.4	12.6	12.5	11.3	11.4	4.1
$\mathcal{F}_3$	20.8	11.6	12.7	11.67	9.01	3.4

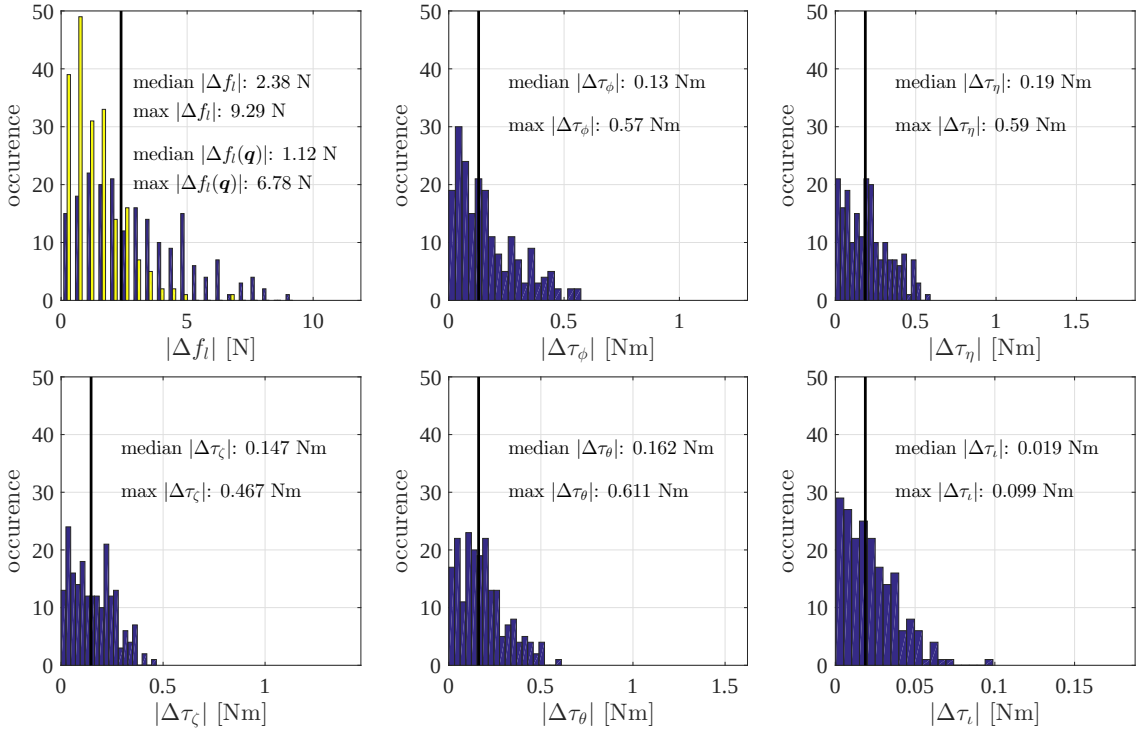

Figure 4.10.: Histogram of the component wise absolute error for a NKLS trained on $\mathcal{F}_1$ using the model-based design to reduce the pose set.

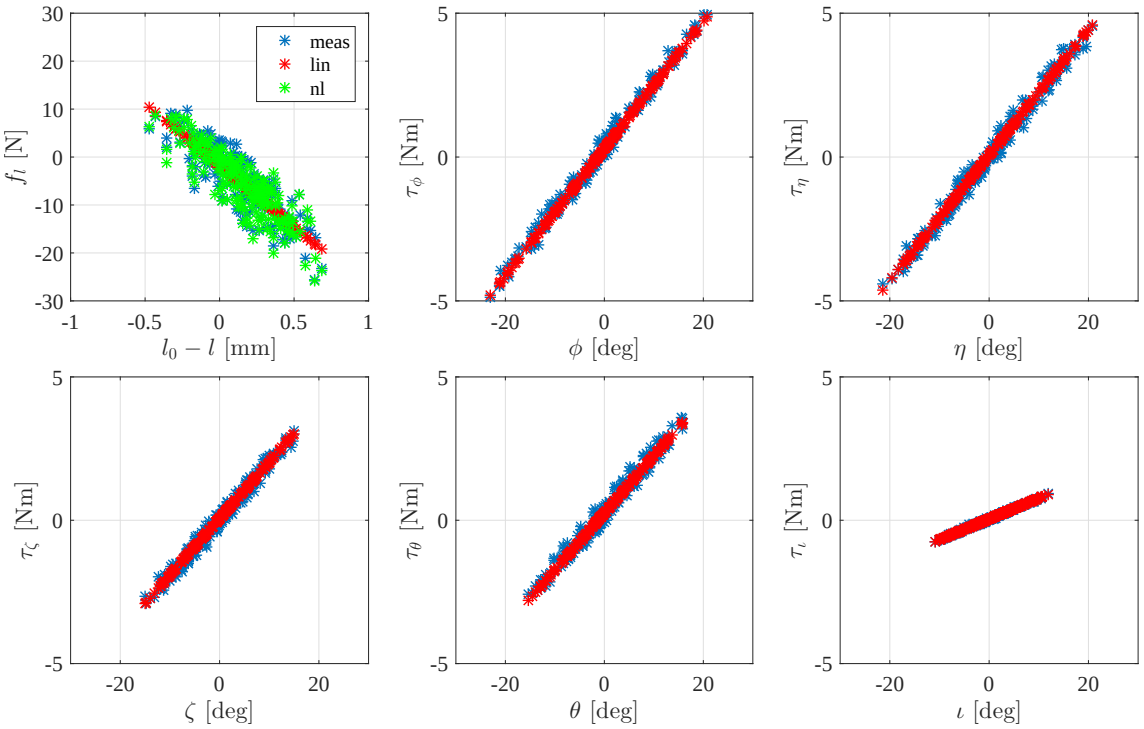

Figure 4.11.: Identified stiffness plot for the NKLS model to illustrate the linear behavior.

Discussion

The aim of this section was to experimentally identify a mapping $\boldsymbol{f}$ (4.4) which incorporates the equilibrium configurations and stiffness characteristic of the real ECM. Two models were suggested for this approximation. The first model is based on the assumption that the restoring force of the mechanism can be approximated by a six dimensional generalized force $\boldsymbol{f}(\boldsymbol{q})$ acting on the origin of the head frame. Each component of $\boldsymbol{f}(\boldsymbol{q})$ is then modeled as a multivariate polynomial (MVP) mapping whereas a fully coupled cubic polynomial in each component of $\boldsymbol{f}$ proved to be a good fit, both in simulations and experiments. Physically, the MVP model hides the nonlinear geometry of the deformation, expressed by $\boldsymbol{q}$, and the material properties of the continuum within one mapping. An advantage of the MVP model is an analytic stiffness matrix $\boldsymbol{K}$ which is computed for the trained mappings in simulation and experiments and compared for the initial straight configuration of the ECM.
In contrast, the NKLS model assumes a known nonlinear kinematic of the mechanism which constitutes of a serial structure of five rotational and one translational joint. In each joint, a linear joint stiffness is assumed. Thereby, the NKLS model represents a comparatively simple identification problem and a fully linear stiffness matrix that provides a good approximation by the linear joint stiffness in the rotational joints. In contrast, the linear stiffness in the translational joint presented a stronger mismatch of the measured and modeled behavior. Therefore, an augmented model is suggested which utilizes a MVP for the stiffness in the translational joint. By this, the model improves highly in accuracy, which could be shown in simulation and experiments.
The stiffness behavior of both models can be assessed by looking at the resulting stiffness matrix $\boldsymbol{K}$. The resulting $\boldsymbol{K}$ for a MVP model trained on $\mathcal{F}_1$ and $\mathcal{F}_3$ is essentially different

as the coefficients on the main diagonal vary an order of magnitude and in their signs. In contrast, the linear stiffness of the NKLS model, especially in the rotational joints, is generally matching in spite of their different underlying wrench sets or if simulation or experimental data is applied.

The successful identified mappings are utilized in a reduced dynamic model with the structural property of (4.3) to address computational efficiency. Both models, the NKLS and the MVP, provide this feature whereas the mean computational time of the MVP model is 0.21 ms and the mean computational time of a (fully linear) NKLS model is 0.004 ms. A boxplot reports the computational time of both models for 200 randomly selected inputs is depicted in Fig. 4.9. Both models possess a nonlinear kinematics. The NKLS model due to the serial kinematic chain and the MVP model due to the representation of the orientation by Euler angles. However, a comparably accurate (fully linear) NKLS model involves the identification of 6 parameters, an NKLS model with nonlinear axial force f_l involves $84 + 5$ parameters for the stiffness modeling whereas the MVP model involves $6 * 84$ parameters. Thus, the higher number of parameters favors the NKLS model. From a computational point of view, models with comparable accuracy, i.e. the NKLS model with nonlinear axial force and a MVP model possess almost the same mean computational time. A cubic, fully coupled regressor needs to be built from $\boldsymbol{q}$ (i.e. the input) in every simulation step for both models which explains this similarity.

4.3. Dynamics of the tendon actuation system

In this section, the dynamics of the tendon actuation system is derived and consists of two paragraphs. The first paragraph describes basically the dynamics of the r tendon actuators. The second paragraph considers the kinematics of the tendons i.e. the relations between the actuator position and the generalized coordinates $\boldsymbol{q} \in \mathbb{R}^{n_{red}}$.

4.3.1. Motor dynamics

The actuation system is composed of r actuators, each of which is connected to a free end of a tendon. An actuator i is rigidly coupled to the tendon i by some kind of transmission element, for example a motor pulley. It is assumed that no cross coupling is present. It is further assumed, that the transmission from the motor to the pulley, e.g. the motor pulley radius, is constant[2].

The transmission ratio from a tendon motor to a tendon is summarized in a constant transmission matrix $\boldsymbol{E} \in \mathbb{R}^{r \times r}$. For a rotational actuator with a motor pulley of radius $r_{m,i} \in \mathbb{R}$ and a gearbox with ratio $w_i \in \mathbb{R}$, the transmission matrix has a diagonal form

$$\boldsymbol{E} = \operatorname{diag}\left(\frac{r_{m,1}}{w_1}, \ldots, \frac{r_{m,i}}{w_i}, \ldots, \frac{r_{m,r}}{w_r} \right). \tag{4.47}$$

As a result of the assumptions, the equation of motion of the tendon actuation system are decoupled and describe the dynamic of the actuator positions summarized in the vector $\boldsymbol{\theta}_m \in \mathbb{R}^r$,

$$\boldsymbol{B}\ddot{\boldsymbol{\theta}}_m = \boldsymbol{\tau}_m - \boldsymbol{\tau}_{fric} - \boldsymbol{E}^T \boldsymbol{u}. \tag{4.48}$$

The quantities in (4.48) are the diagonal motor inertia matrix $\boldsymbol{B} \in \mathbb{R}^{r \times r}$, the motor control input torque $\boldsymbol{\tau}_m \in \mathbb{R}^r$, the frictional torque $\boldsymbol{\tau}_{fric} \in \mathbb{R}^r$. The tendon force $\boldsymbol{u} \in \mathbb{R}^r$

[2] although it might occur that a tendon is tangled on top of another which results in an increased radius.

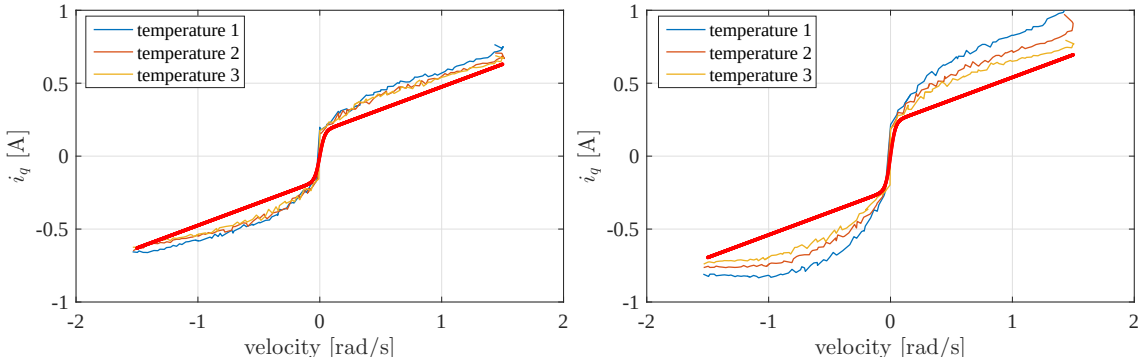

Figure 4.12.: Actual current of two different tendon actuators (left and right figure) w.r.t. to the driven velocities to illustrate the individual dry and viscous friction present in each actuator which is, in addition, dependent on the temperature.

deflects the elastic continuum mechanism and the components of $\boldsymbol{u}$, i.e. the tensions of each tendon are strictly positive

$$u_i > 0, \quad \text{for } i = 1 \dots r. \tag{4.49}$$

The tendon force is generated as a result of the tendon stiffness, summarized in the tendon stiffness matrix $\boldsymbol{K}_t \in \mathbb{R}^r$, and a difference in the position of the two ends,

$$\boldsymbol{u} = \boldsymbol{K}_t \left(\boldsymbol{E}\boldsymbol{\theta}_m - \boldsymbol{l}(\boldsymbol{q}) \right) \tag{4.50}$$

with the actual tendon length $\boldsymbol{l}(\boldsymbol{q}) \in \mathbb{R}^r$. As introduced in the beginning of this chapter, the stiffness of the tendons is sufficiently high and thus, the tendon motor position and the actual tendon length do not defer.

Friction

The friction torque $\boldsymbol{\tau}_{fric}$ arises from the friction present in the motor bearings and from a gearbox, if present. To identify the frictional torque present in the actuator, a piece vice constant velocity profile is commanded to a velocity controlled actuators. By that, a simple friction model consisting of viscous and dry friction is clearly detectable if the amount of current is plotted w.r.t. to the velocities. For the tendon actuators of the spatial test bed, these measurements have been carried out, whereas Fig. 4.12 reports on the measurements for three different subsequently executed measurements which increase the temperature of the motor. The plot shows the desired current that is given to the motor over the measured velocities, i.e. the numerical derivative of the motor position $\boldsymbol{\theta}_m$. At zero velocity, there are in general effects like Stiction or the Strebeck friction present which would need much more sophisticated measurement setups and identification procedures and results in a much deeper analysis which is beyond the scope of this thesis. To match the behavior of the the measured motor friction, maintain central symmetry and provide smoothness, the friction model reported in [116] is applied which assumes that the friction curve of motor i can be modeled by the following expression:

$$\tau_{fric,i} = k_{\tau,\, i_q} \left(i_{c,i} \, \tanh(c_i \, \dot{\theta}_{m,i}) + d_{v,i} \dot{\theta}_{m,i} \right). \tag{4.51}$$

In equation (4.51), the motor constant $k_{\tau,\, i_q} \in \mathbb{R}$, which is assumed constant, and relates the amount of current necessary to generate a specific torque. The other quantities are the

Table 4.10.: Table reporting on the identified friction parameters for a simple friction model.

motor	k_{τ,i_q} [Nm/A]	i_c [Nm]	d_{visc} [Nms/rad]	c
motor m25	0.08	0.165	0.31	25
motor m32	0.08	0.230	0.31	22

dry friction constant $i_{c,i} \in \mathbb{R}$, the constant of the viscous friction $d_{v,i} \in \mathbb{R}$ and the constant to adjust the slope of the friction model when crossing zero velocity $c_i \in \mathbb{R}$. By observing the measured behavior of two different motors of the same type in Fig. 4.12, it can be clearly stated that the friction profile is motor specific and thus need to be identified for each motor separately. Furthermore, a clear temperature dependency can be seen and therefore, the to be identified parameters should not overestimate the friction properties to eliminate overcompensation. The identified model using (4.51) are shown by the red curves in Fig. 4.12 whereas the associated parameters are found in Tab. 4.10.

4.3.2. Tendon coupling

The actuation system is coupled to the dynamics of the elastic continuum mechanism by the r tendons. In general, the coupling introduced by the tendons is an elastic coupling due to the elasticity of the tendons. However, as the stiffness of the continuum is considered to be essentially lower, the stiffness of the tendon system is neglected throughout the present thesis. Therefore only the nonlinear kinematic coupling due to the routing of the tendons is considered.

The linear velocity (and force) of the tendons $\dot{\boldsymbol{l}}_t \in \mathbb{R}^r$ $(\boldsymbol{u})$ are linearly coupled to the rotational velocity (and torque) of the actuators $\dot{\boldsymbol{\theta}}_m \in \mathbb{R}^r$ $(\boldsymbol{\tau}_m)$ by the transmission matrix (4.47) yielding

$$\dot{\boldsymbol{l}}_t = \boldsymbol{E}\dot{\boldsymbol{\theta}},\ \boldsymbol{\tau}_m = \boldsymbol{E}^T\boldsymbol{u} \tag{4.52}$$

In contrast, the coupling of the tendons onto the generalized coordinates is nonlinear due to their routing which is expressed by the tendon coupling matrix $\boldsymbol{P}(\boldsymbol{q}) \in \mathbb{R}^{n\times r}$,

$$\boldsymbol{P}(\boldsymbol{q})^T = \left(\frac{\partial \boldsymbol{l}(\boldsymbol{q})}{\partial \boldsymbol{q}}\right) \tag{4.53}$$

which yields for the velocity and torque coupling the following

$$\dot{\boldsymbol{l}}_t = \boldsymbol{P}(\boldsymbol{q})^T\dot{\boldsymbol{q}},\ \boldsymbol{\tau}_q = \boldsymbol{P}(\boldsymbol{q})\boldsymbol{u}. \tag{4.54}$$

In the controller design, the coupling matrix will be of specific importance as it describes the effect of the control action $\boldsymbol{u}$ onto the dynamics of the system $\boldsymbol{\tau}_q \in \mathbb{R}^n$. Moreover, the routing of the tendons determines the shape of (4.53) and therefore influences the closed loop behavior essentially. The coupling matrix (4.53) is derived in this work by projecting the configuration dependent unitary tendon direction vector ${}_{\mathcal{B}}\boldsymbol{e}^{\mathcal{H}}_{t,i} \in \mathbb{R}^3$ for the $i = 1 \dots r$ tendons onto a generalized force and a generalized torque that acts on the origin of the head frame $\mathcal{H}$. The current ${}_{\mathcal{B}}\boldsymbol{e}^{\mathcal{H}}_{t,i}$ is computed by geometric relations which is basically the normalized tendon direction vector $\boldsymbol{t}_{t,i}(\boldsymbol{q}) \in \mathbb{R}^3$, i.e. the vector difference between the contact point of the i-th tendon at the top platform ${}_{\mathcal{B}}\boldsymbol{r}_{t,i}(\boldsymbol{q}) \in \mathbb{R}$

$${}_{\mathcal{B}}\boldsymbol{r}_{t,i}(\boldsymbol{q}) = {}_{\mathcal{B}}\boldsymbol{r}_L + \boldsymbol{A}_{\mathcal{B}\mathcal{H}\mathcal{H}}\boldsymbol{r}_{t,i} \tag{4.55}$$

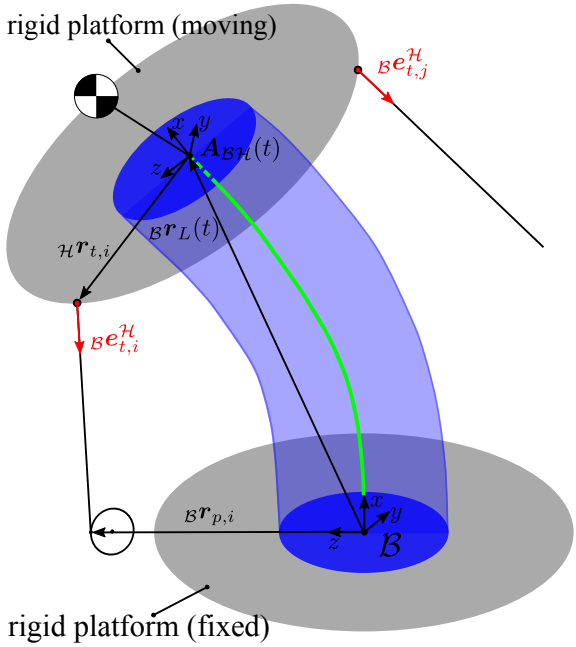

Figure 4.13.: Schematic illustration of the unitary tendon direction vector $_{\mathcal{B}}\boldsymbol{e}^{\mathcal{H}}_{t,i}$ of the ith tendon and the geometric relation to the pose of the ECM.

and the contact point of the tendon on the pulley in the base frame $_{\mathcal{B}}\boldsymbol{r}_{p,i}(\boldsymbol{q}) \in \mathbb{R}^3$ for the i th tendon

$$_{\mathcal{B}}\boldsymbol{t}_{t,i}(\boldsymbol{q}) = {}_{\mathcal{B}}\boldsymbol{r}_{p,i}(\boldsymbol{q}) - {}_{\mathcal{B}}\boldsymbol{r}_{t,i}(\boldsymbol{q}). \tag{4.56}$$

Using (4.56), the unitary tendon direction is given to

$$_{\mathcal{B}}\boldsymbol{e}_{t,i} = \frac{1}{||\boldsymbol{t}_{t,i}(\boldsymbol{q})||}\boldsymbol{t}_{t,i}(\boldsymbol{q}) = \frac{1}{\boldsymbol{l}_{t,i}(\boldsymbol{q})}\boldsymbol{t}_{t,i}(\boldsymbol{q}) \tag{4.57}$$

in which the vector norm of the tendon direction vector is replaced with the tendon length $\boldsymbol{l}(\boldsymbol{q})$. A graphical illustration is depicted in Fig. 4.13. By this derivation, the generalized forces $(f_x,\ f_y,\ f_z)^T$ and torques $(\tau_x,\ \tau_y,\ \tau_z)^T$ can be computed to

$$\underbrace{\begin{pmatrix} f_x \\ f_y \\ f_z \\ \tau_x \\ \tau_y \\ \tau_z \end{pmatrix}}_{_{\mathcal{B}}\boldsymbol{f}_c} = \underbrace{\begin{pmatrix} _{\mathcal{B}}\boldsymbol{e}^{\mathcal{H}}_{t,1} & _{\mathcal{B}}\boldsymbol{e}^{\mathcal{H}}_{t,2} & \dots & _{\mathcal{B}}\boldsymbol{e}^{\mathcal{H}}_{t,r} \\ _{\mathcal{B}}\boldsymbol{e}^{\mathcal{H}}_{t,1} \times {}_{\mathcal{B}}\boldsymbol{r}_{t,1} & _{\mathcal{B}}\boldsymbol{e}^{\mathcal{H}}_{t,2} \times {}_{\mathcal{B}}\boldsymbol{r}_{t,2} & \dots & _{\mathcal{B}}\boldsymbol{e}^{\mathcal{H}}_{t,r} \times {}_{\mathcal{B}}\boldsymbol{r}_{t,r} \end{pmatrix}}_{\boldsymbol{P}(\boldsymbol{q})^*} \boldsymbol{u} \tag{4.58}$$

To project the generalized forces and torques along the generalized directions, the configuration Jacobian $\boldsymbol{J}_{\chi,q}$ (4.6) is used and therefore the coupling matrix defined in (4.53) is computed using the geometric relationship (4.58) and $\boldsymbol{J}_{\chi,q}$,

$$\boldsymbol{P}(\boldsymbol{q}) = \boldsymbol{J}^T_{\chi,q}\boldsymbol{P}(\boldsymbol{q})^*. \tag{4.59}$$

4.4. Summary

A reduced nonlinear model was derived in the present chapter for the purpose of model-based control. Two major requirements are demanded including 1) fast computation, 2) maintaining the structure given by (3.1), as both facilitate the implementation of model-based control algorithms.
Based on observations made in a preliminary study, the assumption has been made that the dynamic effects of the continuum can be neglected and that the deformation of the continuum, i.e. the motion of the system, can be described in good approximation by the position and orientation of the head. The tendon actuation system consists of tendon actuators with friction which are elastically coupled to the motion of the continuum assuming linear tendon stiffness. Structurally, the overall model is conforming with an elastic joint robotic manipulator.
Following the assumptions, a reduced mechanical model for the ECM is setup and experimentally identified in the first part of the chapter. A physical interpretation of the model is a rigid body, the head, on top of a multidimensional spring system which embodies the geometry of the deformation and the stiffness characteristics of the continuum. The multidimensional spring system is considered to be a nonlinear generalized force $\boldsymbol{f} \in \mathbb{R}^6$ and each component is considered as a nonlinear mapping f_i that maps poses in the workspace, denoted as the train set $\mathcal{C}$ to nonlinear generalized forces. Subsequently, multivariate polynomial (MVP) mapping and a serial nonlinear kinematic model with linear joint stiffness (NKLS) are examined, and experimentally identified. The identification process is based on sensor data of additional sensors and was performed with a robotic manipulator on the spatial test bed, see paragraph 2.2.2. The full cubic MVP proved to be the best fit which implies 84 coefficients for each of the 6 components (504 parameters). The higher complexity however, comes with slightly higher fitting accuracy compared with the NKLS model. In this model, only one stiffness value is identified per virtual joint yielding the linear relationship. The model approximation is solid for a pure NKLS model and if a nonlinear relationship is applied for the axial component, the fit is accurate involving a total of 89 parameters.
Interestingly, the MVP model does not yield similar stiffness values or coefficients within the approach, which was exemplary compared by stiffness matrices of the initial-straight configuration. In contrast, the linear stiffness coefficients of the NKLS model are closely matching in simulation and experiments although two different workspaces are examined.
In the second section of the chapter, the basic expressions of the tendon actuator dynamics are presented which are used within the design of the tendon tension controller and the model-based pose controller.

CHAPTER 5

State estimation

This chapter will treat different state estimation concepts for elastic continuum mechanism of the present class. A dynamic controller based on a model shall provide set point or trajectory control for the position and orientation of the upper platform (the head). To achieve this, the dynamic controllers of this work must receive the full state of the system at each control cycle[1]. Except for one theoretical study presented in the control Chapter 6, the state of the system is defined as the set of kinematic variables that represent the pose of the upper platform and their corresponding velocities, see Fig. 5.1. In particular, the pose is defined as the position and orientation of the moving platform (top), represented by frame $\mathcal{H}$, with respect to the inertial fixed platform (bottom), represented by the frame $\mathcal{B}$, see Fig. 5.1. In previous chapters, the pose is denoted as $\boldsymbol{q} \in \mathbb{R}^n$ (4.14) whereas their corresponding velocity is the temporal derivative $\dot{\boldsymbol{q}} \in \mathbb{R}^n$.
The following six requirements are defined, in order of priority, which should be incorporated in the estimation algorithms and will be used for comparison.

1. The state estimation algorithm should provide the pose $\boldsymbol{q}$ with sufficient accuracy. A competing concept is the static finite element model, see Section 3.4.4, which is able to predict the pose with a maximum error of 6 mm and 6 deg. Hence, it is required to provide a pose estimate with a higher accuracy.

2. The state estimation algorithm should provide a pose corresponding velocity $\dot{\boldsymbol{q}}$ with no perceptible lag.

3. The algorithms used in estimation should enable a real-time execution. In the hardware experiments later on, the lowest sampling frequency of the sensor information is 300 Hz and this rate should not be violated by the estimation algorithm.

4. It is required that the sensors necessary for estimation need to be fully integrated at the elastic continuum mechanism and do not jeopardize the concept of mechanical robustness.

[1] In general, a (nonlinear) dynamic controller does not require the full state and thus this statement is by no means exhaustive.

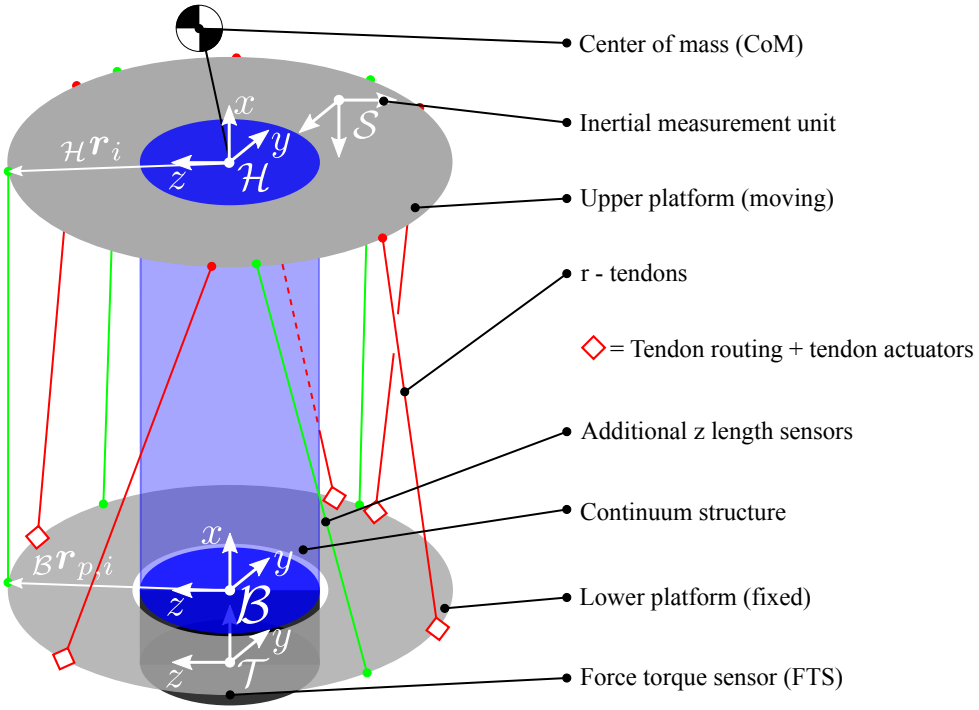

Figure 5.1.: Schematic illustration of the sensor arrangement on an tendon driven elastic continuum mechanism.

5. As collision of the ECM with the environment cannot be excluded, the estimation algorithm needs to provide a reliable state also during collisions[2].

6. It is required, that the amount of sensors is kept minimally to reduce the integration and maintenance effort.

The first requirement ensures that the pose of the upper platform can be estimated accurately, which will not only be relevant for the controller, also for manipulation tasks if the mechanism is involved in such. Elastic continuum mechanism can be used in a variety of applications and are not limited to humanoid necks. In the latter case, cameras (the eyes) are attached to the upper platform and for a vision based manipulation task or locomotion, the pose is of interest. Furthermore, the corresponding velocity $\dot{\boldsymbol{q}}$ shall be estimated with no perceptible lag which is captured in the second requirement.
The third requirement accounts for the fact that the state of an ECM cannot be measured directly and adequate models are utilized. The estimation is executed in real-time which require that this model can be computed online without perceptible time loss.
The fourth requirement accounts for mobility, as ECM's of the present class shall be used in mobile systems. Sensors based on which the estimation is carried out should be mobile as well and therefore no inertial fixed camera(s) are applied within the estimation which is accounted for in the third criterion. Furthermore, techniques based 2 D position information of a camera system attached on the mechanism are not of interest as these impose a major integration effort and would not be suitable for several continuum mechanism serially attached to each other.

[2]In this context, collisions do only occur on the head whereas collisions or external disturbances acting on the continuum mechanism are excluded.

The design paradigm of an ECM is mechanical robustness, i.e. the capability to withstand external collisions which shall not be limited by the integrated sensors which is summarized in the fifth requirement. Furthermore, the estimation concepts need to provide an accurate state if an external collision or disturbance is present.
Additional sensors, i.e. sensors which are not integrated within the tendon actuation system, are required by some of the estimation. These additional systems demand integration and maintenance effort which cannot be neglected due to their time consumption and their risk of failure. Therefore, competing design are assessed by the amount of additional sensors to be integrated which is formulated in the sixth requirement.

The first section in the following will discuss the different available sensor information, the model of the sensor and the physical relationship towards the state of the elastic continuum mechanism. In the three following sections, state estimation concepts are discussed based on geometric, static and dynamic models. To assess their capabilities, several hardware experiments are performed which compare them.

A submitted publication [81] by the author of this thesis deals with the estimation of the $\boldsymbol{q} \in \mathbb{R}^6$ based on the length measurements, see Section 5.2.3. Herein, a placement strategy is presented which is also part of the publication. Additionally, the publication covers a condensed version of the dynamic state estimation concept 5.4.2.

5.1. Sensor information

The following paragraph will present the available sensor information that are used for the state estimation of a tendon-driven elastic continuum mechanism. The tendon length sensors are integrated in the tendon actuation system and therefore can be considered as functionally mandatory. The other introduced sensors demand a mechatronic integration effort which needs to be accounted for according to requirement five.

5.1.1. Length sensors

The length sensor information include r tendons length measurements and $z \in \mathbb{Z}$ additional length measurements. Their possible arrangement is depicted in Fig. 5.1. The length sensors measurements are modeled to be composed of a relative length $\Delta\boldsymbol{l} \in \mathbb{R}^{z+r}$ and an initial length $\boldsymbol{l}_0 \in \mathbb{R}^{z+r}$, corresponding to an initial pose $\boldsymbol{q}_0$. Furthermore, it is assumed that the measurements are affected be mean-free Gaussian noise expressed by the additive noise term $\Delta\boldsymbol{l}_n$. Then, the total measured sensor length $\tilde{\boldsymbol{l}} \in \mathbb{R}^{r+z}$ is expressed by

$$\tilde{\boldsymbol{l}} = \begin{pmatrix} \tilde{\boldsymbol{l}}_t \\ \tilde{\boldsymbol{l}}_s \end{pmatrix} = \boldsymbol{l}_0 + \Delta\boldsymbol{l} + \Delta\boldsymbol{l}_n, \tag{5.1}$$

where $\tilde{\boldsymbol{l}}_t \in \mathbb{R}^r$ corresponds to the tendon measurements and $\tilde{\boldsymbol{l}}_s \in \mathbb{R}^z$ to measurements of additional sensors.

Tendons

The first r relative distance measurements are provided by the tendon actuators. The measured tendon actuator position $\tilde{\boldsymbol{\theta}}_m \in \mathbb{R}^r$ is modeled as the sum of the true motor position measurement (4.48) and mean free Gaussian noise $\boldsymbol{\theta}_n \in \mathbb{R}^r$,

$$\tilde{\boldsymbol{\theta}}_m = \boldsymbol{\theta}_m + \boldsymbol{\theta}_n. \tag{5.2}$$

The free tendon length $\tilde{\boldsymbol{l}}_t \in \mathbb{R}^r$ is therefore measured identical to equation (5.1)

$$\tilde{\boldsymbol{l}}_t = \boldsymbol{l}_{t,0} + \boldsymbol{E}\left(\boldsymbol{\theta}_m + \boldsymbol{\theta}_n\right), \tag{5.3}$$

with the constant transmission matrix $\boldsymbol{E} \in \mathbb{R}^{r\times r}$ defined in (4.47).

Additional length sensors

Additional $z \in \mathbb{Z}$ sensors will be placed on the mechanism which measure distances between the lower and the upper platform, see Fig. 5.1. Their sensor readings are denoted as $\tilde{\boldsymbol{s}} \in \mathbb{R}^z$ which is an abstract electrical signal that consists of the electrical signal due to a change in length $\boldsymbol{s} \in \mathbb{R}^z$ and sensor noise $\boldsymbol{s}_n \in \mathbb{R}^z$ which is assumed to be mean free and Gaussian,

$$\tilde{\boldsymbol{s}} = \boldsymbol{s} + \boldsymbol{s}_n. \tag{5.4}$$

The sensor readings correspond linearly to a relative change in the free sensor length by a constant calibration matrix $\boldsymbol{K}_{cs} \in \mathbb{R}^{z\times z}$ which yields for the free sensor length,

$$\tilde{\boldsymbol{l}}_s = \boldsymbol{l}_{s,0} + \boldsymbol{K}_{cs}\tilde{\boldsymbol{s}}. \tag{5.5}$$

Summary

The total $z + r$ length measurement information are expressed by combining (5.1), (5.3) and (5.5)

$$\underbrace{\begin{pmatrix} \boldsymbol{l}_t \\ \boldsymbol{l}_s \end{pmatrix}}_{\tilde{\boldsymbol{l}}} = \underbrace{\begin{pmatrix} \boldsymbol{l}_{t,0} \\ \boldsymbol{l}_{s,0} \end{pmatrix}}_{\boldsymbol{l}_0} + \underbrace{\begin{pmatrix} \boldsymbol{E}\boldsymbol{\theta}_m \\ \boldsymbol{K}_{cs}\boldsymbol{s} \end{pmatrix}}_{\Delta\boldsymbol{l}} + \underbrace{\begin{pmatrix} \boldsymbol{E}\boldsymbol{\theta}_n \\ \boldsymbol{K}_{cs}\boldsymbol{s}_n \end{pmatrix}}_{\Delta\boldsymbol{l}_n}. \tag{5.6}$$

In paragraph 4.3.2, a model for the pose dependent tendon length $\boldsymbol{l}_t(\boldsymbol{q})$ (4.57) is given. Geometrically, the tendon actuator position sensors therefore measure the change of the magnitude of the tendon direction vectors, i.e. the length of the i th vector from a known point in the base ${}_{\mathcal{B}}\boldsymbol{r}_{p,i} \in \mathbb{R}^3$ to a known point on the moving platform ${}_{\mathcal{H}}\boldsymbol{r}_i \in \mathbb{R}^3$, see Fig. 5.1. The additional sensors also measure a pose dependent change in length, as they are stretched out between the lower and the upper platform, see Fig. 5.1. In summary, the pose dependent length measurements are expressed as

$$l_i(\boldsymbol{q}) = ||{}_{\mathcal{B}}\boldsymbol{r} + \boldsymbol{A}_{\mathcal{B}\mathcal{H}}{}_{\mathcal{H}}\boldsymbol{r}_i - {}_{\mathcal{B}}\boldsymbol{r}_{p,i}||_2 \;\text{ for } i = 1\ldots z + r. \tag{5.7}$$

5.1.2. Force torque sensor (FTS)

At the clamped end of the ECM, a force torque sensor (FTS) is mounted which measures three forces and three torques. Physically, the FTS provides the reaction forces and torques that are imposed by the continuum when it is deformed. The location of the FTS is illustrated in Fig. 5.1.

The forces and torques measured by the FTS are denoted ${}_{\mathcal{T}}\tilde{\boldsymbol{w}}_{\mathrm{FTS}} \in \mathbb{R}^6$ with respect to the sensor coordinate frame $\mathcal{T}$. The measurements consists of the true forces and torques ${}_{\mathcal{T}}\boldsymbol{w}_{\mathrm{FTS}} \in \mathbb{R}^6$, an inherent bias ${}_{\mathcal{T}}\boldsymbol{w}_{\mathrm{FTS,b}} \in \mathbb{R}^6$ and sensor mean free Gaussian noise ${}_{\mathcal{T}}\boldsymbol{w}_{\mathrm{FTS,n}} \in \mathbb{R}^6$,

$${}_{\mathcal{T}}\tilde{\boldsymbol{w}}_{\mathrm{FTS}} = {}_{\mathcal{T}}\boldsymbol{w}_{\mathrm{FTS}} + {}_{\mathcal{T}}\boldsymbol{w}_{\mathrm{FTS,b}} + {}_{\mathcal{T}}\boldsymbol{w}_{\mathrm{FTS,n}}. \tag{5.8}$$

The sensor readings are transformed to the base $\mathcal{B}$ by the adjoint[3] $\mathbf{Ad}^T_{\mathcal{TB}} \in \mathbb{R}^{6\times6}$ of a constant and known homogeneous transformation matrix $\boldsymbol{T}_{\mathcal{TB}} \in \mathbb{R}^{4\times4}$,

$$ {}_{\mathcal{B}}\boldsymbol{w}_{\mathrm{FTS}} = \mathbf{Ad}^T_{\mathcal{TBT}} \boldsymbol{w}_{\mathrm{FTS}}. \tag{5.9} $$

The measured wrench ${}_{\mathcal{B}}\boldsymbol{w}_{\mathrm{FTS}}$ in the base can be interpreted to incorporate information about the full state as ${}_{\mathcal{B}}\boldsymbol{w}_{\mathrm{FTS}}$ and is related to the equation of motion (4.3) by

$$ \boldsymbol{M}(\boldsymbol{q})\ddot{\boldsymbol{q}} + \boldsymbol{k}(\boldsymbol{q},\dot{\boldsymbol{q}}) = \boldsymbol{J}^T_{\chi,q}(\boldsymbol{q}) \underbrace{\left({}_{\mathcal{B}}\boldsymbol{w}_{\mathrm{FTS}} - \begin{pmatrix} \mathbf{0} \\ {}_{\mathcal{B}}\boldsymbol{r}_L \times {}_{\mathcal{B}}\boldsymbol{f}_{\mathrm{FTS}} \end{pmatrix} \right)}_{{}_{\mathcal{B}}\boldsymbol{w}^{\mathcal{H}}_{\mathrm{FTS}}}, \tag{5.10} $$

where ${}_{\mathcal{B}}\boldsymbol{w}^{\mathcal{H}}_{\mathrm{FTS}} \in \mathbb{R}^6$ is the wrench applied at the origin of $\mathcal{H}$, expressed in $\mathcal{B}$.

5.1.3. Inertial measurement unit

To enhance a velocity estimation and for the establishment of the dynamic estimation process, an Inertial Measurement Unit (IMU) is attached at the moving platform (see Fig. 5.1). The IMU measures the linear acceleration ${}_{\mathcal{S}}\tilde{\boldsymbol{a}} \in \mathbb{R}^3$ and the angular velocity ${}_{\mathcal{S}}\tilde{\boldsymbol{\omega}} \in \mathbb{R}^3$ of a sensor frame $\mathcal{S}$ which is fixed to $\mathcal{H}$ in a known position $\boldsymbol{r}_{\mathcal{HS}} \in \mathbb{R}^3$ and orientation $\boldsymbol{A}_{\mathcal{HS}} \in \mathbb{R}^{3\times3}$. The model of the acceleration measurement is additively composed of the true acceleration ${}_{\mathcal{S}}\boldsymbol{a} \in \mathbb{R}^3$, a bias on the acceleration signal ${}_{\mathcal{S}}\boldsymbol{a}_b \in \mathbb{R}^3$ modeled as random walk processes [61], sensor noise ${}_{\mathcal{S}}\boldsymbol{a}_n \in \mathbb{R}^3$ which is considered to be mean free and Gaussian and the acceleration due to gravity ${}_{\mathcal{B}}\boldsymbol{a}_g \in \mathbb{R}^3$,

$$ {}_{\mathcal{S}}\tilde{\boldsymbol{a}} = {}_{\mathcal{S}}\boldsymbol{a} + {}_{\mathcal{S}}\boldsymbol{a}_b + {}_{\mathcal{S}}\boldsymbol{a}_n + \boldsymbol{A}^T_{\mathcal{BS}}{}_{\mathcal{B}}\boldsymbol{a}_g. \tag{5.11} $$

The model of the angular velocity measurement is additively composed of the true angular velocity ${}_{\mathcal{S}}\boldsymbol{\omega} \in \mathbb{R}^3$, a bias on the angular velocity signal ${}_{\mathcal{S}}\boldsymbol{\omega}_b \in \mathbb{R}^3$ modeled as random walk processes [61] and sensor noise ${}_{\mathcal{S}}\boldsymbol{\omega}_n \in \mathbb{R}^3$ which is considered to be mean free and Gaussian,

$$ {}_{\mathcal{S}}\tilde{\boldsymbol{\omega}} = {}_{\mathcal{S}}\boldsymbol{\omega} + {}_{\mathcal{S}}\boldsymbol{\omega}_b + {}_{\mathcal{S}}\boldsymbol{\omega}_n. \tag{5.12} $$

Again, the measurements of the IMU can be represented by the state of the system. In this context, the acceleration measurements (5.11) and the measured angular rates (5.12) are related to the acceleration of the origin and the angular velocity of $\mathcal{H}$ by

$$ {}_{\mathcal{B}}\ddot{\boldsymbol{r}}_L = \boldsymbol{A}_{\mathcal{BH}}\boldsymbol{A}_{\mathcal{HS}} \left({}_{\mathcal{S}}\boldsymbol{a} + {}_{\mathcal{S}}\dot{\boldsymbol{\omega}} \times \boldsymbol{r}_{\mathcal{HS}} \right), \quad \dot{\boldsymbol{\theta}}_L = \boldsymbol{J}_{\chi,\theta\mathcal{S}}\boldsymbol{\omega}, \tag{5.13} $$

using the rotational part of the representation Jacobian (4.6).

5.2. State estimation based on geometric models

The present section will present state estimation concepts which are based on geometric models of the mechanism. Herein, the state, in general, is incorporated in some geometric relations who are measured by sensors. Throughout this section, methods are proposed that estimate the pose only, $\boldsymbol{q} \in \mathbb{R}^6$, and the corresponding velocity $\dot{\boldsymbol{q}} \in \mathbb{R}^6$ will be computed by numerical differentiation. The pose estimation is carried out with $z + r \in \mathbb{N}$ configuration dependent length measurements $\tilde{\boldsymbol{l}} \in \mathbb{R}^{z+r}$, see paragraph 5.1.1, and their

[3] For details about wrench transformation by adjoints, see [117].

corresponding geometric model in equation (5.7).
For the present case of an underactuated system (the pose is described by $\boldsymbol{q} \in \mathbb{R}^6$), the $r < 6$ tendon length measurements are not sufficient to estimate the full pose as the Jacobian matrix $\boldsymbol{P}^T(\boldsymbol{q}) \in \mathbb{R}^{r\times 6}$,

$$\dot{\boldsymbol{l}} = \boldsymbol{P}^T(\boldsymbol{q})\dot{\boldsymbol{q}}, \quad \text{with} \quad \boldsymbol{P}^T(\boldsymbol{q}) = \frac{\partial \boldsymbol{l}(\boldsymbol{q})}{\partial \boldsymbol{q}}, \tag{5.14}$$

known as the transpose of the tendon coupling matrix (4.59), has a $6 - r$ dimensional Nullspace which yields that components or linear combinations of $\boldsymbol{q} \in \mathbb{R}^6$ in this Nullspace cannot be estimated from the measurements. This fact is strongly connected to the rank observability criterion [118] which states that if the nonlinear observability matrix $\boldsymbol{O}(\boldsymbol{q})$ is rank deficient, the problem is (locally) not observable. The nonlinear observability matrix is built upon Lie derivatives of the measurement equation (5.7) and the coupling matrix (4.59) is the zero-order Lie derivative and corresponds to the static part of $\boldsymbol{O}(\boldsymbol{q})$.
To tackle this problem, two approaches are presented in the following. As a first approach in Section 5.2.2, $\boldsymbol{q}$ is represented by a reduced set of kinematic parameters $\boldsymbol{q}_{\text{red}} \in \mathbb{R}^r$. This new representation removes the Nullspace in $\boldsymbol{P}(\boldsymbol{q})$ and the problem becomes formally observable. The second approach in Section 5.2.3 completes the base of the coupling matrix (5.14), by adding the additional length sensors information.
Despite of the two approaches, $\boldsymbol{q}$ is estimated in this section based on the nonlinear error function $\boldsymbol{e}_l(\boldsymbol{q}) \in \mathbb{R}^{z+r}$ of the measured and the modeled sensor length. The estimation is then based on a minimization of an objective function,

$$\min_{\tilde{\boldsymbol{q}}} || \underbrace{\tilde{\boldsymbol{l}} - \boldsymbol{l}(\boldsymbol{q})}_{\boldsymbol{e}_l(\boldsymbol{q})} ||_2^2, \tag{5.15}$$

which is the squared norm of the error and the result is an estimate of the pose $\hat{\boldsymbol{q}} \in \mathbb{R}^{n_{\text{red}}}$. For this minimization problem, several different algorithms are presented and assessed in the next section.

5.2.1. Optimization algorithms

A solution to equation (5.15) need to be provided to estimate the pose of the ECM. Essentially, the optimization problem needs to be solved in real time which means that the utilized algorithm need to converge within a hardware time cycle to find the minimum. The optimization problem is affected by a nonlinear, non-convex objective functions and parameters with different (physical) units which usually require a scaling that imposes higher computational loads. This section describes several assessed optimization methods that have been used for state estimation in this work. All algorithms have been implemented in MATLAB based on the comprehensive book by Madsen and Nielsen [119], which provides also good reference to the interested reader, as the algorithms are treated superficial in the following.

Gradient-based methods

Based on the gradient[4] of (5.15), a downward direction is computed to find a minimum. The *Steepest Descent* (SD)-method applies the negative direction of the gradient as search direction to ensure a minimization of (5.15) and the step length is computed based on

[4]The gradient is the partial derivative of the objective function (5.15) with respect to $\boldsymbol{q}$.

a soft-line search to lower the computational demands [119]. The SD-method is easy to implement and is known to work well in the initial stage of the optimization. The convergence in the final stage is usually linear and slow. The *Conjugate Gradient* (CG) method tries to overcome the slow convergence of the steepest-descent at the final stage as it takes the descent direction of the previous step into account. For problems with a high number of n variables, this technique may be faster than the Newton methods, since it does not require matrix operations, but only uses vectors [119].
Both gradient-based methods are strongly affected by ill-conditioned problems, i.e. different scales in $\boldsymbol{q}$, which results in a high condition number of the Hessian matrix[5]. To improve the condition number and therefore the convergence time, the gradient is suggested to be multiplied with a positive definite symmetric matrix and a standard strategy is to use the inverse of the diagonalized Hessian [120].

Newton methods

Newton methods are based on the gradient and the Hessian matrix. As the computation of the Hessian matrix is time expensive for higher (e.g. six) dimensional problems, the *Quasi-Newton* (QN) method suggests to approximate the Hessian based on the *BFGS Formula* [119]. For an optimization problem of the present kind where the objective function consists of a vector error function $\boldsymbol{e}_l(\boldsymbol{q})$ and if the initial step is near the solution, the Hessian can be linearly approximated by the Jacobian matrix of the error function $\boldsymbol{e}_l(\boldsymbol{q})$ which is called *Gauss-Newton* (GN)-method.
The main disadvantages reported for Newton-type methods are, that they are only working well if the initial value is close to the solution and that the computation of Hessian and its inverse can be very time expensive for highly dimensional problems. Nevertheless the convergence in the final stage is quadratic and this method is less affected by ill-conditioned problems [119].

Powell's dog leg method

This trust region method, called *Dog-Leg* (DL) method, is currently considered the best method for solving nonlinear equations [119][p.130]. Powell suggested an approximation of the current search direction using a combination of the SD and the GN direction [119] and thus is called a hybrid method. The main drawback is that it requires to check at least one condition at every iteration, which makes the time per iteration step slower than pure Newton-type or gradient-based methods.

Summary: Optimization methods

The Table 5.1 sums up the given advantages and disadvantages of the discussed methods above. In Section 5.5.1, above algorithms are tested on the real problem to assess their suitability.

5.2.2. Reduced kinematic models

The tendon actuation system is necessary to drive the mechanism in its workspace. An estimation algorithm that requires information of the actuation system only is advantageous

[5]The Hessian matrix is the partial derivative of the gradient with respect to $\boldsymbol{q}$, i.e. the second partial derivative of the objective function (5.15)

Table 5.1.: Comparison of the algorithms Steepest Descent (SD), Conjugate Gradient (CG), Quasi Newton (QN), Gauss Newton (GN), and Powell's Dog Leg (DL). Criterion satisfied "very good" (++), "good" (+), "bad" (−), "very bad" (−−) and "no clear statement" (∘).

Criterion	**SD**	**CG**	**QN**	**GN**	**DL**
Low number of operations[a] per iteration	++	+	−	−	∘[b]
Fast convergence in the final stage	−−	−	+	+	+
No scaling required with ill conditioned problems	−−	−	+	+	+
Suitability for nonlinear systems	∘	∘	∘	∘	++

[a] Without considering the line-search algorithm.
[b] No statement as different strategies are used.

as no additional sensors need to be integrated in the system. A full six DoF pose is not observable from these measurements which is treated in this paragraph by approximating $\boldsymbol{q} \in \mathbb{R}^6$ by a reduced set of kinematic variables $\boldsymbol{q}_{\text{red}} \in \mathbb{R}^r$.

Constant curvature kinematics

The first approach to represent $\boldsymbol{q}$ is the well-known constant curvature assumption which is discussed by Webster *et al.* [94]. A rather short derivation of the kinematic equations is presented in the following.
Linear strains and curvatures have been introduced in Section 3.1 as local kinematic variables that describe the deformation of a beam along ν. The assumption now is that these curvatures are constant and that the linear strains reduce to an axial strain only, also constant, whereas the shear strains are neglected due to an assumed infinite stiffness in the shear directions. By these assumptions the local curvature vector ${}_{\mathcal{N}}\boldsymbol{\kappa} \in \mathbb{R}^3$ is constant along the arc-length ν and only changing in time. Using the director representation of the orientation of the head frame,

$$\boldsymbol{A}_{\mathcal{B}\mathcal{H}} = \left({}_{\mathcal{B}}\boldsymbol{d}_{1,L},\, {}_{\mathcal{B}}\boldsymbol{d}_{2,L},\, {}_{\mathcal{B}}\boldsymbol{d}_{3,L}\right), \tag{5.16}$$

and the definition of the curvatures (3.12), the following set of differential equations with constant coefficients, the curvatures $(\kappa_1,\, \kappa_2,\, \kappa_3)$, can be derived

$$\begin{aligned}
{}_{\mathcal{B}}\boldsymbol{d}'_{1,L} &= \kappa_3 {}_{\mathcal{B}}\boldsymbol{d}_{2,L} - \kappa_2 {}_{\mathcal{B}}\boldsymbol{d}_{3,L}, \\
{}_{\mathcal{B}}\boldsymbol{d}'_{2,L} &= \kappa_1 {}_{\mathcal{B}}\boldsymbol{d}_{3,L} - \kappa_3 {}_{\mathcal{B}}\boldsymbol{d}_{1,L}, \\
{}_{\mathcal{B}}\boldsymbol{d}'_{3,L} &= \kappa_2 {}_{\mathcal{B}}\boldsymbol{d}_{1,L} - \kappa_1 {}_{\mathcal{B}}\boldsymbol{d}_{2,L}.
\end{aligned} \tag{5.17}$$

Based on the assumption for the linear strains ${}_{\mathcal{N}}\gamma_x$, the position of the head ${}_{\mathcal{B}}\boldsymbol{r}_L$ can be computed using the solution of (5.17) for ${}_{\mathcal{B}}\boldsymbol{d}_{1,L}$,

$${}_{\mathcal{B}}\boldsymbol{r}'_L = \gamma_x {}_{\mathcal{B}}\boldsymbol{d}_{1,L}. \tag{5.18}$$

Equation (5.17) describes an initial value problem of a set of ordinary differential equations with constant coefficients that can be solved analytically. In combination with (5.18), an

approximation of the pose $\boldsymbol{q}$ based on three constant curvatures and a constant axial strain $(\boldsymbol{\kappa}^T,\, \gamma_x)^T$ is given and the objective function (5.15) is reformulated to

$$\min_{\bar{\boldsymbol{\kappa}}, \bar{\gamma_x}} ||\tilde{\boldsymbol{l}}_t - \boldsymbol{l}_t(\boldsymbol{\kappa}, \gamma_x)||_2^2. \tag{5.19}$$

The estimation accuracy of the objective function (5.19) is evaluated in a simulation study, reported in Fig. 5.2.

Simplified kinematic model

Similar to the previous paragraph, this section reports on a second possibility to approximate the full pose $\boldsymbol{q}$. The approach is inspired by the investigations reported in Section 3.5.4, where the workspace of the spatial system is approximated by the kinematic variables denoted $\boldsymbol{q}_{\text{red}} = (\phi,\, \eta\, \iota,\, \epsilon)^T$ and their geometric arrangement depicted in Fig. 3.14. In Section 3.5.4, errors below 2 mm and 2 deg are reported for this approximation which supports the feasibility of this approach. With that, the objective function (5.15) reduces

$$\min_{\bar{\phi}, \bar{\eta}, \bar{\iota}, \bar{\epsilon}} ||\tilde{\boldsymbol{l}}_t - \boldsymbol{l}_t(\phi,\, \eta\, \iota,\, \epsilon)||_2^2, \tag{5.20}$$

and the achievable accuracy is tested in simulation, see Fig. 5.2.

Simulation results

The estimation accuracy of the proposed kinematic approximation is tested in simulation based on the static spatial FEM model for a mechanism with $r = 4$ tendons. The workspace of the mechanism is sampled by a randomized configuration of tendon tension forces in the range [0, 100] N. The DL-optimization algorithm is applied for the minimization problems, equation (5.19) and equation (5.20) respectively. The achieved estimation accuracy of both objective functions is compared by the component wise absolute error of the predicted pose $\hat{\boldsymbol{q}}$, by each individual kinematic mapping, and the pose $\boldsymbol{q}$ computed by the FEM model. A boxplot of the absolute error for each component of the pose is depicted in Fig. 5.2 which states that both mappings yield a comparable accuracy for the estimation of $\boldsymbol{q}$ with (slight) advantage towards the reduced kinematic mapping due to the lower median values in z, θ_x and θ_y. Based on above findings and the fact that the constant curvature kinematics possess a singularity when the mechanism is straight, i.e. $\kappa_2 = 0$ or $\kappa_3 = 0$, the kinematic mapping based on $(\phi,\, \eta\, \iota,\, \epsilon)^T \in \mathbb{R}^4$ seems more promising and is tested on the hardware. The achievable accuracy, the suitability for real time as well as the quality of the derived velocity are reported in Section 5.5.

5.2.3. Six DoF kinematic model

The full pose $\boldsymbol{q} \in \mathbb{R}^6$ is estimated in the following and the length measurements of the tendons only are not sufficient due to the Nullspace of the coupling matrix (5.14). Therefore, z additional sensors shall be placed on the elastic continuum mechanism, as indicated in Fig. 5.1, to complete the base of $\boldsymbol{P}(\boldsymbol{q})^T$ (5.14). This problem is discussed in the following paragraph whereas the achievable accuracy is reported in Section 5.5.

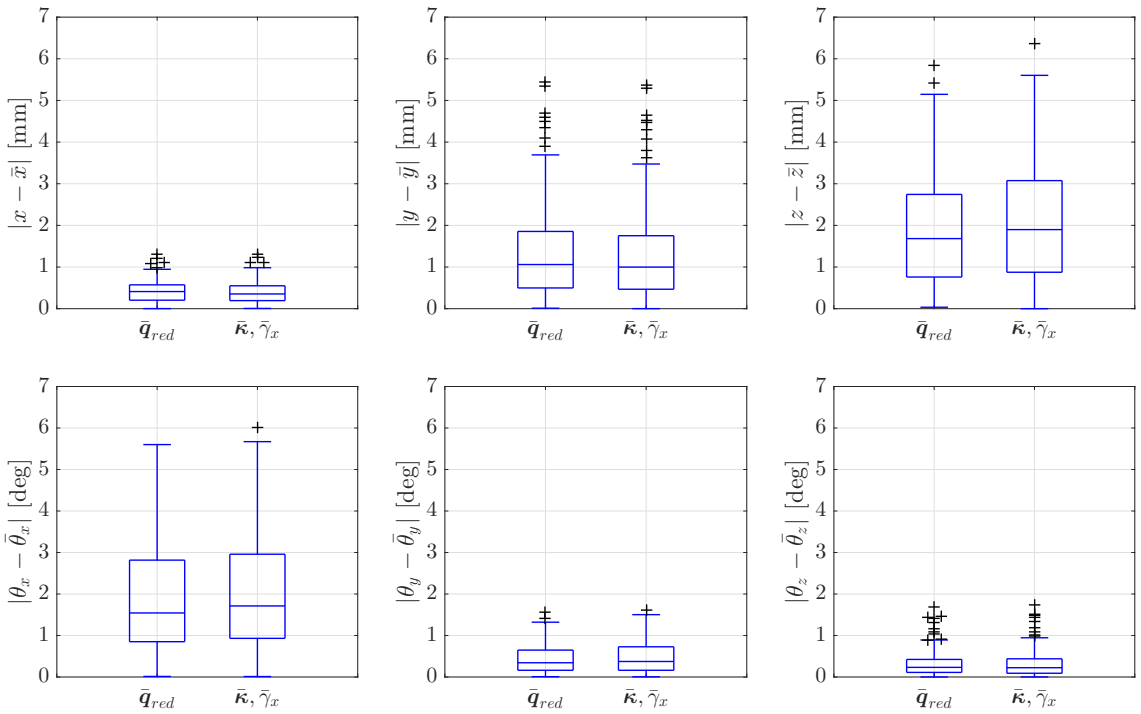

Figure 5.2.: Simulative comparison of the pose estimation based on the reduced kinematic models using tendon measurements with an assumed tendon noise of 1 mm. The minimization is carried out with the DL algorithm as it provided the fastest convergence.

Placement of the additional sensors

The problem of "where to place sensors" to achieve accurate estimation results has been addressed by several authors. A common approach in the field of observer design is to look at the observability Gramian [121] of the nonlinear state space equations. The Gramian is computed by linearizing the dynamics along a trajectory. It is valuable for dynamic observability problems, but it does not conclude on estimation quality at static poses. Others propose to use the condition number [122] of the observability matrix as a measure to place sensors. A high condition number indicates that one or more measurements do not affect the prediction of the pose and a condition number of ≈ 1 means that all measurements have a similar effect on the estimation problem which is desirable. The neck system incorporates $r = 4$ tendons and the condition number of $\boldsymbol{P}(\boldsymbol{q}_0) \in \mathbb{R}^{4\times 6}$, computed at the initial pose $\boldsymbol{q}_0$, is ≈ 27. As a fictional example, two sensors that directly measure two components of $\boldsymbol{q}$ are integrated, e.g. sensors that measure y and θ_x directly. This adds two unitary row vectors to $\boldsymbol{P}(\boldsymbol{q}_0)$ and completes its base. For any combination of two unitary vectors, the condition number of $\boldsymbol{P}(\boldsymbol{q}_0)$ remains ≥ 27 although some components of $\boldsymbol{q}$ can be measured directly, an ideal scenario. As a result, the condition number is less informative and a custom metric is introduced which fits the present problem of arranging additional length sensors. In this work, the sensors are placed by examining $\boldsymbol{P}(\boldsymbol{q})$, which can be interpreted as *the effect of a small change in* $\boldsymbol{q}$ *onto a change in* $\boldsymbol{l}$, i.e.

$$\Delta \boldsymbol{l} = \boldsymbol{P}^T(\boldsymbol{q})\Delta \boldsymbol{q}. \tag{5.21}$$

Herein, the total change in $\boldsymbol{l}$ with respect to the i th component of $\boldsymbol{q}$ is captured by the columnwise Euclidean norm of $\boldsymbol{P}(\boldsymbol{q})$, denoted as $n_i \in \mathbb{R}$ for $i \in \{x, y, z, \theta_x, \theta_y, \theta_z\}$. First, the norms of the columns of $\boldsymbol{P}(\boldsymbol{q})$ of the tendon-driven elastic continuum mechanism with $r = 4$ is depicted in the top of Fig. 5.3. Two histograms present the six column norms n_i, separated for translations and rotations. The depicted distributions of n_i are computed in a simulation. Here, a beam finite element model, derived in [77], computes 200 static poses $\boldsymbol{q}$ of the continuum mechanism by applying uniformly distributed tendon tensions in the range of $[0, 70]$ N.

Several different sensor configurations are generated systematically to study the corresponding characteristic of the norms. A sensor configuration k is specified by the base configuration, either a), b) or c) and a number of [1, 22] that specifies the insertion on the upper plate. In the bottom of Fig. 5.3, four configurations are illustrated namely a)-1, b)-1 and c)-1, with the same sensor length, and c)-1 with a shorter sensor length. Although, theoretically $z = 2$ is enough for a full rank of $\boldsymbol{P}(\boldsymbol{q})$, redundant sensor information are considered in the following to prohibit the case that $\boldsymbol{P}(\boldsymbol{q})$, at a certain $\boldsymbol{q}$, looses rank. To present a comprehensible study and ensure symmetric sensor placement, $z = 4$ is chosen for the subsequent analysis. Three measures are used to evaluate a sensor configuration, depicted in the histograms, and explained in the following:

- The mean value of a distribution n_i is denoted $\bar{n}_i \in \mathbb{R}$. Generally speaking, a high $\bar{n}_i$ is desirable.

- A high mean value $\bar{n}_i$ of distribution i, compared to the other mean values $\bar{n}_j$, translates that the component i of the pose can be distinguished better in the sensor readings. Thus, for a uniform quality, the distance in between mean values $a_{i,j} = \bar{n}_i - \bar{n}_j \in \mathbb{R}$ for $i \neq j$ needs to be small.

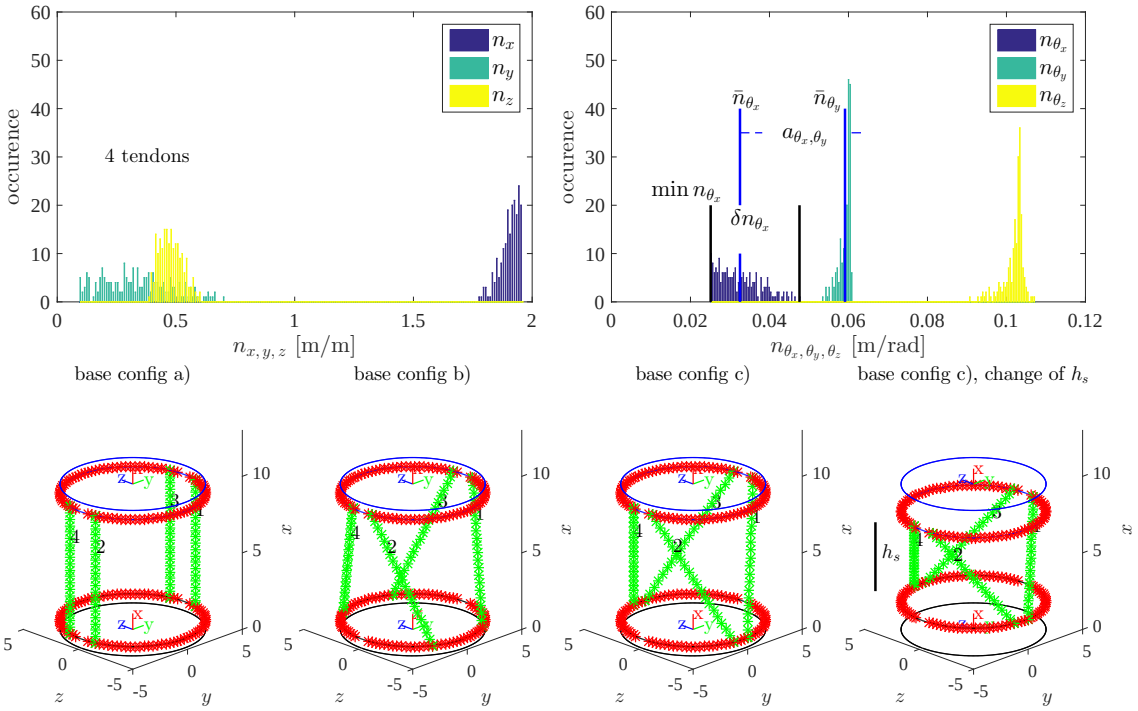

Figure 5.3.: Top: Distribution of the column norms n_i of the tendon coupling for the tendon-driven elastic continuum neck. Bottom: Illustration of the different initial configurations, termed a)-1, b)-1 c)-1 and c)-1 with a shorter sensor length h_s.

- A narrow distribution of a norm n_i, indicated by a small $\delta n_i \in \mathbb{R}$, translates that the effect of q_i onto the sensor readings is similarly high all over the workspace and is desired.

The above considerations are captured into a worst case metric. For the metric, the magnitude of a column norm n_i is normalized to the interval [0, 1] to ensure invariance under change of units, however the metric is not invariant to a change of coordinates.
An overall high $\bar{n}_i^k \in \mathbb{R}$ of a configuration k is ensured by maximising the smallest minimum value of all distributions $\min n_i^k$,

$$\max_k \left(\min_{\min n_i^k} \left(\min n_x^k, \ldots, \min n_{\theta_z}^k \right) \right). \tag{5.22}$$

To ensure that the distributions lie in a close range, the maximum distance $a_{i,j}^k$ of configuration k needs to be smaller compared to other configurations

$$\min_k \left(\max_{a^k} a_{i,j}^k \right) \ \forall i, j \text{ with } i \neq j. \tag{5.23}$$

A narrow distribution δn_i^k is ensured if the maximum distribution of a configuration k is smaller compared to other configurations,

$$\min_k \left(\max_{\delta n_i^k} \left(\delta n_x^k, \ldots, \delta n_{\theta_z}^k \right) \right). \tag{5.24}$$

Clearly, the three criteria might suggest a different sensor configuration, hence a configuration k is assumed superior compared with the others if it fulfils each of the three criteria in average at best. Another possibility to find the superior sensor configuration is to apply multi-objective optimization methods to find e.g. Pareto-Optimal solutions [123]. To evaluate the defined criterion, a simulation study is presented in the following. In this study, the connection of the additional sensors in the bottom is kept constant and the insertion point in the top plate is varied. Five different initial configurations are used to study the norm. Configuration a), b) and c) are using the same sensor length h_s but different positions in the bottom, as it is illustrated in the bottom of Fig. 5.3. Secondly, the free sensor length $h_s \in \mathbb{R}$ of c) is varied in two simulations to examine the influence on the norms and again, the insertion points are varied. To evaluate the defined criterion, a simulation study is presented in the following. In this study, the connection of the additional sensors in the bottom is kept constant and the insertion point in the top plate is varied. Five different initial configurations are used to study the norms which are displayed in Fig. 5.3. Configuration a), b) and c) are using the same sensor length h_s but different position in the bottom. Secondly, the free sensor length $h_s \in \mathbb{R}$ of c) is varied in two simulations to examine the influence on the norms and again, the insertion points are varied. Six of the 22 configurations of this study for insertion a) are illustrated in the top row of Fig. 5.4. Please note that the insertions points are varied symmetrically.
A result for base configuration a) is depicted in Fig. 5.4. Bar-plots of the associated column norm distribution with column mean $\bar{n}_i^k$ and their maximum and minimum value for all sampled insertions $1 - 22$ are depicted. The blue horizontal rectangle depicts the column norms of the tendons, i.e. the configuration which need to be improved. By applying the defined criteria, three sensor configuration are identified which fulfill these, in average, at best (ranked with 1, 2 and 3), namely configuration $k = a) - 9$, $k = a) - 8$ and

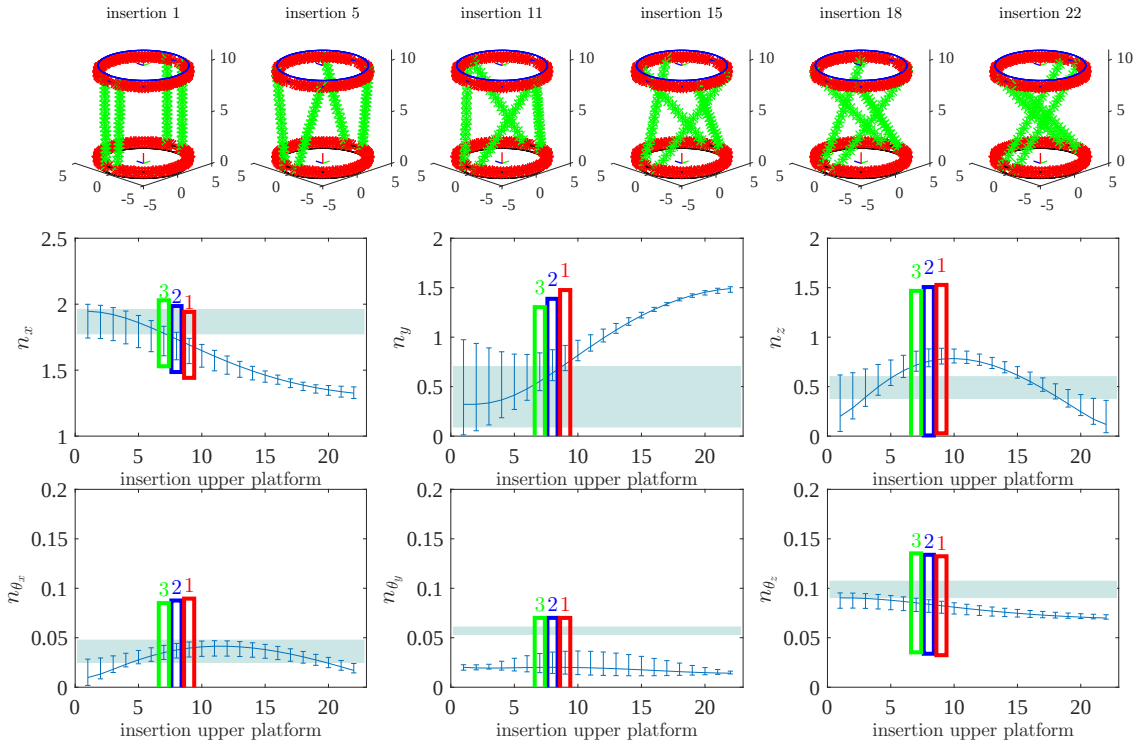

Figure 5.4.: Simulation study of base configuration a) (see Fig. 5.3). The top row illustrates six of the sampled 22 sensor insertion points (insertion 1 ... 22). Axes are in [cm]. In the bottom, bar plots illustrate the mean value and the range of all column norms and the blue horizontal rectangles indicate the initial distribution of the column norms of the tendons. The red (blue and green) vertical box indicate the best (second and third best) sensor configuration assessed by the defined criteria.

$k = a) - 7$. It can be seen, that the configurations are chosen which possess high column means $\bar{n}_i^k$, a small distance $a_{i,j}^k$ at the same time whereas the distribution of the norms δn_i^k are comparably small.

The results of the simulation study for base configurations, a), b) and c) as well as two different free sensor length for c) are depicted in Fig. 5.5. Here, only the mean values are plotted for clarity. From Fig. 5.5, subsequent findings can be reported:

- The base configuration a), b) c) highly affects the norms in θ_y and θ_z whereas the insertions in the top do not affect them much. This can be seen by comparing the blue, red and black line for n_{θ_y} and n_{θ_z}.
- Different insertions in the upper platform strongly affect the norms in y, z and θ_x.
- The norm in x is the highest and the norm in θ_x is (in average) the lowest (a motion in θ_x does not yield a high sensor elongation). The only way to achieve higher n_{θ_x} is by a shorter sensor length h_s which can be seen by comparing the black, the black dashed and black point-dashed line.

Based on the simulation study Fig. 5.5, three configurations of sensors are implemented in hardware based on the following considerations. They are highlighted by $*$ in Fig. 5.5,

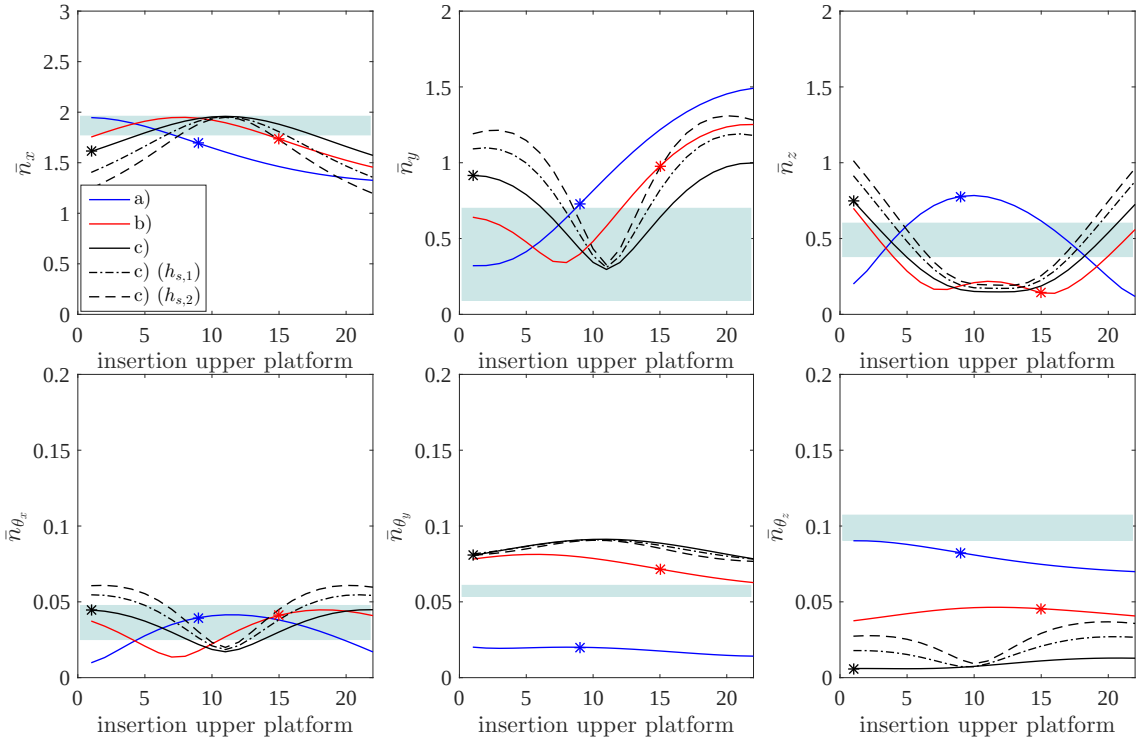

Figure 5.5.: Results of the simulation study for the sampled configuration. The blue rectangle expresses the distribution of the norms of the tendons, for comparison reasons.

and shown in Fig. 5.6. Configuration a)-9 and c)-1 are expected to yield similar results in the estimation of y, z and θ_x, indicated by similar norms whereas they should perform differently in θ_y and θ_z. However, it needs to be evaluated if the strong coupling in the motion, especially in y, θ_z and z, θ_y has an effect on the estimation. For base configuration b), no performance improvement, except in n_y, with respect to one norm can be assessed, see Fig. 5.5. Thus, b)-15 is chosen to represent a counter example which should perform worst.

5.3. State estimation based on static models

The fundamental assumption of this section is that the necessary sensor information are provided in a high sampling rate and that the utilized model can be computed at a similar (high) rate. As a consequence, the overall motion of the system can be treated quasi-statical. Chapter, 3 and 4, provided different models that describe the static behavior of the elastic continuum mechanisms. In a nutshell, the static equation of both models can be described by

$$\boldsymbol{k}(\boldsymbol{q}, \boldsymbol{0}) - \boldsymbol{J}_{\chi,q}^{T}{}_{\mathcal{B}}\boldsymbol{f}_c = \boldsymbol{0}, \tag{5.25}$$

where $\boldsymbol{k}(\boldsymbol{q}, \boldsymbol{0}) \in \mathbb{R}^n$ are the generalized internal and gravitational forces, the configuration space Jacobian $\boldsymbol{J}_{\chi,q}$ (4.6) that projects an external Cartesian wrench ${}_{\mathcal{B}}\boldsymbol{f}_c \in \mathbb{R}^n$, applied at the tip of the elastic continuum mechanism, onto the generalized directions.
The overall goal of the static estimation is to use measurements that represent the externally applied wrench and compute (estimate) $\boldsymbol{q}$ based on equation (5.25). Two different

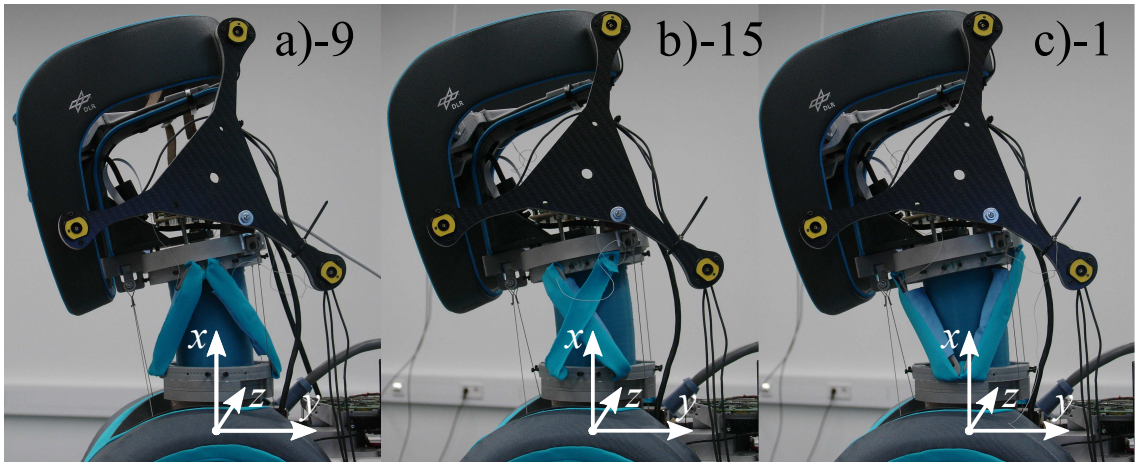

Figure 5.6.: Implemented sensor configurations on the robot DAVID which were suggested by the simulation study.

kinds of the measured quantities shall be discussed in the following to represent $\boldsymbol{J}^T_{\chi,q\mathcal{B}}\boldsymbol{f}_c$:

1. Tendon tension forces and a projection by the coupling matrix:

$$\boldsymbol{J}^T_{\chi,q\mathcal{B}}\boldsymbol{f}_c = \boldsymbol{P}(\boldsymbol{q})\boldsymbol{u}_t$$

2. The base force torque sensor, see equation (5.10) and a projection onto the generalized directions:

$$\boldsymbol{J}^T_{\chi,q\mathcal{B}}\boldsymbol{f}_c = \boldsymbol{J}^T_{\chi,q\mathcal{B}}\boldsymbol{w}^{\mathcal{H}}_{\mathrm{FTS}}$$

For $\boldsymbol{k}(\boldsymbol{q},\boldsymbol{0})$, three alternatives can be utilized, namely:

1. The FEM-model where $\boldsymbol{q}$ corresponds to the configuration (position and orientation) of the whole centerline (3.42).

2. The multivariate polynomial model (MVP) of Chapter 4 where $\boldsymbol{q}$ corresponds to pose of the head represented by
$(x,\, y,\, z,\, \theta_x,\, \theta_y,\, \theta_z)^T$

3. The nonlinear kinematic linear spring (NKLS) model of Chapter 4 where $\boldsymbol{q}$ corresponds to pose of the head represented by $(l,\, \phi,\, \eta,\, \zeta,\, \theta,\, \iota\,)^T$.

The listed possibilities are assessed based on the requirement listed in the introduction. A requirement for the state estimation algorithm is that it provides an estimate in real time and external collisions shall not affect the quality. However, an external collision adds an external wrench that acts on the mechanisms, deforming it. In this case, the prediction ability when using the tendon tension forces is not given any more. Therefore, in the context of the present thesis, the tension measurements of the tendons are not considered, which also yields that the estimation concept of the present section will rely on ${}_{\mathcal{B}}\boldsymbol{w}_{\mathrm{FTS}} \in \mathbb{R}^6$, the measured clamping forces and torques by the force torque sensor.
To enable a fast estimation, the FEM model in the current implementation is to slow, in contrast the RNM model despite of the used approach is proven computationally efficient, see Fig. 4.9, and thus will be applied.
In summary, the estimation of the state based on a static model is carried out using the

following equation, where the "restoring forces and torques" $\boldsymbol{f}(\boldsymbol{q})$ modeled by a MVP or NKLS model are related to attack at the origin of $\mathcal{B}$ using a correction term ${}_{\mathcal{B}}\Delta\boldsymbol{\tau}^{\mathcal{HB}} \in \mathbb{R}^6$,

$$\underbrace{{}_{\mathcal{B}}\boldsymbol{f}(\boldsymbol{q})}_{\text{using MVP or NKLS}} + \underbrace{\begin{pmatrix} \boldsymbol{0} \\ {}_{\mathcal{B}}\boldsymbol{r}_L \times \begin{pmatrix} {}_{\mathcal{B}}f_x \\ {}_{\mathcal{B}}f_y \\ {}_{\mathcal{B}}f_z \end{pmatrix} \end{pmatrix}}_{\text{correction of point of attack}={}_{\mathcal{B}}\Delta\boldsymbol{\tau}^{\mathcal{HB}}} + \boldsymbol{g}(\boldsymbol{q}) - \boldsymbol{J}_{\chi,q}^{T}\,{}_{\mathcal{B}}\boldsymbol{w}_{\text{FTS}} = \boldsymbol{0},$$

$${}_{\mathcal{B}}\boldsymbol{w}_{\text{FTS}} = \boldsymbol{J}_{\chi,q}^{-T}\left({}_{\mathcal{B}}\boldsymbol{f}(\boldsymbol{q}) + {}_{\mathcal{B}}\Delta\boldsymbol{\tau}^{\mathcal{HB}}(\boldsymbol{q}) + \boldsymbol{g}(\boldsymbol{q})\right) = {}_{\mathcal{B}}\tilde{\boldsymbol{f}}(\boldsymbol{q}). \tag{5.26}$$

The partial derivative of ${}_{\mathcal{B}}\tilde{\boldsymbol{f}}(\boldsymbol{q})$ in equation (5.26) with respect to $\boldsymbol{q}$ can be computed analytically (taking advantage of the MVP or NKLS model). As a result, equation (5.26) is locally linearized using a Taylor approximation of first order to solve for the desired pose $\boldsymbol{q}$,

$$\begin{aligned} {}_{\mathcal{B}}\boldsymbol{w}_{\text{FTS}} &\approx {}_{\mathcal{B}}\tilde{\boldsymbol{f}}(\boldsymbol{q}_0) + \left.\frac{\partial {}_{\mathcal{B}}\tilde{\boldsymbol{f}}(\boldsymbol{q})}{\partial \boldsymbol{q}}\right|_{\boldsymbol{q}_0} (\boldsymbol{q} - \boldsymbol{q}_0)\,, \\ &\approx {}_{\mathcal{B}}\tilde{\boldsymbol{f}}(\boldsymbol{q}_0) + \tilde{\boldsymbol{K}}(\boldsymbol{q}_0)\,(\boldsymbol{q} - \boldsymbol{q}_0)\,, \\ \rightarrow \boldsymbol{q} &\approx \boldsymbol{q}_0 + (\tilde{\boldsymbol{K}}(\boldsymbol{q}_0))^{-1}\left(\boldsymbol{w}_{\text{FTS}} - {}_{\mathcal{B}}\tilde{\boldsymbol{f}}(\boldsymbol{q}_0)\right). \end{aligned} \tag{5.27}$$

A major drawback of the approach is that $\tilde{\boldsymbol{K}}$ needs to be computed which involves 3$^{\text{rd}}$ tensorial quantities requiring a high implementation effort although they are analytically expressible. In the experiments, it needs to be evaluated if the locally derived inverse model is able to predict the real behavior, assessed in the experiments in Sec. 5.5. Similar to the geometric state estimation, equation (5.27) provides the pose $\boldsymbol{q}$ and the corresponding velocity will be derived by a numerical derivative.

Discussion & summary

In the previous section, a state estimation algorithm is suggested which estimates the pose based on a static equilibrium of measured reaction forces and torques and a model including the forces and torques due to the deformation and gravity. A local linearization of this equilibrium equation at an initial point $\boldsymbol{q}_0$ is proposed based on which the pose is computed. Similarly, the solution of the finite element method is computed. Here, the whole configuration of the beams centerline (position and orientation) is computed based on local linearization, however an iterative solution with a Netwon-Raphson algorithm is applied. Supposing a fast computation, the FEM model would also be suitable and could be applied in (5.27). However, as the force residuals and the stiffness matrix is computed and assembled element wise, higher computational times are expected. Furthermore, the identified material properties reported in Sec. 3.4.4 predict the pose not accurate enough which limits. In this case, a combination of the static state estimation and the geometric state estimation concept could be applied.

5.4. State estimation based on dynamic models

This section treats a dynamic state estimation concept. In contrast to the concepts discussed before which required a convergence in every time step in a real time implementation, a dynamic estimation converges over time. The concept discussed in the following is

inspired by a state estimation technique known from mobile systems, such as unmanned autonomous vehicles or legged systems. These concepts dominantly apply an Extended Kalman Filter (EKF) which fuses data of an IMU and kinematic information from cameras, i.e. two dimensional position information.
In this Section, sensor data of the length sensors and an IMU are fused in an EKF. The dynamic model of the EKF is inspired by the approaches of the mobile-robotics community, see e.g. [61, 60]. It is a simple dynamic model which numerically integrates the acceleration and angular velocity measurements of the IMU (5.13) to a pose. Due to the bias in the IMU readings, this numerical integration tends to drift, especially the double integration of the acceleration. To correct this drift, the bias of the acceleration (5.11) and the gyroscope (5.12), modeled as random walk process, are incorporated in an augmented state $\boldsymbol{\psi} \in \mathbb{R}^{15}$ which consists of

$$\boldsymbol{\psi} = \left(\boldsymbol{q}^T,\, {}_{\mathcal{B}}\boldsymbol{v}_L^T,\, {}_{\mathcal{S}}\boldsymbol{a}_b^T,\, {}_{\mathcal{S}}\boldsymbol{\omega}_b^T\right)^T. \tag{5.28}$$

As the angular velocity is measured by the IMU only the linear of the head velocity ${}_{\mathcal{B}}\boldsymbol{v}_L$ respecting $\mathcal{B}$ (3.14) is estimated. Within the EKF framework, discussed in Section 5.4.2, the state $\boldsymbol{\psi}_{t_i}$ is considered as discrete in time, $\boldsymbol{\psi}_{t_i} = \boldsymbol{\psi}(t = t_i)$. Furthermore, $\boldsymbol{\psi}_k$ is considered as a statistical quantity with mean value $\hat{\boldsymbol{\psi}}_{t_i} \in \mathbb{R}^{15}$ and Gaussian distribution

$$\boldsymbol{\psi}_{t_i} \sim \mathcal{N}(\hat{\boldsymbol{\psi}}_{t_i},\, \boldsymbol{\Psi}) \tag{5.29}$$

with the state covariance matrix $\boldsymbol{\Psi}_{t_i} \in \mathbb{R}^{15\times 15}$.

5.4.1. State space equations

The simple dynamic model corresponds to the relationship of the IMU readings presented in equation (5.13) which is integrated,

$$\begin{pmatrix} {}_{\mathcal{B}}\boldsymbol{r}_{L,t_i} \\ \boldsymbol{\theta}_{t_i} \\ {}_{\mathcal{B}}\boldsymbol{v}_{L,t_i} \\ {}_{\mathcal{S}}\boldsymbol{a}_{b,t_i} \\ {}_{\mathcal{S}}\boldsymbol{\omega}_{b,t_i} \end{pmatrix} = \begin{pmatrix} {}_{\mathcal{B}}\boldsymbol{r}_{L,t_i-1} \\ \boldsymbol{\theta}_{t_i-1} \\ {}_{\mathcal{B}}\boldsymbol{v}_{L,t_i-1} \\ {}_{\mathcal{S}}\boldsymbol{a}_{b,t_i-1} \\ {}_{\mathcal{S}}\boldsymbol{\omega}_{b,t_i-1} \end{pmatrix} + (t_i - t_{i-1}) \begin{pmatrix} {}_{\mathcal{B}}\boldsymbol{v}_{L,t_i-1} \\ \boldsymbol{J}_{\chi,\theta}^{-1}({}_{\mathcal{S}}\tilde{\boldsymbol{\omega}}_{t_i-1} - {}_{\mathcal{S}}\boldsymbol{\omega}_{b,t_i-1} - {}_{\mathcal{S}}\boldsymbol{\omega}_{n,t_i-1}) \\ \boldsymbol{A}_{\mathcal{BS}}({}_{\mathcal{S}}\tilde{\boldsymbol{a}}_{t_i-1} - {}_{\mathcal{S}}\boldsymbol{a}_{b,t_i-1} - {}_{\mathcal{S}}\boldsymbol{a}_{n,t_i-1}) - {}_{\mathcal{B}}\boldsymbol{a}_g \\ \boldsymbol{0} \\ \boldsymbol{0} \end{pmatrix}. \tag{5.30}$$

Please note that the slowly varying bias of the IMU is modeled quasi-static. Equation (5.30) is discrete state space dynamics and can be written in the general form

$$\boldsymbol{\psi}_{t_i} = \boldsymbol{\varsigma}(\boldsymbol{\psi}_{t_i-1},\, {}_{\mathcal{S}}\tilde{\boldsymbol{a}}_{t_i},\, {}_{\mathcal{S}}\tilde{\boldsymbol{\omega}}_{t_i},\, {}_{\mathcal{S}}\boldsymbol{a}_{n,t_i},\, {}_{\mathcal{S}}\boldsymbol{\omega}_{n,t_i}), \tag{5.31}$$

required by the EKF algorithm (see Section 5.4.2), with the input vector $({}_{\mathcal{S}}\tilde{\boldsymbol{a}}_{t_i}^T,\, {}_{\mathcal{S}}\tilde{\boldsymbol{\omega}}_{t_i}^T)^T \in \mathbb{R}^6$ at time instance $t = t_i$ and the mean free Gaussian process noise vector $({}_{\mathcal{S}}\boldsymbol{a}_{n,t_i}^T {}_{\mathcal{S}}\boldsymbol{\omega}_{n,t_i}^T)^T \in \mathbb{R}^6$ at time instance t_i,

$$\begin{pmatrix} {}_{\mathcal{S}}\boldsymbol{a}_{n,t_i} \\ {}_{\mathcal{S}}\boldsymbol{\omega}_{n,t_i} \end{pmatrix} \sim \mathcal{N}(\boldsymbol{0},\, \boldsymbol{S}). \tag{5.32}$$

Herein $\boldsymbol{S} \in \mathbb{R}^{6\times 6}$ is denoted process covariance matrix. Furthermore, the so-called measurement equation is required. As mentioned, the length sensor measurements (5.7) shall be used,

$$\boldsymbol{y}_{t_i} = \boldsymbol{l}(\boldsymbol{\psi}_{t_i}) + \boldsymbol{w}_k \overset{(5.7)}{=} \boldsymbol{l}(\boldsymbol{q}_{t_i}) + \Delta\boldsymbol{l}_{n,t_i}, \tag{5.33}$$

with the mean free Gaussian measurement noise $\boldsymbol{w}_{t_i} \in \mathbb{R}^{z+r}$

$$\boldsymbol{w}_{t_i} = \Delta \boldsymbol{l}_{n,t_i} \sim \mathcal{N}(\boldsymbol{0}, \boldsymbol{Q}), \tag{5.34}$$

and the measurement covariance matrix $\boldsymbol{Q} \in \mathbb{R}^{z+r \times z+r}$.

5.4.2. Extended Kalman Filter (EKF)

The following paragraph briefly summarizes the relevant equation of an EKF which are necessary for the implementation. A broader introduction to the topic including the full derivation of the equations below can be found in Thrun *et. al* [124].
For simplicity, the input vector $\boldsymbol{u}_{t_i} = ({}_{\mathcal{S}}\tilde{\boldsymbol{a}}_{t_i}^T, {}_{\mathcal{S}}\tilde{\boldsymbol{\omega}}_{t_i}^T)^T$ and the process noise vector $\boldsymbol{s}_{t_i} = ({}_{\mathcal{S}}\boldsymbol{a}_{n,t_i}^T {}_{\mathcal{S}}\boldsymbol{\omega}_{n,t_i}^T)^T$ are defined for the following developments. The EKF algorithm consists of two phases, the prediction phase and the update phase. In the prediction phase, the *a priori estimation* of the state and its covariance, denoted $\boldsymbol{\psi}_{t_i,t_i-1} \in \mathbb{R}^{15}$ and $\boldsymbol{\Psi}_{t_i,t_i-1} \in \mathbb{R}^{15\times 15}$, are computed based on the nonlinear state dynamics (5.31),

$$\begin{aligned} \boldsymbol{\psi}_{t_i,t_i-1} &= \boldsymbol{\varsigma}(\boldsymbol{\psi}_{t_i-1}, \boldsymbol{u}_{t_i}, \boldsymbol{s}_{t_i}), \\ \boldsymbol{\Psi}_{t_i,t_i-1} &= \boldsymbol{\Sigma}\boldsymbol{\Psi}_{t_i-1,t_i-1}\boldsymbol{\Sigma}^T + \boldsymbol{L}\boldsymbol{S}\boldsymbol{L}^T, \end{aligned} \tag{5.35}$$

where the matrices $\boldsymbol{\Sigma} \in \mathbb{R}^{15\times 15}$ and $\boldsymbol{L} \in \mathbb{R}^{15\times 12}$ represent the following partial derivatives of the state space model,

$$\boldsymbol{\Sigma} = \left.\frac{\partial \boldsymbol{\varsigma}}{\partial \boldsymbol{\psi}}\right|_{\boldsymbol{\psi}_{t_i-1,t_i-1}, \boldsymbol{u}_{t_i}}, \quad \boldsymbol{L} = \left.\frac{\partial \boldsymbol{\varsigma}}{\partial \boldsymbol{s}}\right|_{\boldsymbol{\psi}_{t_i-1,t_i-1}, \boldsymbol{u}_{t_i}}. \tag{5.36}$$

The update phase afterward is then applied to compute *a postiori* state estimate and covariance matrix, denoted as $\boldsymbol{\psi}_{t_i,t_i} \in \mathbb{R}^{15}$ and $\boldsymbol{\Psi}_{t_i,t_i} \in \mathbb{R}^{15\times 15}$,

$$\begin{aligned} \boldsymbol{\psi}_{t_i,t_i} &= \boldsymbol{\psi}_{t_i,t_i-1} + \boldsymbol{K}_{t_i}(\tilde{\boldsymbol{l}}_{t_i} - \boldsymbol{y}_{t_i}) \\ \boldsymbol{\Psi}_{t_i,t_i} &= \boldsymbol{\Psi}_{t_i,t_i-1} - \boldsymbol{K}_{t_i}\boldsymbol{C}\boldsymbol{\Psi}_{t_i,t_i-1} \end{aligned} \tag{5.37}$$

with the length measurements $\tilde{\boldsymbol{l}}_{t_i}$ of equation (5.1) and the Kalman Gain $\boldsymbol{K}_{t_i} \in \mathbb{R}^{15\times z+r}$ and the difference between the measurement model (5.33) and the sensor data (5.6). The Kalman Gain is computed by using the a priori estimate of $\boldsymbol{\Psi}_{t_i,t_i-1}$ and the partial derivative of the measurement equation with respect to $\boldsymbol{\psi}$, $\boldsymbol{C} \in \mathbb{R}^{z+r\times 15}$ and the noise $\boldsymbol{w}$, $\boldsymbol{V} \in \mathbb{R}^{z+r\times z+r}$

$$\begin{aligned} \boldsymbol{C} &= \left.\frac{\partial \boldsymbol{l}(\boldsymbol{q})}{\partial \boldsymbol{\psi}}\right|_{\boldsymbol{\psi}_{t_i,t_i-1}, \boldsymbol{u}_{t_i}} \overset{\text{with equation(5.14)}}{=} \left(\boldsymbol{P}^T(\boldsymbol{q}), \boldsymbol{0}_{3\times 3}, \boldsymbol{0}_{3\times 3}, \boldsymbol{0}_{3\times 3}\right), \\ \boldsymbol{V} &= \left.\frac{\partial \boldsymbol{g}}{\partial \boldsymbol{w}}\right|_{\boldsymbol{\psi}_{t_i,t_i-1}, \boldsymbol{u}_{t_i}} = \text{Identity matrix} \end{aligned} \tag{5.38}$$

With above quantities, the Kalman gain is computed to

$$\begin{aligned} \boldsymbol{K}_{t_i} &= \boldsymbol{\Psi}_{t_i,t_i-1}\boldsymbol{C}^T(\boldsymbol{C}\boldsymbol{\Psi}_{t_i,t_i-1}\boldsymbol{C}^T + \boldsymbol{V}\boldsymbol{Q}\boldsymbol{V}^T), \\ &= \boldsymbol{\Psi}_{t_i,t_i-1}\boldsymbol{C}^T(\boldsymbol{C}\boldsymbol{\Psi}_{t_i,t_i-1}\boldsymbol{C}^T + \boldsymbol{Q}). \end{aligned} \tag{5.39}$$

To begin the state estimation, an initial state $\boldsymbol{\psi}_{0,0} \in \mathbb{R}^{15}$ and initial state covariance $\boldsymbol{\Psi}_{0,0} \in \mathbb{R}^{15\times 15}$ need to be provided to the algorithm. The choice of the initial state covariance $\boldsymbol{\Psi}_{0,0}$ is crucial since it determines how well the algorithm shall "trust" $\boldsymbol{\psi}_{0,0}$. For example, if a large covariance is supplied initially, the EKF will take some time to converge to the true state based on the measurements while simultaneously decrease the covariance $\boldsymbol{\Psi}_{k,k}$.

Extension: State estimation based on ECM dynamics

A second approach based on a dynamic model can be derived from equation (5.10), i.e. the equation of motion of the elastic continuum mechanism which are driven by the applied wrench that is measured and projected wrench of the force torque sensor ${}_{\mathcal{B}}\boldsymbol{w}_{FTS}^{\mathcal{H}} \in \mathbb{R}^6$. These equation, and the measurement equation (5.7) the provide the tendon length, can be applied in a nonlinear observer structure e.g. a nonlinear *Luenberger Observer*. The fundamental idea of a Luenberger observer to force the dynamic model (5.10 to track the measured output $\tilde{\boldsymbol{l}}$ (5.6) of the real system by performing output tracking control based on an additional (virtual) control input, see e.g. [125]. If the control converges, the nonlinear observer provides and estimate of the state $(\bar{\boldsymbol{q}}^T, \dot{\bar{\boldsymbol{q}}}^T)$ and the closed loop system is described by,

$$\boldsymbol{M}(\bar{\boldsymbol{q}})\ddot{\bar{\boldsymbol{q}}} + \boldsymbol{k}(\bar{\boldsymbol{q}}, \dot{\bar{\boldsymbol{q}}}) = {}_{\mathcal{B}}\boldsymbol{w}_{FTS}^{\mathcal{H}} + \boldsymbol{K}_{luen}(\bar{\boldsymbol{q}})(\tilde{\boldsymbol{l}} - \boldsymbol{l}(\bar{\boldsymbol{q}})). \tag{5.40}$$

Different approaches are suggested for the design of the nonlinear observer gain matrix $\boldsymbol{K}_{luen}(\boldsymbol{q}) \in \mathbb{R}^{z+r \times z+r}$ depending on the number of measurements and the approach [125].

5.4.3. Summary

In summary, this section discussed a dynamic state estimation concept based on an Extended Kalman Filter (EKF) based on a simple dynamic model. In the experimental comparison, it is evaluated if the additional information, necessary for this approach, will add accuracy in the estimated state. In addition, a possible extension is provided which includes the equation of motion (4.3) in the estimation process. This concept however will not be compared in experiments.

5.5. Experimental comparison

As the potential concepts shall be used in real-time control, they will be tested on the real hardware and evaluated based on the requirements defined in the introduction. The spatial test bed is shown in Fig. 5.7. The data of the IMU and the length sensors are acquired by a micro controller board at 300 Hz and sent via Ethernet to a Linux real-time (rt-) host by a custom protocol. The same protocol is used for the FTS data which provides its data with 1 kHz (data-rates up to 7 kHz are possible). The data of the $r = 4$ tendon actuators is acquired at 3 kHz and sent via the SpaceWire® protocol to the rt-host. The sensor data is provided to real-time executable models of the geometric, static and dynamic state estimations by a custom middleware, whereas the executable are build using the Real-Time-Workshop of MATLAB/Simulink. Foremost, accuracy of the estimated pose is required which will be evaluated with the K-series optical measurement system [126] that serves as ground truth. The inertial fixed camera system with three lenses localizes the position of active LEDs with an accuracy of 37 μm in its workspace. A marker target consists of three LEDs. One target is attached to the upper platform, see Fig. 5.7 and one target is attached to the base. The mass properties of the moving target is known and accounted for in the computation of the vector of gravitational forces. The measurements of each target are transformed to a full pose (position & orientation). After calibration and referencing using a registration tool, the pose of both targets can be related to the motion of the head frame $\mathcal{H}$ expressed in $\mathcal{B}$. The neck system is moved by commanding desired tendon tension forces for each of the $r = 4$ tendon actuators and a local tendon tension force controller for each actuator is implemented. This controller will be described in

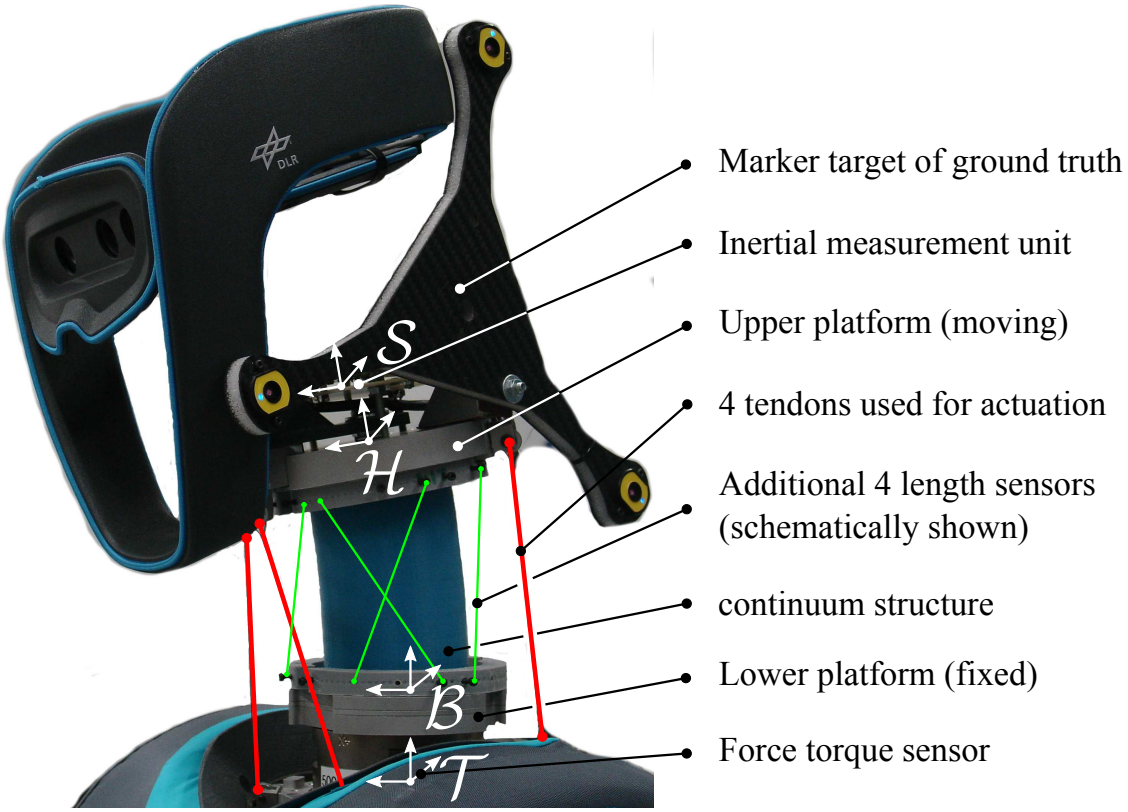

Figure 5.7.: Experimental setup used for the state estimation experiments.

Chapter 6.2. The accuracy and reliability of the implemented state estimation is evaluated in three experiments, reaching several static poses, moving along actuated trajectories and motions of the system induced by external disturbances. Before the discussion of the experimental results, the sensor accuracy is evaluated and the initialization process is explained.

5.5.1. Sensor accuracy and initialization

Length sensor measurements

The accuracy of the length sensor model is assessed experimentally. Therefore the pose dependent error vector $\boldsymbol{e}_l(\boldsymbol{q}) \in \mathbb{R}^8$ (5.15) is computed at 200 static poses based on the length sensor information (5.6) and the corresponding model $\boldsymbol{l}(\boldsymbol{q})$ (5.7). To compute $\boldsymbol{e}(\boldsymbol{q})$, the pose $\boldsymbol{q}$ measured by the ground truth is utilized. The left column of Fig. 5.8 shows the component wise absolute error for each sensor reading which states a maximum error of 2 mm for the tendons and 3 mm for the additional sensors. The origins of these errors are inaccuracies in the geometric data of the tendon routing of the length sensors, unmodeled elasticities and friction. Based on the experimental characterization of the length measurements with almost Gaussian distribution, the covariance $\boldsymbol{Q} \in \mathbb{R}^{8\times8}$ (5.34) in the EKF is chosen as diagonal matrix with a maximum squared error of $(2\text{ mm})^2$,

$$\boldsymbol{Q} = (2\text{ mm})^2 \boldsymbol{I}_{z+r}. \tag{5.41}$$

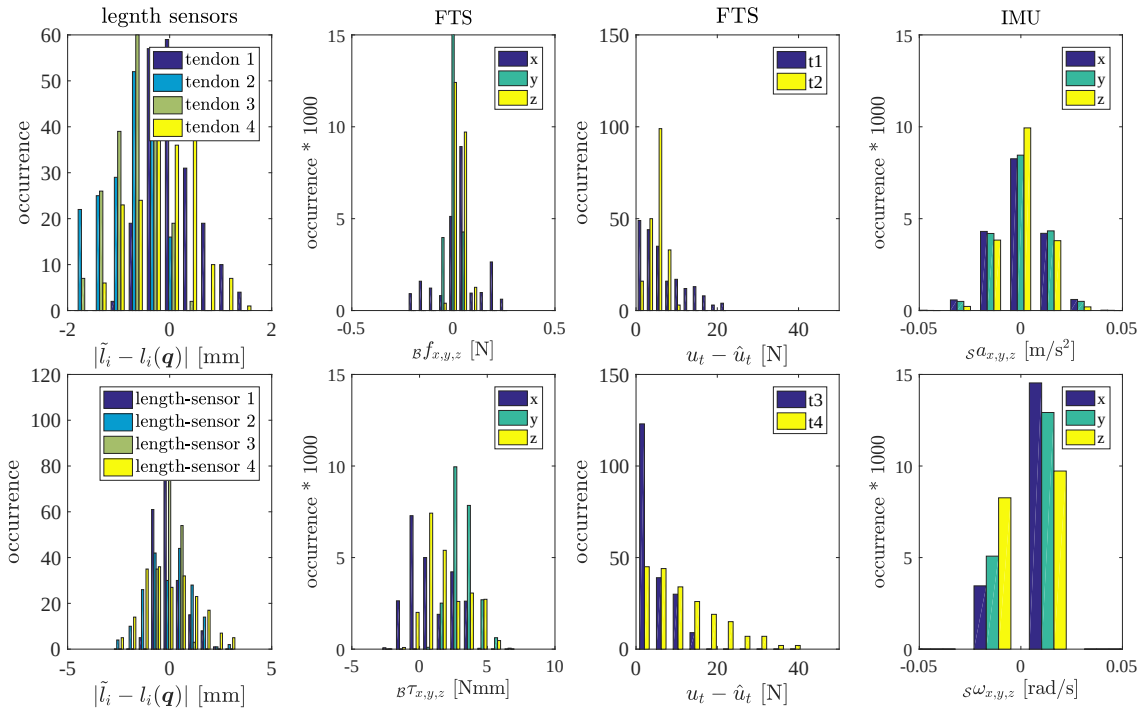

Figure 5.8.: Sensor information used for state estimation. First column: Pose dependent error $\boldsymbol{e}(\boldsymbol{q})$ of the length sensors recorded at 200 test poses in the workspace. Second column: Sensor readings of the FTS at rest to visualize the bias ${}_{\mathcal{B}}\boldsymbol{w}_{\text{FTS,b}}$ and noise ${}_{\mathcal{B}}\boldsymbol{w}_{\text{FTS,n}}$ component. Third column: Error between the tendon tension force readings and the projected FTS readings. Fourth column: Sensor readings of the IMU at rest with removed bias ${}_{\mathcal{S}}\boldsymbol{a}_b$, ${}_{\mathcal{S}}\boldsymbol{\omega}_b$ to state assess noise ${}_{\mathcal{S}}\boldsymbol{a}_n$, ${}_{\mathcal{S}}\boldsymbol{\omega}_n$ component.

Force torque sensor measurements

The sensor readings of the FTS are assessed at rest to identify the inherent bias and the sensor-noise. The second column of Fig. 5.8 show these measurements at rest which state a maximal noise of 0.2 N/0.002 Nm whereas determined offsets in the readings, i.e. the mean values, are stored to correct the data on line. In a second step, the calibration gains delivered by the manufacturer need to be checked which is assessed by statically loading the sensor with known masses at known distances which create known forces and torques. After adjusting the gains, the FTS data is compared with the measured tendon tensions by projecting the FTS-readings into the tendon space using the inverse of the coupling matrix and the corresponding error of 200 poses in the workspace is reported in Fig. 5.8. According to the shown histograms of the absolute error, the tendon measurements incorporate larger errors (up to 40 N), especially the tendon tension of tendon 4. A possible reason for this high error is the calibration of the tendon tension sensors which is error-prone.

IMU measurements

To assess the IMU data, recordings of a resting IMU are presented which are also used to identify the process covariance $\boldsymbol{S}$. The data is shown in Fig. 5.8, with removed sensor biases. By looking at the sensor noise a Gaussian distribution is present and the maximum noise values are used for the process covariance,

$$\boldsymbol{S} = \begin{pmatrix} (0.05\ m/s^2)^2 \boldsymbol{I}_3 & \boldsymbol{0} \\ \boldsymbol{0} & (0.02\ rad/s)^2 \boldsymbol{I}^{3\times 3} \end{pmatrix}, \tag{5.42}$$

with the identity matrices $\boldsymbol{I}_3 \in \mathbb{R}^{3\times 3}$, $\boldsymbol{I}_{z+r} \in \mathbb{R}^{z+r\times z+r}$ and the null matrix $\boldsymbol{0} \in \mathbb{R}^{3\times 3}$.

Optimization algorithm

Several optimization algorithms are introduced in paragraph 5.2.1, with given advantages and disadvantages, which shall minimize the objective function (5.15) in the geometric estimation approach. To test and compare the algorithms with each other, an offline evaluation is performed based on measurements of the real system. In this evaluation, four methods minimize the objective function $||\boldsymbol{e}_l(\boldsymbol{q})||_2^2$ (5.15) including the $r = 4$ tendons and $z = 4$ additional length sensors. Fig. 5.9 shows the results in two plots which illustrate the number of step sizes necessary to minimize $||\boldsymbol{e}_l(\boldsymbol{q})||_2^2$ below a threshold of 0.002 [-]. It can be clearly seen that the DL-algorithm outperforms the others as this algorithm manages to converge at every data sample and needs four iteration steps at maximum (only at one sample). The CG method does not converge at most samples whereas the SD and the QN method do converge (with some outliers) however the amount of steps necessary for the convergence is considerably higher compared to the DL-algorithm. In summary, the DL-algorithm is used for the real-time implementation.

Initialization of state and covariance

The proposed state estimation concepts do need an initial guess of the pose and corresponding velocity. As all the experiments start in a resting configuration, the velocity is initialized correspondingly, $\dot{\boldsymbol{q}}_0 = \boldsymbol{0}$. The pose $\boldsymbol{q}_0$ is initialized based on the ground truth in the experiments to generate a comparable initial configuration for every algorithm. Physically, $\boldsymbol{q}_0$ corresponds to the pose where the ECM is at rest and a pretension of 10 N is acting in each tendon. Using $\boldsymbol{q}_0$, further quantities necessary for initial step are computed,

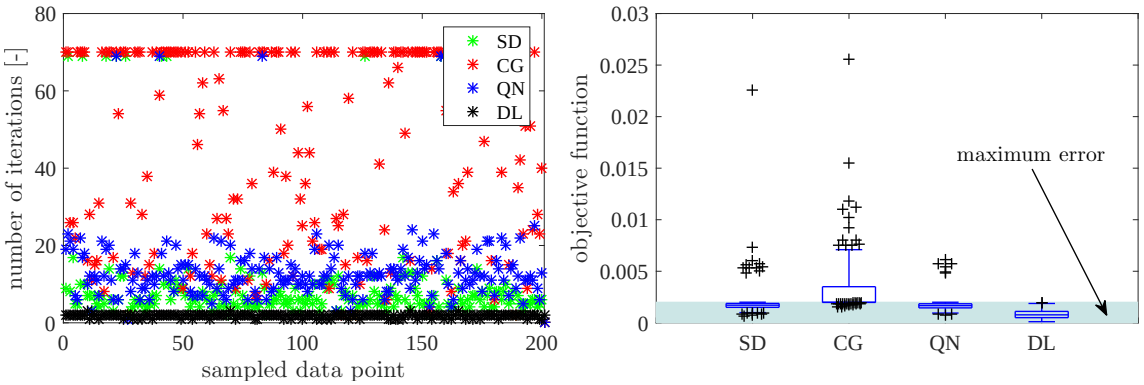

Figure 5.9.: Evaluation of the introduced optimization algorithm, Steepest Descent (SD), Conjugate Gradient (CG), Quasi Newton (QN) and Powell's Dog Leg (DL). Left plot: Number of iteration necessary for the four algorithms to converge, i.e. minimize the objective function to be smaller the 0.002 [-]. The number of iterations is truncated at 70 to save time. Right plot: Boxplot of the objective function after the minimization. If the error is within the blue area, the corresponding algorithm has converged as the objective function is below the defined threshold of 0.002.

i.e. the initial tendon length $\boldsymbol{l}_0$, the initial state of the EKF $\boldsymbol{\psi}_0$ including the initial bias for the acceleration and gyroscope. As a result, the initial confidence in the state is high which results in a small state covariance and $\boldsymbol{\Psi}_{0,0}$ is initialized with block diagonal shape and the sub matrices for the pose $\boldsymbol{\Psi}^q_{0,0} \in \mathbb{R}^{6\times6}$, the linear velocity $\boldsymbol{\Psi}^v_{0,0} \in \mathbb{R}^{3\times3}$ and IMU bias $\boldsymbol{\Psi}^{a,\omega}_{0,0} \in \mathbb{R}^{6\times6}$ are initialized,

$$\boldsymbol{\Psi}^q_{0,0} = \text{diag}\left(1^2\text{mm}^2,\, 1^2\text{mm}^2,\, 1^2\text{mm}^2,\, 2^2\text{deg}^2,\, 2^2\text{deg}^2,\, 2^2\text{deg}^2\right) \tag{5.43}$$

$$\boldsymbol{\Psi}^v_{0,0} = \text{diag}\left(1^2\text{mm/s}^2,\, 1^2\text{mm/s}^2,\, 1^2\text{mm/s}^2\right) \tag{5.44}$$

$$\boldsymbol{\Psi}^{a,\omega}_{0,0} = \text{diag}\left(1^2(\text{mm/s}^2)^2,\, 1^2(\text{mm/s}^2)^2,\, 1^2(\text{mm/s}^2)^2,\, 1^2\text{deg/s}^2,\, 1^2\text{deg/s}^2,\, 1^2\text{deg/s}^2\right) \tag{5.45}$$

5.5.2. Reaching static poses

In this experiment, the system is driven to 200 static poses in the workspace by commanding corresponding tendon tension forces[6]. The poses are chosen in order to cover the reachable workspace of the ECM uniformly. Therefore, the 200 are chosen according to the model-free design technique, discussed in Section 4.2.3, that maximizes the minimum distance in between the poses. In the experimental process, the pose is estimated by each concept online whereas data of the estimation and the camera are recorded at each static pose. As the static accuracy is of interest in this section, the velocity part of the state is not reported. The pose estimation accuracy is reported by the RMSE of $|\boldsymbol{q} - \hat{\boldsymbol{q}}|$, given in Tab. 5.2 and the absolute prediction error $|\boldsymbol{q} - \hat{\boldsymbol{q}}|$, given by boxplots in Fig. 5.10.

At first, the different alternatives of the sensor placement strategy are discussed, indicated by a)-9, b)-15 and c)-1. The presented sensor placement strategy in Section 5.2.3 suggested three sensor configurations, depicted in Fig. 5.6 which have been experimentally

[6]Please note that different combinations of the tendon tension forces are used for experimental evaluation.

Table 5.2.: RMSE of the estimated pose using the proposed algorithms.

	RMSE [mm]			RMSE [deg]		
algorithm	x	y	z	θ_x	θ_y	θ_z
$\boldsymbol{q}$ a)-9	0.64	0.97	2.07	1.10	0.72	1.37
$\boldsymbol{q}$ b)-15	0.83	1.62	4.23	2.68	0.77	1.59
$\boldsymbol{q}$ c)-1	0.10	3.34	0.66	1.24	1.19	1.39
$\boldsymbol{q}_{\text{red}}$	0.48	0.68	0.74	1.98	1.39	1.60
$\boldsymbol{q}$ stat	3.76	3.54	4.30	5.96	5.60	2.00
$\boldsymbol{q}$ EKF	0.80	1.65	2.10	1.14	0.73	1.44

tested regarding their estimation accuracy. Configuration a)-9 and c)-1 are proposed to deliver good estimates and b)-15 should perform worse according to the defined criteria. It can be observed that the sensor configuration b)-15, which was chosen as a counter example, indeed predicts the pose less accurate especially in the z and in the θ_x direction. Sensor configuration a)-9 and c)-1 possess similar accuracy for the prediction of θ_x (as predicted by the column norms in Section 5.2.3) whereas the prediction of z is less accurate for a)-9. In contrast, the estimation of z is more accurate for c)-1 compared to all other configuration. At first glance, these results are not well incorporated in simulation study. However, the motion of the elastic continuum mechanism is strongly coupled along the y, θ_z and z, θ_y direction, i.e. a bending motion involves a rotation and a translation. Configuration a)-9 provided a low norm in θ_y whereas configuration c)-1 provided a low norm in θ_z. Due to the motion coupling, these low norms along the rotations yield that coupled translations are also estimated worst. As a result of the sensor placement, an adequate sensor placement can improve the estimation quality tremendously, i.e. by using sensors in configuration a)-9 (or c)-1), the estimation accuracy can be improved by 62% (61%) along θ_x or 50% (80%) along z in comparison to sensor configuration b)-15, which is assessed as a bad configuration. Configuration a)-9 seems the most promising and was therefore used for the EKF.

In a second assessment, the different state estimation algorithms are compared which are, the geometric approach based on a reduced kinematic "q_{red}", and the estimation of the full pose $\boldsymbol{q}$ based on the geometric approach "a)-9", the static approach "stat" and the "EKF" is discussed. The geometric approach based on the reduced kinematic model is able to provide the most accurate estimates for the translations which can be seen in the top row of the boxplot Fig. 5.10 and in the RSME table 5.2. The reduced kinematic model uses cylindrical coordinates to describe the position which is additionally coupled by k_y, k_z to the orientation which appears a good choice. For the orientations, the six-DoF geometric model and the EKF with configuration a)-9 provide the highest accuracy. The static estimation concept is not accurate at all in the current implementation. Possible reasons are that the inversion of the augmented stiffness matrix $\tilde{\boldsymbol{K}}$ (5.27) including the multivariate polynomial model is strongly nonlinear and the local linearization is not suitable.

In summary, the prediction error for the geometric approach using the reduced model $\boldsymbol{q}_{\text{red}}$, the Six-DoF model with configuration $\boldsymbol{q}$ a)-9 and the dynamic approach, including the full pose and a)-9 $\boldsymbol{q}$ EKF are comparable. It is noticeable, that the reduced model $\boldsymbol{q}_{\text{red}}$ predict the translations better than the models with the full pose. In contrast, these models predict the rotational part of the pose more accurately compared with $\boldsymbol{q}_{\text{red}}$. The

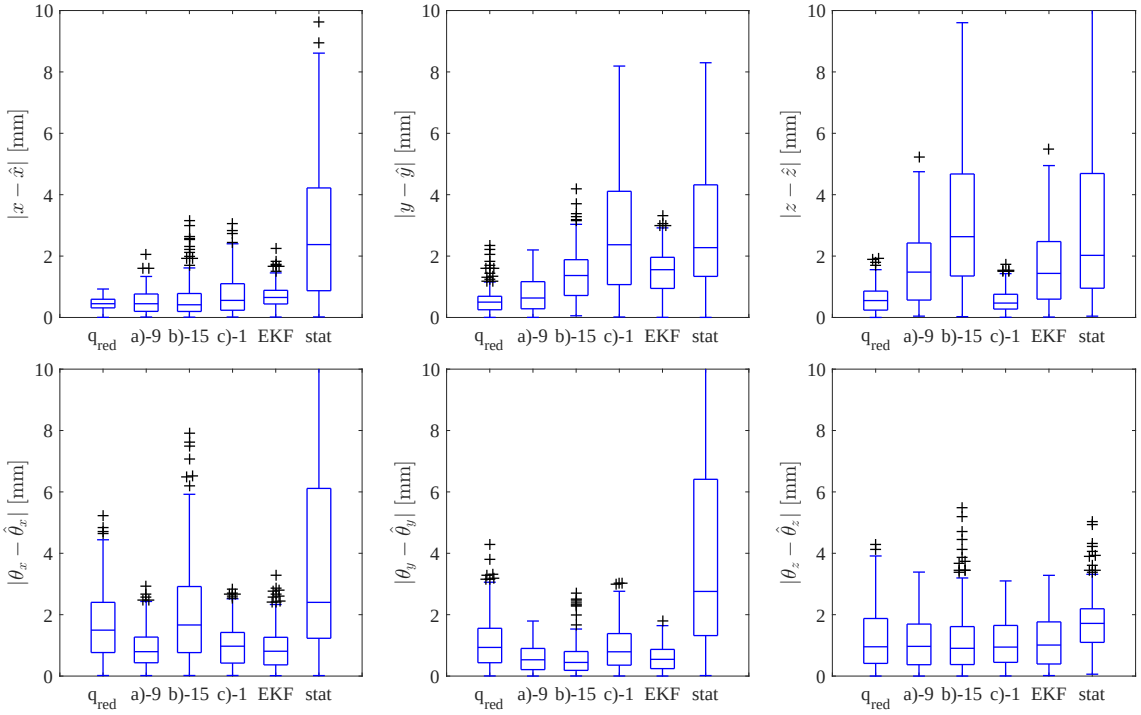

Figure 5.10.: Box plot for the online absolute pose estimation error $|q_i - \hat{q}_i|$ using the introduced state estimation concepts. The geometric concepts are indicated by q_{red}, using reduced kinematic model or different sensor configurations, here a)-9, b)-15 and c)-1, to estimate the full pose. The static and dynamic concept are indicated by "stat" and "EKF" respectively.

prediction accuracy of a nonlinear-optimization using DL-algorithm (for estimation $\boldsymbol{q}$ a)-9) is comparable with the EKF with a slight favor towards the nonlinear optimization due to smaller errors for the prediction along y.

5.5.3. Actuated dynamic motion

The first dynamic evaluation is based on dynamic motions where the head is actuated to perform a typical motion which consist of "look down to the right hand", "look down" followed by "look down to the left hand", see Fig. 5.11. The corresponding estimation performance for the pose is shown in Fig. 5.15.

It can be observed, that the absolute estimation error of the geometric and dynamic state estimation algorithms are comparable and are below 3 mm and 3 deg whereas the static estimation yields high errors, similar to the pose reaching experiment. A further similarity is that the estimation error is bigger for z and θ_x. Interestingly, the EKF estimates θ_x better than the NLS optimization although the same measurement equations are necessary. The IMU contributes by integrating the gyroscope signals which explains this improvement. Furthermore, it can be assessed that the NLS ("DL-a)") loses accuracy at some points, which is visible by higher spikes in the red curve, e.g. in the x plot which raise the assumption, that a velocity based on a numerical differentiation will be affected.

Fig. 5.16 shows the linear part of the estimated velocity for the algorithms. The static state estimation concept predicts the pose inaccurate, thus the velocity investigation is left out. For comparison, the velocity of the ground-truth is plotted as well which is generated

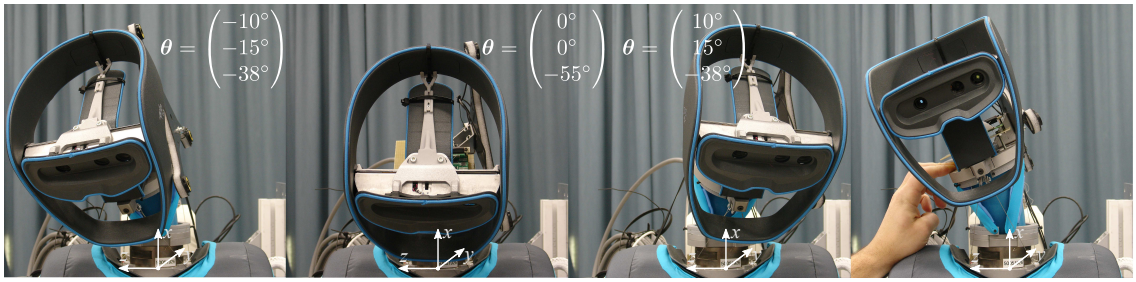

Figure 5.11.: Typical motion of the head "look down to the right hand", "look down" followed by "look down to the left hand" and corresponding head angles. Most right picture: Manual interaction with the neck to test the pose estimation for externally applied forces.

based on a numerical differentiation. The following observations can be drawn. In general, the quality of the estimated velocities is comparable throughout the algorithm. However, the bigger steps of the DL-algorithm observed in the pose indeed result in higher noise in the velocity. As suspected, the bigger jumps of the DL algorithm in the pose estimate yield high spikes in the velocity (which are also present in the rotational velocity). Theoretically, a numerical derivative is not possible at these jumps. Practically, the high spikes are not desired as they need to be absorbed within software. The EKF based velocity estimation provides less noise resulting and smoother velocity estimates. A small lag in the velocity estimation is detectable for the EKF, e.g. in ${}_{\mathcal{B}}v_{L,y}$ (middle column). As the motion starts, the estimated velocity lags behind the ground truth. As fast motions are actuated, this problem might be handled with an IMU that provides higher sampling rates (> 300 Hz).

The estimation results during dynamic motion, see Fig. 5.15, states (small) asymmetrical estimation errors which is e.g. perceivable in the top row for y and z. A possible reason of this asymmetry is the varying accuracy reported for the length measurements, Fig. 5.8. The distributions state that the four tendons and the four sensors provide different errors w.r.t. to their model which might result from unmodeled effects such as elasticity, friction, a varying sensor resolution or linearity issues. Similar to the pose reaching, the concept based on the static model is the most inaccurate and will not be assessed in the last experiment. For the estimation using the reduced kinematic model, it can be observed that the estimation error is higher in y as observed in the pose reaching experiment.

5.5.4. Manual interaction

A requirement of state estimation is to provide reliable estimates in the case of externally applied disturbances. To assess this condition, the neck is manually moved around, see Fig. 5.11. By commanding a constant tendon tension force to the actuators, it is possible to move the system by hand and drive it to feasible poses. The incorporation of the length measurements assume always fully tensioned tendons, i.e. straight lines between the connection in the bottom and the moving platform. Therefore, this experiment assess, if this assumption is violated during a manual interaction or disturbance.

The corresponding absolute estimation error $\boldsymbol{q} - \hat{\boldsymbol{q}}$ is shown in Fig. 5.17 for the dynamic state estimation concept only. As the geometric state estimation concept based on the full pose "DL a)-9" yielded a similar performance, it is not shown in Fig. 5.17. It can be stated that the performance of the estimation is not affected by an external force as the estimation accuracy is comparable with the other two experiments.

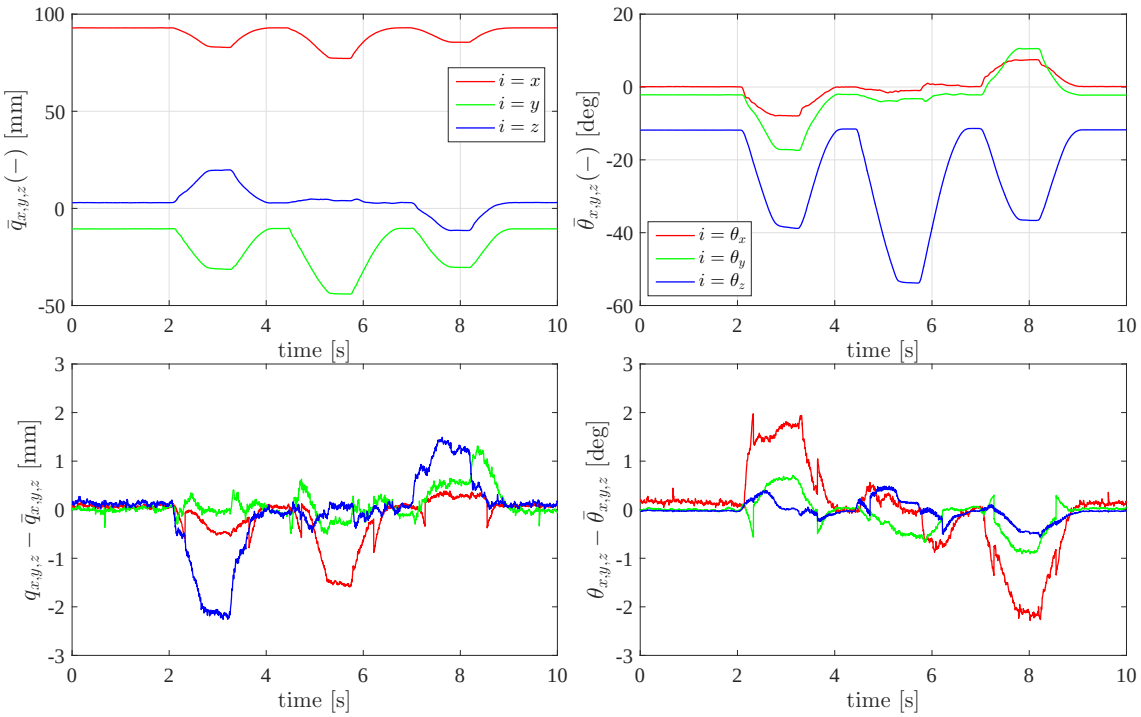

Figure 5.12.: Estimation of the pose during actuated dynamic motions. Top row: Measured (-) components of the pose $\boldsymbol{q}$ using the ground truth. Rows below: Corresponding component wise estimation error $\boldsymbol{q} - \bar{\boldsymbol{q}}$ using the DL algorithm in sensor configuration a)-9.

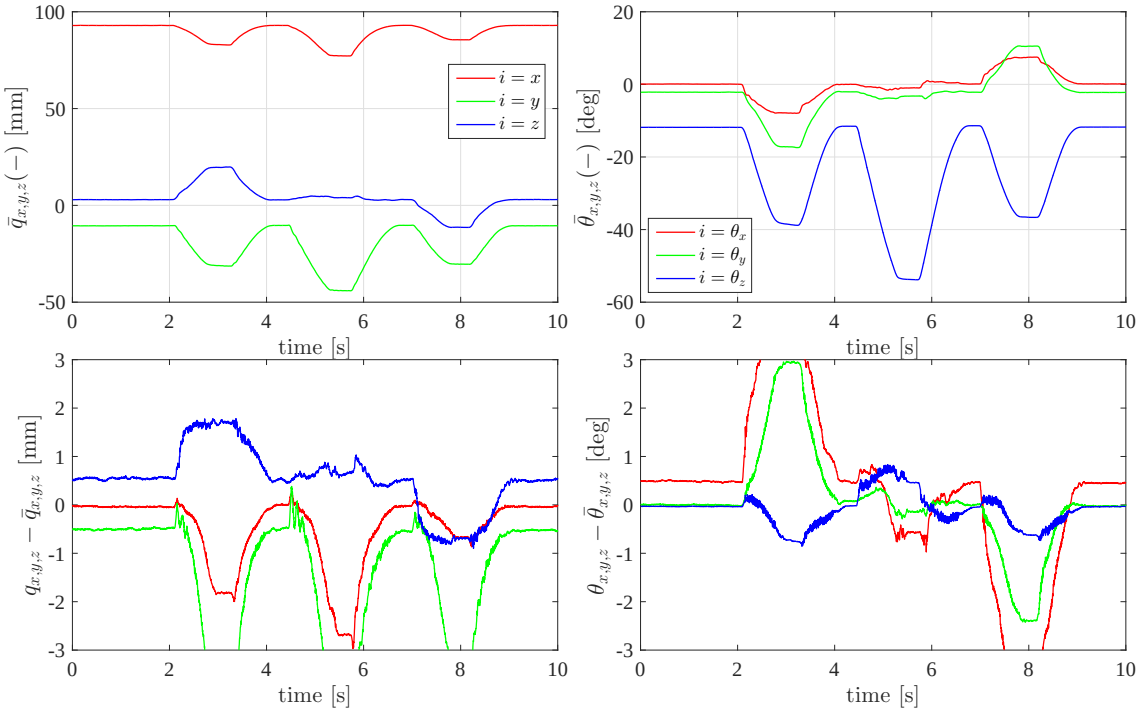

Figure 5.13.: Estimation of the pose during actuated dynamic motions. Top row: Measured (-) components of the pose $\boldsymbol{q}$ using the ground truth. Rows below: Corresponding component wise estimation error $\boldsymbol{q} - \bar{\boldsymbol{q}}$ using the DL algorithm and the reduced kinematic model $\boldsymbol{q}_{\text{red}}$.

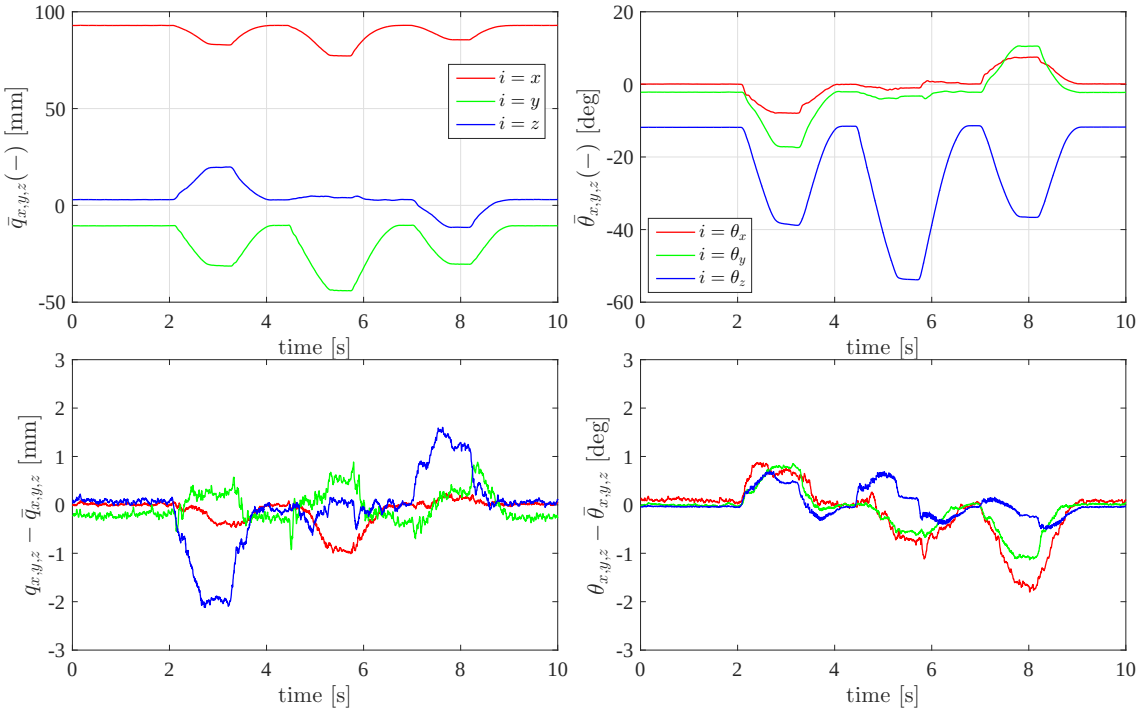

Figure 5.14.: Estimation of the pose during actuated dynamic motions. Top row: Measured (-) components of the pose $\boldsymbol{q}$ using the ground truth. Rows below: Corresponding component wise estimation error $\boldsymbol{q} - \bar{\boldsymbol{q}}$ using the EKF algorithm in sensor configuration a)-9.

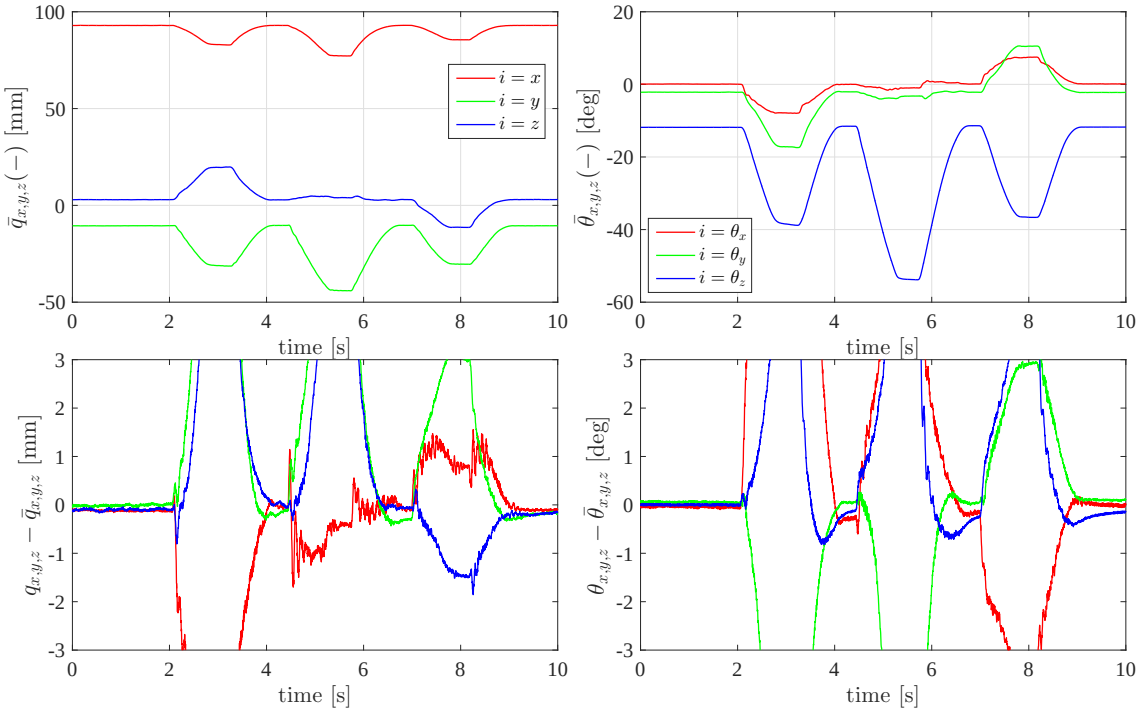

Figure 5.15.: Estimation of the pose during actuated dynamic motions. Top row: Measured (-) components of the pose $\boldsymbol{q}$ using the ground truth. Rows below: Corresponding component wise estimation error $\boldsymbol{q} - \bar{\boldsymbol{q}}$ using the static state estimation concept.

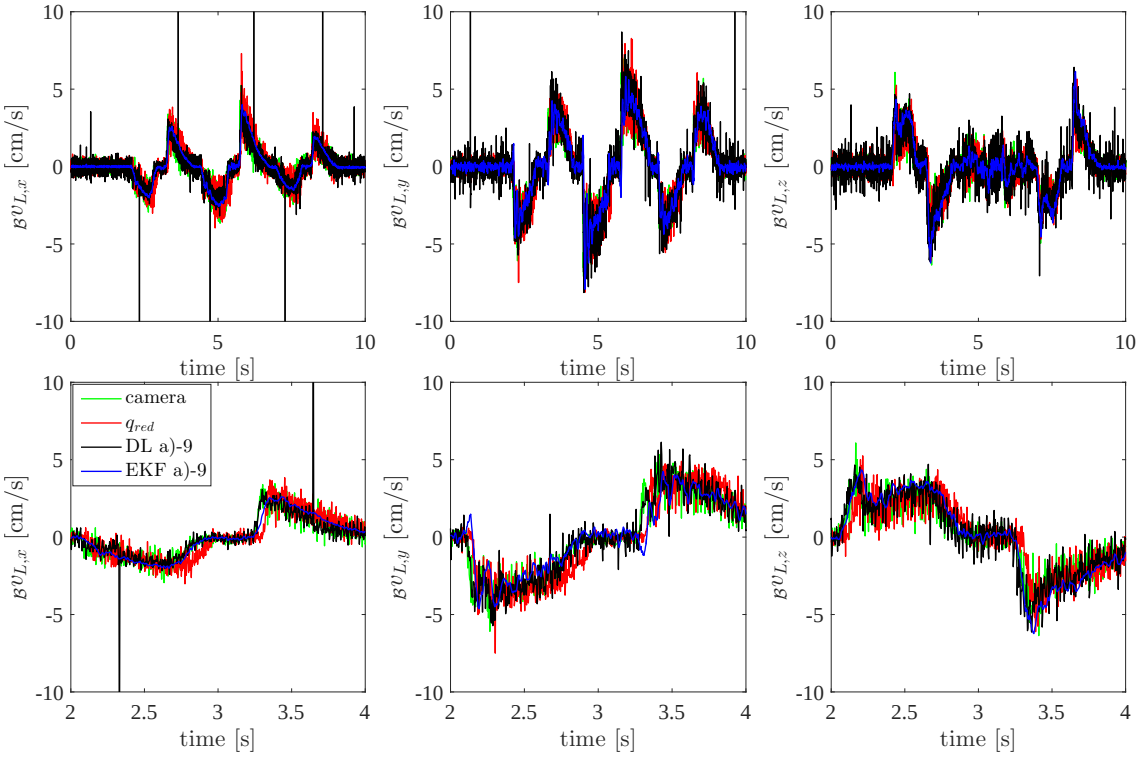

Figure 5.16.: Estimation of the linear velocity during actuated dynamic motions for the geometric ("q_{red}" and "DL a)-9") and dynamic ("EKF") state estimation concepts. The predicted velocity of the static concept is left out as the pose error is to big. Top row: Full motion. Bottom row: Zoomed view.

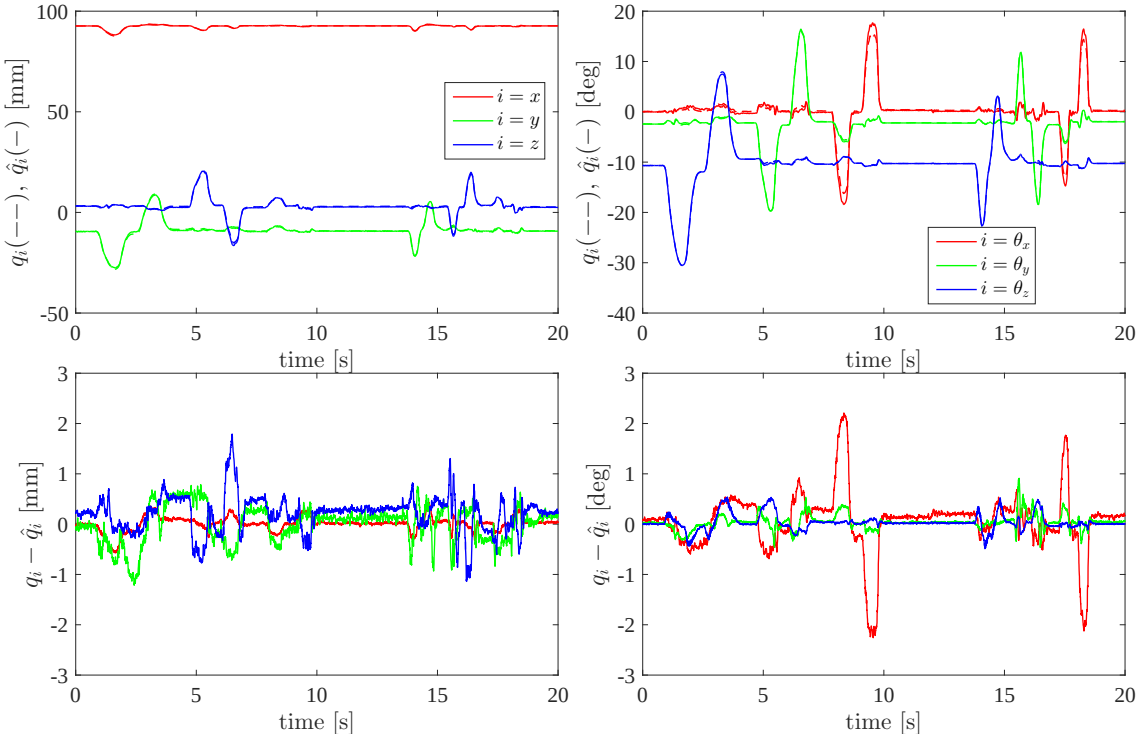

Figure 5.17.: Estimation performance during in manually induced motions of the EKF. Top row: Measured (–) and estimated (-) components of the pose $\boldsymbol{q}$. Bottom: Corresponding component wise estimation error $\boldsymbol{q} - \bar{\boldsymbol{q}}$.

5.6. Discussion and summary

This chapter provided State Estimation Concepts (SECs) that rely on geometric, static or dynamic models of the state and corresponding measurements which are acquired from sensors attached on the system.

Two geometric SECs are introduced. Their commonality is the sensor information that provides the length of some vector starting at the upper and ending at the lower platform. The first geometric SEC applies a kinematic reduction to represent the six DoF pose of the upper platform by four kinematic variables summarized in $\boldsymbol{q}_{\text{red}}$. The SEC manages to estimate $\boldsymbol{q}_{\text{red}}$ in real time whereas the full pose can be generated by a geometric forward kinematics and the corresponding velocity is acquired by numerical differentiation. The main advantage here is that no additional sensors are needed as the r length measures are provided by the tendon actuators. For static poses, the estimation performs comparable to other concepts with lower errors in the translations and higher errors in the rotation. The numerically derived velocity corresponds to the ground truth with higher noise and some spikes which are the result of a bigger step suggested by the optimization algorithm that solves the nonlinear least square problem. The concept is robust against external disturbances applied at the head, in contrast, if a tendon is affected, the estimation cannot be trusted any more. A disadvantage of this SEC is an incorporated error by the kinematic approximation which cannot be overcome. As the tendon actuators provide data in 3 kHz and the optimization algorithm converges in 2 steps at maximum, the SEC could be run in 1-3 kHz which would improve the latency and the noise in the velocity estimation.

The second geometric SEC estimates the six DoF pose with the help of additional length

sensors and the corresponding velocity is given by a numerical differentiation of the pose estimate. This SEC proved to be the most accurate regarding static poses. During dynamic motions, spikes in the estimated pose occurred which is, again, a result of a big step that is performed to solve the nonlinear least square problem. Similar to the former case, the numerically derived velocity is affected which is a disadvantage. A further disadvantage is the increased model dimension and a sensor sampling rate of 300 Hz which slows down the real-time computation. As additional sensors are applied on the system an increased integration effort is mandatory, including sensor calibration and referencing. In the current implementation, the sensors are exposed to external collision as they are placed on the circumference of the ECM which might lead to sensor failure in during a collision. On the other hand, during collision on the head, the SEC proved reliable which could be shown in real experiments.
The specific placement of the additional is crucial and highly affects the estimation quality. Several arrangements of additional sensors are suggested. In this simulation performed study, the total amount of sensors was limited to four. By including more sensors, limitations of a specific sensor configuration could be overcome. For example, sensor configuration a)-9 provides good estimates in y and worst estimates in z whereas c)-1 provides good estimates in z and worst estimates in y. By combining both arrangements, the weaknesses of both configurations can be canceled.

The static SEC in the current implementation did not prove suitable due to a high estimation error at static poses and during dynamic motions. However, it might be extended to a dynamic concept using a classical Luenberger observer as discussed in the corresponding section.

The dynamic SEC fuses the length information of the tendons, the length information of the additional sensors and IMU measurements. In the present implementation, the dynamic SEC proved to provide the most accurate estimation of the pose during dynamic motions and the smoothest velocity estimate. During collision exerted on the head, reliable estimates are given, in contrast, if the additional sensors or the tendons are affected, the estimation is not reliable. Due to an augmented state, the equations are of dimension 15 which does affect the computational demands, however as the estimation converges over time, the real-time model is not affected. The major drawback of the approach is the integration effort as 4 additional sensors and an IMU need to be integrated, calibrated and referenced.
For future implementations, an IMU with a higher sampling rate, e.g. 3 kHz or higher, is to be integrated to combine fast measurements of the IMU during dynamic motions and slower measurements of additional sensors for the static accuracy. Here, two sampling rates are to be introduced in the filter to account for the information of the sensors and the IMU. Furthermore, the nonlinear optimization and the EKF can be combined. In this case, the nonlinear optimization serves as measurement, here the full pose is measured, which is fused together with the IMU to improve the velocity estimate and the accuracy during dynamic motions. Another second extension of the EKF is to incorporate the state and measurement covariance as a confidence measure. For example, if a sensor (a tendon or a additional sensor) breaks or is disconnected, the measurement covariance of this particular sensor could be strongly increased and therefore, this sensor information will not be used in the fusion process anymore.

For the implementation of the model-based control approaches and their experimental verification, the geometric concept based on the reduced kinematic variables is imple-

mented in a 3 kHz real-time implementation as it provides the best compromise in accuracy and integration effort in the current form. The decision is based on above consideration and Table 5.3 which summarizes the advantages and disadvantages of the evaluated SECs.

Table 5.3.: Comparison of the different state estimation concepts (SE concepts). Requirement satisfied "very good" (++), "good" (+), "bad" (−), "very bad" (−−) and "no clear statement" (∘).

SE Concept estimation of	geometric $\boldsymbol{q}_{\text{red}}$ (3.65)	geometric $\boldsymbol{q}$ (4.14)	static $\boldsymbol{q}$ (4.14)	dynamic (EKF) $\boldsymbol{\psi}$ (5.28)
Requirement 1 Pose estimation accuracy	−	+	−−	++
Requirement 2 Velocity estimation accuracy	+	+	∘	++
Requirement 3 Computational demands	++	+	+	+
Requirement 4 Sensor mobility and robustness	++	+	+	+
Requirement 5 Reliability during collision	+	+	∘	+
Requirement 6 Integration and maintenance	++	−	−	−−

CHAPTER 6

Model-based control

A tendon-driven continuum mechanism can be used in a variety of applications that usually involve a coordinated deformation of the continuum to move the upper platform spatially. To induce this deformation of the continuum, a controller is needed. In this respect, the main objective is to control the pose of the upper platform that is attached to the end of the continuum mechanism which can be described by the generalized coordinates $\boldsymbol{q} \in \mathbb{R}^6$. The control input to the system are motor torques of the tendon actuators $\boldsymbol{\tau}_m \in \mathbb{R}^r$ to generate positive tendon tensions $u_i \geq 0 \ \forall \ i = 1 \dots r$ which deform the continuum mechanism. As outlined earlier, the present work considers the problem of $r < 6$ which implies an underactuated system and demands that reference tracking can only be demanded for r outputs, denoted $\boldsymbol{y} \in \mathbb{R}^r$.

The fundamental concept for the developed controller relies upon the time scale difference between the dynamics of the tendon actuation and the dynamics of the ECM, and is called singular perturbation approach. The approach allows decomposing the two dynamic systems, which are mechanically coupled by the tendons, into a slow and a fast part and justifies a separate controller design for each part. The major attention of this chapter is dedicated to the design of the slow part which aims to control the position and orientation of the upper platform (the head) by commanding desired tendon tension forces $\boldsymbol{u}_d \in \mathbb{R}^r$. Nonlinear model-based control approaches are discussed for set point control as it can be experimentally evaluated for all concepts. In contrast, tracking control is only mentioned as it would imply to generate dynamically consistent trajectories for the system which is not in scope of the present thesis.

The presented control approaches are partially published in conference proceedings. The partial feedback linearization concept is discussed in [84]. The control approach based on a linear $\mathscr{H}_\infty$ control is presented in [82] and the fractional order lag controller is presented in [83]. Furthermore, an extension to the MIMO case is discussed in this thesis.
The theoretical foundation of the proposed approach, the control problem and the desired performance will be specified in the next section before the controller derivation is presented.

6.1. Control structure, set point generation & desired performance

6.1.1. Control structure

The dynamic model of the system that is to be controlled is composed of the dynamics of the elastic continuum mechanism (4.3) which is elastically coupled, by equation (4.50) to the dynamics of the tendon actuators (4.48). As these equation a fundamental for the controllers developed in the following, they are recalled:

$$\boldsymbol{M}(\boldsymbol{q})\ddot{\boldsymbol{q}} + \boldsymbol{k}(\boldsymbol{q}, \dot{\boldsymbol{q}}) = \boldsymbol{P}(\boldsymbol{q})\boldsymbol{u}, \tag{6.1}$$

$$\boldsymbol{y} = \boldsymbol{h}(\boldsymbol{q}), \tag{6.2}$$

$$\boldsymbol{u} = \boldsymbol{K}_t \left(\boldsymbol{E}\boldsymbol{\theta}_m - \boldsymbol{l}(\boldsymbol{q}) \right), \tag{6.3}$$

$$\boldsymbol{B}\ddot{\boldsymbol{\theta}}_m + \boldsymbol{E}^T\boldsymbol{u} = \boldsymbol{\tau}_m - \boldsymbol{\tau}_{fric}. \tag{6.4}$$

Above equations are structurally similar to the dynamic model of a flexible joint robotic manipulator [127]. The outputs $\boldsymbol{y} \in \mathbb{R}^r$ of the system play a crucial role and are defined later on. The proposed control structure in the following is based on the singular perturbation approach [128] which assumes that the tendon tension dynamics (6.4) and the dynamics of the ECM (6.1) have different time scales, namely the tendon actuator dynamics are faster compared with the dynamics of the ECM. This assumption is justified by the considerably smaller inertia of the motors and the much higher stiffness of the tendons. Similarly, the motors in the tendon actuation system are considered as torque sources while commanding currents or voltages and neglecting the dynamics of the current control loop.

Similar to the work of Ott *et al.* [129], who applied the singular perturbation approach on a flexible joint robot, the presented control structure is composed of two separate control laws, an outer loop slow controller $\boldsymbol{\tau}_s \in \mathbb{R}^r$ and an inner loop, fast controller $\boldsymbol{\tau}_f \in \mathbb{R}^r$. The outer loop is considered as constant for the design of the inner loop. This implies that the control law for $\boldsymbol{\tau}_f$ can be designed while treating the ECM to be in steady state $\boldsymbol{q} = const.$ and the elastic coupling is therefore (6.3) neglected. In the design of the outer loop, the inner loop error is neglected arguing that, because of its speed, the inner loop is stabilized before the outer loop is disturbed. In [129], a control law for the motor torques $\boldsymbol{\tau}_m \in \mathbb{R}^r$ is proposed which is adapted for the present case to

$$\boldsymbol{\tau}_m = \boldsymbol{\tau}_s - \underbrace{\boldsymbol{E}^T \left(\boldsymbol{K}_{u,p}\boldsymbol{u} + \boldsymbol{K}_{u,d}\dot{\boldsymbol{u}} \right)}_{\boldsymbol{\tau}_f}. \tag{6.5}$$

For the control of the slow system, above assumption considers a settled tension dynamics $\dot{\boldsymbol{u}} = \boldsymbol{0}$, which yields for (6.4) with (6.5) neglecting motor friction,

$$\begin{aligned} \boldsymbol{B}\ddot{\boldsymbol{\theta}}_m + \boldsymbol{E}^T\boldsymbol{u} &= \boldsymbol{\tau}_s - \boldsymbol{E}^T \left(\boldsymbol{K}_{u,p}\boldsymbol{u} + \underbrace{\boldsymbol{K}_{u,d}\dot{\boldsymbol{u}}}_{=\boldsymbol{0}} \right), \\ \boldsymbol{E}^T \left(\boldsymbol{I} + \boldsymbol{K}_{u,p} \right) \boldsymbol{u} &= \boldsymbol{\tau}_s - \boldsymbol{B}\ddot{\boldsymbol{\theta}}. \end{aligned} \tag{6.6}$$

Using equation (6.6) in (6.1) and the second derivative of (6.3) with $\ddot{\boldsymbol{u}} = \boldsymbol{0}$, the dynamics

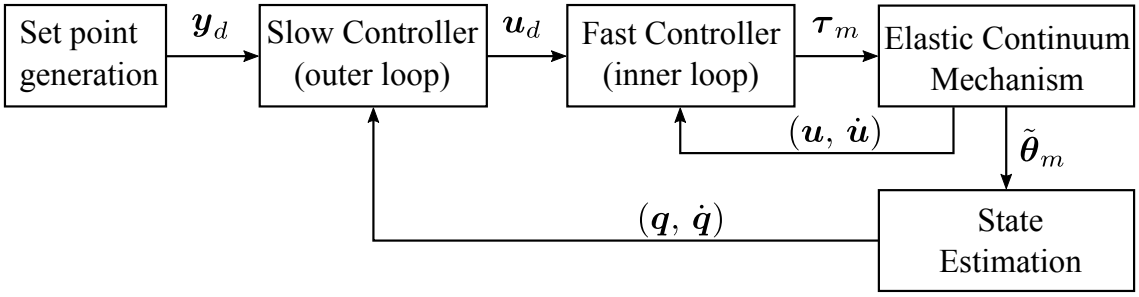

Figure 6.1.: Block diagram of the proposed control structure which consists of an inner, faster control loop that accounts for a fast convergence of the tendon tension $\boldsymbol{u}$ to desired tension $\boldsymbol{u}_d$ and an outer, slower control loop that accounts for set point control of the ECM dynamics to reach desired outputs $\boldsymbol{y}_d$.

equation of the slow part are,

$$\begin{aligned}\Big(\boldsymbol{M}(\boldsymbol{q}) + \boldsymbol{P}(\boldsymbol{q})\left(\boldsymbol{E}^T(\boldsymbol{I}+\boldsymbol{K}_{u,p})\right)^{-1}\boldsymbol{B}\boldsymbol{E}^{-1}\boldsymbol{P}(\boldsymbol{q})^T\Big)\,\ddot{\boldsymbol{q}} + \boldsymbol{k}(\boldsymbol{q},\dot{\boldsymbol{q}}) \\ +\boldsymbol{P}(\boldsymbol{q})\left(\boldsymbol{E}^T(\boldsymbol{I}+\boldsymbol{K}_{u,p})\right)^{-1}\boldsymbol{B}\boldsymbol{E}^{-1}\dot{\boldsymbol{P}}(\boldsymbol{q})^T\dot{\boldsymbol{q}} \\ = \boldsymbol{P}(\boldsymbol{q})\left(\boldsymbol{E}^T(\boldsymbol{I}+\boldsymbol{K}_{u,p})\right)^{-1}\boldsymbol{\tau}_s,\end{aligned} \tag{6.7}$$

which are modified in comparison to (6.1) by a reflected motor inertia $\boldsymbol{B}$ on the ECM dynamics and a corresponding Coriolis and centrifugal term.
By choosing $\boldsymbol{\tau}_s = \left(\boldsymbol{E}^T(\boldsymbol{I}+\boldsymbol{K}_{u,p})\right)\boldsymbol{u}_d$ with a new control input $\boldsymbol{u}_d \in \mathbb{R}^r$, the control law for the motor torques (6.5) equates

$$\boldsymbol{\tau}_m = \boldsymbol{E}^T\left(\boldsymbol{u}_d + \boldsymbol{K}_{u,p}(\boldsymbol{u}_d - \boldsymbol{u}) - \boldsymbol{K}_{u,d}\dot{\boldsymbol{u}}\right), \tag{6.8}$$

and $\boldsymbol{u}_d$ can be designed according to a certain control law based on the dynamic equation (6.7). Due to a positive definite choice of $\boldsymbol{K}_{u,p}$, the reflected motor inertia is scaled. In practice, the terms related to the motor inertia of the tendon actuators are dropped as $\boldsymbol{B}$ is comparably small considering the inertia of the attached rigid body. Thus, (6.7) is simplified for the controller design of the slow part,

$$\boldsymbol{M}(\boldsymbol{q})\ddot{\boldsymbol{q}} + \boldsymbol{k}(\boldsymbol{q},\dot{\boldsymbol{q}}) = \boldsymbol{P}(\boldsymbol{q})\boldsymbol{u}_d. \tag{6.9}$$

The full structure of the proposed controller is illustrated by the block diagram shown in Fig. 6.1. Under the assumption that above consideration of the tendon tension controller, i.e. the inner loop, hold and that the state estimation provides the pose and corresponding velocity without delay, a control law for $\boldsymbol{u}_d$ can be used which is applied for classical underactuated systems, e.g. underactuated rigid-link manipulators [130] or quadrotors [131]. As mentioned, a maximum of r outputs can be controlled denoted as the vector of outputs $\boldsymbol{y}$ which is in general a nonlinear function of the state. However for the designed nonlinear feedback controllers, the knowledge of the full state is required and thus fed back as indicated in Fig. 6.1.

6.1.2. Set point generation

An arbitrary combination for the components of the desired outputs $\boldsymbol{y}_d \in \mathbb{R}^r$ is not admissible due to the tendon coupling and the elastic coupling of the continuum structure. For

this reason, admissible desired outputs need to be generated. In general, desired outputs $\boldsymbol{y}_d$, corresponding velocities $\dot{\boldsymbol{y}}_d \in \mathbb{R}^r$ and accelerations $\ddot{\boldsymbol{y}}_d \in \mathbb{R}^r$ need to be dynamically consistent with the equation of motion (6.1) and need to be reachable with positive tendon tension forces,

$$\begin{aligned} \boldsymbol{q}_d &= \boldsymbol{h}^{-1}(\boldsymbol{y}_d), \\ 0 &\leq u_{d,i}, \quad \forall i = 1 \dots r, \\ \boldsymbol{M}(\boldsymbol{q}_d)\ddot{\boldsymbol{q}}_d + \boldsymbol{k}(\boldsymbol{q}_d, \dot{\boldsymbol{q}}_d) &= \boldsymbol{P}(\boldsymbol{q}_d)\boldsymbol{u}_d. \end{aligned} \tag{6.10}$$

The solution of (6.10) is not in scope of the present thesis and will not be treated. Instead, reachable set points $\boldsymbol{y}_d$ are ensured by manually specifying positive tendon forces $\boldsymbol{u}_{d,init} \in \mathbb{R}^r$ which are used to solve the static equilibrium,

$$\boldsymbol{k}(\boldsymbol{q}_d, \boldsymbol{0}) - \boldsymbol{P}(\boldsymbol{q}_d)\boldsymbol{u}_{d,init} = \boldsymbol{0}, \tag{6.11}$$

Equation (6.11) is solved offline using an iterative Newton-Raphson scheme. A smooth transient towards $\boldsymbol{y}_d$ is then ensured by generating a four times differentiable steps from $\boldsymbol{y}_{init}$ to $\boldsymbol{y}_d$ which ensures smoothness also for $\dot{\boldsymbol{y}}_d$ and $\ddot{\boldsymbol{y}}_d$.

6.1.3. Desired performance

The above described scheme to generate set points implies that the workspace of the real system is limited by the maximum tolerable tendon tensions of 70 N and the resulting maximum and minimum values for $\boldsymbol{q}_d$ and $\boldsymbol{y}_d$. Tendon slackness should be avoided by demanding a constant pretension $u_{pre,i} = 10$ N for $i = 1 \dots r$. Furthermore, it is desirable to have a negligible steady-state error and a step response with a settling time of ≈ 1 s. Furthermore, the closed loop system needs to be robust against external disturbances and exhibit a critically damped behavior when excited.

6.2. Tendon tension control

The fast control loop handles the tendon tension control and basically ensures that desired tendon tensions $\boldsymbol{u}_d \in \mathbb{R}^r$ are realized by the tendon actuators. The tendon tension control law is given in (6.8) and will be modified to compensate for dry frictional effects,

$$\boldsymbol{\tau}_m = \boldsymbol{E}^T \left(\boldsymbol{u}_d + \boldsymbol{K}_{u,p}(\boldsymbol{u}_d - \boldsymbol{u}) - \boldsymbol{K}_{u,d}\dot{\boldsymbol{u}}\right) + \tilde{\boldsymbol{\tau}}_{fric}, \tag{6.12}$$

where $\tilde{\boldsymbol{\tau}}_{fric}$ is based on the identified friction model in Section 4.3.1. The structure of the control law in (6.12) is a state feedback with reference tracking and an additional feedforward term. The measured tendon tension and the derivative are feedback, illustrated in the block diagram Fig. 6.1. The feedback signal originates from a tendon tension sensor in each tendon path.
The closed loop dynamics of system (6.4) and controller (6.12) equates to

$$\begin{aligned} \boldsymbol{B}\ddot{\boldsymbol{\theta}} + (\boldsymbol{\tau}_{fric} - \tilde{\boldsymbol{\tau}}_{fric}) &= \boldsymbol{E}^T \left(\boldsymbol{u}_d + \boldsymbol{K}_{u,p}(\boldsymbol{u}_d - \boldsymbol{u}) - \boldsymbol{K}_{u,d}\dot{\boldsymbol{u}}\right) \\ (\boldsymbol{E}^T(\boldsymbol{I} + \boldsymbol{K}_{u,p}))^{-1} \left(\boldsymbol{B}\ddot{\boldsymbol{\theta}} + (\boldsymbol{\tau}_{fric} - \tilde{\boldsymbol{\tau}}_{fric}) + \boldsymbol{K}_{u,d}\dot{\boldsymbol{u}}\right) &= \boldsymbol{u}_d - \boldsymbol{u} \end{aligned} \tag{6.13}$$

with the identity matrix $\boldsymbol{I} \in \mathbb{R}^{r \times r}$. In case of zero reference $\boldsymbol{u}_d = \boldsymbol{0}$, the system can be manually move around as the back drive ability of the system is enhanced since remaining friction $(\boldsymbol{\tau}_{fric} - \hat{\boldsymbol{\tau}}_{fric})$ and the motor inertia $\boldsymbol{B}$ is scaled by $\boldsymbol{E}^T(\boldsymbol{I} + \boldsymbol{K}_{u,p})$.

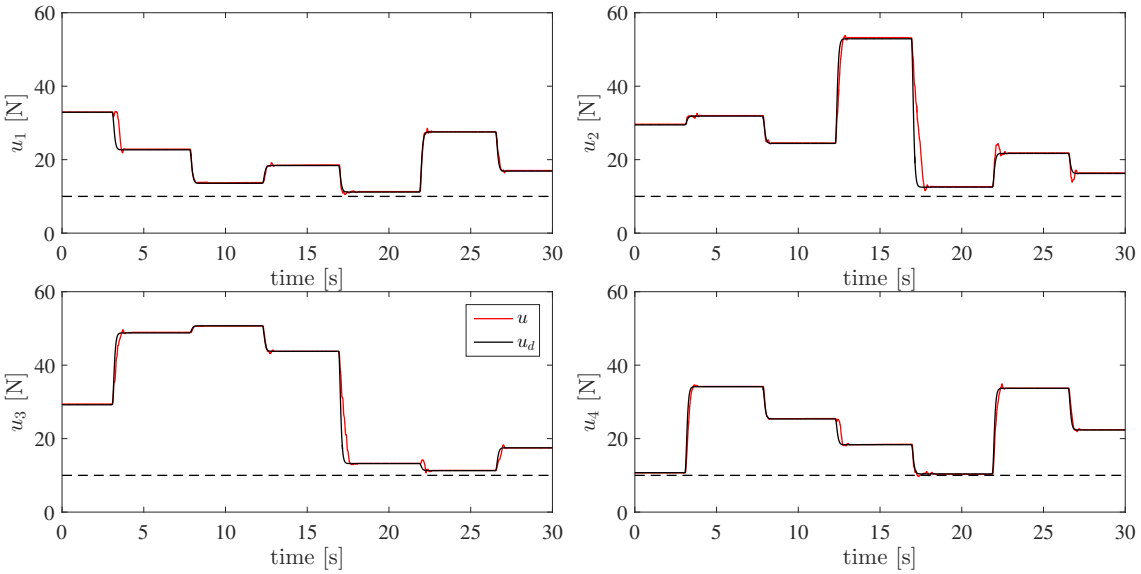

Figure 6.2.: The measured performance of the tendon tension controller in real experiments. A sequence of 200 different combinations of $r = 4$ desired tendon tension set points is reached whereas the plot shows a representative excerpt of the experiments. The absolute steady state error of the tendon tension controller is less than 0.5 N. In the transient phase, small mismatches between the reference $u_{d,i}$ and the measured tendon tension u_i can be observed. Especially when a large negative step is present (between 15s and 20s for tendon $i = 2$ and $i = 3$), the fast response of the continuum counteracts the control action.

Later on, the motion controllers will be tested on the real system, the spatial system described in section 2.2.2, which brings the necessity to select the matrices $\boldsymbol{K}_{u,p}$ and $\boldsymbol{K}_{u,d}$. For these experiments, the gain matrices are chosen in diagonal structure with the same values on the diagonal,

$$\begin{aligned} \boldsymbol{K}_{u,p} &= k_{u,p}\,\boldsymbol{I}_r \quad k_{u,p} = 8, \\ \boldsymbol{K}_{u,d} &= k_{u,d}\,\boldsymbol{I}_r \quad k_{u,d} = 0.8, \end{aligned} \tag{6.14}$$

and the identity matrix $\boldsymbol{I}_r \in \mathbb{R}^{r\times r}$. In Fig. 6.2, an excerpt of a sequence of several set points for $\boldsymbol{u}_d$ is shown which indicates that the $r = 4$ independent controllers perform a stable response to different input steps. In total, 200 different set points are reached and at steady state, the RMSE is 0.5 N at maximum for all of the four controllers. As a coupled motion is performed and the r tendons are mechanically coupled at the upper platform of the ECM, this experiment also highlights the robustness of the designed tension controller against external disturbances.

As mentioned in the beginning, the tendon tensions used in the feedback are measured by tendon tension sensors in each tendon path. From a mechatronic point of view, it is very demanding to integrate one tension sensor in each path due to additional space requirements and necessary electronics for signal conditioning and AD conversion. As a second concept, one could apply the measurements of the force-torque sensor (FTS) which is located at the clamped end of the continuum, see Section 5.1.2. The sensor measures the clamping forces and torques, denoted ${}_{\mathcal{B}}\boldsymbol{w}^{\mathcal{B}}_{FTS} \in \mathbb{R}^6$ which can be transformed to a wrench

applied at the upper platform by a corresponding, pose dependent adjoint $\boldsymbol{A}d_{\mathcal{BH}\,\mathcal{B}}\boldsymbol{w}^{\mathcal{B}}$. By a projection of $\boldsymbol{A}d_{\mathcal{BH}\,\mathcal{B}}\boldsymbol{w}^{\mathcal{B}}$ into the direction of the tendons, using the pseudo inverse of the tendon coupling matrix $\boldsymbol{P}(\boldsymbol{q})^{+} \in \mathbb{R}^{r\times 6}$, the measurement of the FTS can be applied to measure the tension forces,

$$\boldsymbol{A}d_{\mathcal{BH}\,\mathcal{B}}\boldsymbol{w}^{\mathcal{B}}_{FTS} = {}_{\mathcal{B}}\boldsymbol{w}^{\mathcal{H}}_{FTS}, \tag{6.15}$$

$$\boldsymbol{u}_{FTS} = \boldsymbol{P}^{+}(\boldsymbol{q}){}_{\mathcal{B}}\boldsymbol{w}^{\mathcal{H}}_{FTS}. \tag{6.16}$$

With equation (6.16), the control law of the fast loop is reformulated to

$$\begin{aligned}&\boldsymbol{\tau}_m = \\ &\boldsymbol{E}^T\left(\boldsymbol{u}_d + \boldsymbol{K}_{u,p}(\boldsymbol{u}_d - \boldsymbol{P}^{+}(\boldsymbol{q}){}_{\mathcal{B}}\boldsymbol{w}^{\mathcal{H}}_{FTS}) - \boldsymbol{K}_{u,d}(\dot{\boldsymbol{P}}^{+}(\boldsymbol{q}){}_{\mathcal{B}}\boldsymbol{w}^{\mathcal{H}}_{FTS} + \boldsymbol{P}^{+}(\boldsymbol{q}){}_{\mathcal{B}}\dot{\boldsymbol{w}}^{\mathcal{H}}_{FTS})\right) + \tilde{\boldsymbol{\tau}}_{fric}.\end{aligned} \tag{6.17}$$

Remark: Commonly, the FTS sensor provides high data rates which is in line with the assumption of a fast control loop. However, the estimated pose is necessary for the adjoint (6.15) and the tendon coupling matrix (6.16). This would imply a correspondingly fast pose estimation which cannot be guaranteed. Equation (6.17) requires the inversion of the coupling matrix and its temporal derivative. In certain configuration, the matrix might be ill-posed which implies higher computational demands for the inversion and bigger numerical errors which might be amplified in case of a temporal derivative which definitely limits the approach and would yield a comparably small gain for $\boldsymbol{K}_{u,d}$. Furthermore, in case of an external collision or interaction with the system, the force torque sensor measurement do not predict the tendon tensions correctly as the static equilibrium assumed for equation $\boldsymbol{u}_{FTS} = \boldsymbol{P}^{+}(\boldsymbol{q}){}_{\mathcal{B}}\boldsymbol{w}^{\mathcal{H}}_{FTS}$ is not valid any more.

6.3. $\mathscr{H}_\infty$-synthesis using a structured description of nonlinearities

This section treats an approach to derive a control law for the slow control loop based on a standard approach from the field of automatic control, termed linear $\mathscr{H}_\infty$ control. The objective is to control the pose of the ECM expressed by $\boldsymbol{q} \in \mathbb{R}^6$ which is described by the dynamic equation of the slow control loop (6.9). The approach is motivated the properties of the closed control loop, e.g. the bandwidth, can be explicitly specified in the approach and robust stability can be guaranteed.

In control theory, linear $\mathscr{H}_\infty$ control is a well-known concept and an extensive introduction to this control approach is provided in the books of Zhou *et al.* [132] or by Åström [133]. In general, a linear dynamic feedback controller is designed in the frequency domain and resulting closed loop fulfills predefined properties, e.g. bandwidth or disturbance rejection. Linear $\mathscr{H}_\infty$ control can guarantee robust stability with respect to model uncertainties and underactuated systems can be treated without specific consideration as shown in [134, 135]. Parametric uncertainties can be explicitly incorporated in the design approach as shown by Djukanovic [136] using the structured singular value framework. Amann [137] extended this framework and describes dynamic nonlinearities as norm bounded uncertainties. In this respect, the dynamics of the system are separated in a linear part and an uncertain, i.e. nonlinear part. The nonlinear part can then be described by Taylor expansions in the fully actuated case [137], Fourier series [138] or manually identified transfer functions [139] for single-input single-output systems.

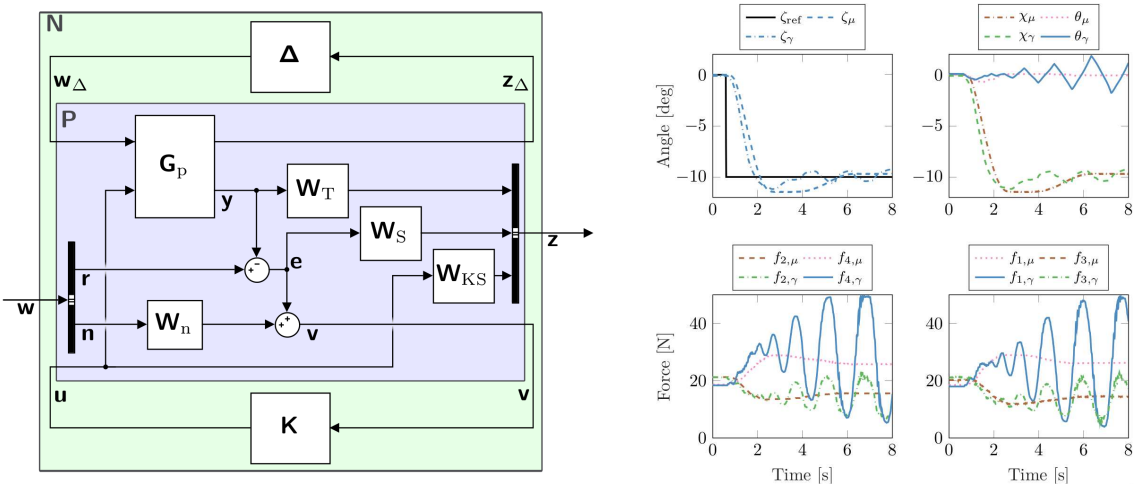

Figure 6.3.: Left: Block diagram of the augmented plant which is fundamental for the presented linear $\mathscr{H}_\infty$ controller design. Experimental results of the closed loop performing a reference step $\zeta_d = -10$ deg. The robustified controller $\mathbf{K}_\mu$ is able to stabilize the system whereas the controller $\mathbf{K}_\gamma$ results in an unstable behavior which is undesired.

In this section, an approach is presented that extends the work by [137], i.e. treating the nonlinearities as uncertainties, to an underactuated, multi-input multi-output (MIMO) system. For the obtained model, a linear $\mathscr{H}_\infty$ controller is synthesized using known nonlinearities explicitly in the design process. The described approach is published in Shu *et al.* [82][1]. Therefore, the following section will present the main ideas of this approach and a more detailed description can be found in [82, 140].

Linear $\mathscr{H}_\infty$ synthesis is a frequency domain based approach and demands an augmented structure of the underlying closed loop which will be explained in the following and which is illustrated on the left side of Fig. 6.3 in a block diagram. For the design, an augmented closed loop transfer function $\mathbf{N}(s) \in \mathbb{C}^{12\times16}$, with frequency variable $s \in \mathbb{C}$, is considered which relates an augmented input $\mathbf{w}(s) \in \mathbb{C}^{12}$ to an augmented output $\mathbf{z}(s) \in \mathbb{C}^{16}$. Here, the augmented input consists of a reference $\mathbf{r}(s) \in \mathbb{C}^6$ and a measurement noise signal $\mathbf{n}(s)$ whereas $\mathbf{z}(s)$ consists of the outputs of the system $\mathbf{y}(s) \in \mathbb{C}^6$, the control error $\mathbf{e}(s) = \mathbf{r}(s) - \mathbf{y}(s) \in \mathbb{C}^6$ and the input $\mathbf{u}(s) \in \mathbb{C}^4$. A dynamic controller $\mathbf{K}(s) \in \mathbb{C}^{6\times4}$ is found by minimizing the worst case effect from $\mathbf{w}(s)$ to $\mathbf{z}(s)$,

$$\min_{\mathbf{K}} ||\mathbf{N}(s)||_\infty \leq \gamma, \tag{6.18}$$

with the upper bound $\gamma \in \mathbb{R}$ on the closed-loop gain $||\mathbf{N}(s)||_\infty$. The dynamic controller transfer function $\mathbf{K}(s)$ has a fixed dimension. However, internal states occur in the synthesis which can be of higher dimensions. The underlying plant dynamics are the equation

[1]The publication is based on a Master's thesis of Shu [140] which was supervised by the author of this thesis.

of the slow control loop (6.9), in first order form,

$$\begin{pmatrix} \boldsymbol{q} \\ \dot{\boldsymbol{q}} \end{pmatrix} = \boldsymbol{\sigma}(\boldsymbol{q}, \dot{\boldsymbol{q}}) + \boldsymbol{\Gamma}(\boldsymbol{q})\boldsymbol{u}_d, \tag{6.19}$$

$$\boldsymbol{\sigma}(\boldsymbol{q},\, \dot{\boldsymbol{q}}) = \begin{pmatrix} \dot{\boldsymbol{q}} \\ -\boldsymbol{M}(\boldsymbol{q})^{-1}\boldsymbol{k}(\boldsymbol{q}, \dot{\boldsymbol{q}}) \end{pmatrix},\ \boldsymbol{\Gamma}(\boldsymbol{q}) = \begin{pmatrix} \boldsymbol{0} \\ \boldsymbol{M}(\boldsymbol{q})^{-1}\boldsymbol{P}(\boldsymbol{q}) \end{pmatrix}, \tag{6.20}$$

which are approximated by first-order Taylor approximation, i.e. linearization around a small deviation $\boldsymbol{\eta} \in \mathbb{R}^{12}$ of the equilibrium point $(\boldsymbol{q}_0^T, \boldsymbol{0})^T,\ \boldsymbol{u}_{d,0} = const.$ that satisfies

$$\boldsymbol{\sigma}(\boldsymbol{q}_0,\, \boldsymbol{0}) + \boldsymbol{\Gamma}(\boldsymbol{q}_0,\, \boldsymbol{0})\boldsymbol{u}_{d,0} = \boldsymbol{0}. \tag{6.21}$$

Knowledge about the nonlinear part of the system is then explicitly incorporated in the design process by transforming the second order term in the Taylor approximation

$$\dot{\boldsymbol{\eta}} = \left[\boldsymbol{A} + \frac{1}{2}\frac{\partial^2 \boldsymbol{\sigma}}{\partial(\boldsymbol{q}^T,\, \dot{\boldsymbol{q}}^T)^2}\bigg|_{\boldsymbol{q}_0, \dot{\boldsymbol{q}}_0}\right]\boldsymbol{\eta} + \left[\boldsymbol{B} + \frac{\partial \boldsymbol{\Gamma}}{\partial \boldsymbol{q}}\bigg|_{\boldsymbol{q}_0}\boldsymbol{\eta}\right]\boldsymbol{u}_\eta, \tag{6.22}$$

into norm bounded parametric uncertainties with an uncertain parameter $\boldsymbol{\delta} \in \mathbb{R}^{12}$ which varies in the bounds for each component $\eta_{j,min} \leq \eta_j \leq \eta_{j,max}$,

$$\dot{\boldsymbol{\eta}} = \left[\boldsymbol{A} + \sum_{j=1}^{12} \hat{\boldsymbol{A}}_j \delta_j\right]\boldsymbol{\eta} + \left[\boldsymbol{B} + \sum_{j=1}^{12} \hat{\boldsymbol{B}}_j \delta_j\right]\boldsymbol{u}_\eta. \tag{6.23}$$

The system (6.23) can be further transformed using a Linear Fractional Transformation (LFT), see[132], to a perturbable system $\mathbf{G}_p(s)$ and a real valued block diagonal uncertainty matrix $\boldsymbol{\Delta} \in \mathbb{R}^{31\times 31}$, see Fig. 6.3. To find a solution of (6.18), the closed-loop $\mathbf{N}(s)$ needs to be specified and thus the frequency dependent weights for the sensitivity $\mathbf{W}_S(s)$, the complementary sensitivity $\mathbf{W}_T(s)$, the noise $\mathbf{W}_n(s)$ and the control action transfer function $\mathbf{W}_{KS}(s)$ need to be chosen, see Fig. 6.3. As the weights are dynamic and thus can be designed with a different bandwidth, conflicting goals are circumvented. For example, it is not possible to generally minimize $\mathbf{e}(s)$ and $\mathbf{u}(s)$ in the whole frequency range. In this case, the sensitivity $\mathbf{W}_S(s)$ has a high gain at lower frequencies, to account for small steady state error, whereas $\mathbf{W}_{KS}(s)$ has a high gain at high frequencies to account for the limited actuator dynamics.

Two controllers are designed in [82]. A robust $\mathscr{H}_\infty$ controller $\mathbf{K}_\mu$ is designed using a μ-synthesis with the DK–Iteration algorithm, see [141], which explicitly considers the obtained uncertainty in the controller design. To evaluate the effect of the robust design a classical mixed synthesis $\mathscr{H}_\infty$ controller $\mathbf{K}_\gamma$ according to [132] is designed for which the uncertainty $\boldsymbol{\Delta}$ is neglected and no additional robustification is performed.

Experimental results for the controller $\mathbf{K}_\gamma$ are shown in Fig. 6.3. The performed reference step $\zeta_d = -10°$ results in an unstable system which can be observed by increasing oscillations in the tendon forces and in the angles ζ_γ and χ_γ. This instability is also present if the system is manually disturbed e.g. at its initial, straight configuration which is not shown here. A different behavior can be seen with the robust $\mathbf{K}_\mu$ controller, see 6.3. Here the step response is stable. Furthermore, an overshoot of ζ_μ can be observed which is only gradually corrected and a small stationary error is present. As a result, the robustification of in the controller design yielded a desirable performance as the controller is able to stabilize the system. However, the robust behavior of the $\mathbf{K}_\mu$ results in a strongly conservative control behavior and the closed loop takes ≈ 4 s to stabilize which is far away from the desired settling time of 1 s (see Sec. 6.1.3).

6.4. Feedback Control

The goal of the present section is to derive a control law for $\boldsymbol{u}_d \in \mathbb{R}^r$, i.e. the slow outer control loop, see Fig. 6.1 with the dynamic equation in (6.9). The controller should ensure set point regulation for the position and orientation of the upper platform which is described by $\boldsymbol{q} \in \mathbb{R}^6$. Due to the underactuation ($r < 6$), it is only possible to control a maximum number of r outputs, denoted $\boldsymbol{y} \in \mathbb{R}^r$. The designed controller of the present section ensures set point regulation for desired outputs $\boldsymbol{y}_d \in \mathbb{R}^r$ by shaping the closed loop error dynamics to possess a certain property. This goal is achieved by a nonlinear feedback of known dynamic properties of the system and a novel control input. Two approaches are presented which are based on a transformation of the dynamic equations to the Input Output Normal Form (IONF).

6.4.1. Input Output Normal Form (IONF)

For underactuated systems with r control inputs, a maximum number of r outputs $\boldsymbol{y} \in \mathbb{R}^r$ can be controlled which are, in general, represented by a nonlinear function $\boldsymbol{h} \in \mathbb{R}^r$

$$\boldsymbol{y} = \boldsymbol{h}(\boldsymbol{q}). \tag{6.24}$$

The input output normal form, also denoted *Byrnes/Isidori input ouput normal form* due its origin, is a concept from differential geometric control theory and a comprehensive introduction is given by the fundamental work of Isidori [142]. Isidori gives a generic formalism to derive the IONF that involves 1) r directional derivatives of (6.24) along the nonlinear state space equations (6.9), i.e. *Lie-derivatives*, and 2) a nonlinear coordinate transformation $\boldsymbol{\phi}(\boldsymbol{q}) \in \mathbb{R}^n$ to new coordinates,

$$\begin{pmatrix} \boldsymbol{y} \\ \boldsymbol{q}_r \end{pmatrix} = \boldsymbol{\phi}(\boldsymbol{q}) = \begin{pmatrix} \boldsymbol{h}(\boldsymbol{q}) \\ \phi_{r+1}(\boldsymbol{q}) \\ \vdots \\ \phi_n(\boldsymbol{q}) \end{pmatrix}. \tag{6.25}$$

In (6.25), $\boldsymbol{q}_r \in \mathbb{R}^{6-r}$ are denoted the remaining coordinates and the transformation $\boldsymbol{\phi}(\boldsymbol{q})$ need to be a local diffeomorphism, i.e. the its Jacobian $\frac{\partial \boldsymbol{\phi}(\boldsymbol{q})}{\boldsymbol{q}}$ need to be nonsingular. For a more comprehensive treatment, see [142]. For second order nonlinear systems, i.e. multi-body systems, the transformation to the IONF can be achieved in a simpler way which avoids the explicit computation of lie-derivatives. Following the work of Seifried [143], equation (6.24) and a corresponding second order derivative,

$$\ddot{\boldsymbol{y}} = \boldsymbol{H}(\boldsymbol{q})\ddot{\boldsymbol{q}} + \dot{\boldsymbol{H}}(\boldsymbol{q})\dot{\boldsymbol{q}}, \tag{6.26}$$

is applied in (6.9) to

$$\ddot{\boldsymbol{y}} = \boldsymbol{H}(\boldsymbol{q})\boldsymbol{M}(\boldsymbol{q})^{-1}\left(\boldsymbol{P}(\boldsymbol{q})\boldsymbol{u}_d - \boldsymbol{k}(\boldsymbol{q}, \dot{\boldsymbol{q}})\right) + \dot{\boldsymbol{H}}(\boldsymbol{q})\dot{\boldsymbol{q}}, \tag{6.27}$$

which represents the IONF for a general multi-body system. A control law for $\boldsymbol{u}_d$ can now be developed to regulate $\boldsymbol{y}$ to desired set points or track a desired trajectory.

In the present work, the nonlinear transformation (6.25) is a permutation of the generalized coordinates by the matrix $\boldsymbol{\Pi} \in \mathbb{R}^{6\times 6}$ that splits $\boldsymbol{q}$ into the outputs $\boldsymbol{y}$ and the remaining coordinates $\boldsymbol{q}_r$,

$$\begin{pmatrix} \boldsymbol{q}_r \\ \boldsymbol{y} \end{pmatrix} = \boldsymbol{\Pi}\boldsymbol{q} = \boldsymbol{\phi}(\boldsymbol{q}). \tag{6.28}$$

Equation (6.28) yields that the matrix $\boldsymbol{H} \in \mathbb{R}^{r\times r}$ is also a (constant) permutation matrix. In other words, as the overall goal is to control the pose which is described by the generalized coordinates, a subset of these coordinates is chosen as an output. This allows to divide (6.9) into a block structure, by applying corresponding permutation matrices, which leads to the following expressions[2] for the mass matrix, Coriolis and centrifugal matrix, vector of gravitational forces, tendon coupling and nonlinear Cartesian spring forces,

$$\boldsymbol{M} = \begin{pmatrix} \boldsymbol{M}_{rr} & \boldsymbol{M}_{ry} \\ \boldsymbol{M}_{yr} & \boldsymbol{M}_{yy} \end{pmatrix}, \quad \boldsymbol{k}(\boldsymbol{q}, \dot{\boldsymbol{q}}) = \begin{pmatrix} \boldsymbol{k}_r \\ \boldsymbol{k}_y \end{pmatrix}, \quad \boldsymbol{P} = \begin{pmatrix} \boldsymbol{P}_r \\ \boldsymbol{P}_y \end{pmatrix}. \tag{6.29}$$

To generate the IONF, the dynamics of $\boldsymbol{q}_r$ can be expressed using (6.29),

$$\ddot{\boldsymbol{q}}_r = \boldsymbol{M}_{rr}^{-1}(\boldsymbol{P}_r\boldsymbol{u}_d - \boldsymbol{k}_r - \boldsymbol{M}_{ry}\ddot{\boldsymbol{y}}). \tag{6.30}$$

Then, (6.30) is set into equation (6.9) which yields

$$\ddot{\boldsymbol{y}} = \bar{\boldsymbol{M}}^{-1}\left(\bar{\boldsymbol{P}}\boldsymbol{u}_d - \bar{\boldsymbol{k}}\right) \tag{6.31}$$

and coincides with equation (6.27). The introduced quantities are

$$\bar{\boldsymbol{M}} = (\boldsymbol{M}_{yy} - \boldsymbol{M}_{yr}\boldsymbol{M}_{rr}^{-1}\boldsymbol{M}_{ry}) \in \mathbb{R}^{r\times r}, \tag{6.32}$$

$$\bar{\boldsymbol{k}} = \boldsymbol{k}_y - \boldsymbol{M}_{yr}\boldsymbol{M}_{rr}^{-1}\boldsymbol{k}_r \in \mathbb{R}^r, \tag{6.33}$$

$$\bar{\boldsymbol{P}} = \boldsymbol{P}_y - \boldsymbol{M}_{yr}\boldsymbol{M}_{rr}^{-1}\boldsymbol{P}_r \in \mathbb{R}^{r\times r}. \tag{6.34}$$

In summary, the IONF is composed of the dynamics of the outputs (6.31) and the dynamics of the remaining coordinates (6.30), often denoted as the internal dynamics of the system. The following two paragraphs will now derive control laws for $\boldsymbol{u}_d$ that shape the dynamics of the output error $\boldsymbol{e}_y \in \mathbb{R}^r$ which is the difference between $\boldsymbol{y}$ and a desired output $\boldsymbol{y}_d \in \mathbb{R}^r$,

$$\boldsymbol{e}_y = \boldsymbol{y} - \boldsymbol{y}_d. \tag{6.35}$$

This is done by canceling the output dynamics of the system, demanding a non-singular $\bar{\boldsymbol{M}}^{-1}(\boldsymbol{q})\bar{\boldsymbol{P}}(\boldsymbol{q})$ which is similar to the inverse dynamics approach of fully actuated systems. As the internal dynamics (6.30) appear through the transformation, one needs to guarantee that the internal dynamics remain stable for the desired control law, which is otherwise not applicable.

Remark: If the system is differentially flat, the internal dynamics can be decoupled from the control law and therefore cannot get unstable through the control action. In a differentially flay system, a flat output exist from which the full state and the input can be determined by a finite number of derivatives of the output. Flatness of nonlinear system is described by the fundamental work of Flies *et al.* [144] which also provide some examples to become familiar with the topic.

6.4.2. Partial feedback linearization

The goal of the partial feedback linearization is to shape exponentially stable output error dynamics, for the output error (6.35). This is achieved by a nonlinear feedback and a novel control input $\bar{\boldsymbol{u}} \in \mathbb{R}^r$,

$$\boldsymbol{u}_d = \bar{\boldsymbol{P}}^{-1}\left(\bar{\boldsymbol{M}}\bar{\boldsymbol{u}} + \bar{\boldsymbol{k}}\right), \tag{6.36}$$

[2]The functional relations will be dropped out, except in the cases where it will be explicitly needed.

to linearize and decouple of the output dynamics (6.31) to

$$\ddot{\boldsymbol{y}} = \bar{\boldsymbol{u}}. \tag{6.37}$$

By designing the new control input to

$$\bar{\boldsymbol{u}} = \ddot{\boldsymbol{y}}_d - \boldsymbol{K}_p(\boldsymbol{y} - \boldsymbol{y}_d) - \boldsymbol{K}_d(\dot{\boldsymbol{y}} - \dot{\boldsymbol{y}}_d) \tag{6.38}$$

with positive definite matrices $\boldsymbol{K}_p, \boldsymbol{K}_d \in \mathbb{R}^{r\times r}$ and a reference trajectory for $(\boldsymbol{y}_d, \dot{\boldsymbol{y}}_d, \ddot{\boldsymbol{y}}_d)$. The control law (6.38) exponentially regulates the error $\boldsymbol{y} - \boldsymbol{y}_d$ to zero as the closed loop behavior is described by

$$\ddot{\boldsymbol{e}}_y + \boldsymbol{K}_d\dot{\boldsymbol{e}}_y + \boldsymbol{K}_p\boldsymbol{e}_y = \boldsymbol{0}. \tag{6.39}$$

The control law (6.38) is applicable if and only if the internal dynamics (6.30) are stable. A formal stability proof for (6.30) is often quite complex especially due to the strong coupling in the inputs by the tendon coupling $\boldsymbol{P}(\boldsymbol{q})$. Therefore, the concept of zero dynamics is applied [142]. The zero dynamics of the system correspond to the internal dynamics under the constraint that the output is constant, e.g. $\boldsymbol{y} = \boldsymbol{y}_0$ which implies $\dot{\boldsymbol{y}} = \ddot{\boldsymbol{y}} = \boldsymbol{u} = \boldsymbol{0}$, which yields

$$\boldsymbol{M}_{rr}\ddot{\boldsymbol{q}}_r + \boldsymbol{k}_r = \boldsymbol{P}_r\bar{\boldsymbol{P}}^{-1}\bar{\boldsymbol{k}}. \tag{6.40}$$

For the given examples, the stability of (6.40) is assessed.

6.4.3. Passivity based approach

The goal of the passivity based approach is to create a more robust behavior of the closed loop system and render the dynamics of the output error (6.35) to be passive. This control approach also compensates for the nonlinear term $\bar{\boldsymbol{k}}(\boldsymbol{q}, \dot{\boldsymbol{q}})$ but keeps the imposed inertia properties of the output dynamics $\bar{\boldsymbol{M}}$. By designing the a new control law which is composed of a nonlinear feedback and a new input $\bar{\boldsymbol{u}} \in \mathbb{R}^r$,

$$\boldsymbol{u}_d = \bar{\boldsymbol{P}}^{-1}\left(\bar{\boldsymbol{u}} + \bar{\boldsymbol{k}}\right), \tag{6.41}$$

the output dynamics are shaped to

$$\bar{\boldsymbol{M}}\ddot{\boldsymbol{y}} = \bar{\boldsymbol{u}}. \tag{6.42}$$

The novel control input $\bar{\boldsymbol{u}}$ will be chosen to

$$\bar{\boldsymbol{u}} = \bar{\boldsymbol{M}}\ddot{\boldsymbol{y}}_d - \boldsymbol{K}_p(\boldsymbol{y} - \boldsymbol{y}_d) - (\boldsymbol{K}_d + \bar{\boldsymbol{C}})(\dot{\boldsymbol{y}} - \dot{\boldsymbol{y}}_d). \tag{6.43}$$

The additional matrix $\bar{\boldsymbol{C}} \in \mathbb{R}^{r\times r}$ is introduced in order to produce a skew symmetric term of the form

$$(\dot{\bar{\boldsymbol{M}}} - 2\bar{\boldsymbol{C}}) = -(\dot{\bar{\boldsymbol{M}}} - 2\bar{\boldsymbol{C}})^T, \tag{6.44}$$

to generate a control law which renders the closed loop dynamics to be passive. To determine $\bar{\boldsymbol{C}}$, the approach proposed in [145] is followed, which is based on the property that the Coriolis and centrifugal matrix of the system (6.1) fulfills $\dot{\boldsymbol{M}} = \boldsymbol{C} + \boldsymbol{C}^T$ which is valid for the given system. After rearranging of (6.29), the matrix can be found to

$$\begin{aligned}
\bar{\boldsymbol{C}} =& \boldsymbol{C}_1 + \boldsymbol{C}_2, \\
\boldsymbol{C}_1 =& \boldsymbol{C}_{yy} - \boldsymbol{C}_{yr}\boldsymbol{M}_{rr}^{-1}\boldsymbol{M}_{ry} + \boldsymbol{M}_{yr}\boldsymbol{M}_{rr}^{-1}\boldsymbol{C}_{ry}, \\
\boldsymbol{C}_2 =& \boldsymbol{M}_{yr}\boldsymbol{M}_{rr}^{-1}\boldsymbol{C}_{rr}\boldsymbol{M}_{rr}^{-1}\boldsymbol{M}_{ry}.
\end{aligned} \tag{6.45}$$

The closed loop error dynamics for the passivity-based controller are

$$\bar{\boldsymbol{M}}\ddot{\boldsymbol{e}}_y + \bar{\boldsymbol{C}}\dot{\boldsymbol{e}}_y + \boldsymbol{K}_d\dot{\boldsymbol{e}}_y + \boldsymbol{K}_p\boldsymbol{e}_y = \boldsymbol{0} \tag{6.46}$$

which are passive and the zero-dynamics correspond to equation (6.40).

Table 6.1.: Controller gains for simulation example 1 & 2

PFL	Gains	PBC	Gains	PFL-FEM	Gains
$\boldsymbol{K}_p$	$k_{p,1} = 50000\frac{N}{m}$	$\boldsymbol{K}_p$	$k_{p,1} = 33000\frac{N}{m}$	$\boldsymbol{K}_p$	$k_{p,1} = 1000\frac{N}{m}$
	$k_{p,2,3,4} = 50000\frac{\mathrm{Nm}}{\mathrm{rad}}$		$k_{p,2} = 91\frac{\mathrm{Nm}}{\mathrm{rad}}$		$k_{p,2} = 1000\frac{\mathrm{Nm}}{\mathrm{rad}}$
			$k_{p,3} = 18\frac{\mathrm{Nm}}{\mathrm{rad}}$		
			$k_{p,4} = 44\frac{\mathrm{Nm}}{\mathrm{rad}}$		
$\boldsymbol{K}_d$	$k_{d,1} = 500\frac{\mathrm{Ns}}{\mathrm{m}}$	$\boldsymbol{K}_d$	$k_{d,1} = 330\frac{\mathrm{Ns}}{\mathrm{m}}$	$\boldsymbol{K}_d$	$k_{d,1} = 100\frac{\mathrm{Ns}}{\mathrm{m}}$
	$k_{d,2,3,4} = 1000\frac{\mathrm{Nms}}{\mathrm{rad}}$		$k_{d,2} = 2\frac{\mathrm{Nms}}{\mathrm{rad}}$		$k_{d,2} = 100\frac{\mathrm{Nms}}{\mathrm{rad}}$
			$k_{d,3} = 0.35\frac{\mathrm{Nms}}{\mathrm{rad}}$		
			$k_{d,4} = 0.87\frac{\mathrm{Nms}}{\mathrm{rad}}$		

Simulation example 1

In the first example, the reduced nonlinear model based on the NKLS-model of the continuum is applied and the designed controller are examined. The generalized coordinates are $\boldsymbol{q} = (l,\, \phi,\, \eta,\, \zeta,\, \theta,\, \iota)$, see equation (4.28) and the outputs are chosen to $\boldsymbol{y} = (l,\, \zeta, \theta,\, \iota)^T$. After a set point is reached in the simulation study, the system is externally disturbed whereas afterward, the system is driven back to the initial configuration. The desired set point is generated as described in Section 6.1.2 with $\boldsymbol{u}_{d,init} = (10,\, 40,\, 40,\, 10)^T$ which corresponds to a motion to the front and yields that l, η, ζ are majorly moved. The disturbance torque is applied along θ only with 1 Nm for 0.3 s. The controller gains $\boldsymbol{K}_p$, $\boldsymbol{K}_d \in \mathbb{R}^{4\times4}$ for the partial feedback linearization (PFL) and the passivity based approach (PBC) are summarized in Tab. 6.1 and the simulated behavior is given in Fig. 6.4. The simulated behavior displays no significant difference between the PFL and the PBC as both controllers present a stable response and track the desired output perfectly without perceptible control error. As a perfect knowledge of the physical parameters is assumed in the simulation, this is not surprising. However, it needs to be noted that the external disturbance which is applied on θ is visible in ϕ, one of the remaining coordinates, and the controller is not able to damp this motion. In contrast, good vibration damping can be assessed in θ. By the nonlinear feedback, the states of the internal dynamics are rendered unobservable which might be the explanation for the shown characteristic.
The second and fourth column of Fig. 6.4 displays the control action $\boldsymbol{u}_d$ and the projected compensation of $\bar{\boldsymbol{P}}(\boldsymbol{q})^{-1}\bar{\boldsymbol{f}} \in \mathbb{R}^4$ for each tendon $i = 1, 2, 3, 4$. Here, the term $\bar{\boldsymbol{f}} \in \mathbb{R}^4$ is generated similarly to equation (6.33),

$$\begin{aligned} \begin{pmatrix} \boldsymbol{f}_r \\ \boldsymbol{f}_y \end{pmatrix} &= \boldsymbol{\Pi}\, \boldsymbol{f}(\boldsymbol{q}), \\ \bar{\boldsymbol{f}} &= \boldsymbol{f}_y - \boldsymbol{M}_{yr}\boldsymbol{M}_{rr}^{-1}\boldsymbol{f}_r. \end{aligned} \tag{6.47}$$

By observation, the major amount of control action is generated by the projected feedback compensation of the continuum spring (6.47). This adds robustness to the closed loop system as the controller gains can be set comparably low.

As mentioned, the nonlinear control law (6.36) and (6.43) are applicable if and only if the internal dynamics of the IONF (6.30) remain stable which is assessed by the concept of zero-dynamics. In the thesis, local asymptotic stability of (6.40) is investigated using Lyapunov's indirect method. As all the Eigenvalues of the linearized zero dynamics[3] are

[3]The equation of motion are linearized around the static equilibrium point $\boldsymbol{q}_0 = (0.95, 0, 0, 0, 0, 0)^T$ which

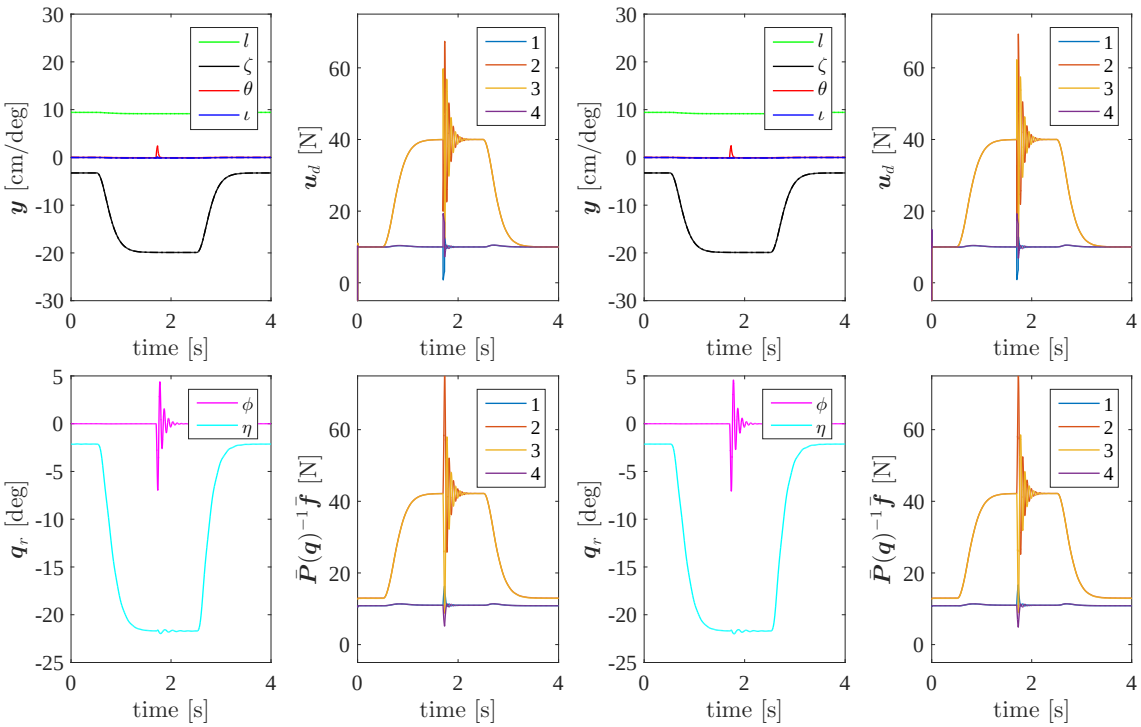

Figure 6.4.: Simulation example 1 which compares the partial feedback linearization (PFL)and the passivity based control (PBC) approach using the equation of motion with the NKLS approximation of the continuum. Column 1-2: Outputs $\boldsymbol{y}$, remaining coordinates $\boldsymbol{q}_r$, control action $\boldsymbol{u}_d$ and nonlinear feedback of the PFL approach. Column 3-4: Outputs $\boldsymbol{y}$, remaining coordinates $\boldsymbol{q}_r$, control action $\boldsymbol{u}_d$ and nonlinear feedback of the PBC approach.

in the left half-plane (-3.75 ± 59.7i, -3.75 ± 57.7i), we can conclude local asymptotic stability of (6.40).

Simulation example 2

The second example treats the partial feedback linearization approach for the dynamic FEM model derived in the Appendix A.1. The generalized coordinates of the system $\boldsymbol{q} \in \mathbb{R}^{3(k_{el}+1)}$ are given in (A.36) and the equation of motion are recalled,

$$\begin{aligned} \boldsymbol{M}(\boldsymbol{q})\ddot{\boldsymbol{q}}+\boldsymbol{k}(\boldsymbol{q},\dot{\boldsymbol{q}}) &= \boldsymbol{C}^{L,T}\boldsymbol{P}(\boldsymbol{q}_L)\boldsymbol{u}_d = \bar{\boldsymbol{P}}(\boldsymbol{q}_L)\boldsymbol{u}_d, \\ \boldsymbol{k}(\boldsymbol{q},\dot{\boldsymbol{q}}) &= \boldsymbol{C}^{L,T}\boldsymbol{C}_H\boldsymbol{C}^L\dot{\boldsymbol{q}}_L + \boldsymbol{f}^{int} + \boldsymbol{f}^{g,beam} + \boldsymbol{f}^{g,head} + \boldsymbol{d}\dot{\boldsymbol{q}}. \end{aligned} \tag{6.48}$$

As the structure of the dynamic FEM equations are comparable to a nonlinear rigid body dynamics, the partial feedback linearization based on the IONF is applicable. In total, $r = 2$ tendons are attached on the system yielding $\boldsymbol{u}_d \in \mathbb{R}^2$. Thus, two outputs can be controlled, selected to

$$\boldsymbol{y} = (x_L,\, \theta_L)^T, \tag{6.49}$$

and the remaining coordinates $\boldsymbol{q}_r \in \mathbb{R}^{3k_{el}+1}$ are

$$\boldsymbol{q}_r = \left(x^1,\, z^1,\, \theta^1,\, \ldots,\, x^{k_{el}},\, z^{k_{el}},\, \theta^{k_{el}},\, z^{k_{el}+1}\right)^T. \tag{6.50}$$

Following the procedure displayed in Section 6.4.2, the output dynamics are linearized and decoupled. The new control input is designed according to (6.38) with positive definite matrices $\boldsymbol{K}_p, \boldsymbol{K}_d \in \mathbb{R}^{2\times 2}$, see Tab. 6.1, and a reference trajectory for $(\boldsymbol{y}_d, \dot{\boldsymbol{y}}_d, \ddot{\boldsymbol{y}}_d)$. The simulative results for the proposed set point controller are given in Fig. 6.5. A similar behavior can be observed compared to the results when using the reduced nonlinear model. As before, the main contribution of to the control action is generated by the nonlinear feedback of the internal forces of the continuum which adds robustness and the internal dynamics is stable with no oscillations. The internal dynamics correspond to the dynamics of the nodal degree of freedom along the centerline and a continuous bending can be observed for the simulated aggressive motion.
While observing the control action for both tendons, it needs to be noted that the tendon which opposes the motion counteracts the motion during the transient phase, i.e. it pulls in the opposite direction of the motion.

6.5. Feedforward compensation of the continuum

In the former section, a control law is suggested which cancel known dynamic properties of the input output normal form (IONF) by feedback under the assumption that the internal dynamics are stable. For the hardware implementation later on, this yields that the full estimated state is used to compute nonlinear forces due to gravity, internal forces of the continuum, Coriolis and centrifugal terms and damping. Due to inaccuracies in the estimated quantities, this might result in an undesired behavior.
In the simulation examples 1 and 2 it is observed, that the amount of control action is mainly resulting from the feedback of the internal forces of the continuum, i.e. the restoring forces of a deformed continuum.

correspond to the straight configuration of the mechanism in which no tendon forces are present, $\boldsymbol{u} = (0,0,0,0)^T$.

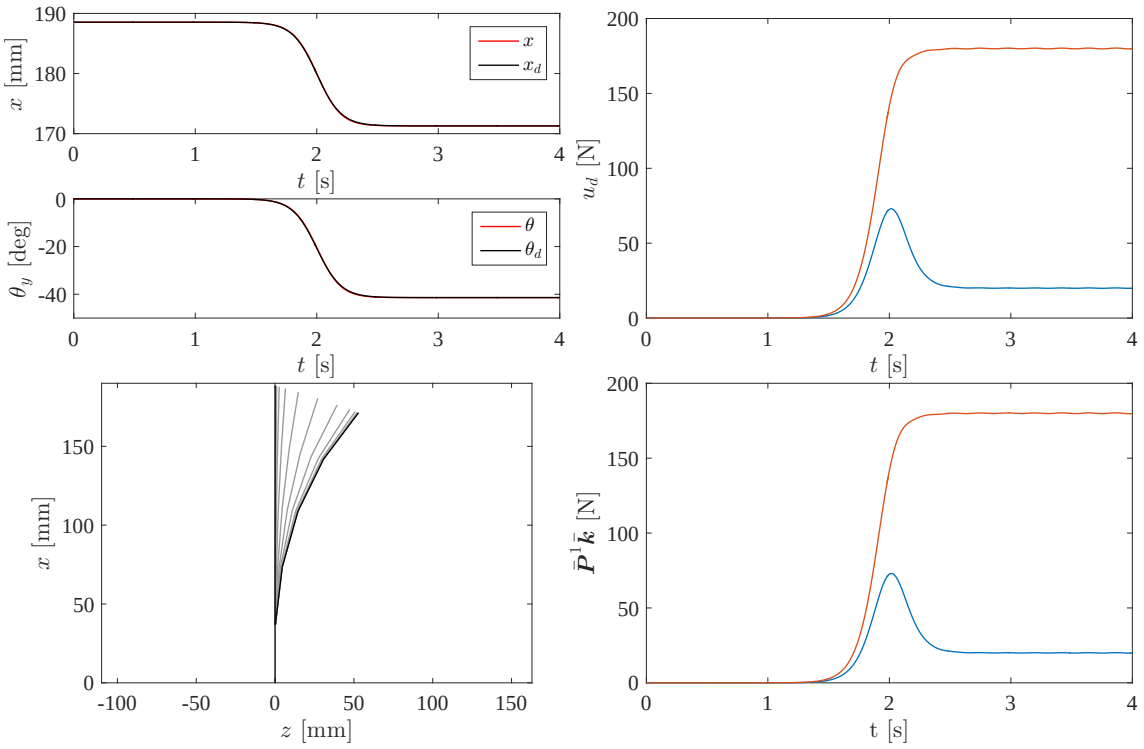

Figure 6.5.: Extension of the partial feedback linearization approach to a beam finite element model to control a set point step of the desired outputs (6.49)

By applying a feedforward control scheme, known dynamic quantities can be compensated based on the desired state of the dynamic equations which avoids feedback of the estimated state and still ensures a compensation of the restoring forces of the continuum, assuming a good knowledge of the model. In this respect, Seifried [146] suggests a composite control law for $\boldsymbol{u}_d$ which consists of a feedforward $\boldsymbol{u}_{d,ff} \in \mathbb{R}^r$ and a feedback part $\boldsymbol{u}_{d,fb} \in \mathbb{R}^r$,

$$\boldsymbol{u}_d = \boldsymbol{u}_{d,ff} + \boldsymbol{u}_{d,fb}. \tag{6.51}$$

For the design of $\boldsymbol{u}_{d,fb}$, Seifried [146] suggest simple linear decoupled controllers on $\boldsymbol{q}_d \in \mathbb{R}^n$, i.e. the derived desired generalized coordinates from $\boldsymbol{y}_d$. For justification, it is argued that the feedback part is only active in cases of disturbances in which the configuration of the system is close to the desired one. The major control effort is carried by the feedforward part. In the following, two approaches are proposed for an underactuated system. At first, a classical inverse model approach is discussed. Second, the so-called servo-control problem is derived and discussed.
The feedforward control law which is derived via model inversion is similar to the one from the partial feedback linearization (6.36) however using the desired state $\boldsymbol{q}_d$, $\dot{\boldsymbol{q}}_d$ and the desired second order derivative of the output $\ddot{\boldsymbol{y}} \in \mathbb{R}^r$,

$$\boldsymbol{u}_{d,ff} = \bar{\boldsymbol{P}}^{-1}(\boldsymbol{q}_d) \left(\bar{\boldsymbol{M}}(\boldsymbol{q}_d) \ddot{\boldsymbol{y}}_d + \bar{\boldsymbol{k}}(\boldsymbol{q}_d, \dot{\boldsymbol{q}}_d) \right). \tag{6.52}$$

In a perfect world in which all dynamic parameters are perfectly known, the control law (6.52) implies that $\ddot{\boldsymbol{y}} - \ddot{\boldsymbol{y}}_d = \boldsymbol{0}$. However, to generate the desired state along a trajectory, the internal dynamics (6.30), a second order differential equation, need to be solved. In summary, the feedforward control law using model inversion consist of three consecutive

steps: 1) the desired outputs need to be differentiated to get $\dot{\boldsymbol{y}}_d$ and $\ddot{\boldsymbol{y}}_d$ 2) the driven internal dynamics (6.30) need to be solved to generate the full desired state $(\boldsymbol{q}, \dot{\boldsymbol{q}})$ and 3) algebraic equation (6.52) need to be applied. Similar to a feedback linearization, the approach is applicable if and only if $\boldsymbol{u}_d$ remains bounded which means that the internal dynamics remain stable.
A second alternative according to [146] for designing a feedforward controller is the servo-constraint approach which considers a desired output $\boldsymbol{y}_d$ in an additional motion constraint $\boldsymbol{c}(\boldsymbol{q}) \in \mathbb{R}^r$ to which the equation of motion (6.9) need to conform with,

$$\begin{aligned} \boldsymbol{M}(\boldsymbol{q})\ddot{\boldsymbol{q}} + \boldsymbol{k}(\boldsymbol{q}, \dot{\boldsymbol{q}}) &= \boldsymbol{P}(\boldsymbol{q})\boldsymbol{u}_d, \\ \boldsymbol{c}(\boldsymbol{q}) = \boldsymbol{h}(\boldsymbol{q}) - \boldsymbol{y}_d &= \boldsymbol{0}. \end{aligned} \tag{6.53}$$

Equation (6.53) is a differential-algebraic equation and its solution yields $\boldsymbol{q}_d$ and the control input $\boldsymbol{u}_d$. Usually, to acquire the solution in real-time on hardware requires higher computational demands which yields that this approach is not suitable for the control problem of this thesis. Nevertheless, controller design based on servo-constraints remains a suitable topic for underactuated continuum mechanisms and a good introduction is given in [147].

In this work, a composite controller according to equation (6.51) is investigated and implemented on the real hardware. The feedback part $\boldsymbol{u}_{d,fb} \in \mathbb{R}^r$ is a simple, decoupled PD-controller,

$$\boldsymbol{u}_{d,fb} = \bar{\boldsymbol{P}}^{-1}(\boldsymbol{q}) \left(\boldsymbol{K}_{c,p} \left(\boldsymbol{y}_d - \boldsymbol{y} \right) + \boldsymbol{K}_{c,d} \left(\dot{\boldsymbol{y}}_d - \dot{\boldsymbol{y}} \right) \right), \tag{6.54}$$

with positive definite gain matrices $\boldsymbol{K}_{c,p}$, $\boldsymbol{K}_{c,d} \in \mathbb{R}^{r \times r}$. The second part is a feedforward actions which is designed based on the inverse model approach. Again, motivated by the fact that the major control action will account for the deformation of the continuum spring, the inverse model considers static quantities only. The control law (6.52) is therefore modified to account only for the terms related to the continuum spring $\bar{\boldsymbol{f}}(\boldsymbol{q}) \in \mathbb{R}^r$,

$$\begin{aligned} \boldsymbol{u}_{d,ff} &= \bar{\boldsymbol{P}}^{-1}(\boldsymbol{q}_d)\bar{\boldsymbol{f}}(\boldsymbol{q}_d), \\ \bar{\boldsymbol{f}}(\boldsymbol{q}_d) &= \boldsymbol{f}_y(\boldsymbol{q}_d) - \boldsymbol{M}_{yr}(\boldsymbol{q})\boldsymbol{M}_{rr}^{-1}(\boldsymbol{q})\boldsymbol{f}_r(\boldsymbol{q}_d), \end{aligned} \tag{6.55}$$

with the quantities given in equation (6.33) and (6.34). The desired pose $\boldsymbol{q}_d$ is generated within the set point generation framework, therefore offline, as explained in section 6.1.2. With equation (6.54) and (6.55), the overall control law design in this section can be summarized to

$$\boldsymbol{u}_d = \bar{\boldsymbol{P}}^{-1}(\boldsymbol{q}) \left(\bar{\boldsymbol{f}}(\boldsymbol{q}_d) + \boldsymbol{K}_{c,p} \left(\boldsymbol{y}_d - \boldsymbol{y} \right) + \boldsymbol{K}_{c,d} \left(\dot{\boldsymbol{y}}_d - \dot{\boldsymbol{y}} \right) \right) \tag{6.56}$$

Simulation example 3

For comparison reasons, the composite control approach (6.51) is investigated in a simulation study. To provide a good comparison, the same simulated procedure is carried out as in simulation example 1. The reduced nonlinear model based on the NKLS-model is applied as dynamic model based on which the designed controller is examined. The generalized coordinates are $\boldsymbol{q} = (l,\, \phi,\, \eta,\, \zeta,\, \theta,\, \iota)$, see equation (4.28) and the outputs are chosen to $\boldsymbol{y} = l, \zeta, \theta, \iota$. A setpoint is reached in the simulation study, and then the system is manually disturbed whereas afterwards, the system is driven back to the initial configuration. The desired set point is generated as described in Section 6.1.2 with $\boldsymbol{u}_{d,init} = [10, 40, 40, 10]^T$ which corresponds to a motion to the front and yields that l, η, ζ

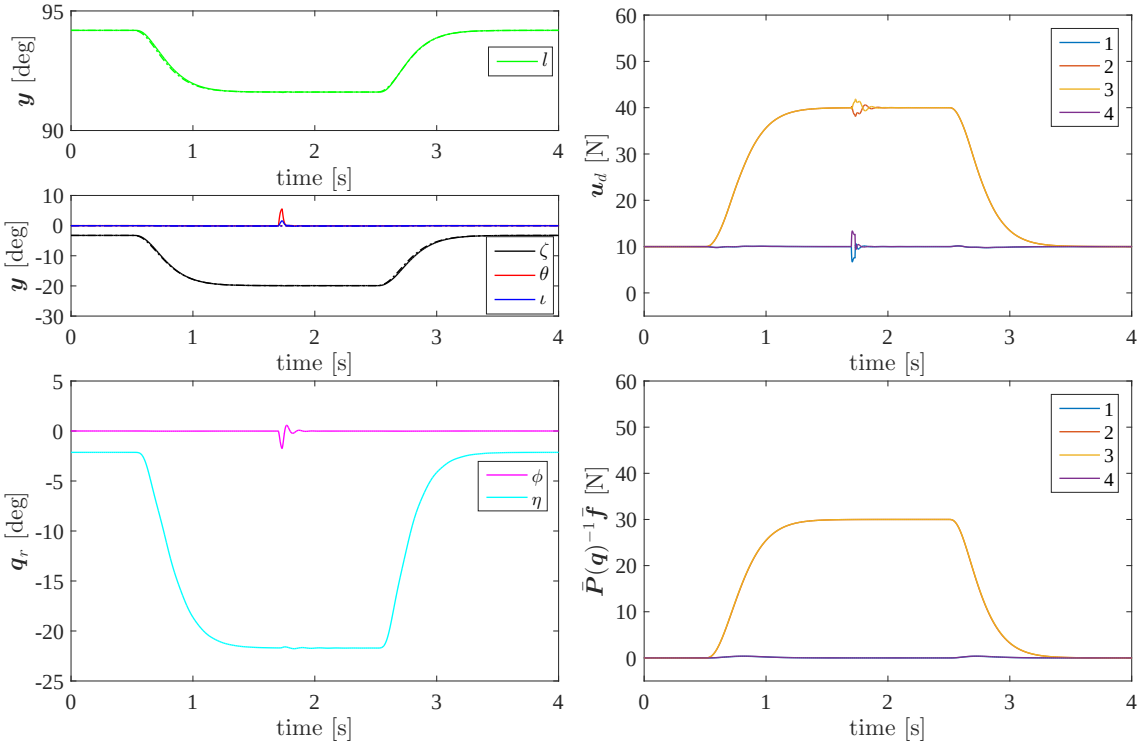

Figure 6.6.: Simulation study using the composite feedback of feedforward and feedback controller. The desired trajectory of $\boldsymbol{y}_d$ is the same as in the simulation example 1

are moved mainly. The disturbance torque is applied along θ only with 1 Nm for 0.3 s. The results of the simulation study are illustrated in Fig. 6.6. A perfect knowledge of the continuum spring is assumed which yields almost perfect tracking in the simulation. However, a slight lack in the real trajectory can be observed in the transient phase of the set point control which is assumed to be due to the neglected effects of inertia and Coriolis forces in the feedforward and therefore could yield to a worst tracking performance. In contrast, the composite controller with the feedforward term can cope with the disturbances much better which can be observed in Fig. 6.6. Especially the oscillation in the remaining coordinates is comparably small and damped much faster. Thus, it is expected that this approach is more robust against disturbances from outside.

6.6. Experimental results

This section will treat an experimental comparison of two controllers. The first controller includes a partial feedback linearization, to linearize and decouple the input-output dynamics and enable a linear control law for the systems along desired outputs (see Section 6.4) and is denoted "PFL" in the following. The second controller of Section 6.5 is designed as a composite feedback which is composed of feedforward control action and a feedback term and is denoted "FF-FB" in the following.
The steady state accuracy, the transient behavior and the robustness against external disturbances of the implemented controller are evaluated in three experiments which are reported by Section 6.6.2, Section 6.6.3 and Section 6.6.4 respectively. Beforehand, the

Table 6.2.: Controller gains empirically tuned for the experiments

PFL	Gains	FF-FB	Gains
$\boldsymbol{K}_p$	$k_{p,1} = 250\frac{N}{m}$	$\boldsymbol{K}_p$	$k_{p,1} = 1\frac{N}{m}$
	$k_{p,2} = 25000\frac{\mathrm{Nm}}{\mathrm{rad}}$		$k_{p,2} = 12\frac{\mathrm{Nm}}{\mathrm{rad}}$
	$k_{p,3} = 50000\frac{\mathrm{Nm}}{\mathrm{rad}}$		$k_{p,3} = 12\frac{\mathrm{Nm}}{\mathrm{rad}}$
	$k_{p,4} = 1500\frac{\mathrm{Nm}}{\mathrm{rad}}$		$k_{p,4} = 9\frac{\mathrm{Nm}}{\mathrm{rad}}$
$\boldsymbol{K}_d$	$k_{d,1} = 2\frac{\mathrm{Ns}}{\mathrm{m}}$	$\boldsymbol{K}_d$	$k_{d,1} = 0.001\frac{\mathrm{Ns}}{\mathrm{m}}$
	$k_{d,2,3} = 200\frac{\mathrm{Nms}}{\mathrm{rad}}$		$k_{d,2} = 0.1\frac{\mathrm{Nms}}{\mathrm{rad}}$
	$k_{d,4} = 120\frac{\mathrm{Nms}}{\mathrm{rad}}$		$k_{d,3} = 0.1\frac{\mathrm{Nms}}{\mathrm{rad}}$
			$k_{d,4} = 0.06\frac{\mathrm{Nms}}{\mathrm{rad}}$

setup of the experiments is present.

6.6.1. Experimental setup

The experiments are carried out on the spatial test bed which is described in Section 2.2.2. The control law of the fast loop is implemented according to Section 6.2 which presents the achieved performance on the same test setup. In the following, three practical issues are given that help to understand the presented experimental results.

Generalized coordinates and output choice: Similar to the simulation examples, the continuum mechanism is described by the generalized coordinates $\boldsymbol{q} = (l,\, \phi,\, \eta,\, \zeta,\, \theta,\, \iota)^T$, see equation (4.28), which implies an approximation of the continuum characteristic by the NKLS model of section 4.2.2. A total number of $r = 4$ outputs are selected to $\boldsymbol{y} = (l,\, \zeta,\, \theta,\, \iota)^T$. The choice of outputs can be motivated by the fact that the motion of ϕ and η is strongly coupled towards the motions of θ, ζ whereas the l-direction can be actuated more independently e.g. by pulling all tendons simultaneously.

Empirical tuning of gain matrices: The gain matrices in equation (6.38) for the PFL controller and in equation (6.54) for the FF-FB controller are empirically tuned in the experiments. Furthermore, a diagonal structure is chosen and the simulation examples provide a good initial guess. The chosen controller matrices are summarized in Tab. 6.2.

Tendon pretension and initialization: A pretension of $\boldsymbol{u}_{pre} = [10,\, 10,\, 10,\, 10]^T$ is added to desired tendon tension forces $\boldsymbol{u}_d \in \mathbb{R}^4$, generated by a controller, to avoid tendon slackness. To initialize the nonlinear controller correctly, the static equilibrium equation is solved,

$$\boldsymbol{k}(\boldsymbol{q}_0, \boldsymbol{0}) = \boldsymbol{P}(\boldsymbol{q}_0)\boldsymbol{u}_{pre} \tag{6.57}$$

to find the initial pose $\boldsymbol{q}_0 \in \mathbb{R}^6$ (and $\boldsymbol{y}_0 \in \mathbb{R}^4$) that correspond to the application of the pretension forces.

6.6.2. Steady state accuracy

The steady state accuracy describes the error between the outputs $\boldsymbol{y}$ and the desired outputs $\boldsymbol{y}_d$ when the system is at rest. Therefore, the transient behavior is not examined. In the experimental study, a total number of 50 set points are reached by both controllers. The set points for $\boldsymbol{y}_d$ (and also $\boldsymbol{q}_d$) are generated by the procedure described in Section 6.1.1 and therefore correspond to static equilibrium points of the mechanism. To compare the steady state accuracy, the component wise output absolute error is computed

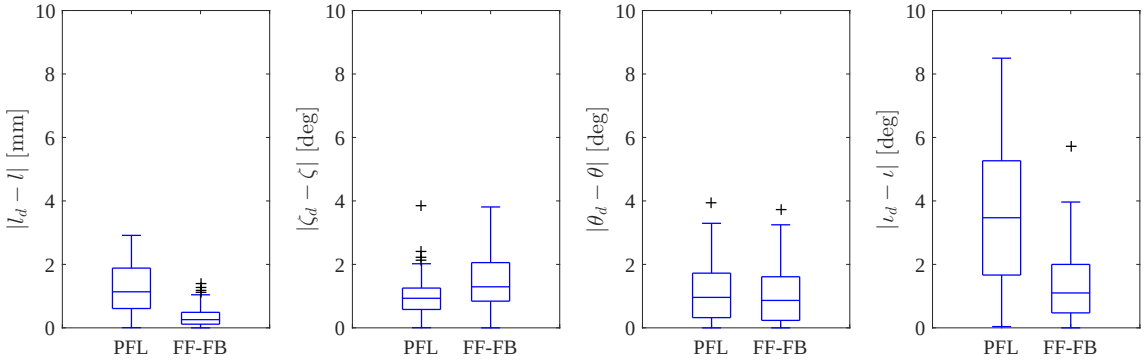

Figure 6.7.: Comparison of partial feedback linearization (PFL) and feedforward control (FF-FB) approach with respect to their steady state accuracy. A total number of 50 poses is sampled in this experiment. The boxplot illustrates the absolute error between desired and measured outputs.

at steady state poses,

$$|l_d - l|, \quad |\zeta_d - \zeta|, \quad |\theta_d - \theta|, \quad |\iota_d - \iota|. \tag{6.58}$$

The steady state error of both controllers is shown in boxplots in Fig. 6.7. Both controller possess a comparable steady state error with median values in between 1 deg and 2 deg. However, it needs to be noted that partial feedback linearization controller possess a considerable higher error in the ι component. In the experiments, it was not possible to tune the corresponding proportional controller gain $k_{p,4}$ high enough to contribute to a smaller error. While increasing this particular gain, the closed loop system tends to get unstable due to an amplification of high-frequency noise. A reason for this behavior might be the state estimation, currently implemented as a nonlinear optimization which performs bigger steps from time to time. In summary, the FF-FB controller provides overall a smaller steady state error and is therefore considered as superior.

6.6.3. Transient behavior

The transient behavior of the closed loop is investigated by a motion sequence where the spatial testbed is driven to 10 consecutively reached set points. The motion starts and ends in the initial configuration. The transition time in between the desired set points is set to 1 sec which generates a dynamic motion. The recorded poses, belonging to this motion sequence, are depicted in Fig. 6.8 and include typical motions of the robotic neck. The corresponding data of the hardware to assess the transient behavior is illustrated in Fig. 6.9 for the PFL controller and in Fig. 6.10 FF-FB-controller. Both figures express the component wise output error $\boldsymbol{y}_d - \boldsymbol{y}$ in the top row. The second row depicts the amount of control action which needs to be generated by the linear part of the respective controller. The overall control law of the PFL-controller is given in equation (6.36) and the second row of Fig. 6.9 expresses the part of (6.36) which belongs to the linear part, i.e. the projected new control input $\bar{\boldsymbol{u}}$ onto the tendon directions,

$$\bar{\boldsymbol{P}}^{-1}\bar{\boldsymbol{M}}\left(\ddot{\boldsymbol{y}}_d - \boldsymbol{K}_p(\boldsymbol{y} - \boldsymbol{y}_d) - \boldsymbol{K}_d(\dot{\boldsymbol{y}} - \dot{\boldsymbol{y}}_d)\right). \tag{6.59}$$

For the case of the FF-FB controller, the second row of Fig. 6.10 depicts the difference between the total desired control action $\boldsymbol{u}_d$ and the feedforward term (6.55).

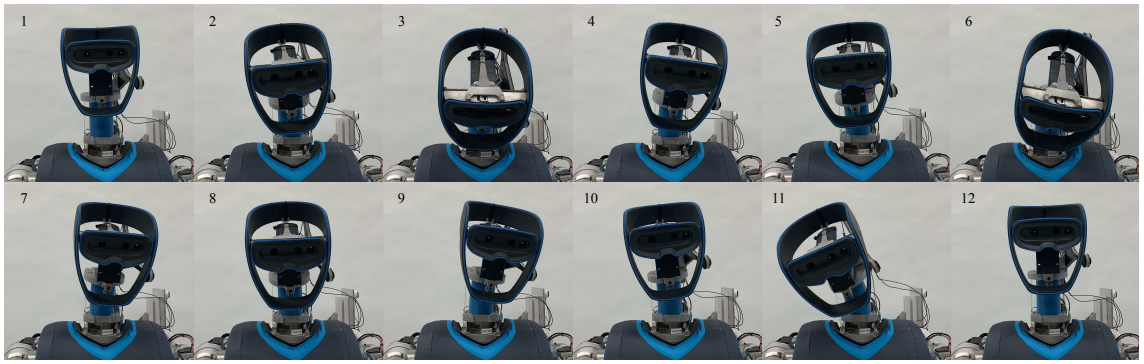

Figure 6.8.: Motion sequence of ten setpoint poses of the robotic neck. The different poses are reached subsequently and the time in between each pose is set to 1 s.

The transient behavior of the PFL controller is stable for the investigated set points and the controller manages to move the system along the 10 desired set points with a transition time of 1 s. However, for the set points 1, 3, 6 and 10 the controller does not manage to stabilize the system to the desired set point in this short time period which can be observed by a non-steady control error. The highest control error is present in ι which coincides with the behavior shown in the "steady state" experiments in paragraph 6.6.2. By looking at the desired tendon tension forces, generated by the PFL controller, two important observations need to be noted. The PFL controller demands high tension forces in the tendons, considering a maximum tolerable tension of 80 N. A possible reason for this is the acceleration feedforward in combination with an insufficient knowledge of the inertia properties as the high tension are demanded in the transient phase. In case the inertia or Coriolis terms are not generated with accurate parameters, the nonlinear feedback might over-compensate these which would result in such high tension forces during the transient. The second observation reveals that the PFL controller desires negative tendon tension forces, which is not feasible as these cannot be realized by the tendons. As introduced in earlier, a pretension $\boldsymbol{u}_{pre}$ is added to $\boldsymbol{u}_d$ to avoid tendon slackness. However, a commanded tension of -40 N (see Fig. 6.9) cannot be compensated by this strategy. As a result, saturation is implemented in the control loop that prevents from commanding negative tensions.

The transient behavior of the FF-FB controller is also stable for the investigated set points and similar to the PFL-controller, all set points are reached in the given amount of time, except set point 1 and 5 which is shown in Fig. 6.10. The highest control error is present in ζ which coincides with the behavior shown in the "steady state" experiments in paragraph 6.6.2. By compensating the continuum spring with the feedforward term $\boldsymbol{u}_{d,ff}$, the feedback term of the composite control law (6.51) does not need to generate high tension forces which can be observed in the lower column of Fig. 6.10. Here, the tension levels remain below 15 N whereas the tension levels of the PFL controller where almost 60 N. Negative tendon tensions are also commanded by the feedback part of the controller during some transients, e.g. from set point 10 back to the initial configuration, however they are below 10 N and are therefore absorbed by the additional pretension forces $\boldsymbol{u}_{pre}$.

6.6.4. Robustness against external disturbances

The robustness of the controllers are examined in the following experiment and Fig. 6.11 depicts the response of the system. Starting from the initial pose, the mechanism is driven

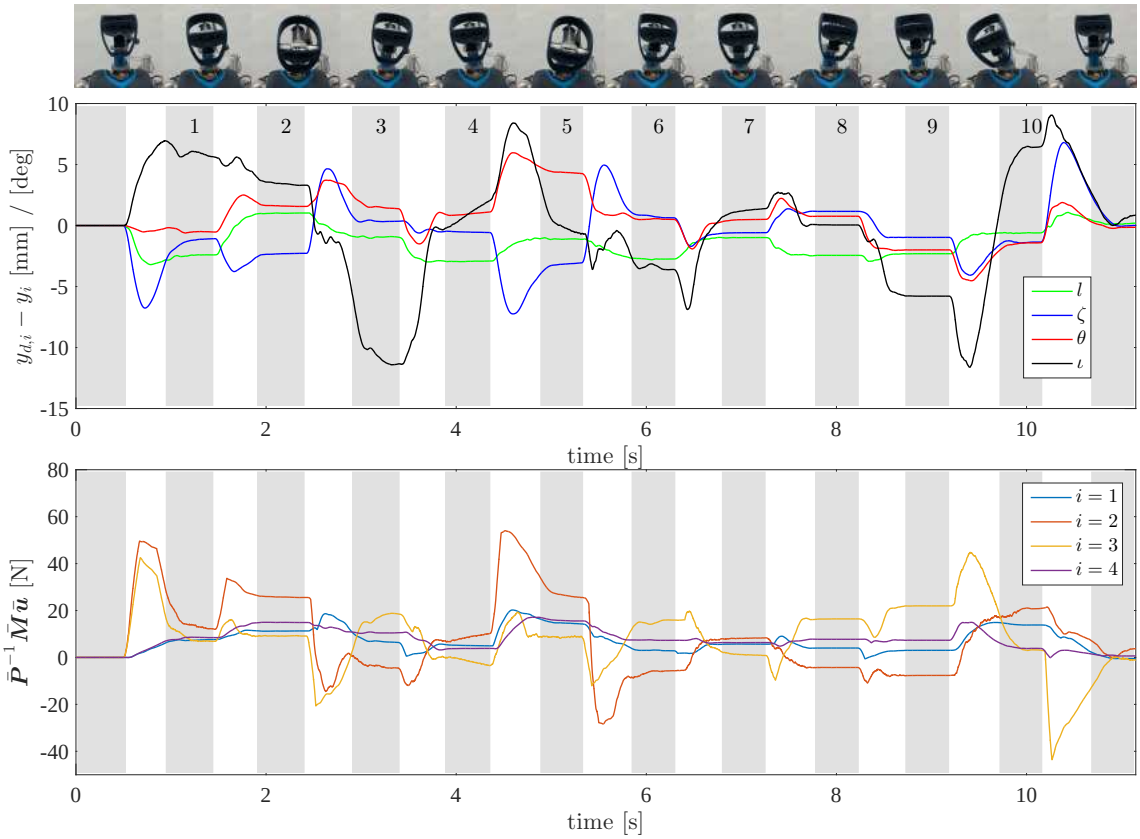

Figure 6.9.: Transient behavior of the PFL controller that drives the system to a sequence of consecutive set points. The grey areas mark the periods at which the desired output has reached it set point. Top row: Component wise output error $\boldsymbol{y}_d - \boldsymbol{y}$. Bottom row: Control action of the feedback part of the controller.

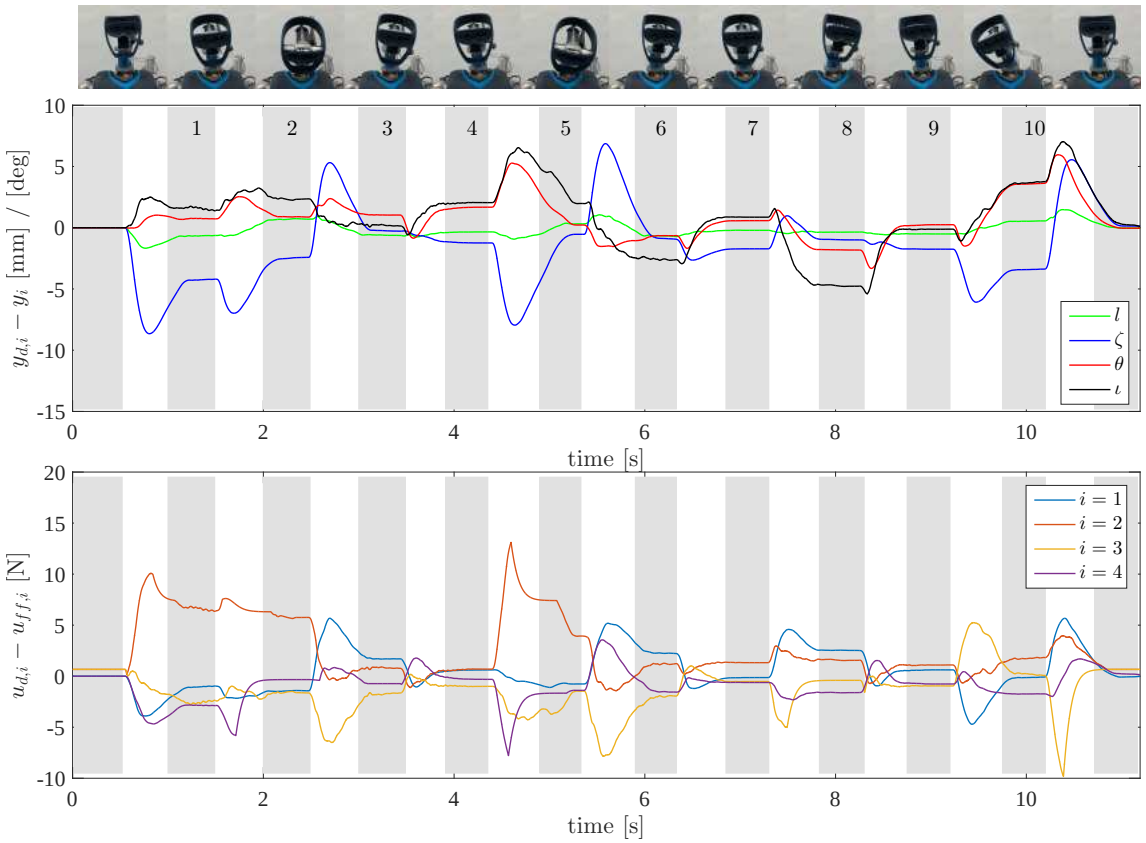

Figure 6.10.: Transient behavior of the FF-FB controller that drives the system to a sequence of consecutive set points. The grey areas mark the periods at which the desired output has reached it set point. Top row: Component wise output error $\boldsymbol{y}_d - \boldsymbol{y}$. Bottom row: Control action of the feedback part of the controller (6.55)

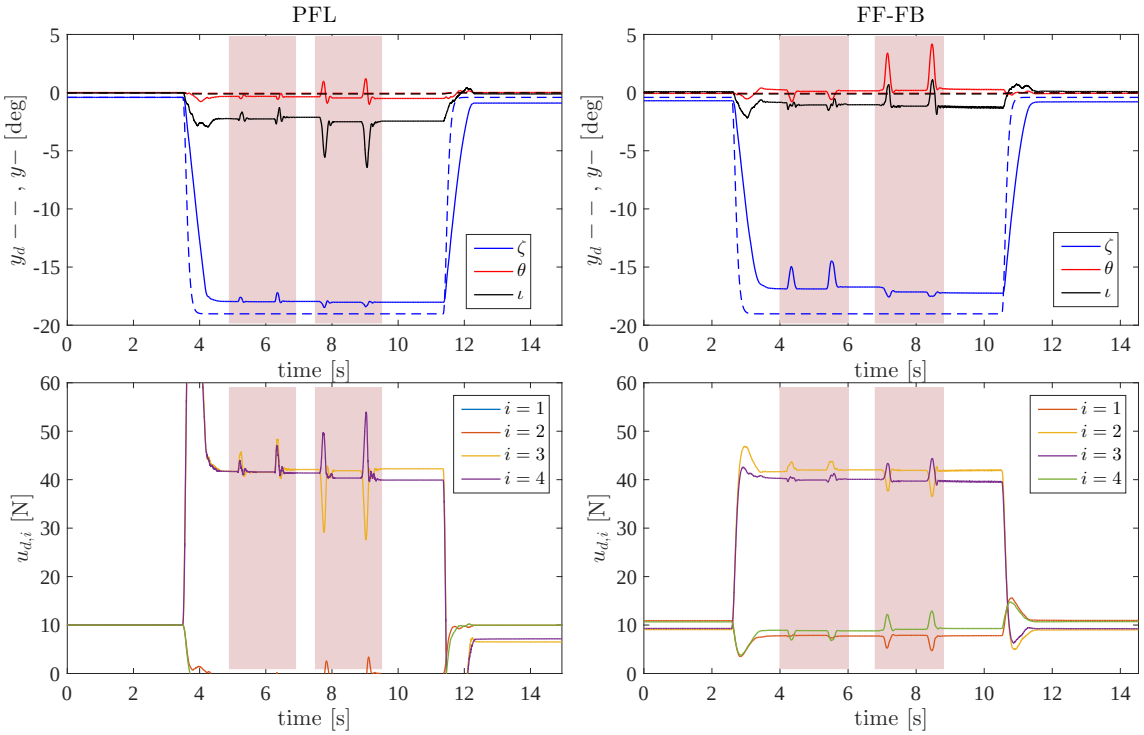

Figure 6.11.: Investigation of the behavior of the closed loop while an external disturbance is applied on the system (indicated by the red time periods). Left column: PFL. Right column: FF-FB.

to a desired set-point $\boldsymbol{y}_d$. After the system has reached steady state, it is manually disturbed, indicated in grey to highlight the corresponding time periods. The disturbance is applied in two directions, the first disturbance acts along the negative y axis and the second disturbance acts along the negative z-axis. After the disturbances, the system is driven back to the initial situation. By observation of the behavior for both controllers shown in Fig. 6.11, it can be stated that both closed loops remain stable under the applied disturbances. Under the assumption that the manual disturbances are similar, the control error of the PFL controller is smaller during the first disturbance compared with the FF-FB controller, which is achieved by higher commanded tensions. In the second disturbances, the control error of both controllers is of similar magnitude but this time, the commanded tendon tension of the PFL controller are considerably higher. This yields that the PFL controller needs to command considerably higher tendon tensions cope with the disturbance.

6.7. Extension: Gain design by Fractional Order Control

Section 6.4 presents the derivation of a control law of for the slow loop that linearizes and decouples the nonlinear dynamics of the output $\boldsymbol{y} \in \mathbb{R}^r$. This partial feedback linearization approach involves a new input $\bar{\boldsymbol{u}} \in \mathbb{R}^r$ which is used to generate exponentially stable output error dynamics by a simple proportional-derivative (PD) control law. The gain matrices are diagonal, due to the decoupled structure of the dynamics, whereas the gains for each coordinate are chosen empirically without a specific consideration of the imposed bandwidth or the incorporated robustness.

The term *fractional order* in Fractional Order Control (FOC) relates to the order of the frequency variable $s \in \mathbb{C}$ which appears when a transfer function of a linear dynamic system is expressed in the frequency domain. For example, an integer order PD controller, with a transfer function in the frequency domain $PD(s) \in \mathbb{C}$ expresses

$$PD(s) = k_p + k_d\, s^1 \tag{6.60}$$

with (integer) order = 1. In fraction order control, the concept of integer orders is extended and allows for a general order = $\alpha \in \mathbb{R}$ (a fractions of an integer). The general derivation of fractional order transfer functions relies on a generalization of integration and differentiation to a non-integer order fundamental continuous integral-differential operator. For an introduction to the topic, the tutorial by Chen *et al.* [148] is recommended or the comprehensive book by Monje *et al.* [149] is suggested.
For linear single-input single output systems, fractional order control is applied experimentally to a variety of applications [150]. Furthermore, systems that incorporate structural compliance [151, 152] are treated. In these works, the compliance led to unwanted oscillations and the designed controller damps these undesired vibrations. For systems in which the structural compliance enables the motion, a fractional order controller lag compensator showed a promising performance. The work is published in Deutschmann *et al.* [83] whereas the controller design is based on a general formalism by Monje *et al.* [153]. In the following section, the design procedure and this preliminary study are discussed. Afterwards, the design procedure is utilized on the spatial system.

6.7.1. Preliminary study: Application of fractional order control onto a Single-Input Single-Output system

The preliminary study treats the planar test bed described in Section 2.2.1. Instead of linearizing the system via nonlinear feedback, the dynamic behavior is experimentally obtained and modeled as a linear time invariant a linear time invariant transfer function $G(s) \in \mathbb{C}$ of second order,

$$G(s) = \frac{K\omega_{\mathrm{n}}^2}{s^2 + 2\delta\omega_{\mathrm{n}}s + \omega_{\mathrm{n}}^2} = \frac{\Theta_{\mathrm{L}}(s)}{\tau_{\mathrm{L}}(s)}. \tag{6.61}$$

The dynamics in x and z are neglected in the following. The transfer function (6.61) relates the tip angle $\theta_L \in \mathbb{R}$ of the planar continuum mechanism and the control action is a generalized torque $\tau_L \in \mathbb{R}$ at the tip that is generated by the two, antagonistically acting tendon forces $\boldsymbol{u} \in \mathbb{R}^2$. The design procedure of the fractional order controller is in the frequency domain which yields that θ_L and τ_L are transformed into the frequency domain to $\Theta_L(s) \in \mathbb{C}$ and $\tau_L(s) \in \mathbb{C}$. The tendon-tension control dynamics is neglected whereas the actuator positions are used to estimate θ_L. In the investigated workspace, the relationship between the actuator positions and θ_L is linear. The experimental identification of (6.61) yields the steady-state gain $K = 0.0631$, the Eigen frequency of the system $\omega_n = 37.8021$, and the linear damping $\delta = 0.4$.

It is outlined above that a fractional order lag compensator is designed in the preliminary study which is adapted from a general fractional order *proportional-integral-derivative* PID controller $PID_{frac}(s) \in \mathbb{C}$ with input filter, see [153],

$$PID_{frac}(s) = k_c x^{\alpha} \underbrace{\left(\frac{\lambda_1 s + 1}{s}\right)^{\lambda}}_{\text{FO PI controller}} \underbrace{\left(\frac{\lambda_2 s + 1}{x\lambda_2 s + 1}\right)^{\alpha}}_{\text{FO lead or lag}}.$$

In [83], it is discussed that the PI part of the controller is not feasible for the present mechanism since external collisions and disturbance are inevitable in continuum mechanism which result in an accumulation of control action due to the integral part. Therefore, a generalized fractional order (FO) $PD^{\alpha}(s) \in \mathbb{C}$ controller is designed,

$$PD^{\alpha}(s) = \left(\frac{\lambda s + 1}{x\lambda s + 1}, \right)^{\alpha}, \tag{6.62}$$

which corresponds to a fractional order lead or lag compensator, depending on the sign of α. The transfer function (6.62) can be physically interpreted as a FO-PD controller plus a noise filter. Three parameters, $\alpha, \lambda, x \in \mathbb{R}$, are incorporated in the controller and will be determined by fulfilling the following requirements. Following [153] specifications related to gain crossover frequency $\omega_{cg} \in \mathbb{R}$, phase margin $\varphi_m \in \mathbb{R}$ and a robustness constraint are going to be considered, due to their importance regarding performance and stability. The design problem is to determine α, λ, x that the controller (6.62) complies with the following:

- **Gain crossover frequency.** The crossover frequency ω_{cg} of a transfer function specifies the bandwidth of the system. The crossover frequency is defined as

$$|PD^{\alpha}(j\omega_{cg})G(j\omega_{cg})|_{\mathrm{dB}} = 0 \text{ dB} \tag{6.63}$$

- **Phase margin.** According to [154], the phase margin φ_m is related to the damping of the system and is an important measure for robustness. The phase margin is defined as

$$\arg(PD^{\alpha}(j\omega_{\mathrm{cg}})G(j\omega_{\mathrm{cg}})) = -\pi + \varphi_{\mathrm{m}} \tag{6.64}$$

- **Robustness to variations in the gain of the plant.** According to [155], this requirement can be addressed by demanding:

$$\left.\frac{d(\arg(PD^{\alpha}(j\omega)G(j\omega)))}{d\omega}\right|_{\omega=\omega_{cg}} = 0 \text{ s} \tag{6.65}$$

Equation (6.65) ensures that the phase of the open loop system $PD^{\alpha}(j\omega)G(j\omega)$ to be flat at $\omega = \omega_{cg}$ and in this way almost constant within in an interval centered at ω_{cg}. This property implies a higher robustness against changes in the steady-state gain whereas a possible overshoot is almost constant within a range, a property which is called "iso-damping" property of the transient. The parameters α, λ, x are found by applying the design method from Monje *et al.* [153], a specified crossover frequency of $\omega_{cg} = 3$ [rad/s] and a specified phase margin of $\varphi_m = 80$ [deg] which results in a controller that is expressed by

$$PD^{\alpha}(s) = 906 \left(\frac{6.97s + 1}{0.0069s + 1} \right)^{-1.12}. \tag{6.66}$$

To evaluate the performance of the controller (6.66), two integer order controller are designed using the same frequency domain related specifications for ω_{cg} and φ_m, which are a integer order PID and a integer order LAG compensator. The corresponding Bode plot of the three designed controller, PID, LAG and $PD^{\alpha}(s)$ (FOC) in open loop is given in the left of Fig. 6.12 which states that each controller (approximately) fulfills the desired specifications. The implementation of a FO controller is usually done by an IO- approximation.

For details and a review see [149]. Here (6.66) is approximated using the MATLAB© routine *invfreqs* which fits the frequency response of the FO controller in a frequency of two decades around the gain crossover frequency, with two poles/zeros:

$$\tilde{PD}^{\alpha}(s) = \frac{0.3908s^2 + 67.3s + 774.4}{s^2 + 7.465s + 0.8204} \tag{6.67}$$

The experimental results confirm that the inaccuracy in the linear approximation of the system dynamics can be handled by these robustness properties of the fractional order controller. Now, it will be discussed to which extent one can make analytic stability statements for the application of the (linear) fractional-order controller to the nonlinear system dynamics. In particular, the passivity properties of the closed-loop system are investigated. As a purely mechanical structure, the continuum mechanism clearly is a passive system with the physical energy as a storage function, considering the input τ_L and the output $\dot{\theta}_L$. This input-output pair represents the physical power between the controller and the mechanism. In the following, it is investigated if the designed controllers represents a passive system w.r.t. the input $\dot{\theta}_L$ and the output $-\tau_L$, i.e. in feedback interconnection with the mechanism. Since passivity is preserved by feedback interconnection of passive subsystems [156], passivity can be concluded of the closed loop system. To investigate passivity of the controllers, a transformed controller transfer function $P(s) = -PD^{\alpha}(s)\frac{1}{s}$ need to be considered, which is in essence, the transfer function transformed to the desired power ports, the input $\dot{\theta}_L$ and the output $-\tau_L$. Passivity requires $\mathrm{Re}(P(j\omega)) \geq 0$ (positive realness) for all frequencies ω, which can be checked with a Nyquist plot. Figure 6.12, right shows the Nyquist plots of $P(s)$ corresponding to the three designed controllers. One can easily observe that the fractional-order controller as well as its finite-order approximation are positive real, while this is not the case for the PID controller. Notice that this analysis assumes that the dynamics of the force-controlled actuators is sufficiently fast so that it can be neglected and thus the desired control torque τ_{L} can be realized instantaneously. While unmodeled dynamics at the level of the continuum mechanism can be handled in this way, unmodeled dynamics at the actuator level would need a different approach.

The left column of Fig. 6.13 depict experimental step responses for a reference step of $\theta_{L,d} = 20$ deg of the closed loop system with the FO controller, the PID controller and the LAG compensator. It can be observed that FO controller overshoots (peak value of 20.44°), as expected due to a phase margin of $\varphi_m = 80$ deg. The final value of the response is 19.65°, i.e. a almost negligible steady-state error due to the absence of an integral component. The PID controller presents zero steady-state error due the integral action. The lag compensator presents a higher steady-state error (final value of 17.77°). The transient of the three controlled systems possesses a similar settling time whereas the rise time for the FO controller is considerably lower. The second column of Fig. 6.13 emphasizes, that the FOC controller can handle smaller and bigger steps as well.

To excite the robustness of the closed-loop system, additional (unmodeled) masses are placed on the top of the mechanism. These additional masses imply a change in the total impedance of the system. The additional masses on the top are progressively increased to $m_{\mathrm{ext}} = \{97, 194, 380, 566, 663, 849\}$ g and corresponding behavior is depicted in Fig. 6.14 for all three controllers. The FO controller presents a robust performance to this variation of the overall impedance, and is able to cope with higher additional masses before the closed loop gets unstable. The PID controller and the lag compensator become unstable for $m_{\mathrm{ext}} = 566$ g, see Fig. 6.14.

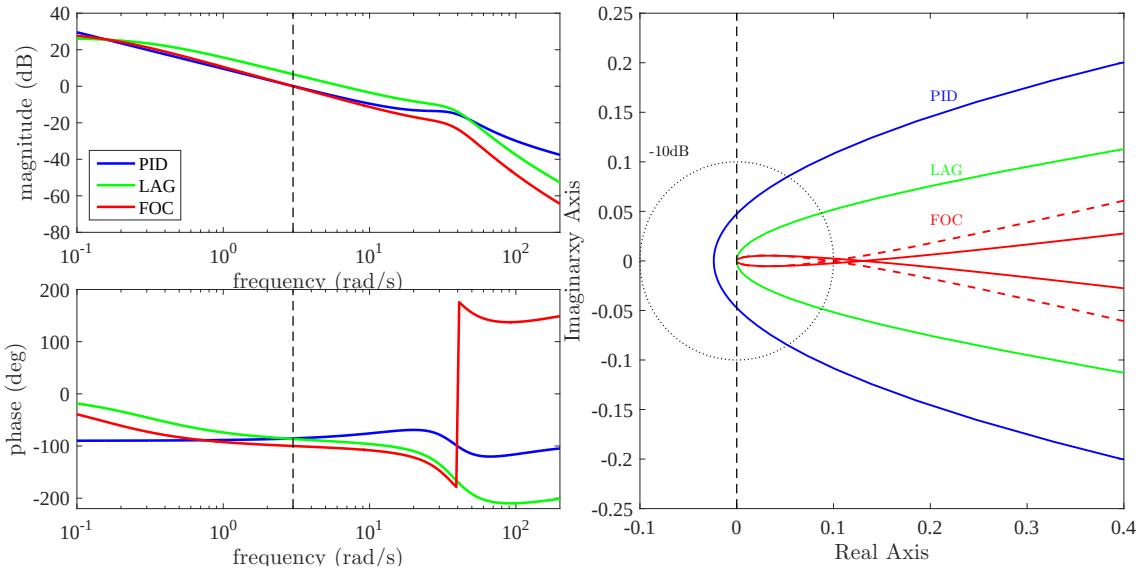

Figure 6.12.: Left: Bode plot open the open loop system for the three designed controllers PID, LAG and the FOC of equation (6.66).Right: Nyquist plot of the designed and transformed controllers, PID (blue), LAG (green), $PD^{\alpha}(s)$ (red) and $\tilde{PD}^{\alpha}(s)$ (red-dashed)

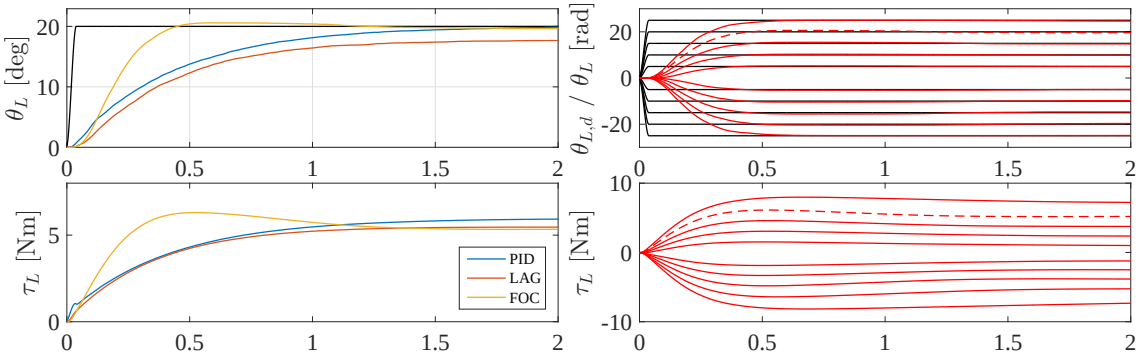

Figure 6.13.: Left: Experimental step responses θ_L of the system in closed-loop and corresponding control inputs τ_L of the three controllers. Right: Experimental step responses of the system with the FO controller (red) for different step inputs with amplitudes in the range $\pm(5°, 25°)$.

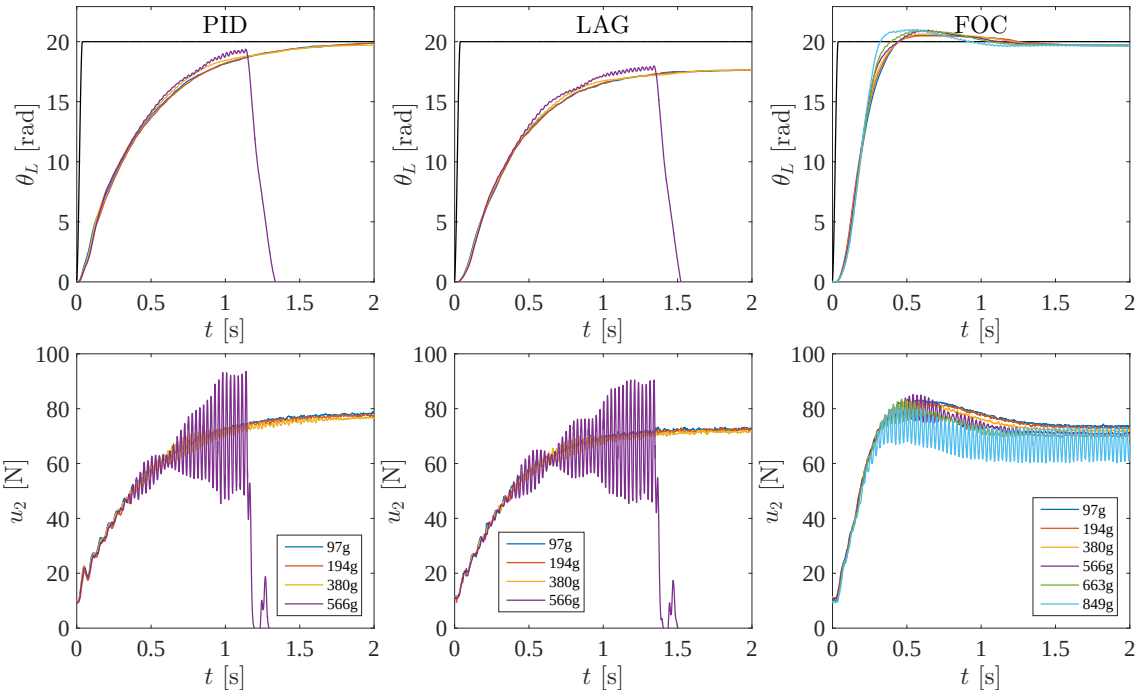

Figure 6.14.: Experiment to investigate the robustness of the designed controllers. Additional unmodeled masses are attached to the mechanism and a reference step of $\theta_{L,d} = 20$ deg is performed. Left: Measured response of the PID controller. The closed loop is not stable for an additional mass of $m = 566$ g which can be observed by high oscillations in the tendon tension u_2. Middle: Measured response of the LAG controller. The closed loop is not stable for an additional mass of $m = 566$ g which can be observed by high oscillations in the tendon tension u_2 Right: Measured response of the FOC controller. The closed loop is on at the border to become unstable for $m = 849$ g which can be observed by oscillations in the tendon tension u_2

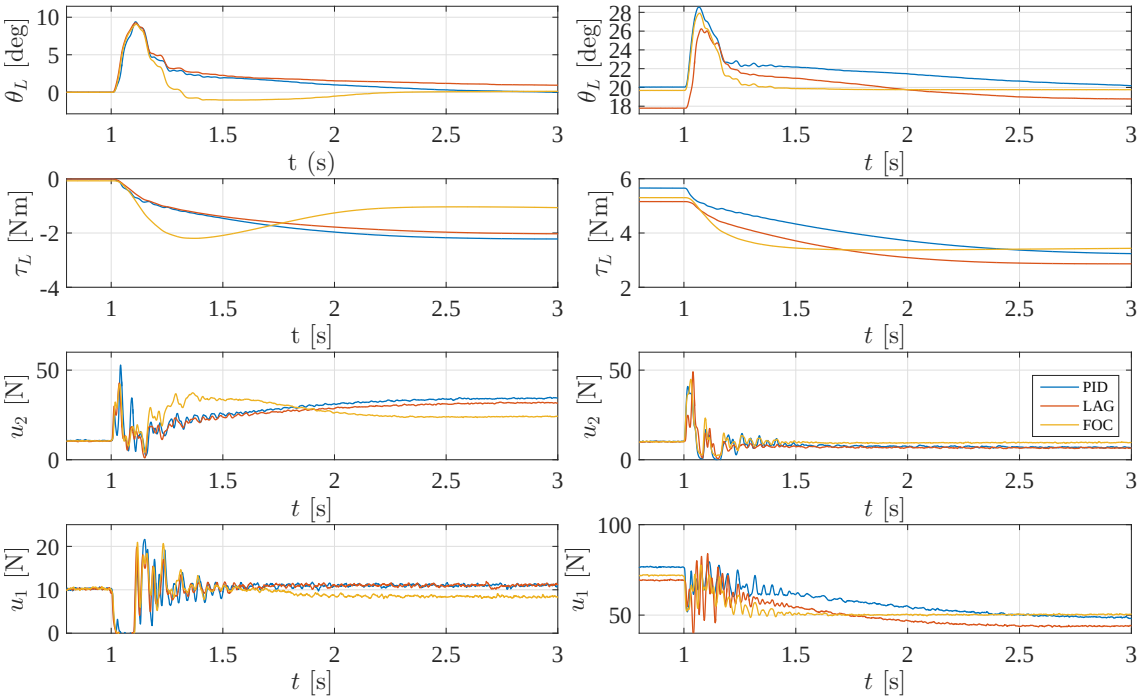

Figure 6.15.: Experimental responses with the FO controller, the PID controller and the integer-order lag compensator in the presence of disturbances. Left: 0° tip deflection. Right: 20° tip deflection.

A requirement for the present mechanism is to handle external disturbances which are investigated in a last experiment. Here, the system is controlled to a desired set point at which it is disturbed by a falling mass of ≈ 1 kg which is attached to the tip in order to generate reproducible disturbances. The experiment is carried out at two different set points, $\theta_{\cdot} = 0°$ and $\theta_L = 20°$. The results are shown in Fig. 6.15. A robust performance is obtained by all controllers. However, the disturbance rejection property of the FO controller is superior compared to the inter order controllers, which can be observed by a faster return to the set point. The reported behavior is sustained by a video that shows the experiments, see https://www.youtube.com/watch?v=ivR-3bN0LVA&feature=youtu.be.

In summary, the fractional order controller provides a better trade-off between accuracy and bandwidth than the integer-order controllers, the controller possesses a superior disturbance rejection time and shows a higher robustness to unmodeled dynamic effects. Due to the promising results, it will be applied to the spatial system which is treated in the subsequent section.

6.7.2. Application on a Multi-Input Multi-Output System

The subsequent section will present the application of a fractional order control onto multi-input multi-output (MIMO) systems. A similar design procedure as presented in the last section is reported including 1) measurement of the real input-output behavior and 2) design of SISO controllers for each input-output pair. For the application of this framework, a general MIMO system needs decoupled and linearized which can be done by a partial feedback linearization as discussed in Section 6.4. The resulting linearized output dynamics (6.37) represents, in terms of a linear transfer function, r double integrators which and

Table 6.3.: Approximation of the linearized input-output dynamics as second order transfer functions and corresponding fractional order PD-controller

Input-Output pair	$G_i(s)$	$PD_i^{\alpha}(s)$
$i = 1$	$\frac{0.007585}{s^2+6.745s+18.46}$	$177610 + 49250s^{0.7}$
$i = 2$	$\frac{0.1344}{s^2+2.981s+9.484}$	$4322 + 3171s^{0.69}$
$i = 3$	$\frac{0.02268}{s^2+1.561s+7.798}$	$18459 + 18952s^{0.68}$
$i = 4$	$\frac{0.6777}{s^2+5.052s+14.05}$	$1459 + 588s^{0.68}$

relate an input $\bar{\boldsymbol{u}} \in \mathbb{R}^r$, here generalized accelerations, up to generalized positions $\boldsymbol{y} \in \mathbb{R}^r$. In the following, this concept is applied on the spatial testbed (Section 2.2.2) which is linearized and decoupled by feedback. Basically, the same control law that has been experimentally applied for the experiments of Section 6.6, is used in the following and the drawback of experimental tuned gains is overcome by using a fractional order controller tuned by the tuning method described by Monje *et al.* [153]. In theory, a transfer function with a double integrator would imply that only damping is needed to generate a flat phase for robustness [151], see equation (6.65). However, based on observation on the real hardware, the output dynamics cannot be fully decoupled and linearized due to parameter mismatches and unmodeled parameters like friction. Therefore, the input-output characteristic is measured for each of the $r = 4$ outputs experimentally and approximated by second order transfer functions for each input-output pair, see Tab. 6.3. To emphasize the applicability, a fractional order PD-control is tuned by specifying a flat phase (6.65), phase margin (6.64) and crossover frequency (6.63). Similar to the preliminary study presented in Section 6.7.1, a crossover frequency of 3 [rad/s] and a phase margin of 80 [deg] seems suitable as a settling time for the transient response should be approximately 1 s with a slight overshoot to overcome velocity dependent friction. However, the fractional order PD controller tuned with these specifications does not provide suitable results in the experiments as the control action in steady state is not sufficient. Therefore, a higher cross-over frequency is specified to 100 [rad/s]. The tuned controllers which use the adapted specifications are given in the second column of Tab. 6.3.

Experimental results are presented in the following and experimental procedure covers the same transient motions and the disturbance test of Section 6.6. The steady state accuracy is similar to PFL controller and is therefore not specifically reported. The dynamic motion sequence is depicted in Fig. 6.16. A lower overall control error can be observed in the first row of Fig. 6.16 in comparison to the controller that uses empirically tuned gains of Fig. 6.9. However, the controller action is opposed onto the system in a fast manner, indicated by high slopes in the beginning of each motion which is not desired. Abrupt accelerations and decelerations are induced and might violate the time scale assumption based on which the overall control approach is based. For the investigated set points, the control loop is observed to be stable. However, an oscillatory behavior of the closed loop is present and can be observed at set-point five. Here, tendon $i = 3$ performs small oscillation which indicates that the time-scale property is violated and therefore a re-tuning of the controller needs to be reconsidered.

To investigate the robustness of the fractional order controller, an experiment is per-

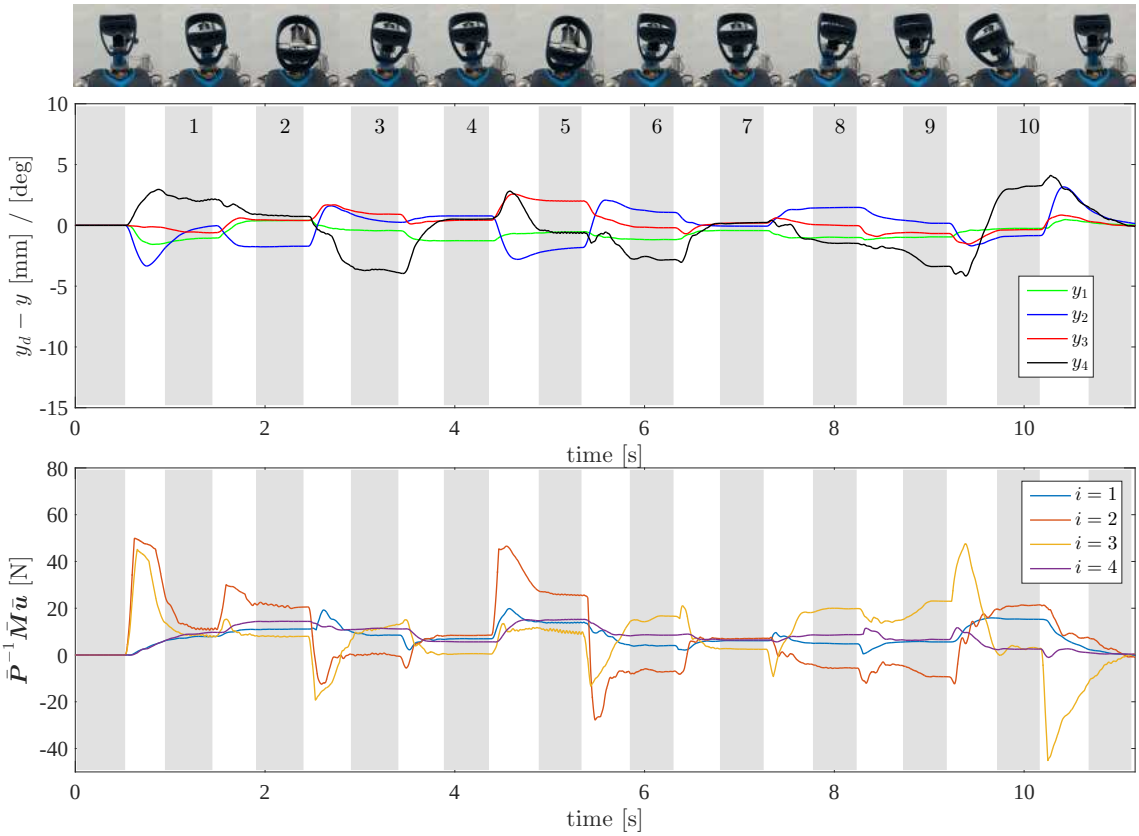

Figure 6.16.: Transient behavior of the a partial feedback linearization controller in combination with four fractional order controllers for the linearized output dynamics. A sequence of setpoint is reached consecutively. The grey areas mark the periods at which the desired output has reached its set point. Top row: Component wise output error $\boldsymbol{y}_d - \boldsymbol{y}$. Bottom row: Control action of the fractional order PD controller (see Tab. 6.3).

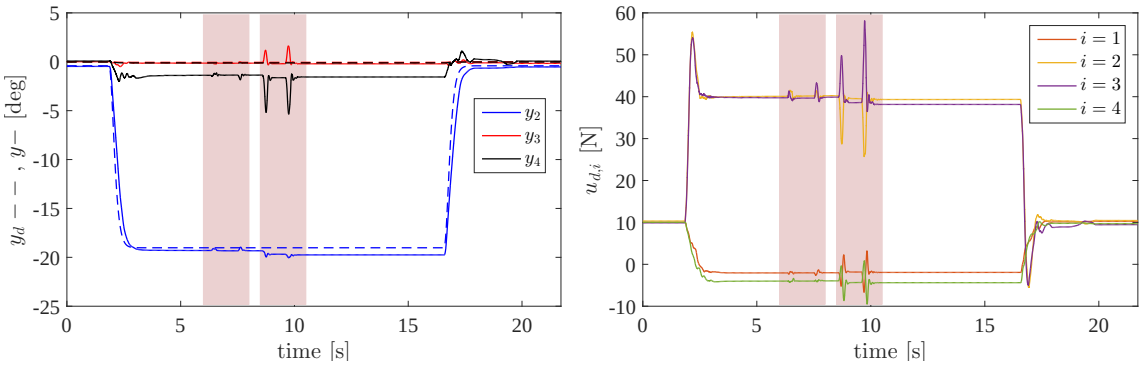

Figure 6.17.: Closed loop behavior of the feedback linearized system which is controlled by four fractional order PD controllers. A comparably simple motion is performed whereas in the indicated time periods, an external (manual) disturbance is applied on the system.

formed which consists of a simple planar motion that drives the spatial testbed to a desired setpoint. Here, the system is manually disturbed in two different directions which is followed by driving the system back to the initial configuration. The response of the closed loop is depicted in Fig. 6.17. The closed loop remains stable under the disturbance, however the induced desired tendon tensions are comparably high. Furthermore, the fractional order controller is still commanding negative tendon tensions which in fact cannot be realized due to a hard saturation of the control-input as tendons can only pull.

In summary, this Section discussed the applicability of a fractional order controller onto tendon-driven continuum mechanism. The approach can handle robustness and a desired bandwidth of the closed loop at the same time and showed a superior performance on a SISO system. As it is a linear approach requiring SISO system, a combination with the feedback-linearizing controller is experimentally tested on the spatial testbed. Theoretical considerations for the controller design were not applicable on the real hardware due to unmodeled effects and due to the fact that the feedback linearization might not be able to fully linearize and decoupled the input output dynamics. Therefore, the input-output behavior is experimentally obtained for the $r = 4$ outputs. Although the steady state accuracy could be slightly improved with the application of the presented fractional order PD controller, compared to the empirically tuned ones, the measured behavior is oscillatory during certain motions and the control action is volatile, therefore a robust closed loop cannot be reported in the current implementation.

6.8. Extension: Distribution of tendon tension

The use of tendons as a power transmission element in mechanisms in general provides several advantages. For example, the actuation units can be placed remotely, which lowers the link-sided inertia, and by a proper design of the tendon routing the generated torque at the link side can be increased. A major disadvantage that arises from the application of tendons is their inherent saturation which allows the transmission of positive tensions only. From a control perspective, a saturation of the control input is present which is usually difficult to include in a control law.
In the present thesis, this problem is address by setting a "user defined" pretension forces, empirically chosen, which are added to the desired tendon tensions of the slow control

law. By generating desired set points as described in Section 6.1.2, it is ensured that the generated setpoint is a static equilibrium using positive tensions in each tendon. For the application of the class of mechanism, it is desired to perform spatial motions. The current set point generation is therefore not feasible as it would either require specifying a six dimensional pose of the upper platform or demanding the desired tendon tension forces that correspond to the desired pose in the application. In contrary, it seems more suitable that a user desires a position or orientation only and an algorithm computes a desired pose from the user desired values. This section will address this new problem by two essentially different methods. Both methods enables, that either the position or the orientation only of the upper platform can be specified and the corresponding remaining coordinates of a full pose are computed under the constraint that the required tendon forces remain positive. The transient of the motion is not considered in this presented extension, therefore the static equilibrium equation is considered,

$$\boldsymbol{k}(\boldsymbol{q}, \boldsymbol{0}) = \boldsymbol{P}(\boldsymbol{q})\boldsymbol{u}, \tag{6.68}$$

for the setpoint generation in the following.

In general, the problem is that one wants to command a subset of the desired pose as setpoint, denoted the task coordinates $\boldsymbol{q}_t \in \mathbb{R}^m$, with $m < n$, whereas a full pose need to be generated with the constraint that this pose yields positive tendon tension forces. In principles, a constraint optimization problem needs to be solved,

$$\begin{aligned} \underset{\boldsymbol{u},\, \boldsymbol{q}_p}{\arg\min} \quad & \boldsymbol{k}(\boldsymbol{q}_p,\, \boldsymbol{q}_t, \boldsymbol{0}) - \boldsymbol{P}(\boldsymbol{q}_p,\, \boldsymbol{q}_t)\boldsymbol{u}, \\ & \boldsymbol{u} - \boldsymbol{u}_{pre} \geq \boldsymbol{0}, \end{aligned} \tag{6.69}$$

which finds an adapted set of the not specified generalized coordinates, denoted $\boldsymbol{q}_p \in \mathbb{R}^{n-m}$ while ensuring that the corresponding tendon tension forces are bigger than a specified threshold $\boldsymbol{u} > \boldsymbol{u}_{pre}$, with $\boldsymbol{u}_{pre} \in \mathbb{R}^r$. The constraint minimization can be solved using state-of-the-art constrained optimization solvers, see [123]. In the following, two specific methods to deal with the above problem are introduced which results in a fast computation of the solution by utilizing the gained knowledge of model.

6.8.1. Projection of pretensions

In rigid-link, tendon driven mechanisms a redundant tendon actuation is required [117]. By looking at the corresponding coupling matrix $\boldsymbol{P}(\boldsymbol{q}) \in \mathbb{R}^{n \times r}$ where $r > n$ applies here, it appears that only part of the tendon tensions are generating a generalized torque $\boldsymbol{\tau}_q \in \mathbb{R}^n$. Therefore, it is possible to adjust an internal tendon tension force $\boldsymbol{u}_{int} \in \mathbb{R}^r$,

$$\boldsymbol{u} = \boldsymbol{P}(\boldsymbol{q})^+ \boldsymbol{\tau}_q + \boldsymbol{u}_{int}, \tag{6.70}$$

where $\boldsymbol{P}(\boldsymbol{q})^+$ is the generalized pseudo inverse. The pseudo inversion can be weighted such that the solution minimizes specific cost function [157]. The non-weighted Moore-Penrose pseudo inverse minimizes the internal tension and distributes them equally. The introduced internal tendon forces can be chosen such that it points into the Nullspace of $\boldsymbol{P}(\boldsymbol{q})$ and therefore does not generate a torque into the direction of $\boldsymbol{\tau}_q$. With the Nullspace projector $(\boldsymbol{I} - \boldsymbol{P}(\boldsymbol{q})^+ \boldsymbol{P}(\boldsymbol{q})) \in \mathbb{R}^{r \times r}$ according to [158], this projection can be realized by

$$\boldsymbol{u}_{int} = (\boldsymbol{I} - \boldsymbol{P}(\boldsymbol{q})^+ \boldsymbol{P}(\boldsymbol{q}))\boldsymbol{u}_{pre}. \tag{6.71}$$

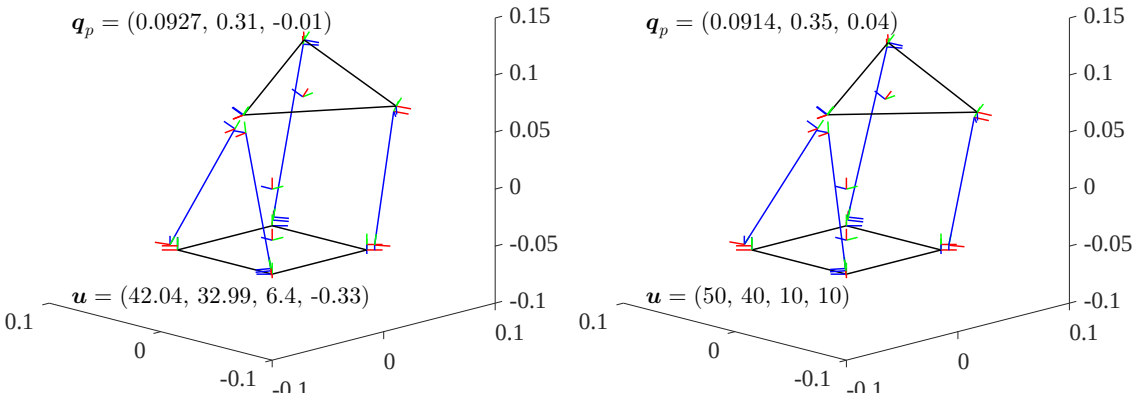

Figure 6.18.: Left: Simulated configuration of the spatial testbed using the Nullspace projection approach to compute $\boldsymbol{q}_p$ and a suitable set of tendon tensions $\boldsymbol{u}$. Right: Simulated configuration of the spatial testbed using the generated suitable set points.

In the present thesis the above concept is adapted for tendon-driven continuum mechanisms which are underactuated. As mentioned, only a subset of $\boldsymbol{q} \in \mathbb{R}^n$, namely the task coordinates $\boldsymbol{q}_t \in \mathbb{R}^m$, are specified. By demanding that the number of task coordinates is, at least, smaller by one than the number of tendons, $m + 1 \leq r$, equation (6.68) is split up into two equation,

$$\begin{aligned} \boldsymbol{k}(\boldsymbol{q}_p, \boldsymbol{q}_t) &= \boldsymbol{P}(\boldsymbol{q}_p, \boldsymbol{q}_t)\boldsymbol{u}, \\ \boldsymbol{k}_p(\boldsymbol{q}_p, \boldsymbol{q}_t) &= \boldsymbol{P}_p(\boldsymbol{q}_p, \boldsymbol{q}_t)\boldsymbol{u}, \qquad (6.72) \\ \boldsymbol{k}_t(\boldsymbol{q}_p, \boldsymbol{q}_t) &= \boldsymbol{P}_t(\boldsymbol{q}_p, \boldsymbol{q}_t)\boldsymbol{u}. \qquad (6.73) \end{aligned}$$

Equation (6.72) expresses the generalized torques along $\boldsymbol{q}_p$, denoted $\boldsymbol{k}_p(\boldsymbol{q}) \in \mathbb{R}^{n-m}$ whereas equation (6.73) expresses the generalized torques along $\boldsymbol{q}_t$, denoted $\boldsymbol{k}_t(\boldsymbol{q}) \in \mathbb{R}^m$. As above in (6.71), a Nullspace projector $\boldsymbol{N}_t(\boldsymbol{q}) \in \mathbb{R}^{r \times r}$ for the task coordinates is introduced,

$$\boldsymbol{N}_t(\boldsymbol{q}) = (\boldsymbol{I} - \boldsymbol{P}_t(\boldsymbol{q})^+ \boldsymbol{P}_t(\boldsymbol{q})), \qquad (6.74)$$

which enables to project pretension forces into the Nullspace of $\boldsymbol{P}_t(\boldsymbol{q}) \in \mathbb{R}^{m \times r}$, i.e. does not create a generalized torque along $\boldsymbol{k}_t(\boldsymbol{q})$. However the projection and the computation of the Nullspace projector (6.74) require that the additional constraint equation (6.72) is fulfilled. By inserting (6.74) in (6.73),

$$\boldsymbol{u} = \boldsymbol{P}_t(\boldsymbol{q}_p, \boldsymbol{q}_t)^+ \boldsymbol{k}_t(\boldsymbol{q}_p, \boldsymbol{q}_t) + \boldsymbol{N}_t(\boldsymbol{q}_p, \boldsymbol{q}_t)\boldsymbol{u}_{pre}, \qquad (6.75)$$

the constraint equation (6.72) can be reformulated to

$$\boldsymbol{k}_p(\boldsymbol{q}_p, \boldsymbol{q}_t) - \boldsymbol{P}_p(\boldsymbol{q}_p, \boldsymbol{q}_t) \left(\boldsymbol{P}_t(\boldsymbol{q}_p, \boldsymbol{q}_t)^+ \boldsymbol{k}_t(\boldsymbol{q}_p, \boldsymbol{q}_t) + \boldsymbol{N}_t(\boldsymbol{q}_p, \boldsymbol{q}_t)\boldsymbol{u}_{pre} \right) = \boldsymbol{0}. \qquad (6.76)$$

Equation (6.76) need to be solved for $\boldsymbol{q}_p$ while the desired task coordinates $\boldsymbol{q}_t$ and desired pretensions $\boldsymbol{u}_{pre}$ are provided.

To test this algorithm on a real problem, the spatial test bed is utilized which is described Section 2.2.2. The reduced nonlinear model is utilized using the NKLS model of

Section 4.2.2 which yields that the number of generalized coordinates is $n = 6$ and the number of tendons is $r = 4$. The number of specified task coordinates are $m = 3 < r = 4$ and it is desired to reach the angels $\boldsymbol{q}_t = (\zeta_d,\, \theta_d,\, \iota_d)^T = (-1,\, 12,\, 6)^T$ [deg]. For a this example, a desired pretension is set to $\boldsymbol{u}_{pre} = (10, 10, 10, 10)^T$ [N]. Equation (6.76) is minimized using the Dog-leg method, described in Section 5.2.1, as it proved to be suitable for solving minimization problems for highly nonlinear functions.
By minimizing (6.76), $\boldsymbol{q}_p = (l,\, \phi,\, \eta)^T$ is found to (9.27 [cm], 17 [deg], -1 [deg])^T which corresponds to an equilibrium configuration. However, the suggested tendon tension at this equilibrium configuration is $(42,\, 33,\, 6,\, -0.33)^T$ N which results in an insufficient solutions as tendon tension four is smaller than zero, as illustrated in Fig. 6.18. The Nullspace projection (6.75) ensures that the tendon pretension does not affect a generalized torque in $\boldsymbol{k}_t(\boldsymbol{q})$. By using the Moore-Penrose pseudo inverse of $\boldsymbol{P}_t(\boldsymbol{q})^+$, a inverse is realized that minimizes the internal forces, i.e. the pretensions which is in this case conflicting. To solve the problem, the user specified pretension need to be increased to higher values.
As outlined by this example, the non-weighted Moore-Penrose pseudo inversion ensures an inversion while minimizing the overall internal tension in the tendon. By a different weighting in contrast, the aforementioned goal might be replaced and would ensure a positive tendon tension of all tendons in general.

6.8.2. Generation of suitable set points

In contrast to the former approach, no Nullspace of the coupling matrix is applied. In the following, the constraint optimization problem (6.69) is transformed to simple root finding problem of a function $\tilde{\boldsymbol{k}}(\boldsymbol{q}, \boldsymbol{u}) \in \mathbb{R}^{n+r}$ by the following considerations. First of all for simplicity, a planar system is considered where two tendons are attached to a tendon-driven continuum mechanism, e.g. the planar test bed of Section 2.2.1. It is obvious, that in any case, only one tendon is responsible to move the mechanism to the left and the other tendon is responsible to move the mechanism to the right. This yields directly that, if the motion direction is specified, only the opposing tendon might go slack. This thought experiment is transformed to a spatial mechanism and it is assumed that if the task coordinates $\boldsymbol{q}_t \in \mathbb{R}^m$ are specified, at least one tendon does not contribute to the motion and might go slack. Therefore, this tendon, denoted tendon $i = *$ is chosen and constraint to have a fixed pretension value of $u_{pre} \in \mathbb{R}$. With that, the function for the root-finding problem $\tilde{\boldsymbol{k}}(\boldsymbol{q}, \boldsymbol{u}) \in \mathbb{R}^{n+r}$ is constructed from static equilibrium equation (6.68), a constraint equation that ensures that the desired task coordinates $\boldsymbol{q}_{d,t} \in \mathbb{R}^m$ are achieved and the constraint for tendon $*$ is fulfilled,

$$\underbrace{\begin{pmatrix} \boldsymbol{k}(\boldsymbol{q}) \\ \boldsymbol{q}_{d,t} \\ u_* \end{pmatrix} - \begin{pmatrix} \boldsymbol{P}(\boldsymbol{q})\boldsymbol{u} \\ \boldsymbol{q}_t \\ u_{pre} \end{pmatrix}}_{\tilde{\boldsymbol{k}}(\boldsymbol{q},\boldsymbol{u})} = \boldsymbol{0}, \tag{6.77}$$

which is solved explicitly to find $(\boldsymbol{q},\, \boldsymbol{u})$. As the Jacobian matrix of (6.77) can be computed analytically, a fast solution can be guaranteed which enables an implementation directly within a real-time code that runs on the hardware. Tendon $*$ is identified by looking at the $r \times m$ sub matrix of the transposed of the coupling matrix $\boldsymbol{P}_t(\boldsymbol{q})^T \in \mathbb{R}^{r \times m}$, evaluated at the initial pose $\boldsymbol{q}_0 \in \mathbb{R}^n$. Then, tendon $*$ is selected as the tendon with the highest negative change in tendon length $\Delta\boldsymbol{l} \in \mathbb{R}^r$ for a desired change in the task coordinates,

$$\min_{*} (\Delta \boldsymbol{l}) = \min \left(\boldsymbol{P}_t(\boldsymbol{q}_0)^T \left(\boldsymbol{q}_{d,t} - \boldsymbol{q}_{t,0} \right) \right). \tag{6.78}$$

The physical interpretation is that tendon $*$ is selected as the tendon that gets considerably longer compared to the other tendon for performing the motion to the desired task coordinates. Algorithm 3 finds the solution to (6.77) by applying a iterative Newton-Raphson solution scheme. Here, a `trigger` variable (Boolean) distinguishes if the algorithm should be executed or not to avoid unnecessary executions and is set if a change in $\boldsymbol{q}_{d,t}$ is detected by software.

Algorithm 3 Algorithm to find a configuration $\boldsymbol{q}_p$ and suitable tendon forces $\boldsymbol{u}$ for a desired task coordinates $\boldsymbol{q}_{d,t}$

specify pretension u_{pre}
specify desired task coordinates $\boldsymbol{q}_{d,t}$
specify maximum number of iterations max_iter $\in \mathbb{N}$
specify the tolerance $tol \in \mathbb{R}$
set $\boldsymbol{q}_p = \boldsymbol{q}_{p,ti-1}$
set $\boldsymbol{u} = \boldsymbol{u}_{ti-1}$
find tendon $*$ by evaluation of equation (6.78)
if trigger is `False` **then**
  $\boldsymbol{q}_{p,ti} = \boldsymbol{q}_p$
  $\boldsymbol{u}_{ti} = \boldsymbol{u}$
else
  for $i \leftarrow 1$, max_iter **do**
    compute $\tilde{\boldsymbol{f}}(\boldsymbol{q}_p, \boldsymbol{q}_{d,t}, \boldsymbol{u})$
    compute $\tilde{\boldsymbol{K}}(\boldsymbol{q}_p, \boldsymbol{q}_{d,t}, \boldsymbol{u}) = \frac{\partial \tilde{\boldsymbol{f}}(\boldsymbol{q}_p, \boldsymbol{q}_{d,t}, \boldsymbol{u})}{\partial (\boldsymbol{q}^T, \boldsymbol{u}^T)^T}$
    if $||\tilde{\boldsymbol{f}}||_2 < tol$ **then**
      `break`
    end if
    update the pose: $\begin{pmatrix} \boldsymbol{q} \\ \boldsymbol{u} \end{pmatrix} = \begin{pmatrix} \boldsymbol{q} \\ \boldsymbol{u} \end{pmatrix} - \tilde{\boldsymbol{K}}^{-1}\, \tilde{\boldsymbol{f}}$
    if $i =$ max_iter **then**
      algorithm did not converge
    end if
  end for
  set $\boldsymbol{q}_{p,ti} = \boldsymbol{q}_p$
  set $\boldsymbol{u}_{ti} = \boldsymbol{u}$
end if

The above derived method is again applied on the previous example of the last section. Here, the spatial system described in Section 2.2.2 is used. The reduced nonlinear model is utilized using the NKLS model of Section 4.2.2 which yields that the number of generalized coordinates is $n = 6$ and the number of tendons is $r = 4$. The number of specified task coordinates are $m = 3 < r = 4$ and it is desired to reach the angels $\boldsymbol{q}_t = (\zeta_d,\, \theta_d,\, \iota_d)^T = (-1,\, 12,\, 6)^T$ [deg]. For this example, a desired pretension is set to $u_{pre} = 10$ [N]. The Algorithm 3 is applied and finds a suitable configuration for $\boldsymbol{q}_p$ and corresponding tendon tensions $\boldsymbol{u}$ while demanding that the tendon which performs the largest negative motion, see equation (6.78), is set constantly to 10 N. The solution is depicted in the right of Fig. 6.18 and the algorithm determines $\boldsymbol{q}_p = (l,\, \phi,\, \eta)^T$ to (9.14 [cm], -19 [deg], -2 [deg])^T which corresponds to an equilibrium configuration whereas the found tendon tension at this equilibrium configuration is $(50,\, 40,\, 10,\, 10)^T$ N. First of all, this algorithm ensures

that the desired task coordinates are reached and a positive tendon tension is ensured. It is obvious, that this method implies higher tendon tension forces and overall a slightly different $\boldsymbol{q}_p$ in comparison to the projection based approach.

6.9. Summary

The previous chapter derived nonlinear model-based control approaches to control the configuration space of the upper platform of tendon-driven continuum mechanisms. Based on the hypothesis that the dynamics of the tendon actuators and the dynamics of the continuum mechanism possess a different time scale, a composite control law is derived which contains a control action of the fast loop and a control action of the slow loop. The fast loop ensures tracking of desired tendon tension forces. The control law of the slow loop accounts for the set point control for the upper platform of the continuum mechanisms and was of primer interest.

As a first approach, a linear $\mathscr{H}_\infty$ controller is derived for the class of mechanism. Knowledge about nonlinearities of the system is incorporated in the approach by a transformation of the equation of motion into a parameter-affine state space representation which can be specifically treated in the synthesis of a linear robust $\mathscr{H}_\infty$ controller. In practice, the robust control approach presented a stable response of the closed loop system. However, the pursuit design strategy for the controller minimizes the worst case effect of known disturbances and parameter mismatches which results in a conservative controller that does not fulfill the specified performance. In the following, two other nonlinear control approaches are derived that treats the underactuation present in this class of mechanisms specifically by a transformation of the dynamic equations to the input-output normal form. This allows deriving a model-based control law for the dynamics of the output which are chosen as a subset of the configuration space variables. Two essentially different approaches are proposed. The first approach is a feedback compensation controller which cancels known dynamic properties of the output dynamics by nonlinear feedback. An additional, new control input is introduced that allows imposing the error dynamics of the closed loop passivity or exponentially stability. The second approach contains a feedforward control action, to account for steady-state accuracy, and a feedback control action to account for disturbances and is based on an adapted inverse dynamics approach. The performance of the controllers is tested in three dedicated hardware experiments which account for steady state accuracy, the transient behavior during dynamic motions and external disturbances. The desired performance specifications are met in both approaches. A strong feature of both controllers is the provision of the control action that deforms the mechanism. In steady-state, this contribution to the control action is high and the feedback gains can be set comparably low which adds robustness to the closed loop system, a desired property. Comparable steady state accuracy is assessed for both controllers for 50 poses in the workspace. The partial feedback linearization controller yields maximum root mean square error (RMSE) for the control error of 1 mm in position and 3.5 deg in orientation. The composite controller in contrast achieves a maximum RMSE of 0.5 mm in the position and 1.5 deg in orientation. Both approaches are able to handle external disturbances with a similar disturbance rejection capability. The pure feedback controller however, reaches the physical limitations of the tendon actuation regularly. As tendons are only able to pull and commanded negative tendon tension forces need to be prohibited, saturation in software need to be utilized which is in general undesired. The composite controller in

contrast, is able to reach all desired set points, despite of fast motions or external disturbances are present, without reaching these limits. A drawback of both approaches is that the controller gains are tuned empirically in the experiments. This issue is addressed by an extension of the partial feedback approach. A preliminary study is presented which utilizes a linear fractional order controller to control the orientation of a planar testbed of Section 2.2.1. It is possible to stabilize the nonlinear system with a linear fractional order lag compensator at different setpoint and the robust performance could be achieved which was not possible with PID controller designed with the same specifications. For the spatial testbed in contrast, the fractional order controller did not yield a considerable increase in the performance compared to the empirically designed PD controllers. A reason for this might be that the assumption of a fully linearized and decoupled output dynamics is jeopardized in practice due to unmodeled effects like friction and the dynamics of the actuation or the state estimation.

The second extension addresses an application driven problem. In general it is not convenient to command a complete six dimensional pose, i.e. the generalized coordinates, as the corresponding kinematic variables are highly coupled in the workspace. In contrast, the orientation (or the position) of the upper platform, denoted as the task coordinates, are fairly decoupled. The presented extension enables to generate feasible set points for the generalized coordinates of the upper platform by specifying the task coordinates only. Two algorithms are suggested which additionally consider, that the mandatory tendon tensions at the setpoint are positive. The first approach is based on a projection of a user defined pretension in to the Nullspace of the coupling matrix of the task coordinates. The projection employs an inversion which is performed using the Moore-Penrose pseudo inverse and yields that the overall internal tendon tension is minimum. At some poses, this yields that the user defined pretension need to be set considerably higher as otherwise, the tensions in the tendons is not positive. The other approach formulates additional constraint equation and identifies one tendon which does not contribute to reach the task-space coordinates. This tendon then is constraint on a fixed, positive pretension and ensures overall that positive tensions are present.

Overall, the composite controller that contains a feedforward and a feedback action in combination with the set point generation that ensures desired positive tendon tension forces seems to handle the control task, i.e. set point regulation of an underactuated continuum mechanism with nonlinear tendon coupling at best.

CHAPTER 7

Summary & outlook

Intrinsic passive compliance in robotic systems was considered as a drawback in the past, but can be a feature today. A novel perception for passive compliance in robots among the robotic community set a paradigm shift in the design of new system such as the highly elastic humanoid robot David [159] or the two legged system C-Runner [160]. These systems possess (adjustable) mechanical compliance which are deliberately introduced in the actuation and separate the motor dynamics from the link side. Since a control law cannot react in the very first instant of an external impact, the intrinsic mechanical compliance serves as the only protection of the robot. Some robotic systems of the described kind additionally employ tendons as a power transmission element from the actuators to the link. This enables remotely placed actuators with lower inertia, smaller form factor and high dynamics for the link side. As a result novel compliant actuators based on tendon-driven continuum mechanisms are investigated more recently in research and it is envisioned to combine the above mentioned advantages with the capability to design a highly integrated structure with intrinsic actuation and sensing such that a motion with several degrees of freedom can be realized.

The present doctoral thesis contributes towards this ultimate goal by examining a class of tendon-driven continuum mechanisms and develops specifically designed approaches for modeling, state estimation and control. The treated class covers mechanisms with a beam-like, continuum structure manufactured out of soft material that is placed in between two rigid platforms. A fixed number of tendons are attached to the upper platform and a coordinated loading of the tendons will deform the continuum and position the upper platform spatially. The main objective of this thesis is to develop modeling, state estimation and control approaches for the motion of the upper platform which are applicable on real hardware system.

In the modeling domain, this doctoral thesis presented two approaches. The first one is dedicated to the analysis of the class of mechanisms whereas the second one is dedicated for model-based control. To analyze the statics and dynamics, an initial experimental study revealed that a general nonlinear Timoshenko beam model predicts all incorporated deformations. With the corresponding kinematic assumptions, the nonlinear beam model is analytically derived and adapted for the present class of mechanisms to include a nonlinear material law in the compression direction and nonlinear tendon coupling. In

contrast to prior works that assume beam like structure in robotics research, a beam finite element discretization is applied and provides equations with a reduced size, compared to a volumetric finite element model, and the common structure of a multi-body system. By a careful identification of the material parameters, the experimentally obtained behavior of two different prototype systems can be predicted with a mean error in position and orientation of 0.5 mm and 0.8 deg for the planar and a mean error in position and orientation of 2.3 mm and 2.6 deg for the spatial system. The developed model was fundamental thereafter for the developments throughout the present doctoral thesis and has been applied in Chapter 4, Chapter 5 and Chapter 6 for workspace analysis. However, a mean computational time of 0.12 s to solve the equations of the spatial system in the present implementation prevents the model from the usage in real time-control.
The second contribution to the modeling domain addresses computational efficiency and is used within model-based controllers on the real hardware. Herein, it is suggested to abstract tendon-driven continuum mechanisms as a rigid body on top of a nonlinear spring system which essentially reduces the number of degrees of freedom and therefore improves the computational efficiency. The modeling of the rigid body and the tendon coupling is equivalent to the beam finite element model. The description of the continuum mechanism in contrary incorporates the novelty. An approximation is introduced that describes the nonlinear spring system, either by an abstract spatial Cartesian spring, or by a series of joints that contain linear springs. For the experimental identification of both models, a uniform procedure is introduced for the class of mechanism and tested on several real continuum mechanisms. In the first alternative, the Cartesian components of the nonlinear spring are approximated by full cubic polynomial function of the pose of the upper platform. Consequently, the geometry of the deformation and material properties are hidden within the polynomial coefficients. Due to the polynomial structure, an analytically stiffness matrix can be derived, which is symmetric, whereas it could be shown that the restoring forces of the continuum can be predicted with a maximum root mean square error (RMSE) of 1.57 N and 0.08 Nm. The serial kinematic structure of the second modeling alternative consists of five rotational and one prismatic joint and a linear joint elasticity is introduced in each of the six joints. The abstraction is inspired by elastic joint robotic manipulators due to serial kinematic arrangement whereas the experiment expressed a good approximation capability of the restoring forces and torques with maximum RMSE of 3.3 N and 0.26 Nm. In contrast to methods from the state of the art, which are based on a given kinematic structure using constant curvatures, no singularities are incorporated in the workspace which is a great benefit. Secondly, the introduced approach including the calibration ensured that the equilibrium poses of the model are equivalent to the ones from a real continuum mechanism. In this way, the steady-state accuracy of model-based controllers is enhanced which try to compensate for such nonlinear terms.
In this respect, the research question **Q 1** "Can we capture the static and dynamic behavior of the system in a uniform, computationally efficient, reduced model without losing accuracy and dynamic effects?" is answered by two different approaches which derive the equation of motion and the static equilibrium equation for the class of mechanism. They are uniform in the sense that the resulting equations possess a common structure whereas the computational efficiency is only given for the second, substantially reduced model described in Chapter 4.

State estimation is indispensable for the model-based nonlinear control approaches presented in this thesis. Furthermore, it is envisioned to apply mechanisms of the defined class as generic joint modules, however geometric forward and inverse kinematics cannot be ap-

plied which brings the necessity of state estimation. The present doctoral thesis introduces three state estimation concepts. For the class of tendon-driven continuum mechanisms, a different problem is addressed compared to the state of the art as the shape of the continuum is not of interest. In contrast, dynamic motions of the upper platform are investigated and therefore the pose and velocity of the upper platform is searched. Herein, the present thesis contributes with the derivation and experimental comparison of geometric, static and dynamic state estimation concepts that rely on the information of on board sensors. The presented static estimation concept yielded no suitable results due to large estimation errors at static poses and during dynamic motions. For the remaining concepts, a geometric estimation concept based on length measurements, e.g. tendon lengths, offers the highest accuracy at static possess, with a maximum RMSE of 1.3 mm for the position and 1.0 deg for the orientation. During dynamic motions or interactions in contrast, a dynamic estimation concept provides a higher accuracy, as the overall position and orientation error stay below 2 mm and 2 deg. The gained accuracy might result from the data fusion which is carried out in the dynamic estimation concept. The length information are fused in an Extended Kalman Filter together with linear accelerations and angular rates of an inertial measurement unit. As the dynamic concept is comparably accurate at static locations, and velocities are estimated in the filter as well, the dynamic state estimation concept is suggested as the answer to the posted research question **Q 2** "Which methods are applicable to estimate the relevant states of the system to use them in feedback control?". However, the concept relies on many sensors that have been integrated for a first prototype which required a higher effort for integration, calibration and maintenance. This needs to be carefully counterbalanced by the gained accuracy for each application specifically.

In order to position the upper platform of the mechanism spatially, a coordinated tension need to be applied for each tendon. A common approach from the literature is a so called "kinematic controller" for which desired task space variables, that describe the pose of the upper platform, are transformed to desired actuation space variables based on a kinematic transformation. Then, a local actuation control loop ensures set point control or reference tracking. The goal of the present doctoral thesis is to reach desired set points with the upper platform dynamically and external disturbances shall be handled by the controller. Therefore, the commonly applied control loop is insufficient as external contacts or the dynamics of the mechanism, perceptible in the transient behavior, are not addressed by this control approach. Furthermore, the intrinsic underactuation of tendon-driven continuum mechanisms is not specifically treated in state-of-the-art approaches. The illustrated short comings are addressed by the presented configuration space controllers in this doctoral thesis.
The fundamental assumption for the design of model-based controllers is that the dynamics of the tendon actuation and the dynamics of the continuum possess a different time scale. Based on this, the overall dynamics can be decoupled into a fast and a slow control loop and a separate control law is then derived for each loop. To control the slow dynamic system, i.e. the position and orientation of the continuum mechanism, a linear- $\mathscr{H}_\infty$ controller, a nonlinear feedback linearization, and a composite controller with feedforward and feedback action is proposed. By design, the $\mathscr{H}_\infty$ controller yields a robust performance but the conservative control action does not fulfill the set performance specifications. It is a standard approach from automatic control and the underactuation is not specifically treated. In the design of the other two controller laws, this is substantially different. Here, the idea is to reduce the control design of the original underactuated system to control

a lower order nonlinear system, termed input-output normal form. The order of these dynamic equations is limited by the number of inputs and thus ensure a full actuation. As a first approach here, a partial feedback linearization is performed that linearizes and decouples the output dynamics and a novel control input ensures reference tracking. Secondly, an approach based on the inverse output dynamics is proposed that generates a suitable feedforward action based on the desired setpoint whereas an additional feedback term ensures that external disturbances are regulated.
The experiments assess set point control for the defined outputs which majorly express the orientation of the upper platform. The setpoints are reached dynamically under external disturbances. Both controllers are able to stabilize the system during all experiments. With regard to the posted research question **Q 3** "Which model-based control methods enable set point regulation of an underactuated continuum mechanism with nonlinear tendon coupling ?", the thesis recommends the composite approach with feedforward and feedback action as it exhibits a lower steady state error and more robust behavior in the examined dynamic motions and under external disturbances.

The overall outcome of the present doctoral thesis is a novel treatment of a continuum in robotics research. The novelty here includes the description of the overall system as a tendon-driven multi-body system modeled by a nonlinear rigid-body dynamics. In combination with the proposed real-time pose and velocity estimation allows to use this nonlinear model in real-time control. Furthermore, the structural properties of the model allow employing classical control methods for underactuated multi-body systems which adapted to provide set point control for the upper platform. The main focus of the algorithms were accuracy, to predict the real behavior, mobility, as only onboard sensors are employed and real-time capability since the algorithm shall be implemented on real robotic systems.

The summary above outlined, that this thesis follows a "classical approach" for the control, commonly applied in robotics research. In a nutshell, a controller cancels known dynamic properties of the system to impose the closed loop dynamics a desired dynamic behavior. By observation, continuum mechanisms seem to have already favorable dynamic properties, like inherent stability or a partial compensation for gravitational forces, which seems conflicting with this "classical approach". In contrast, the control objective and application relevant constraints in the actuation or the desired workspace may be considered already in the design of a continuum mechanism and would render this classical approach unnecessary. Beyond that, one could think of systematically designed structures that allow for motions in specific directions while other directions are highly damped or constraint. Such an embedded design process to fulfill certain control objectives, or vice versa, could help to extend the usage of one single tendon-driven continuum mechanism to a generic joint module based on which serial or parallel robotic manipulators can be built to address future challenges or use cases. To emphasize this roughly sketched procedure, an illustration is given in Fig. 7.1.

To pursue the ultimate goal of highly integrated structures with intrinsic actuation and sensing such that a motion with several degrees of freedom can be realized, general purpose joint modules might be a first step. In this respect, these modules shall realize basic motion capabilities like pitch, yaw, and roll, and are built upon a unified modeling approach that incorporates rigid and elastic bodies. As the main linkage between model-based design and model-based control, the unified model provides accuracy, required in the design, and computational efficiency for the control. A promising approach here is a continuum mechanical model, discretized via the finite element method with, either volumetric or

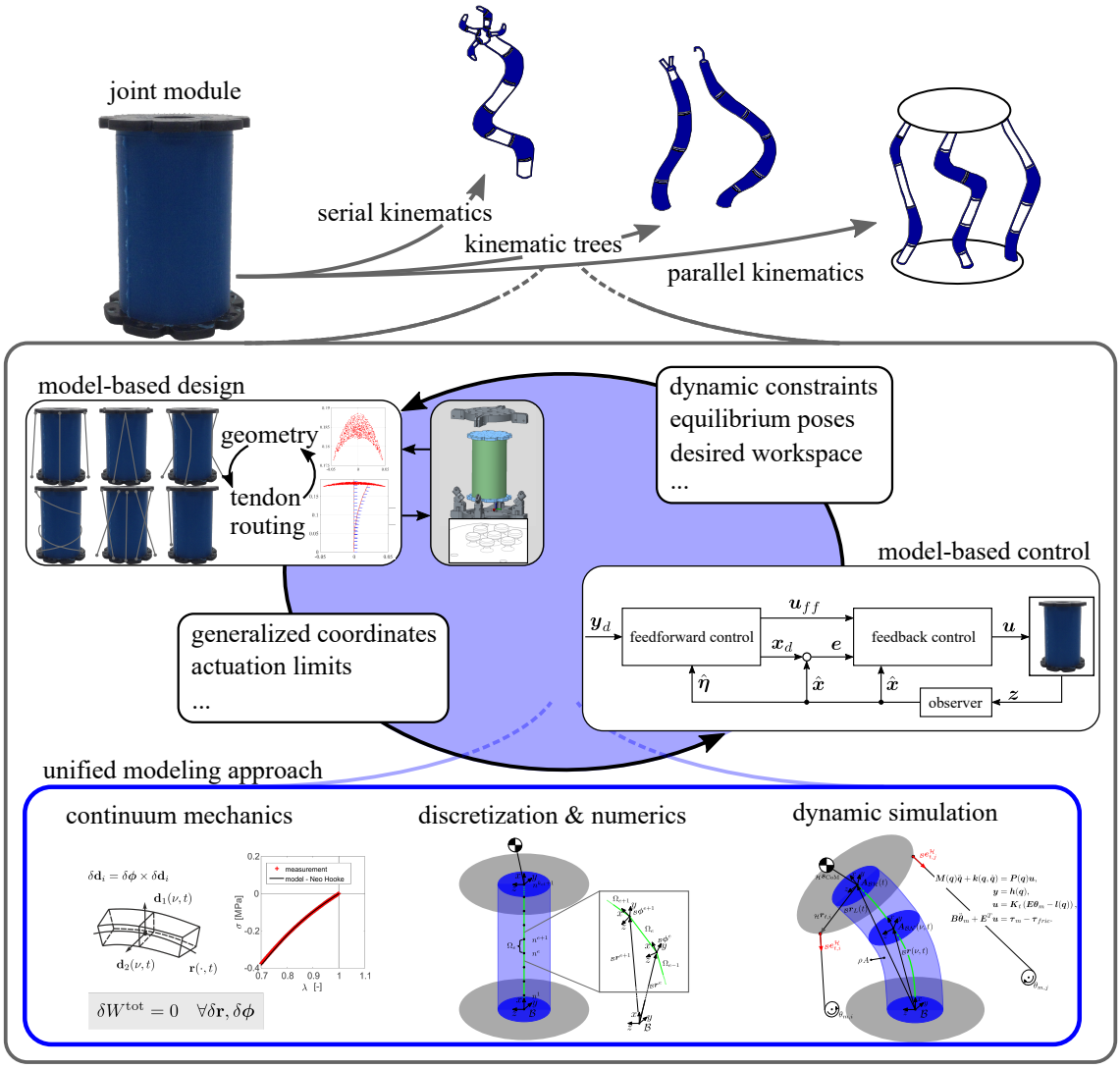

Figure 7.1.: Embedded process to systematically develop generic joint modules based on tendon-driven continuum mechanisms for diverse application scenarios.

beam finite elements, in combination with special shape-functions that already incorporate the characteristic of the deformation and thus minimize the number of necessary nodes. The resulting models for dynamic simulation resemble a multi-body system, i.e. nonlinear ordinary differential equation, which is an advantage since the field of automatic control provides sufficient methods for system analysis and controller design.

Contrary to the "classical approach", the properties of the closed loop system are shaped in the design of the continuum's geometry and the routing of the tendons. Herein, a framework needs to be developed which arranges tendon channels or pulleys and shapes structural properties to achieve a large workspace with specified deformations of the mechanism while reducing the number of actuators. For example, it is envisioned that a feasible tendon routing and the corresponding actuators enable to simultaneously achieve the desired workspace and constraint possible underactuated directions by applying active tendons, coupled tendons or additionally passive tendons.
The material properties of the elastic material shall be exploited within the design and manufacturing process to enhance the modularity for the developed joint modules. Particularly the interface between the elastic and the rigid body of a module need to be optimized to withstand known stresses and enable rapid-prototyping technologies for a fully automated manufacturing.

A controller need to enables the prescribed motions of each module and, on the one hand maintains properties like inherent stability or the impact-absorption capability of the morphology while on the other hand enable dynamic motions without tendon slackness. A model-based controller that assures reference tracking for a subset of the utilized generalized coordinates which integrate constraints due to the underactuation, the input saturation or the kinematic and dynamic coupling is to be developed and needs to by applicable for real hardware systems. In this respect, the complete systems state needs to be observed, being not necessarily Cartesian coordinates, with a minimum number of on-board sensors.

By accomplishing the sketched objectives of the embedded design and control framework for tendon-driven continuum joint modules contributes to the paradigm shift in robotics which tends from rigid to soft material robotics and helps to developed novel robotic systems. Competing designs in this respect are several modules in series or in parallel, see Fig. 7.1, with different target application, for example the challenging field of medical robotics. In this way, the design based on modules enables the fast adaptation towards new or up-coming tasks, whereas the modular concept should not only enable systematic design but also facilitates operation and maintenance of such continuum robots. In the control domain, the sketched framework above results in a joint level controller for each joint module and enables advanced hierarchical task level control strategies for self-collision avoidance [161] or trajectory tracking [162] for the fully assembled manipulator. If these manipulators then interact with each other or the environment, control structures that ensure a stable interaction like [163] are required which can be handled as well by the framework above.

In the near future, the developed control methods are adapted to be applied for a larger tendon-driven mechanism [164] that is currently built at the Institute of Robotics and Mechatronics. A rendering of the envisioned system is depicted in Fig. 7.2. It owns a fixed kinematic structure with two degrees of freedom, passive gravity compensation by a dedicated elastic spring and a redundant tendon actuation with three tendons. The structure of the underlying dynamic equations remain of the form (3.1) however, more tendons

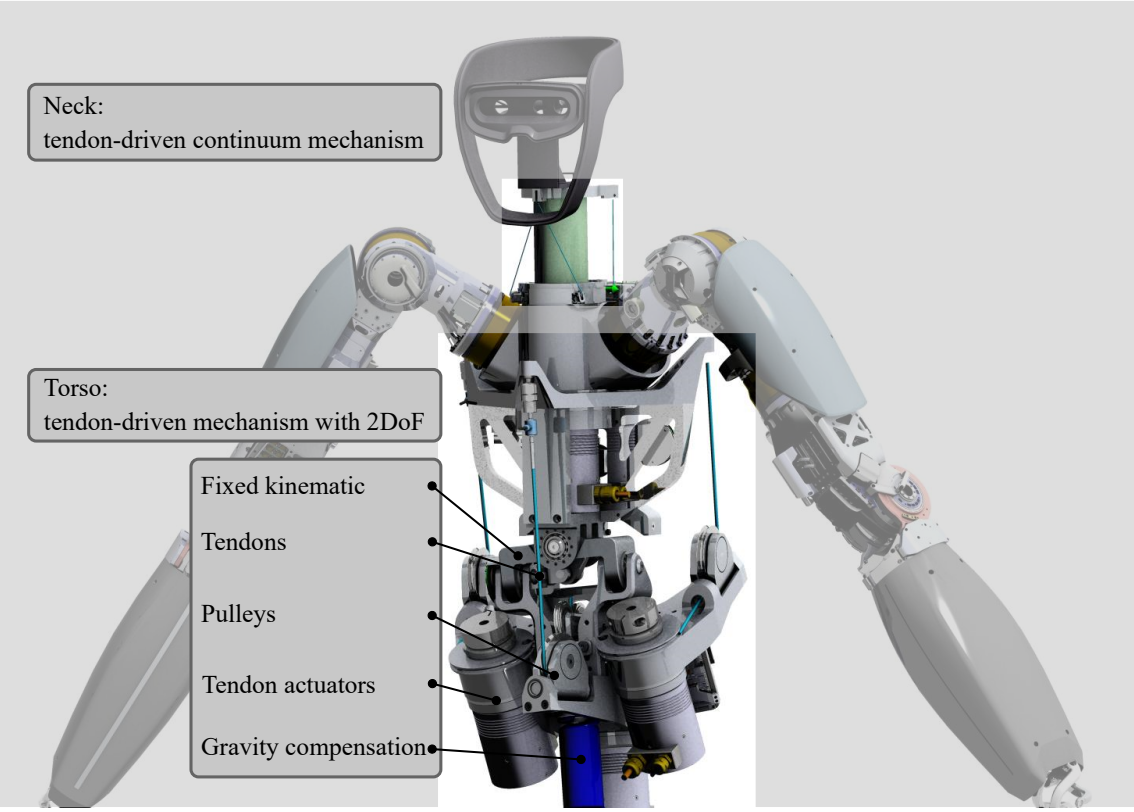

Figure 7.2.: Rendering of the torso prototype, a two degree of freedom tendon-driven mechanism with fixed joint axis and redundant tendon actuation. A passive gravity compensation ensures that the heavy payload of the attached arms and the neck can be carried without using high payload electrical drives to lower the overall weight.

then degrees of freedom $r > n$ are attached which need to be considered in the control approach. To allow for fast motions, a nonlinear compensation of known dynamic properties seems suitable and it is expected that the inertia terms will play a more dominant role due to the large masses. To ensure positive tensions in the tendons, the introduced approaches of Section 6.8 will be adapted for the dynamic case. As depicted in Fig. 7.2, the novel mechanism will be used as the torso for the upper body humanoid David to enlarge the reachable workspace in two handed manipulation tasks. The neck system (Section 2.2.2) will be mechatronically integrated as well. The configuration space control for each of the two discussed robotic system will be handled by approaches from the present thesis. To control the whole body motion in contrast, a control framework with a defined task hierarchy shall be utilized, for example as present by Dietrich [165, 166, 167], which requires a modulation of the control law towards a control interface which can handle desired generalized torques. In conclusion, tendon-driven continuum mechanisms have the potential to be used in new applications for future humanoid robots or robotic manipulators. The combination of flexible materials with traditional rigid links, complex shaped structures with integrated actuation and sensing can be envisioned. In this context, the present thesis lays a foundation by exploring the feasibility of traditional concepts, used in robotics research, for modeling, state estimation and control of continuum mechanisms. It is of high importance that the established concepts for tendon-driven continuum mechanisms

are used, extended and fused together with all involved research areas in robotics to mark the beginning of a new generation of light-weight robots.

APPENDIX A

Example models

A.1. Example 1: Planar system

The planar system is described in Section 2.2.1 and we consider a scheme of the system comprising all necessary quantities in Fig. A.1 for the subsequent mathematical developments.

In the following, the dynamic equations for the planar system are derived which is explained in detail in Chapter 3. In principal, the kinematic relations are established at first that describe the motion of the system. Afterward, the virtual work contributions of the forces acting on the system are setup and discretized along the beam (along ν). As it is a planar system, the orientation is simply defined by an angle which simplifies the equation of motion significantly and the following section will try to express all equation as detail as possible as they were implemented in MATLAB/Simulink later on.

Kinematics

For the planar system, the kinematic quantities ${}_{\mathcal{B}}\boldsymbol{r}(\nu,t) \in \mathbb{R}^3$ and $\boldsymbol{A}_{\mathcal{BN}}(\nu,t) \in \mathbb{R}^{3\times3}$ are reduced to the x,z-plane which yields,

$$ {}_{\mathcal{B}}\boldsymbol{r}(\nu,t) = \begin{pmatrix} x(\nu,t) \\ 0 \\ z(\nu,t) \end{pmatrix}, \quad \boldsymbol{A}_{\mathcal{BN}}(\nu,t) = \begin{pmatrix} \cos(\theta(\nu,t)) & 0 & \sin(\theta(\nu,t)) \\ 0 & 1 & 0 \\ -\sin(\theta(\nu,t)) & 0 & \cos(\theta(\nu,t)) \end{pmatrix}. \tag{A.1} $$

With that, the generalized functions are reduced to

$$ (x(\nu,t),\, z(\nu,t),\, \theta(\nu,t))^T. \tag{A.2} $$

Again, we want to look at the position and orientation of the head at Q ($\nu = L$)

$$ \begin{aligned} {}_{\mathcal{B}}\boldsymbol{r}_{OQ}(t) =& {}_{\mathcal{B}}\boldsymbol{r}(\nu = L,t) = (x_L(t),\, 0,\, z_L(t))^T, \\ \boldsymbol{A}_{\mathcal{BH}}(t) =& \boldsymbol{A}_{\mathcal{BN}}(\nu = L,t) = \begin{pmatrix} \cos(\theta_L(t)) & 0 & \sin(\theta_L(t)) \\ 0 & 1 & 0 \\ -\sin(\theta_L(t)) & 0 & \cos(\theta_L(t)) \end{pmatrix}, \end{aligned} \tag{A.3} $$

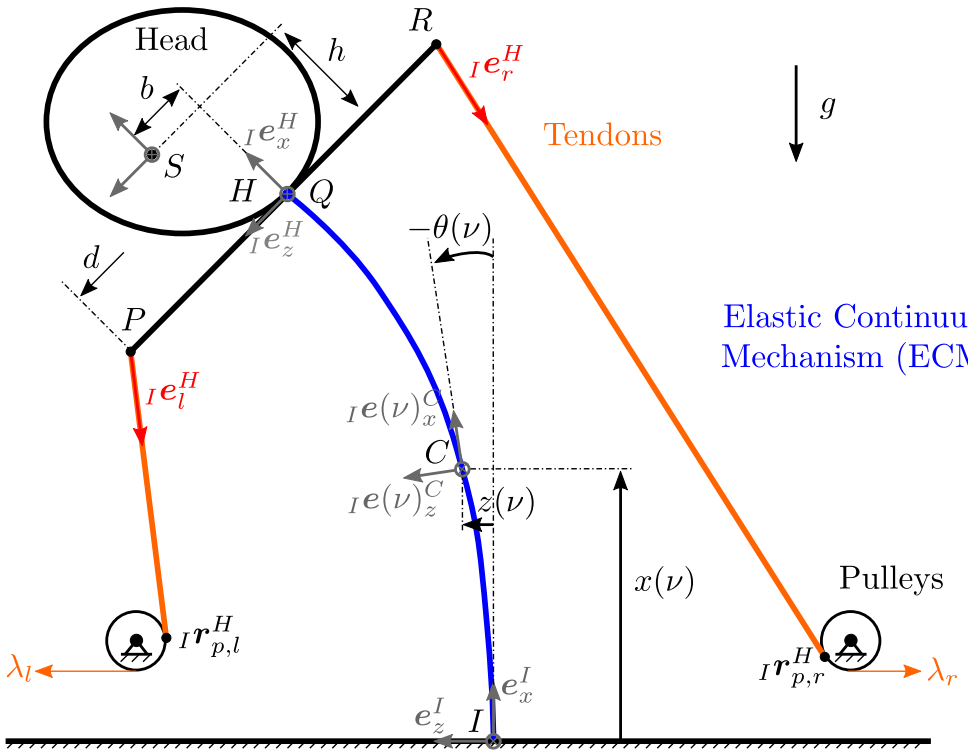

Figure A.1.: Scheme of the planar model

and the position of the center of mass (CoM) of the head,

$$\begin{aligned}{}_{\mathcal{B}}\boldsymbol{r}_{OS}(t) =& {}_{\mathcal{B}}\boldsymbol{r}_{OQ}(t) + \boldsymbol{A}_{\mathcal{B}\mathcal{H}}(t)\,{}_{\mathcal{H}}\boldsymbol{s}_H = {}_{\mathcal{B}}\boldsymbol{r}_{OQ}(t) + h\,{}_{\mathcal{B}}\boldsymbol{e}_x^{\mathcal{H}}(t) + b\,{}_{\mathcal{B}}\boldsymbol{e}_z^{\mathcal{H}}(t),\\ =& \begin{pmatrix} x_L(t) + h\cos(\theta_L(t)) + b\sin(\theta_L(t)) \\ 0 \\ z_L(t) - h\sin(\theta_L(t)) + b\cos(\theta_L(t)) \end{pmatrix}. \end{aligned} \tag{A.4}$$

Furthermore, the position of the left and the right tendon connection point in P and R is needed,

$${}_{\mathcal{B}}\boldsymbol{r}_{OP}(t) = \begin{pmatrix} x_L(t) \\ 0 \\ z_L(t) \end{pmatrix} + d \begin{pmatrix} \sin(\theta_L(t)) \\ 0 \\ \cos(\theta_L(t)) \end{pmatrix}, \tag{A.5}$$

$${}_{\mathcal{B}}\boldsymbol{r}_{OR}(t) = \begin{pmatrix} x_L(t) \\ 0 \\ z_L(t) \end{pmatrix} - d \begin{pmatrix} \sin(\theta_L(t)) \\ 0 \\ \cos(\theta_L(t)) \end{pmatrix}. \tag{A.6}$$

The temporal and spatial evolution of the centerline shall be described. Thus, the linear (3.9) and angular velocities (3.10), the linear strain measure (3.11) and the curvature vector (3.12) are needed. Furthermore, the variations $\delta(\dots)$ of several quantities are necessary. For the position of the centerline, we find the spatial and temporal derivative as well as the variation to be

$${}_{\mathcal{B}}\dot{\boldsymbol{r}}(\nu,t) = \begin{pmatrix} \dot{x}(\nu,t) \\ 0 \\ \dot{z}(\nu,t) \end{pmatrix},\ {}_{\mathcal{B}}\boldsymbol{r}'(\nu,t) = \begin{pmatrix} x'(\nu,t) \\ 0 \\ z'(\nu,t) \end{pmatrix},\ {}_{\mathcal{B}}\delta\boldsymbol{r}(\nu,t) = \begin{pmatrix} \delta x(\nu,t) \\ 0 \\ \delta z(\nu,t) \end{pmatrix}. \tag{A.7}$$

The linear strain measure equates to

$$
\begin{aligned}
{}_{\mathcal{N}}\boldsymbol{\gamma}(\nu,t) =& \begin{pmatrix} \gamma_x(\nu,t) \\ 0 \\ \gamma_z(\nu,t) \end{pmatrix} = \boldsymbol{A}_{\mathcal{BN}}^T(\nu,t)\,{}_{\mathcal{B}}\boldsymbol{r}'(\nu,t) \\
=& \begin{pmatrix} x'(\nu,t)\cos(\theta(\nu,t)) - z'(\nu,t)\sin(\theta(\nu,t)) \\ 0 \\ x'(\nu,t)\sin(\theta(\nu,t)) + z'(\nu,t)\cos(\theta(\nu,t)) \end{pmatrix},
\end{aligned} \tag{A.8}
$$

and for the curvature vector and its variation we find

$$
\begin{aligned}
{}_{\mathcal{B}}\hat{\boldsymbol{k}}(\nu,t) =& \theta'(\nu,t) \begin{pmatrix} -\sin(\theta(\nu,t)) & 0 & \cos(\theta(\nu,t)) \\ 0 & 0 & 0 \\ -\cos(\theta(\nu,t)) & 0 & -\sin(\theta(\nu,t)) \end{pmatrix} \boldsymbol{A}_{\mathcal{BN}}^T(\nu,t) \\
=& \begin{pmatrix} 0 & 0 & 1 \\ 0 & 0 & 0 \\ -1 & 0 & 0 \end{pmatrix} \theta'(\nu,t) = \begin{pmatrix} 0 \\ \theta'(\nu,t) \\ 0 \end{pmatrix}\hat{} = \boldsymbol{\phi}'(\nu,t),
\end{aligned} \tag{A.9}
$$

$$
{}_{\mathcal{B}}\delta\boldsymbol{k}(\nu,t) = \begin{pmatrix} 0 \\ \delta\theta'(\nu,t) \\ 0 \end{pmatrix}. \tag{A.10}
$$

The angular velocity vector reduces to

$$
\begin{aligned}
{}_{\mathcal{B}}\hat{\boldsymbol{\omega}}(\nu,t) =& \dot{\theta}(\nu,t) \begin{pmatrix} -\sin(\theta(\nu,t)) & 0 & \cos(\theta(\nu,t)) \\ 0 & 0 & 0 \\ -\cos(\theta(\nu,t)) & 0 & -\sin(\theta(\nu,t)) \end{pmatrix} \boldsymbol{A}_{\mathcal{BN}}^T(\nu,t), \\
=& \begin{pmatrix} 0 & 0 & 1 \\ 0 & 0 & 0 \\ -1 & 0 & 0 \end{pmatrix} \dot{\theta}(\nu,t) = \begin{pmatrix} 0 \\ \dot{\theta}(\nu,t) \\ 0 \end{pmatrix}\hat{} = \dot{\boldsymbol{\phi}}(\nu,t).
\end{aligned} \tag{A.11}
$$

For the velocity ${}_{\mathcal{B}}\boldsymbol{v}_{OS}(t) \in \mathbb{R}^3$ and the acceleration ${}_{\mathcal{B}}\boldsymbol{a}_{OS}(t) \in \mathbb{R}^3$ of the CoM of the head, we find

$$
\begin{aligned}
{}_{\mathcal{B}}\boldsymbol{v}_{OS}(t) =& {}_{\mathcal{B}}\dot{\boldsymbol{r}}_{OS}(t) = {}_{\mathcal{B}}\dot{\boldsymbol{r}}_{OQ}(t) + \dot{\boldsymbol{A}}_{\mathcal{BH}}(t) \begin{pmatrix} h \\ 0 \\ b \end{pmatrix}, \\
=& {}_{\mathcal{B}}\dot{\boldsymbol{r}}_{OQ}(t) + {}_{\mathcal{B}}\hat{\boldsymbol{\omega}}_L(t)\boldsymbol{A}_{\mathcal{BH}}(t) \begin{pmatrix} h \\ 0 \\ b \end{pmatrix}, \\
=& \begin{pmatrix} \dot{x}_L(t) \\ 0 \\ \dot{z}_L(t) \end{pmatrix} + h\dot{\theta}_L(t) \begin{pmatrix} -\sin(\theta_L(t)) \\ 0 \\ -\cos(\theta_L(t)) \end{pmatrix} + b\dot{\theta}_L(t) \begin{pmatrix} \cos(\theta_L(t)) \\ 0 \\ -\sin(\theta_L(t)) \end{pmatrix},
\end{aligned} \tag{A.12}
$$

and

$$
\begin{aligned}
{}_{\mathcal{B}}\boldsymbol{a}_{OS}(t) =& {}_{\mathcal{B}}\dot{\boldsymbol{v}}_{OS}(t) = {}_{\mathcal{B}}\ddot{\boldsymbol{r}}_{OQ}(t) + {}_{\mathcal{B}}\dot{\boldsymbol{\omega}}_L(t) \times (h_{\mathcal{B}}\boldsymbol{e}_x^{\mathcal{H}}(t) + b_{\mathcal{B}}\boldsymbol{e}_z^{\mathcal{H}}(t)) \\
&+ {}_{\mathcal{B}}\boldsymbol{\omega}_L(t) \times \left({}_{\mathcal{B}}\boldsymbol{\omega}_L(t) \times (h_{\mathcal{B}}\boldsymbol{e}_x^{\mathcal{H}}(t) + b_{\mathcal{B}}\boldsymbol{e}_z^{\mathcal{H}}(t))\right) \\
=& \begin{pmatrix} \ddot{x}_L(t) \\ 0 \\ \ddot{z}_L(t) \end{pmatrix} + h\ddot{\theta}_L(t) \begin{pmatrix} -\sin(\theta_L(t)) \\ 0 \\ -\cos(\theta_L(t)) \end{pmatrix} + b\ddot{\theta}_L(t) \begin{pmatrix} \cos(\theta_L(t)) \\ 0 \\ -\sin(\theta_L(t)) \end{pmatrix} \\
&+ h\dot{\theta}_L^2(t) \begin{pmatrix} -\cos(\theta_L(t)) \\ 0 \\ \sin(\theta_L(t)) \end{pmatrix} + b\dot{\theta}_L^2(t) \begin{pmatrix} -\sin(\theta_L(t)) \\ 0 \\ -\cos(\theta_L(t)) \end{pmatrix}
\end{aligned} \tag{A.13}
$$

In prevision of the following equations, we will need the variational form of the CoM, the left and the right tendon connection point,

$$
{}_{\mathcal{B}}\delta\boldsymbol{r}_{OS}(t) = \begin{pmatrix} \delta x_L(t) \\ 0 \\ \delta z_L(t) \end{pmatrix} + \delta\theta_L(t) \begin{pmatrix} -h\sin(\theta_L(t)) + b\cos(\theta_L(t)) \\ 0 \\ -h\cos(\theta_L(t)) - b\sin(\theta_L(t)) \end{pmatrix}, \tag{A.14}
$$

$$
{}_{\mathcal{B}}\delta\boldsymbol{r}_{OP}(t) = \begin{pmatrix} \delta x_L(t) \\ 0 \\ \delta z_L(t) \end{pmatrix} + d\delta\theta_L(t) \begin{pmatrix} \cos(\theta_L(t)) \\ 0 \\ -\sin(\theta_L(t)) \end{pmatrix}, \tag{A.15}
$$

$$
{}_{\mathcal{B}}\delta\boldsymbol{r}_{OR}(t) = \begin{pmatrix} \delta x_L(t) \\ 0 \\ \delta z_L(t) \end{pmatrix} - d\delta\theta_L(t) \begin{pmatrix} \cos(\theta_L(t)) \\ 0 \\ -\sin(\theta_L(t)) \end{pmatrix}. \tag{A.16}
$$

Equations of motion

Following Chapter 3, the equation of motion of the system are derived using the principal of virtual work and in equation (3.20) it is stated that the system is composed of the virtual work due to static forces δW^{stat} and due to the virtual work of the dynamic forces δW^{dyn} which will be derived in the following. Similar to (3.21), we can separate the virtual work of the static forces into δW^{int} and δW^{ext}.[1]
The virtual work of the internal forces δW^{int} for the present case can be found according to (3.22) and the internal forces ${}_{\mathcal{N}}\boldsymbol{n}(\nu) \in \mathbb{R}^3$ are transformed in the inertial frame with the component-wise formulation for the planar case

$$
\begin{pmatrix} {}_{\mathcal{B}}n_x \\ 0 \\ {}_{\mathcal{B}}n_z \end{pmatrix} = \boldsymbol{A}_{\mathcal{B}\mathcal{N}}{}_{\mathcal{N}}\boldsymbol{n} = \boldsymbol{A}_{\mathcal{B}\mathcal{N}} \begin{pmatrix} N \\ 0 \\ Q_z \end{pmatrix} = \begin{pmatrix} N\cos(\theta) + Q_z\sin(\theta) \\ 0 \\ -N\sin(\theta) + Q_z\cos(\theta) \end{pmatrix}, \tag{A.17}
$$

with $N \in \mathbb{R}$ and $Q_z \in \mathbb{R}$ being the normal and shear force at a cross section at ν. Due to the planar case, ${}_{\mathcal{N}}\boldsymbol{m} = {}_{\mathcal{B}}\boldsymbol{m} \in \mathbb{R}^3 = M_{\mathcal{B}}\boldsymbol{e}^y$. $M \in \mathbb{R}$ being the internal moment at a cross

[1] In the following, the explicit dependency on ν and t are left out as they are clear for the development, except from cases where it is needed.

section at ν. With the following relationships,

$$
\begin{aligned}
{}_{\mathcal{N}}\delta\boldsymbol{k} &= {}_{\mathcal{B}}\delta\boldsymbol{k} = \begin{pmatrix} 0 \\ \delta\theta' \\ 0 \end{pmatrix}, && \text{(A.18)}\\
{}_{\mathcal{N}}\delta\boldsymbol{\gamma} &= \\
&= \begin{pmatrix} \delta x^{'}\cos(\theta) - x^{'}\sin(\theta)\delta\theta - \delta z^{'}\sin(\theta) - z'\cos(\theta)\delta\theta \\ 0 \\ \delta x^{'}\sin(\theta) + x^{'}\cos(\theta)\delta\theta + \delta z^{'}\cos(\theta) - z'\sin(\theta)\delta\theta \end{pmatrix} && \text{(A.19)}
\end{aligned}
$$

and equation (A.17), the internal virtual work (3.22) is simplified to

$$
\begin{aligned}
\delta W^{int} &= -\int_0^L \left[\underbrace{{}_{\mathcal{N}}\boldsymbol{n}^T \boldsymbol{A}_{\mathcal{BN}}^T}_{{}_{\mathcal{B}}\boldsymbol{n}^T} \begin{pmatrix} \delta x' - \delta\theta z' \\ 0 \\ \delta z' + \delta\theta x' \end{pmatrix} + \begin{pmatrix} 0 \\ M \\ 0 \end{pmatrix}^T \begin{pmatrix} 0 \\ \delta\theta' \\ 0 \end{pmatrix} \right] d\nu, \\
&= -\int_0^L \delta x' {}_{\mathcal{B}}n_x + \delta z' {}_{\mathcal{B}}n_z + \delta\theta' M + \delta\theta(x' {}_{\mathcal{B}}n_z - z' {}_{\mathcal{B}}n_x) d\nu. && \text{(A.20)}
\end{aligned}
$$

The same constitutive laws are applied as in equation (3.15), (3.18) for the shear and normal forces are applied whereas for the bending stiffness, equation (3.16) reduces to

$$
M = EI\theta'. \tag{A.21}
$$

The virtual work of the external forces is derived in (3.26) which is split up into the virtual work of the gravitational force and the virtual work of the tendon actuation. The virtual work of the tendon actuation (3.31) can be computed to

$$
\begin{aligned}
\delta W^{tendon} =& \begin{pmatrix} \delta x_L \\ 0 \\ \delta z_L \end{pmatrix}^T \left({}_{\mathcal{B}}\boldsymbol{e}_{tl}^{\mathcal{H}} f_{tl} + {}_{\mathcal{B}}\boldsymbol{e}_{tr}^{\mathcal{H}} f_{tr} \right) + \delta\theta_L d\, {}_{\mathcal{B}}\boldsymbol{e}_z^H \times \left({}_{\mathcal{B}}\boldsymbol{e}_{tl}^{\mathcal{H}} f_{tl} - {}_{\mathcal{B}}\boldsymbol{e}_{tr}^{\mathcal{H}} f_{tr} \right) \\
=& \begin{pmatrix} \delta x_L \\ 0 \\ \delta z_L \end{pmatrix}^T \begin{pmatrix} {}_{\mathcal{B}}\boldsymbol{e}_{tl}^{\mathcal{H}} & {}_{\mathcal{B}}\boldsymbol{e}_{tr}^{\mathcal{H}} \end{pmatrix} \begin{pmatrix} f_{tl} \\ f_{tr} \end{pmatrix} \\
&+ \delta\theta_L d \begin{pmatrix} {}_{\mathcal{B}}\boldsymbol{e}_z^H \times {}_{\mathcal{B}}\boldsymbol{e}_{tl}^{\mathcal{H}} & - {}_{\mathcal{B}}\boldsymbol{e}_z^H \times {}_{\mathcal{B}}\boldsymbol{e}_{tr}^{\mathcal{H}} \end{pmatrix} \begin{pmatrix} f_{tl} \\ f_{tr} \end{pmatrix} \\
=& \delta\boldsymbol{q}_L^T \boldsymbol{P}(\boldsymbol{q})\boldsymbol{u}, && \text{(A.22)}
\end{aligned}
$$

with the unit tendon direction vectors for left ${}_{\mathcal{B}}\boldsymbol{e}_{tl} \in \mathbb{R}^3$ and right ${}_{\mathcal{B}}\boldsymbol{e}_{tr} \in \mathbb{R}^3$ tendon, depicted in Fig. A.1, $\boldsymbol{q}_L = (x_L,\, z_L,\, \theta_L)^T = \boldsymbol{q}(\nu = L)$, the inputs $\boldsymbol{u} \in \mathbb{R}^2$,

$$
\boldsymbol{u} = \begin{pmatrix} f_{tl} \\ f_{tr} \end{pmatrix}, \tag{A.23}
$$

and the tendon coupling matrix $\boldsymbol{P}(\boldsymbol{q}_L) \in \mathbb{R}^{3\times 2}$,

$$
\boldsymbol{P}(\boldsymbol{q}_L) = \begin{pmatrix} {}_{\mathcal{B}}e_{x,tl} & {}_{\mathcal{B}}e_{x,tr} \\ {}_{\mathcal{B}}e_{z,tl} & {}_{\mathcal{B}}e_{z,tr} \\ d\left(\cos(\theta_L) {}_{\mathcal{B}}e_{x,tl} - \sin(\theta_L) {}_{\mathcal{B}}e_{z,tl}\right) & d\left(\cos(\theta_L) {}_{\mathcal{B}}e_{x,tr} + \sin(\theta_L) {}_{\mathcal{B}}e_{z,tr}\right) \end{pmatrix}. \tag{A.24}
$$

Furthermore, we have arranged the terms that the inputs $\boldsymbol{u} = (f_{tl},\ f_{tr})^T \in \mathbb{R}^2$ are coupled to the respective generalized coordinates by the input matrix $\boldsymbol{P}(\boldsymbol{q}) \in \mathbb{R}^{3\times 2}$. For the second term in (3.26) the gravitational effects of the continuum and the gravitational effect of the head mass are considered. With gravitational force of the continuum (3.29) the virtual work equates to

$$\begin{aligned}
\delta W^{grav} = &\int_0^L {}_{\mathcal{B}}\delta x \rho A g d\nu + {}_{\mathcal{B}}\delta x_L m_H g \\
&+ \delta\theta_L \left({}_B\boldsymbol{r}_{0S} - {}_B\boldsymbol{r}_{0Q}\right) \times \begin{pmatrix} -m_H g \\ 0 \\ 0 \end{pmatrix} \\
= &-\rho A g \int_0^L \delta x(\nu) d\nu - m_H g \left(\delta x_L + \delta\theta_L (b\cos(\theta_L) - h\sin(\theta_L))\right) \\
= &-\rho A g \int_0^L \delta x(\nu) d\nu - m_H g \begin{pmatrix} \delta x_L \\ 0 \\ \delta\theta_L \end{pmatrix}^T \begin{pmatrix} 1 \\ 0 \\ h\sin(\theta_L) - b\cos(\theta_L) \end{pmatrix}.
\end{aligned} \tag{A.25}$$

Within the identification process in Section. 3.4, instead of the tendon forces and the gravity forces, an external force ${}_B\boldsymbol{n}_w \in \mathbb{R}^3$ and and ${}_BM_w \in \mathbb{R}$ is exerted at point Q whose virtual work is

$$\delta W^w = {}_B\boldsymbol{n}_W \delta \begin{pmatrix} \delta x_L \\ 0 \\ \delta z_L \end{pmatrix} + M_w \delta\theta_L. \tag{A.26}$$

According to (3.36) the virtual work of the dynamic forces is separated into the part from the rigid body dynamics of the head and the part from the continuum dynamics of the beam. The virtual work of the dynamic forces from the rigid body can be established to

$$\begin{aligned}
\delta W^{dyn,head} = &- {}_{\mathcal{B}}\delta\boldsymbol{r}_{OS}^T m_{H\mathcal{B}}\boldsymbol{a}_{OS} - \delta\theta_L J_{yy}\ddot{\theta}(L), \\
&\underbrace{= -\begin{pmatrix} \delta x_L \\ 0 \\ \delta z_L \end{pmatrix}^T m_{H\mathcal{B}}\boldsymbol{a}_{OS}}_{1} \\
&\underbrace{+ h\delta\theta_L \begin{pmatrix} \sin(\theta_L) \\ 0 \\ \cos(\theta_L) \end{pmatrix}^T m_{H\mathcal{B}}\boldsymbol{a}_{OS}}_{2} \\
&\underbrace{-b\delta\theta_L \begin{pmatrix} \cos(\theta_L) \\ 0 \\ -\sin(\theta_L) \end{pmatrix}^T m_{H\mathcal{B}}\boldsymbol{a}_{OS}}_{3} - \delta\theta_L J_{yy}\ddot{\theta}_L.
\end{aligned} \tag{A.27}$$

For for the 1. part, it follows

$$\begin{aligned}
1 &= -m_H \delta x_L \ddot{x}_L - m_H \delta z_L \ddot{z}_L + m_H h \ddot{\theta}_L \left(\delta x \sin(\theta_L) + \delta z_L \cos(\theta_L)\right) \\
&+ m_H b \ddot{\theta}_L \left(-\delta x_L \cos(\theta_L) + \delta z_L \sin(\theta_L)\right) \\
&+ m_H h \dot{\theta}_L^2 \left(\delta x_L \cos(\theta_L) - \delta z_L \sin(\theta_L)\right) \\
&+ m_H b \dot{\theta}_L^2 \left(\delta x_L \sin(\theta_L) + \delta z_L \cos(\theta_L)\right) \\
&= \delta \boldsymbol{q}_L^T \begin{pmatrix} -m_H & 0 & m_H(h\sin(\theta_L) - b\cos(\theta_L)) \\ 0 & -m_H & m_H(h\cos(\theta_L) + b\sin(\theta_L)) \\ 0 & 0 & 0 \end{pmatrix} \ddot{\boldsymbol{q}}_L \\
&+ \delta \boldsymbol{q}_L^T \begin{pmatrix} 0 & 0 & m_H(h\cos(\theta_L) + b\sin(\theta_L)) \\ 0 & 0 & m_H(b\cos(\theta_L) - h\sin(\theta_L)) \\ 0 & 0 & 0 \end{pmatrix} \dot{\boldsymbol{q}}_L^2
\end{aligned} \tag{A.28}$$

For the 2. part, it follows

$$\begin{aligned}
2 &= m_H h \delta\theta_L \left[\sin(\theta_L)\ddot{x}_L + \cos(\theta_L)\ddot{z}_L - h\ddot{\theta}_L - b\dot{\theta}_L^2\right] \\
&= \delta \boldsymbol{q}_L^T \begin{pmatrix} 0 & 0 & 0 \\ 0 & 0 & 0 \\ m_H h \sin(\theta_L) & m_H h \cos(\theta_L) & -m_H h^2 \end{pmatrix} \ddot{\boldsymbol{q}}_L \\
&+ \delta \boldsymbol{q}_L^T \begin{pmatrix} 0 & 0 & 0 \\ 0 & 0 & 0 \\ 0 & 0 & -m_H h b \end{pmatrix} \dot{\boldsymbol{q}}_L^2
\end{aligned} \tag{A.29}$$

For the 3, part, it follows

$$\begin{aligned}
3 &= -m_H b \delta\theta_L \left[\cos(\theta_L)\ddot{x}_L - \sin(\theta_L)\ddot{z}_L + b\ddot{\theta_L} - h\dot{\theta}_L^2\right] \\
&= \delta \boldsymbol{q}_L^T \begin{pmatrix} 0 & 0 & 0 \\ 0 & 0 & 0 \\ -m_H b \cos(\theta_L) & m_H b \sin(\theta_L) & -m_H b^2 \end{pmatrix} \ddot{\boldsymbol{q}}_L \\
&+ \delta \boldsymbol{q}_L^T \begin{pmatrix} 0 & 0 & 0 \\ 0 & 0 & 0 \\ 0 & 0 & m_H b h \end{pmatrix} \dot{\boldsymbol{q}}_L^2
\end{aligned} \tag{A.30}$$

With above equations, we find the following expression for the virtual work of the dynamic forces

$$\delta W^{dyn,head} = -\delta \boldsymbol{q}_L^T \boldsymbol{M}_H(\boldsymbol{q}_L)\ddot{\boldsymbol{q}}_L - \delta \boldsymbol{q}_L^T \boldsymbol{C}_H(\boldsymbol{q}_L, \dot{\boldsymbol{q}}_L)\dot{\boldsymbol{q}}_L \tag{A.31}$$

with the massmatrix $\boldsymbol{M}_H(\boldsymbol{q}_L) \in \mathbb{R}^{3\times 3}$

$$\boldsymbol{M}_H(\boldsymbol{q}_L) = \begin{pmatrix} m_H & 0 & m_H\, l_a \\ 0 & m_H & -m_H\, l_b \\ m_H\, l_a & -m_H\, l_b & J_{yy} + m_H(b^2 + h^2) \end{pmatrix} \tag{A.32}$$

$$\begin{aligned}
l_a &= (-h\sin(\theta_L) + b\cos(\theta_L)) \\
l_b &= (h\cos(\theta_L) + b\sin(\theta_L))
\end{aligned} \tag{A.33}$$

and the Coriolis and centrifugal $\boldsymbol{C}_H(\boldsymbol{q}, \dot{\boldsymbol{q}}) \in \mathbb{R}^{3\times3}$ matrix

$$\boldsymbol{C}_H(\boldsymbol{q}_L, \dot{\boldsymbol{q}}_L) = \begin{pmatrix} 0 & 0 & -m_H(h\cos(\theta_L) + b\sin(\theta_L)) \\ 0 & 0 & m_H(-b\cos(\theta_L) + h\sin(\theta_L)) \\ 0 & 0 & 0 \end{pmatrix} \tag{A.34}$$

The virtual work from the dynamic forces of the continuum mechanism are as follows

$$\begin{aligned}
\delta W^{dyn,beam} &= -\int_0^L {}_{\mathcal{B}}\delta\boldsymbol{r}(\nu,t)^T \rho A {}_{\mathcal{B}}\ddot{\boldsymbol{r}}(\nu,t) + \delta\theta(\nu,t)\rho J_{yy}\ddot{\theta}(\nu,t)d\nu \\
&= -\int_0^L \begin{pmatrix} \delta x(\nu,t) \\ 0 \\ \delta z(\nu,t) \end{pmatrix}^T \rho A \begin{pmatrix} \ddot{x}(\nu,t) \\ 0 \\ \ddot{z}(\nu,t) \end{pmatrix} + \delta\theta(\nu,t)\rho J_{yy}\ddot{\theta}(\nu,t)d\nu \\
&= -\int_0^L \rho A(\delta x(\nu,t)\ddot{x}(\nu,t) + \delta z(\nu,t)\ddot{z}(\nu,t)) + \rho J_{yy}\delta\theta(\nu,t)\ddot{\theta}(\nu,t)d\nu \\
&= -\int_0^L \rho \begin{pmatrix} \delta x(\nu,t) \\ \delta z(\nu,t) \\ \delta\theta(\nu,t) \end{pmatrix}^T \begin{pmatrix} A & 0 & 0 \\ 0 & A & 0 \\ 0 & 0 & J_{yy} \end{pmatrix} \begin{pmatrix} \ddot{x}(\nu,t) \\ \ddot{z}(\nu,t) \\ \ddot{\theta}(\nu,t) \end{pmatrix} d\nu \\
&= -\int_0^L \boldsymbol{q}(\nu,t)^T \begin{pmatrix} \rho A & 0 & 0 \\ 0 & \rho A & 0 \\ 0 & 0 & \rho J_{yy} \end{pmatrix} \ddot{\boldsymbol{q}}(\nu,t)d\nu
\end{aligned} \tag{A.35}$$

Now, the virtual work of the system needs to be zero $\delta W = 0$ for all admissible variations δx_{adm}, δz_{adm}, $\delta\theta_{adm}$. An analytic expression to find the generalized functions $\boldsymbol{q}(\nu,t)$ which are a solution to $\delta W = 0$ is not possible. Thus, we will apply the finite element method to discretize the beam along its centerline.

Discretization: The beam finite element method

Following Section 3.3, the finite element method (FEM) is used to reduce the infinite number to a finite number of DoF of the system. To do so, the centerline of the beam, denoted as a region Ω, is divided into $k_{el} \in \mathbb{N}$ elements. Each element $e = [1, k_{el}]$ is defined as a sub region $\Omega_e = [n^e, n^{e+1}] \subset \Omega$ each of which is described by a fixed number of generalized coordinates at the boundaries, i.e. nodes.
The generalized coordinates of the system $\boldsymbol{q}(\nu,t)$ are represented by finite set of coordinates, $\boldsymbol{q} \in \mathbb{R}^{3(k_{el}+1)}$,

$$\boldsymbol{q} = \left(x^1,\, z^1,\, \theta^1,\, \ldots,\, x^{k_{el}+1},\, z^{k_{el}+1},\, \theta^{k_e l+1}\right)^T \in \mathbb{R}^{3(k_{el}+1)}, \tag{A.36}$$

which approximate $\boldsymbol{q}(\nu,t)$ via a summation,

$$\begin{pmatrix} x(\nu,t) \\ z(\nu,t) \\ \theta(\nu,t) \end{pmatrix} = \sum_{e=1}^{k_{el}} \chi_{\Omega^e}(\nu) \begin{pmatrix} x^{h,e}(\nu^e(\nu), \boldsymbol{q}(t)) \\ z^{h,e}(\nu^e(\nu), \boldsymbol{q}(t)) \\ \theta^{h,e}(\nu^e(\nu), \boldsymbol{q}(t)) \end{pmatrix}, \tag{A.37}$$

where $\chi_{\Omega^e}(\nu)$ is again an operator which takes care that summation at the nodes is correct. Following Section 3.3, linear shape functions $\boldsymbol{N}(\nu^e) \in \mathbb{R}^{1\times2}$,

$$\boldsymbol{N}(\nu^e) = (0.5(\nu^e - 1),\, 0.5(\nu^e + 1))\,, \tag{A.38}$$

are applied to interpolate between the nodes e and $e+1$. To do so, the element coordinate $\nu^e \in [-1, 1]$ is introduced, (see equation (3.41)). To connect the DoF of element e with the generalized coordinates of the approximated system (A.36), a connector matrix $\boldsymbol{C}^e_{x,z,\theta} \in \mathbb{R}^{2\times 3(k_{el}+1)}$ for each coordinate of the element is utilized,

$$\begin{pmatrix} x^e \\ x^{e+1} \end{pmatrix} = \boldsymbol{C}^e_x \boldsymbol{q}, \begin{pmatrix} z^e \\ z^{e+1} \end{pmatrix} = \boldsymbol{C}^e_z \boldsymbol{q}, \begin{pmatrix} \theta^e \\ \theta^{e+1} \end{pmatrix} = \boldsymbol{C}^e_\theta \boldsymbol{q}, \tag{A.39}$$

which yields for the shape functions $x^{h,e}$, $z^{h,e}$, $\theta^{h,e} \in \mathbb{R}$,

$$\begin{aligned} x^{h,e}(\nu^e, \boldsymbol{q}) =& \boldsymbol{N}(\nu^e)\boldsymbol{C}^e_x \boldsymbol{q}, \\ z^{h,e}(\nu^e, \boldsymbol{q}) =& \boldsymbol{N}(\nu^e)\boldsymbol{C}^e_z \boldsymbol{q}, \\ \theta^{h,e}(\nu^e, \boldsymbol{q}) =& \boldsymbol{N}(\nu^e)\boldsymbol{C}^e_\theta \boldsymbol{q}. \end{aligned} \tag{A.40}$$

The dynamics of node $k_{el}+1$ is governed by the rigid body dynamics of the head. Therefore, a special connector matrix $\boldsymbol{C}^L \in \mathbb{R}^{3\times 3(k_{el}+1)}$ is introduced,

$$\boldsymbol{q}^L = \begin{pmatrix} x^{k_{el}+1} \\ z^{k_{el}+1} \\ \theta^{k_{el}+1} \end{pmatrix} = \boldsymbol{C}^L \boldsymbol{q}. \tag{A.41}$$

For the subsequent developments, we will need the derivative with respect to ν, the variation and its derivative w.r.t. ν of the shape functions (A.40), as shown in Section 3.3. For the derivative w.r.t. ν, we find

$$\frac{d}{d\nu} x^e(\nu^e) = \frac{dx^e}{d\nu^e}\frac{d\nu^e}{d\nu} \overset{eq.(3.49)}{=} \boldsymbol{N}'\boldsymbol{C}^e_x \boldsymbol{q}, \tag{A.42}$$

here exemplary shown for x, however directly applicable to z and θ as well. In (A.42), the derivative of the shape function occurs which can be found to

$$\boldsymbol{N}' = \frac{2}{\Delta L}(-0.5,\, 0.5). \tag{A.43}$$

For the variation of (A.40) and its special derivative are needed, it can be found:

$$\delta x^e(\nu^e) = \boldsymbol{N}\boldsymbol{C}^e_x \delta\boldsymbol{q}, \; \frac{\partial}{\partial\nu}\delta x^e(\nu^e) = \boldsymbol{N}'\boldsymbol{C}^e_x \delta\boldsymbol{q}. \tag{A.44}$$

The virtual work of the system contains the virtual work of the internal forces (A.20), the tendon forces (A.22), the gravitational forces (A.25), the dynamic forces of the head (A.31) and the dynamic forces of the beam (A.35). Now, as stated earlier, the virtual work of the system needs to be zero for all admissible $\delta\boldsymbol{q}(\nu, t)$. This translates to the case where the generalized coordinates are approximated using the finite elements (A.36) to the following reformulation of the terms for the different virtual works. Using (3.52) and the variation of the element DoF and its spatial derivative (A.44), we can reformulate equation (A.20) to

$$\begin{aligned} \delta W^{int} =& -\int_0^L \delta x'_{\mathcal{B}} n_x + \delta z'_{\mathcal{B}} n_z + \delta\theta' M + \delta\theta(x'_{\mathcal{B}} n_z - z'_{\mathcal{B}} n_x) d\nu, \\ =& -\delta\boldsymbol{q}^T \sum_{e=1}^{k_{el}} \left[\boldsymbol{C}^{e,T}_x \boldsymbol{f}^{int,e}_x + \boldsymbol{C}^{e,T}_z \boldsymbol{f}^{int,e}_z + \boldsymbol{C}^{e,T}_\theta \boldsymbol{f}^{int,e}_\theta \right], \\ =& -\delta\boldsymbol{q}^T \boldsymbol{f}^{int}, \end{aligned} \tag{A.45}$$

with

$$\boldsymbol{f}_x^{int,e} = \int_{-1}^{1} \boldsymbol{N}'^T {}_{\mathcal{B}}n_x d\nu^e, \tag{A.46}$$

$$\boldsymbol{f}_z^{int,e} = \int_{-1}^{1} \boldsymbol{N}'^T {}_{\mathcal{B}}n_z d\nu^e, \tag{A.47}$$

$$\boldsymbol{f}_\theta^{int,e} = \int_{-1}^{1} \boldsymbol{N}'^T M + \boldsymbol{N}^T \left(x'_{\mathcal{B}}n_z - z'_{\mathcal{B}}n_x \right) \frac{\Delta L}{2} d\nu^e. \tag{A.48}$$

The virtual work of the tendon forces, (A.22), can be reformulated with (A.41) to

$$\begin{aligned} \delta W^{tendon} =& \delta \boldsymbol{q}_L^T \boldsymbol{P}(\boldsymbol{q}_L)\boldsymbol{u}, \\ =& \delta \boldsymbol{q}^T \boldsymbol{C}^{L,T} \boldsymbol{P}(\boldsymbol{q}_L)\boldsymbol{u}. \end{aligned} \tag{A.49}$$

Similar, the virtual work of the gravitational forces (A.25) is reformulate using the variation of the element DoF (A.44), (3.52) and (A.41), to

$$\begin{aligned} \delta W^{grav} =& -\rho A g \int_0^L \delta x(\nu) d\nu - m_H g \begin{pmatrix} \delta x_L \\ 0 \\ \delta \theta_L \end{pmatrix}^T \begin{pmatrix} 1 \\ 0 \\ h\sin(\theta_L) - b\cos(\theta_L) \end{pmatrix}, \\ =& -\delta \boldsymbol{q}^T \left[\boldsymbol{f}^{grav,beam} + \boldsymbol{f}^{grav,head} \right] = -\delta \boldsymbol{q}^T \boldsymbol{f}^{grav}, \end{aligned} \tag{A.50}$$

where the introduced terms are

$$\boldsymbol{f}^{grav,beam} = \sum_{e=1}^{k_{el}} \boldsymbol{C}_x^{e,T} \rho A g \int_{-1}^{1} \boldsymbol{N} \frac{\Delta L}{2} d\nu^e, \tag{A.51}$$

$$\boldsymbol{f}^{grav,head} = \boldsymbol{C}^{L,T} m_H g \begin{pmatrix} 1 \\ 0 \\ h\sin(\theta_L) - b\cos(\theta_L) \end{pmatrix}.$$

Again, the virtual work of the external forces used in the identification process (A.26), or another general purposes, equates to

$$\delta W^w = \delta \boldsymbol{q}^T \boldsymbol{C}_L^T \begin{pmatrix} {}_{\mathcal{B}}n_x \\ {}_{\mathcal{B}}n_z \\ M_w \end{pmatrix} \tag{A.52}$$

With equation (A.41), we can reformulate equation the dynamics of the head (A.31) to

$$\begin{aligned} \delta W^{dyn,head} =& -\delta \boldsymbol{q}_L^T \boldsymbol{M}_H(\boldsymbol{q}) \ddot{\boldsymbol{q}}_L - \delta \boldsymbol{q}_L^T \boldsymbol{C}_H(\boldsymbol{q}, \dot{\boldsymbol{q}}) \dot{\boldsymbol{q}}_L, \\ =& -\delta \boldsymbol{q}^T \boldsymbol{C}^{L,T} \left[\boldsymbol{M}_H(\boldsymbol{q}) \boldsymbol{C}^L \ddot{\boldsymbol{q}} + \boldsymbol{C}_H(\boldsymbol{q}, \dot{\boldsymbol{q}}) \boldsymbol{C}^L \dot{\boldsymbol{q}} \right], \end{aligned} \tag{A.53}$$

and for the virtual work of the dynamic force of the beam (A.35), we find a reformulation by applying equation (A.44) and (3.52)

$$\begin{aligned}\delta W^{dyn,beam} =& -\int_0^L \delta \boldsymbol{q}^T(\nu) \begin{pmatrix} \rho A \ddot{x}(\nu) \\ \rho A \ddot{z}(\nu) \\ \rho J_{yy} \ddot{\theta}(\nu) \end{pmatrix} d\nu, \\ =& -\delta \boldsymbol{q}^T \sum_{e=1}^{k_{el}} \left[\boldsymbol{C}_x^{e,T} \int_{-1}^{1} \boldsymbol{N} \rho A \boldsymbol{N}^T \frac{\Delta L}{2} d\nu^e \boldsymbol{C}_x^e \right. \\ &+ \boldsymbol{C}_z^{e,T} \int_{-1}^{1} \boldsymbol{N} \rho A \boldsymbol{N}^T \frac{\Delta L}{2} d\nu^e \boldsymbol{C}_z^e \\ &\left. + \boldsymbol{C}_\theta^{e,T} \int_{-1}^{1} \boldsymbol{N} \rho J_{yy} \boldsymbol{N}^T \frac{\Delta L}{2} d\nu^e \boldsymbol{C}_\theta^e \right] \ddot{\boldsymbol{q}}. \end{aligned} \tag{A.54}$$

Now, equation (A.53) and (A.54) can be summarized to

$$\delta W^{dyn} = -\delta \boldsymbol{q}^T \left(\boldsymbol{M} \ddot{\boldsymbol{q}} + \boldsymbol{C}^{L,T} \boldsymbol{C}_H \boldsymbol{C}^L \dot{\boldsymbol{q}} \right), \tag{A.55}$$

with the overall mass matrix of the system $\boldsymbol{M} \in \mathbb{R}^{3(k_{el}+1)\times 3(k_{el}+1)}$,

$$\begin{aligned} \boldsymbol{M} &= \sum_{e=1}^{k_{el}} \boldsymbol{C}_x^{e,T} \boldsymbol{M}_x \boldsymbol{C}_x^e + \boldsymbol{C}_z^{e,T} \boldsymbol{M}_z \boldsymbol{C}_z^e + \boldsymbol{C}_\theta^{e,T} \boldsymbol{M}_\theta \boldsymbol{C}_\theta^e + \boldsymbol{C}^{L,T} \boldsymbol{M}_H \boldsymbol{C}^L, \\ \boldsymbol{M}_x &= \int_{-1}^{1} \boldsymbol{N} \rho A \boldsymbol{N}^T \frac{\Delta L}{2} d\nu^e, \\ \boldsymbol{M}_z &= \int_{-1}^{1} \boldsymbol{N} \rho A \boldsymbol{N}^T \frac{\Delta L}{2} d\nu^e, \\ \boldsymbol{M}_\theta &= \int_{-1}^{1} \boldsymbol{N} \rho J_{yy} \boldsymbol{N}^T \frac{\Delta L}{2} d\nu^e. \end{aligned} \tag{A.56}$$

and the mass matrix of the head $\boldsymbol{M}_H$ from (A.32). Since the virtual work needs to be zero for all admissible variations $\delta \boldsymbol{q}_{adm} \neq \boldsymbol{0}$, we find the equation of motion of the system,

$$\begin{aligned} -\boldsymbol{M}\ddot{\boldsymbol{q}} - \boldsymbol{C}^L \boldsymbol{C}_H \dot{\boldsymbol{q}} - \boldsymbol{f}^{int} - \boldsymbol{f}^{grav,beam} - \boldsymbol{f}^{grav,head} + \boldsymbol{C}^{L,T} \boldsymbol{P}(\boldsymbol{q}_L) \boldsymbol{u} = 0, \\ \boldsymbol{M}\ddot{\boldsymbol{q}} + \boldsymbol{C}^L \boldsymbol{C}_H \dot{\boldsymbol{q}} + \boldsymbol{f}^{int} + \boldsymbol{f}^{grav,beam} + \boldsymbol{f}^{grav,head} = \boldsymbol{C}^{L,T} \boldsymbol{P}(\boldsymbol{q}_L) \boldsymbol{u} \end{aligned} \tag{A.57}$$

which can be solved by using numerical integration. If the system is deflected statically, equation (A.57) can not be solved by numerical integration as the acceleration and velocity terms vanish. Thus, the static solution of the static equation for a deflected beam with head mass,

$$\begin{aligned} \boldsymbol{f}^{int} + \boldsymbol{f}^{grav,beam} + \boldsymbol{f}^{grav,head} - \boldsymbol{B}(\boldsymbol{q}) \boldsymbol{u} =& \boldsymbol{0}, \\ \boldsymbol{k}(\boldsymbol{q}) =& \boldsymbol{0} \end{aligned} \tag{A.58}$$

can be found by solving the nonlinear equation (A.58) using numerical methods. In this work, the *Newton-Raphson* algorithm is applied to find the solution. For that, we will need the so called stiffness matrix $\boldsymbol{K}(\boldsymbol{q}) \in \mathbb{R}^{3(k_{el}+1)\times 3(k_{el}+1)}$ which is the partial derivative of (A.58) with respect to $\boldsymbol{q}$,

$$\boldsymbol{K}(\boldsymbol{q}) = \frac{\partial \boldsymbol{k}(\boldsymbol{q})}{\partial \boldsymbol{q}}. \tag{A.59}$$

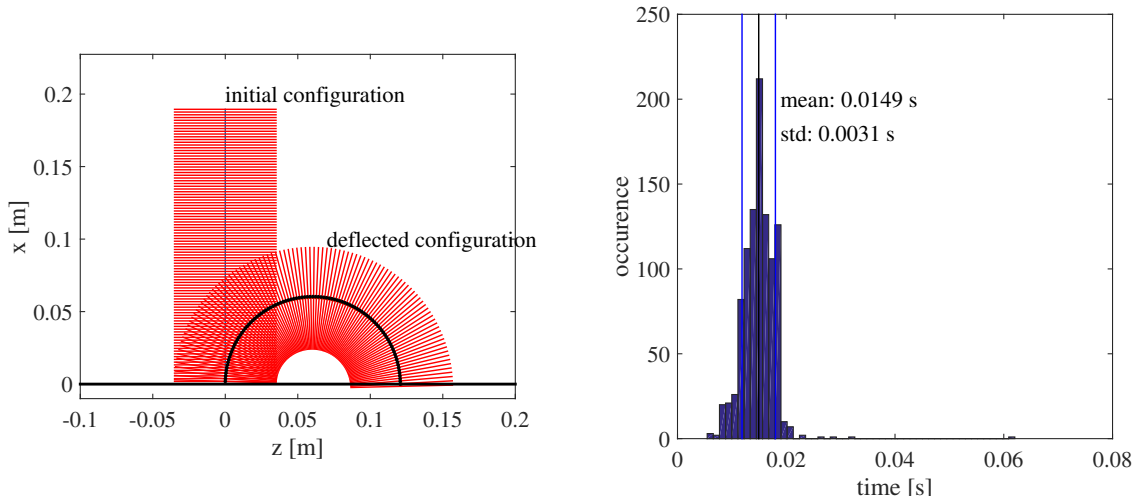

Figure A.2.: Left: Validation of the simulation. The initial configuration of the planar beam, the deflected configuration and a half circle in a black dotted line is shown. The centerline of the deflected configuration should match the black, dotted line. Right: Histogram of the computational time of 1000 randomly selected inputs

The stiffness matrix (A.59) can be derived either explicitly or numerically. For the implementation of the model of the planar system, this was done explicitly. However, is left out in the following.
As mentioned, MATLAB code was generated using the above equations. In order to validate the code, a validation test is reported in the following. For the case of a planar deformation induced by a torque applied at the tip ($\nu = L$) with $M_w \in \mathbb{R}$ in (A.26), the centerline of the beam should poses a circular shape, as for this special case, the static problem has an analytic solution. Further, if we set $M_w = EI/L * \theta_d$, we can directly command a desired tip angle and therefore for $\theta_d = \pi$, the centerline should describe a half circle. In Fig. A.2, simulation results report on the above case whereas the static equation of the beam are solved by a discretization of $k_{el} = 20$ elements. The figure reports only a slight mismatch w.r.t. to the analytic solution.

A.2. Example 2: Spatial system

In this example, the static equilibrium equations for the spatial mechanism described in Section 2.2.2 are derived. Therefore, only the spatial evolution of the coordinates along ν is of interest. For the derivation of the equations, the scheme of the system in Fig. A.3 is considered.

Kinematics

The position of the spatial mechanism is described in (3.3) and the orientation is represented by a positively oriented orthonormal director triad ${}_{\mathcal{B}}\boldsymbol{d}_i(\nu) \in \mathbb{R}^3$ for $i = 1 \dots 3$,

$$\boldsymbol{A}_{\mathcal{BN}}(\nu) = ({}_{\mathcal{B}}\boldsymbol{d}_1(\nu),\, {}_{\mathcal{B}}\boldsymbol{d}_2(\nu),\, {}_{\mathcal{B}}\boldsymbol{d}_3(\nu)), \tag{A.60}$$

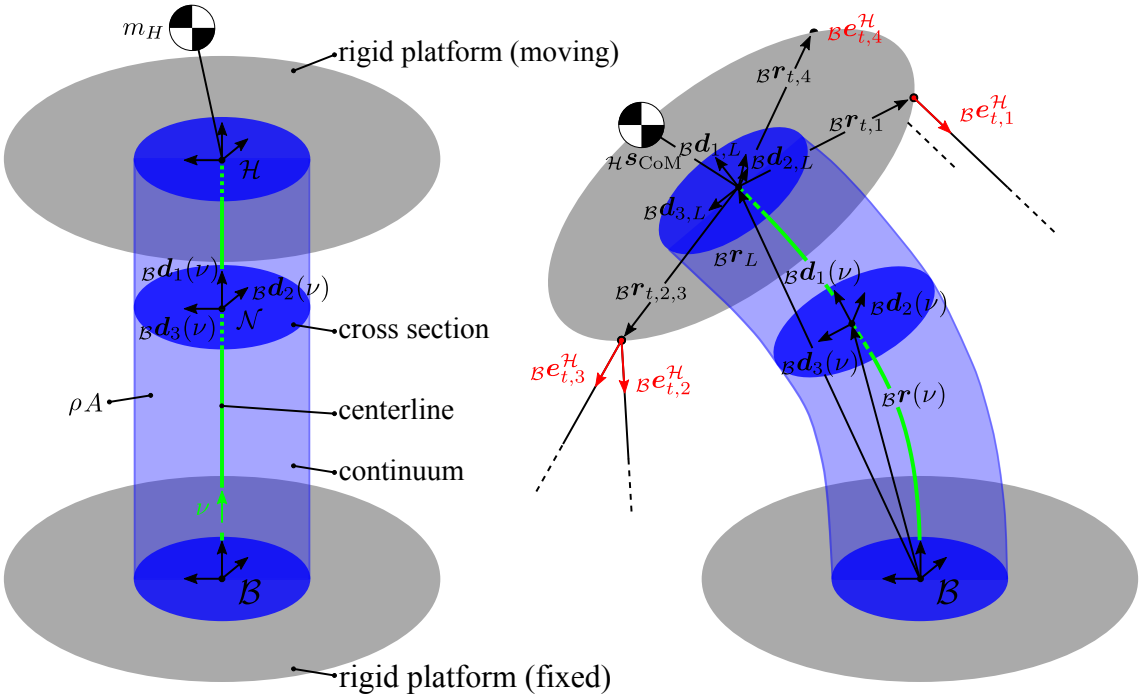

Figure A.3.: Schematic drawing of the spatial system with the associated parameterization.

with the following property:

$$ {}_{\mathcal{B}}\boldsymbol{d}_i(\nu) \cdot {}_{\mathcal{B}}\boldsymbol{d}_j(\nu) = \delta_{ij} \quad i,j = 1,2,3. \tag{A.61} $$

A material surface at ν is spanned by the pair ${}_{\mathcal{B}}\boldsymbol{d}_2(\nu)$, ${}_{\mathcal{B}}\boldsymbol{d}_3(\nu)$ and its respective normal vector is ${}_{\mathcal{B}}\boldsymbol{d}_1(\nu)$. With that, the generalized coordinate function $\boldsymbol{q}(\nu) \in \mathbb{R}^{12}$ is defined to

$$ \boldsymbol{q}(\nu) = ({}_{\mathcal{B}}\boldsymbol{r}^T(\nu),\, {}_{\mathcal{B}}\boldsymbol{d}_1^T(\nu),\, {}_{\mathcal{B}}\boldsymbol{d}_2^T(\nu),\, {}_{\mathcal{B}}\boldsymbol{d}_3^T(\nu))^T, \tag{A.62} $$

and the special location for $\nu = L$ where the head (rigid body) is connected is defined as

$$ \begin{aligned} {}_{\mathcal{B}}\boldsymbol{r}_{OQ} &= {}_{\mathcal{B}}\boldsymbol{r}(\nu = L) = (x_L,\, y_L,\, z_L)^T, \\ \boldsymbol{A}_{\mathcal{B}\mathcal{H}} &= \boldsymbol{A}_{\mathcal{B}\mathcal{N}}(\nu = L) = ({}_{\mathcal{B}}\boldsymbol{d}_{1,L},\, {}_{\mathcal{B}}\boldsymbol{d}_{2,L},\, {}_{\mathcal{B}}\boldsymbol{d}_{3,L}). \end{aligned} \tag{A.63} $$

With equation (A.63) the position of the CoM of the head is

$$ {}_{\mathcal{B}}\boldsymbol{r}_{\mathrm{CoM}} = {}_{\mathcal{B}}\boldsymbol{r}_L + \boldsymbol{A}_{\mathcal{B}\mathcal{H}\mathcal{H}}\boldsymbol{s}_{\mathrm{CoM}}. \tag{A.64} $$

Furthermore, the position of the $r = 4$ tendon connection points, expressed in the base frame, is needed,

$$ {}_{\mathcal{B}}\boldsymbol{r}_{t,k} = \boldsymbol{A}_{\mathcal{B}\mathcal{H}\mathcal{H}}\boldsymbol{r}_{t,k}, \text{ for } k = 1 \ldots 4. \tag{A.65} $$

As we wish to describe the spatial evolution of the centerline, the spatial derivatives of the generalized coordinate function (A.62) are needed and the respective linear strain measure and the curvature vector. Furthermore, their variations are necessary. For the position of a point on the centerline, we find the spatial derivative as well as the variation to be

$$ {}_{\mathcal{B}}\boldsymbol{r}'(\nu) = \left(x'(\nu),\, y'(\nu),\, z'(\nu)\right)^T, \; {}_{\mathcal{B}}\delta\boldsymbol{r}(\nu) = (\delta x(\nu),\, \delta y(\nu),\, \delta z(\nu))^T. \tag{A.66} $$

The linear strain measure (3.11) is the projection of the centerline tangent $\boldsymbol{r}'(\nu)$ in the cross sectional fixed frame

$$\begin{aligned} {}_{\mathcal{N}}\boldsymbol{\gamma}(\nu) =& \boldsymbol{A}_{\mathcal{BN}}^{T}(\nu)\boldsymbol{r}'(\nu), \\ \boldsymbol{r}'(\nu) =& \boldsymbol{A}_{\mathcal{BN}}(\nu)\,{}_{\mathcal{N}}\boldsymbol{\gamma}(\nu) = {}_{\mathcal{B}}\boldsymbol{d}_1(\nu)\,{}_{\mathcal{N}}\gamma_x(\nu) + {}_{\mathcal{B}}\boldsymbol{d}_2(\nu)\,{}_{\mathcal{N}}\gamma_y(\nu) + {}_{\mathcal{B}}\boldsymbol{d}_3(\nu,t)\,{}_{\mathcal{N}}\gamma_z(\nu), \end{aligned} \tag{A.67}$$

and the change in the material orientation along ν is described by the curvature vector (3.12), its component wise description w.r.t. to the director triad[2],

$$k_i = \frac{1}{2}\cdot e_{ijk}\left({}_{\mathcal{B}}\boldsymbol{d}_k(\nu)\cdot {}_{\mathcal{B}}\boldsymbol{d}_j'(\nu)\right), \tag{A.68}$$

and its skew-symmetric representation ${}_{\mathcal{B}}\hat{\boldsymbol{k}}(\nu) = -{}_{\mathcal{B}}\hat{\boldsymbol{k}}(\nu)^T \in \mathbb{R}^{3\times 3}$ with the additional relationship:

$$\begin{aligned} {}_{\mathcal{B}}\boldsymbol{d}_i'(\nu) &= {}_{\mathcal{B}}\hat{\boldsymbol{k}}(\nu)\cdot {}_{\mathcal{B}}\boldsymbol{d}_i(\nu) = {}_{\mathcal{B}}\boldsymbol{k}(\nu)\times {}_{\mathcal{B}}\boldsymbol{d}_i(\nu), \\ {}_{\mathcal{B}}\hat{\boldsymbol{k}}(\nu) &= {}_{\mathcal{B}}\boldsymbol{d}_i'(\nu)\otimes {}_{\mathcal{B}}\boldsymbol{d}_i(\nu) \text{ for } i = 1\ldots 3. \end{aligned} \tag{A.69}$$

Furthermore, the relationship with respect to the variation of the orientation vector is

$${}_{\mathcal{B}}\delta\boldsymbol{\phi}(\nu) = \frac{1}{2}{}_{\mathcal{B}}\boldsymbol{d}_i(\nu)\times {}_{\mathcal{B}}\delta\boldsymbol{d}_i(\nu) \;\text{ for } i = 1\ldots 3, \tag{A.70}$$

and the variation of a director ${}_{\mathcal{B}}\boldsymbol{d}_i(\nu)$ can be expressed as

$${}_{\mathcal{B}}\delta\boldsymbol{d}_i(\nu) = {}_{\mathcal{B}}\delta\boldsymbol{\phi}(\nu)\times {}_{\mathcal{B}}\boldsymbol{d}_i(\nu). \tag{A.71}$$

With the skew symmetric representation of the vector ${}_{\mathcal{B}}\delta\boldsymbol{\phi}(\nu)$, equation (A.71) can be reformulated to

$$\begin{aligned} {}_{\mathcal{B}}\delta\boldsymbol{d}_i(\nu) &= {}_{\mathcal{B}}\delta\hat{\boldsymbol{\phi}}(\nu)\cdot {}_{\mathcal{B}}\boldsymbol{d}_i(\nu), \\ \rightarrow {}_{\mathcal{B}}\delta\hat{\boldsymbol{\phi}}(\nu) &= -{}_{\mathcal{B}}\delta\hat{\boldsymbol{\phi}}^{T}(\nu) = \delta\boldsymbol{A}_{\mathcal{BN}}(\nu)\cdot\boldsymbol{A}_{\mathcal{BN}}^{T}(\nu) \\ {}_{\mathcal{B}}\delta\hat{\boldsymbol{\phi}}_{ij}(\nu) &= {}_{\mathcal{B}}\delta\boldsymbol{d}_i(\nu)\cdot {}_{\mathcal{B}}\boldsymbol{d}_j(\nu) = -{}_{\mathcal{B}}\boldsymbol{d}_i(\nu)\cdot {}_{\mathcal{B}}\delta\boldsymbol{d}_j(\nu) \end{aligned} \tag{A.72}$$

With that, all necessary kinematic quantities are derived to describe the static equilibrium of a geometrically nonlinear Timoshenko beam that deforms spatially.

Static equilibrium equation

The virtual work for a static system (3.21) is additively composed of the virtual work of the internal and the external forces. In the following, we will start with the internal forces followed by the virtual work of the external forces. Again, we will drop the explicit dependency on ν and use it only when quantities are introduced or in cases where it is necessary.

[2] e_{ijk} is the Levi-Civita operator see https://de.wikipedia.org/wiki/Levi-Civita-Symbol

Virtual work of the internal forces

We recal equation (3.22) and split it accordingly in 2 parts,

$$\delta W^{int} = -\int_0^L \underbrace{{}_{\mathcal{N}}\boldsymbol{n}^T {}_{\mathcal{N}}\delta\boldsymbol{\gamma}}_{\delta W^{int,1}} + \underbrace{{}_{\mathcal{N}}\boldsymbol{m}^T {}_{\mathcal{N}}\delta\boldsymbol{k}}_{\delta W^{int,2}} d\nu,$$

and find for the first part using the skew-symmetric representation of the orientation vector (3.5), its variation (A.72) and the variation of (A.67),

$$\begin{aligned}
\delta W^{int,1} &= -\int_0^L \left(\delta\boldsymbol{r}'^T \boldsymbol{A}_{\mathcal{BN}} + \boldsymbol{r}'^T \delta\boldsymbol{A}_{\mathcal{BN}}\right) {}_{\mathcal{N}}\boldsymbol{n}\, d\nu = \int_0^L \left({}_{\mathcal{B}}\delta\boldsymbol{r}'^T - {}_{\mathcal{B}}\delta\hat{\boldsymbol{\phi}}\, {}_{\mathcal{B}}\boldsymbol{r}'^T\right) {}_{\mathcal{B}}\boldsymbol{n}\, d\nu \\
&\overset{(A.70)}{=} -\int_0^L \left({}_{\mathcal{B}}\delta\boldsymbol{r}' + {}_{\mathcal{B}}\boldsymbol{r}' \times (\frac{1}{2}{}_{\mathcal{B}}\boldsymbol{d}_i \times {}_{\mathcal{B}}\delta\boldsymbol{d}_i)\right) {}_{\mathcal{B}}\boldsymbol{n}\, d\nu \\
&\overset{\text{Jacobi identity}}{=} -\int_0^L \left({}_{\mathcal{B}}\delta\boldsymbol{r}' + \frac{1}{2}(({}_{\mathcal{B}}\boldsymbol{r}' {}_{\mathcal{B}}\delta\boldsymbol{d}_i) {}_{\mathcal{B}}\boldsymbol{d}_i - ({}_{\mathcal{B}}\boldsymbol{r}' {}_{\mathcal{B}}\boldsymbol{d}_i) {}_{\mathcal{B}}\delta\boldsymbol{d}_i\right) {}_{\mathcal{B}}\boldsymbol{d}_j {}_{\mathcal{B}}n_j\, d\nu \\
&\overset{(A.61),(A.72)}{=} -\int_0^L \left({}_{\mathcal{B}}\delta\boldsymbol{r}' {}_{\mathcal{B}}\boldsymbol{d}_j + \frac{1}{2}(({}_{\mathcal{B}}\boldsymbol{r}' {}_{\mathcal{B}}\delta\boldsymbol{d}_j) + ({}_{\mathcal{B}}\boldsymbol{r}' {}_{\mathcal{B}}\delta\boldsymbol{d}_j)\right) {}_{\mathcal{B}}n_j \\
&= -\int_0^L \left({}_{\mathcal{B}}\delta\boldsymbol{r}' {}_{\mathcal{B}}\boldsymbol{d}_j + {}_{\mathcal{B}}\delta\boldsymbol{d}_j {}_{\mathcal{B}}\boldsymbol{r}'\right) {}_{\mathcal{B}}n_j
\end{aligned} \tag{A.73}$$

$\delta W^{int,2}$ is also reformulated to

$$\begin{aligned}
\delta W^{int,2} &= -\int_0^L {}_{\mathcal{N}}\boldsymbol{m}\ {}_{\mathcal{N}}\delta\boldsymbol{k} d\nu = -\int_0^L {}_{\mathcal{N}}\boldsymbol{m}\delta(\boldsymbol{A}_{\mathcal{BN}}^T {}_{\mathcal{B}}\boldsymbol{k}) d\nu \\
&= -\int_0^L {}_{\mathcal{N}}\boldsymbol{m}\boldsymbol{A}_{\mathcal{BN}}^T \left(-{}_{\mathcal{B}}\delta\hat{\boldsymbol{\phi}}\, {}_{\mathcal{B}}\boldsymbol{k} + {}_{\mathcal{B}}\delta\boldsymbol{k}\right) \\
&= \int_0^L -{}_{\mathcal{B}}\boldsymbol{m} \cdot ({}_{\mathcal{B}}\delta\boldsymbol{k} - {}_{\mathcal{B}}\delta\boldsymbol{\phi} \times {}_{\mathcal{B}}\boldsymbol{k})\, d\nu \\
&= \int_0^L -{}_{\mathcal{B}}\boldsymbol{m} \cdot (\delta(k_i {}_{\mathcal{B}}\boldsymbol{d}_i) - {}_{\mathcal{B}}\delta\boldsymbol{\phi} \times (k_i {}_{\mathcal{B}}\boldsymbol{d}_i))\, d\nu \\
&= \int_0^L -{}_{\mathcal{B}}\boldsymbol{m} \cdot (\delta k_i {}_{\mathcal{B}}\boldsymbol{d}_i + k_i \delta {}_{\mathcal{B}}\boldsymbol{d}_i - \delta\boldsymbol{\phi} \times (k_i {}_{\mathcal{B}}\boldsymbol{d}_i)) \\
&\overset{(A.71)}{=} \int_0^L -{}_{\mathcal{B}}\boldsymbol{m} \cdot (\delta k_i {}_{\mathcal{B}}\boldsymbol{d}_i + k_i {}_{\mathcal{B}}\delta\boldsymbol{\phi} \times {}_{\mathcal{B}}\boldsymbol{d}_i - {}_{\mathcal{B}}\delta\boldsymbol{\phi} \times (k_i {}_{\mathcal{B}}\boldsymbol{d}_i))\, d\nu \\
&= \int_0^L -{}_{\mathcal{B}}\boldsymbol{m} \cdot \delta k_i {}_{\mathcal{B}}\boldsymbol{d}_i d\nu = \int_0^L -m_i \cdot \delta k_i d\nu \\
&\overset{(A.68)}{=} \int_0^L -{}_{\mathcal{B}}m_i \cdot \frac{1}{2} \cdot e_{ijk} \left({}_{\mathcal{B}}\delta\boldsymbol{d}_k \cdot {}_{\mathcal{B}}\boldsymbol{d}'_j + {}_{\mathcal{B}}\boldsymbol{d}_k \cdot {}_{\mathcal{B}}\delta\boldsymbol{d}'_j\right) d\nu
\end{aligned} \tag{A.74}$$

Virtual work of the external forces

The virtual work of the external forces (3.26) can be split up into a part from the gravitational forces and a part from the tendon actuation, see (3.30). The part due to gravity

is expressed in (3.34),

$$\begin{aligned}
\delta W^{grav} =& -\rho A g \int_0^L \delta x(\nu) d\nu \\
& - m_H g \, {}_{\mathcal{B}}\boldsymbol{e}_x^{\mathcal{B}} \, {}_{\mathcal{B}}\delta \boldsymbol{r}_L - \left({}_{\mathcal{B}}\boldsymbol{s}_{\mathrm{CoM}} \times m_H g \, {}_{\mathcal{B}}\boldsymbol{e}_x^{\mathcal{B}} \right) {}_{\mathcal{B}}\delta \boldsymbol{\phi}_L \\
\overset{\text{with eq (A.70)}}{=}& -\rho A g \int_0^L \delta x(\nu) d\nu - m_H g \, {}_{\mathcal{B}}\boldsymbol{e}_x^{\mathcal{B}} \, {}_{\mathcal{B}}\delta \boldsymbol{r}_L \\
& - \left({}_{\mathcal{B}}\boldsymbol{s}_{\mathrm{CoM}} \times m_H g \, {}_{\mathcal{B}}\boldsymbol{e}_x^{\mathcal{B}} \right) \frac{1}{2} ({}_{\mathcal{B}}\boldsymbol{d}_{i,L} \times {}_{\mathcal{B}}\delta \boldsymbol{d}_{i,L}) \\
=& -\rho A g \int_0^L \delta x(\nu) d\nu - m_H g \, {}_{\mathcal{B}}\boldsymbol{e}_x^{\mathcal{B}} \, {}_{\mathcal{B}}\delta \boldsymbol{r}_L \\
& - \frac{1}{2} \, {}_{\mathcal{B}}\delta \boldsymbol{d}_{i,L} \left({}_{\mathcal{B}}\boldsymbol{s}_{\mathrm{CoM}} \times {}_{\mathcal{B}}\boldsymbol{d}_{i,L} + m_H g \, {}_{\mathcal{B}}\boldsymbol{e}_x^{\mathcal{B}} \times {}_{\mathcal{B}}\boldsymbol{d}_{i,L} \right)
\end{aligned} \tag{A.75}$$

whereas the part of the tendon actuation (3.31) equates to the following:

$$\begin{aligned}
\delta W^{tendon} =& \left(\sum_{k=1}^{4} {}_{\mathcal{B}}\boldsymbol{e}_{t,k}^{\mathcal{H}} u_k \right) {}_{\mathcal{B}}\delta \boldsymbol{r}_L + \left(\sum_{k=1}^{4} {}_{\mathcal{B}}\boldsymbol{r}_{t,k} \times {}_{\mathcal{B}}\boldsymbol{e}_{t,k}^{\mathcal{H}} u_k \right) {}_{\mathcal{B}}\delta \boldsymbol{\phi}_L \\
\overset{\text{with eq (A.70)}}{=}& \left(\sum_{k=1}^{4} {}_{\mathcal{B}}\boldsymbol{e}_{t,k}^{\mathcal{H}} u_k \right) {}_{\mathcal{B}}\delta \boldsymbol{r}_L \\
& + \left(\sum_{k=1}^{r} {}_{\mathcal{B}}\boldsymbol{r}_{t,k} \times {}_{\mathcal{B}}\boldsymbol{e}_{t,k}^{\mathcal{H}} u_k \right) \frac{1}{2} ({}_{\mathcal{B}}\boldsymbol{d}_{i,L} \times {}_{\mathcal{B}}\delta \boldsymbol{d}_{i,L}) \\
=& \left(\sum_{k=1}^{4} {}_{\mathcal{B}}\boldsymbol{e}_{t,k}^{\mathcal{H}} u_k \right) {}_{\mathcal{B}}\delta \boldsymbol{r}_L \\
& + \frac{1}{2} \, {}_{\mathcal{B}}\delta \boldsymbol{d}_{i,L} \left(\sum_{k=1}^{r} {}_{\mathcal{B}}\boldsymbol{r}_{t,k} \times {}_{\mathcal{B}}\boldsymbol{e}_{t,k}^{\mathcal{H}} u_k \right) \times {}_{\mathcal{B}}\boldsymbol{d}_{i,L}
\end{aligned} \tag{A.76}$$

Virtual work of the constraint forces

Due to the choice for the representation of the orientation as directors, additional constraint equations are necessary,

$$g_{ij}(\nu) = ({}_{\mathcal{B}}\boldsymbol{d}_i(\nu) \, {}_{\mathcal{B}}\boldsymbol{d}_j(\nu) - \delta_{ij}) = 0, \text{ for } i, j = 1 \dots 3, \tag{A.77}$$

which ensure that the director triad remains an orthonormal frame. To ensure equation (A.77), constraint forces $\lambda_{ij} \in \mathbb{R}$, i.e. Lagrange multipliers, are introduced. The virtual work of the constraint forces is defined as,

$$\begin{aligned}
\delta W^c =& \int_0^L \lambda_{ij} \delta g_{ij} d\nu = \int_0^L \lambda_{ij} \left({}_{\mathcal{B}}\delta \boldsymbol{d}_i \, {}_{\mathcal{B}}\boldsymbol{d}_j + {}_{\mathcal{B}}\boldsymbol{d}_i \, {}_{\mathcal{B}}\delta \boldsymbol{d}_j \right) d\nu \\
\overset{\lambda_{ij}=\lambda_{ji}}{=}& 2 \int_0^L \lambda_{ij} \, {}_{\mathcal{B}}\delta \boldsymbol{d}_i \, {}_{\mathcal{B}}\boldsymbol{d}_j d\nu
\end{aligned} \tag{A.78}$$

With that, the virtual work contributions of all acting forces are introduced and whereas the sum of all virtual works acting on the static system need to be zero for all admissible variations

$$\delta W^{stat} = \delta W^{int} + \delta W^{tendon} + \delta W^{grav} + \delta W^c = 0, \ \forall \, {}_{\mathcal{B}}\delta \boldsymbol{r}_{adm}, \, {}_{\mathcal{B}}\delta \boldsymbol{d}_{i,adm}, \tag{A.79}$$

which is solved using the beam finite element method derived in the following.

Discretization: The beam finite element method

Again, Section 3.3 is followed for the subsequent developments. The centerline of the beam, denoted as a region Ω, is divided into $k_{el} \in \mathbb{N}$ elements. Each element $e = [1, k_{el}]$ is defined as a sub region $\Omega_e = [n^e, n^{e+1}] \subset \Omega$ each of which is described by a fixed number of generalized coordinates at the boundaries, i.e. nodes, of the element in such a way that the interconnection constraints are fulfilled. The generalized coordinates of the system (A.62) are represented by finite set of coordinates, $\boldsymbol{q} \in \mathbb{R}^{12(k_{el}+1)}$,

$$\boldsymbol{q} = \left({}_{\mathcal{B}}\boldsymbol{r}^1,\, {}_{\mathcal{B}}\boldsymbol{d}_1^1,\, {}_{\mathcal{B}}\boldsymbol{d}_3^1,\, {}_{\mathcal{B}}\boldsymbol{d}_3^1,\, \ldots,\, {}_{\mathcal{B}}\boldsymbol{r}^{k_{el}+1},\, {}_{\mathcal{B}}\boldsymbol{d}_1^{k_{el}+1},\, {}_{\mathcal{B}}\boldsymbol{d}_2^{k_{el}+1},\, {}_{\mathcal{B}}\boldsymbol{d}_3^{k_{el}+1} \right)^T, \tag{A.80}$$

which approximate $\boldsymbol{q}(\nu)$ via a summation,

$$\begin{pmatrix} {}_{\mathcal{B}}\boldsymbol{r}(\nu) \\ {}_{\mathcal{B}}\boldsymbol{d}_1(\nu) \\ {}_{\mathcal{B}}\boldsymbol{d}_2(\nu) \\ {}_{\mathcal{B}}\boldsymbol{d}_3(\nu) \end{pmatrix} = \sum_{e=1}^{k_{el}} \chi_{\Omega^e}(\nu) \begin{pmatrix} \boldsymbol{r}^{h,e}(\nu^e(\nu), \boldsymbol{q}) \\ \boldsymbol{d}_1^{h,e}(\nu^e(\nu), \boldsymbol{q}) \\ \boldsymbol{d}_2^{h,e}(\nu^e(\nu), \boldsymbol{q}) \\ \boldsymbol{d}_3^{h,e}(\nu^e(\nu), \boldsymbol{q}) \end{pmatrix}. \tag{A.81}$$

In this equation, $\chi_{\Omega^e}(\nu)$ is an operator which takes care that summation at the nodes is correct. Following Section 3.3, linear shape functions $\boldsymbol{N}(\nu^e) \in \mathbb{R}^{3\times 6}$ are applied, see equation (3.46) to interpolate between the nodes e and $e+1$. To do so, the element coordinate $\nu^e \in [-1, 1]$ is introduced, (see equation (3.41)). To connect the DoF of element e with the generalized coordinates of the approximated system (A.80), we apply a connector matrix $\boldsymbol{C}^e_{r,d_i} \in \mathbb{R}^{6\times 6(k_{el}+1)}$,

$$\begin{pmatrix} \boldsymbol{r}^e \\ \boldsymbol{r}^{e+1} \end{pmatrix} = \boldsymbol{C}^e_r \boldsymbol{q}, \; \begin{pmatrix} \boldsymbol{d}_i^e \\ \boldsymbol{d}_i^{e+1} \end{pmatrix} = \boldsymbol{C}^e_{d_i} \boldsymbol{q}, \tag{A.82}$$

yielding

$$\boldsymbol{r}^{h,e}(\nu^e, \boldsymbol{q}) = \boldsymbol{N}(\nu^e)\boldsymbol{C}^e_r \boldsymbol{q}, \tag{A.83}$$

$$\boldsymbol{d}_1^{h,e}(\nu^e, \boldsymbol{q}) = \boldsymbol{N}(\nu^e)\boldsymbol{C}^e_{d_1} \boldsymbol{q}, \tag{A.84}$$

$$\boldsymbol{d}_2^{h,e}(\nu^e, \boldsymbol{q}) = \boldsymbol{N}(\nu^e)\boldsymbol{C}^e_{d_2} \boldsymbol{q}, \tag{A.85}$$

$$\boldsymbol{d}_3^{h,e}(\nu^e, \boldsymbol{q}) = \boldsymbol{N}(\nu^e)\boldsymbol{C}^e_{d_3} \boldsymbol{q}. \tag{A.86}$$

The deformation of node $k_{el}+1$ is of interest as it describes the position and orientation of the mechanisms end, i.e. the head for the current application. Therefore, a special connector matrix $\boldsymbol{C}^L \in \mathbb{R}^{12\times 6(k_{el}+1)}$ is introduced,

$$\boldsymbol{q}^L = \begin{pmatrix} \boldsymbol{r}^{k_{el}+1} \\ \boldsymbol{d}_1^{k_{el}+1} \\ \boldsymbol{d}_2^{k_{el}+1} \\ \boldsymbol{d}_3^{k_{el}+1} \end{pmatrix} = \boldsymbol{C}^L \boldsymbol{q}. \tag{A.87}$$

For the subsequent developments, we will need the derivative of the shape functions w.r.t. ν, see equation (3.49), the variation and the derivative of the variation w.r.t. ν, see equation (3.51). With those expressions, the virtual work contribution can be reformulated using the established shape functions.

Starting with the virtual work of the internal forces which was split up in two parts, (A.73) and (A.74). Starting with the first part, we find

$$\begin{aligned}\delta W^{int,1} =& -\sum_{e=1}^{k_{el}+1}\int_{-1}^{1}(\delta\boldsymbol{q}^T\boldsymbol{C}_r^{e,T}\boldsymbol{N}'^T\boldsymbol{N}\boldsymbol{C}_{d_j}^{e}\boldsymbol{q}+\delta\boldsymbol{q}\boldsymbol{C}_{d_j}^{e,T}\boldsymbol{N}^T\boldsymbol{N}'\boldsymbol{C}_r^{e}\boldsymbol{q})_{\mathcal{B}}n_j\,d\nu^e\\ =& -\delta\boldsymbol{q}^T\sum_{e=1}^{k_{el}+1}\int_{-1}^{1}(\boldsymbol{C}_r^{e,T}\boldsymbol{N}'^T\boldsymbol{N}\boldsymbol{C}_{d_j}^{e}\boldsymbol{q}+\boldsymbol{C}_{d_j}^{e,T}\boldsymbol{N}^T\boldsymbol{N}'\boldsymbol{C}_r^{e}\boldsymbol{q})_{\mathcal{B}}n_j\,d\nu^e\\ =& -\delta\boldsymbol{q}^T\boldsymbol{f}^{int,1}(\boldsymbol{q})\end{aligned}\tag{A.88}$$

which can be directly connected to the material laws (3.16). The second part of the internal virtual work (A.74) can be reformulated to

$$\begin{aligned}\delta W^{int,2} =& \int_0^L\frac{1}{2}\delta\boldsymbol{d}_i'\;e_{i,j,k}\,m_j\boldsymbol{d}_k\,d\nu-\int_0^L\frac{1}{2}\delta\boldsymbol{d}_i\;e_{i,j,k}\,m_j\boldsymbol{d}_k'\,d\nu\\ =&\frac{1}{2}\sum_{e=1}^{k_{el}}\int_{-1}^{1}\delta\boldsymbol{q}^T\boldsymbol{C}_{d_i}^{e,T}\left(\boldsymbol{N}'^T\;e_{ijk}m_j\boldsymbol{d}_k-\boldsymbol{N}^T\;e_{ijk}m_j\boldsymbol{d}_k'\right)\;d\nu^e\\ =&\frac{1}{2}\delta\boldsymbol{q}^T e_{ijk}\sum_{e=1}^{k_{el}}\boldsymbol{C}_{d_i}^{e,T}\int_{-1}^{1}m_j\left(\boldsymbol{N}'^T\,\boldsymbol{N}\boldsymbol{C}_{d_k}^{e}\boldsymbol{q}-\boldsymbol{N}^T\,\boldsymbol{N}'\boldsymbol{C}_{d_k}^{e}\boldsymbol{q}\right)\;d\nu^e.\\ =&\delta\boldsymbol{q}^T\boldsymbol{f}^{int,2}(\boldsymbol{q})\end{aligned}\tag{A.89}$$

Afterward, the virtual work of the external forces (A.76) will be reformulated using the connector matrix for the end of the beam (A.87) which yields

$$\begin{aligned}\delta W^{tendon} =&{}_{\mathcal{B}}\delta\boldsymbol{r}_L\left(\sum_{k=1}^{4}{}_{\mathcal{B}}\boldsymbol{e}_{t,k}^{\mathcal{H}}f_{tk}\right)\\ &+\frac{1}{2}\,{}_{\mathcal{B}}\delta\boldsymbol{d}_{i,L}\left(\sum_{k=1}^{4}{}_{\mathcal{B}}\boldsymbol{r}_{t,k}\times{}_{\mathcal{B}}\boldsymbol{e}_{t,k}^{\mathcal{H}}f_{tk}\right)\times{}_{\mathcal{B}}\boldsymbol{d}_{i,L},\\ =&\delta\boldsymbol{q}^T\boldsymbol{C}^{L,T}\begin{pmatrix}\sum_{k=1}^{4}{}_{\mathcal{B}}\boldsymbol{e}_{t,k}^{\mathcal{H}}f_{tk}\\ 0.5\left(\sum_{k=1}^{4}{}_{\mathcal{B}}\boldsymbol{r}_{t,k}\times{}_{\mathcal{B}}\boldsymbol{e}_{t,k}^{\mathcal{H}}f_{tk}\right)\times{}_{\mathcal{B}}\boldsymbol{d}_{1,L}\\ 0.5\left(\sum_{k=1}^{4}{}_{\mathcal{B}}\boldsymbol{r}_{t,k}\times{}_{\mathcal{B}}\boldsymbol{e}_{t,k}^{\mathcal{H}}f_{tk}\right)\times{}_{\mathcal{B}}\boldsymbol{d}_{2,L}\\ 0.5\left(\sum_{k=1}^{4}{}_{\mathcal{B}}\boldsymbol{r}_{t,k}\times{}_{\mathcal{B}}\boldsymbol{e}_{t,k}^{\mathcal{H}}f_{tk}\right)\times{}_{\mathcal{B}}\boldsymbol{d}_{3,L}\end{pmatrix},\\ =&\delta\boldsymbol{q}^T\boldsymbol{C}^{L,T}\boldsymbol{P}(\boldsymbol{q})\boldsymbol{u},\end{aligned}\tag{A.90}$$

with the input vector $\boldsymbol{u}=(f_{t,1},\ldots,f_{t,4})^T\in\mathbb{R}^r$, and the tendon coupling matrix $\boldsymbol{P}(\boldsymbol{q})\in\mathbb{R}^{12\times r}$,

$$\boldsymbol{P}(\boldsymbol{q})=\begin{pmatrix}{}_{\mathcal{B}}\boldsymbol{e}_{t,1}^{\mathcal{H}} & \cdots & {}_{\mathcal{B}}\boldsymbol{e}_{t,4}^{\mathcal{H}}\\ 0.5\left({}_{\mathcal{B}}\boldsymbol{r}_{t,1}\times{}_{\mathcal{B}}\boldsymbol{e}_{t,1}^{\mathcal{H}}\right)\times{}_{\mathcal{B}}\boldsymbol{d}_{1,L} & \cdots & 0.5\left({}_{\mathcal{B}}\boldsymbol{r}_{t,4}\times{}_{\mathcal{B}}\boldsymbol{e}_{t,4}^{\mathcal{H}}\right)\times{}_{\mathcal{B}}\boldsymbol{d}_{1,L}\\ \vdots & \ddots & \vdots\\ 0.5\left({}_{\mathcal{B}}\boldsymbol{r}_{t,1}\times{}_{\mathcal{B}}\boldsymbol{e}_{t,1}^{\mathcal{H}}\right)\times{}_{\mathcal{B}}\boldsymbol{d}_{3,L} & \cdots & 0.5\left({}_{\mathcal{B}}\boldsymbol{r}_{t,4}\times{}_{\mathcal{B}}\boldsymbol{e}_{t,4}^{\mathcal{H}}\right)\times{}_{\mathcal{B}}\boldsymbol{d}_{3,L}\end{pmatrix}.\tag{A.91}$$

For the virtual work of the gravitational forces (A.75), it can be found to

$$\begin{aligned}\delta W^{grav} =& -\rho\, A\, g\, \delta\boldsymbol{q}^T \sum_{e=1}^{k_{el}} \boldsymbol{C}_r^{e,T} \int_{-1}^{1} \boldsymbol{N}^T {}_{\mathcal{B}}\boldsymbol{e}_x \, d\nu^e \\ & - m_H\, g\, \delta\boldsymbol{q}^T \boldsymbol{C}_L^T \begin{pmatrix} {}_{\mathcal{B}}\boldsymbol{e}_x \\ ({}_{\mathcal{B}}\boldsymbol{s}_{\mathrm{CoM}} + {}_{\mathcal{B}}\boldsymbol{e}_x) \times \boldsymbol{d}_{1,L} \\ ({}_{\mathcal{B}}\boldsymbol{s}_{\mathrm{CoM}} + {}_{\mathcal{B}}\boldsymbol{e}_x) \times \boldsymbol{d}_{2,L} \\ ({}_{\mathcal{B}}\boldsymbol{s}_{\mathrm{CoM}} + {}_{\mathcal{B}}\boldsymbol{e}_x) \times \boldsymbol{d}_{3,L} \end{pmatrix}, \\ =& -\delta\boldsymbol{q}^T \left(\boldsymbol{f}^{g,beam} + \boldsymbol{f}^{g,head} \right) \end{aligned} \tag{A.92}$$

As introduced earlier, the representation of the orientation requires constraint forces which also possess a virtual work. This virtual work can be rewritten to

$$\begin{aligned}\delta W^c =& 2 \int_0^L \lambda_{ij}\, {}_{\mathcal{B}}\delta\boldsymbol{d}_i\, {}_{\mathcal{B}}\boldsymbol{d}_j d\nu, \\ =& \delta\boldsymbol{q}^T \sum_{e=1}^{k_{el}} \boldsymbol{C}_{d_i}^{e,T} \int_{-1}^{1} 2\, \lambda_{ij} \boldsymbol{N}^T \boldsymbol{N}\, d\nu^e\, \boldsymbol{C}_{d_j}^{e} \boldsymbol{q}, \\ =& \delta\boldsymbol{q}^T \boldsymbol{f}^c(\boldsymbol{q}) \end{aligned} \tag{A.93}$$

According to (A.79), the total virtual work needs to be zero for all admissible variations $\delta\boldsymbol{q}_{adm} \neq \boldsymbol{0}$ which yields

$$\begin{aligned} \boldsymbol{f}^{int,1}(\boldsymbol{q}) - \boldsymbol{f}^{int,2}(\boldsymbol{q}) + \boldsymbol{f}^{g,beam} + \boldsymbol{f}^{g,head}(\boldsymbol{q}) + \boldsymbol{f}^c(\boldsymbol{q}) - \boldsymbol{C}^{L,T}\boldsymbol{P}(\boldsymbol{q})\boldsymbol{u} = 0 \\ \boldsymbol{k}(\boldsymbol{q}) = \boldsymbol{0}. \end{aligned} \tag{A.94}$$

To solve this equation, the Newton-Raphson method is applied which also needs to compute the partial derivative of (A.94).
As mentioned, MATLAB code was generated using the above equations. In order to validate the code, a validation test is reported in the following. For the case of a planar deformation induced by a torque applied at the tip ($\nu = L$) with $M_w \in \mathbb{R}$ in (3.35), the centerline of the beam should poses a circular shape, as for this special case, the static problem has an analytic solution. Further, if we set $M_w = EI/L * \theta_d$, we can directly command a desired tip angle and therefore for $\theta_d = \pi$, the centerline should describe a half circle. In Fig. A.4, simulation results report on the above case whereas the static equation of the beam are solved by a discretization of $k_{el} = 40$ elements. The beam is bend in two directions, thus a torque along y- and along z- is exerted. The figure reports only a slight mismatch w.r.t. to the analytic solution.

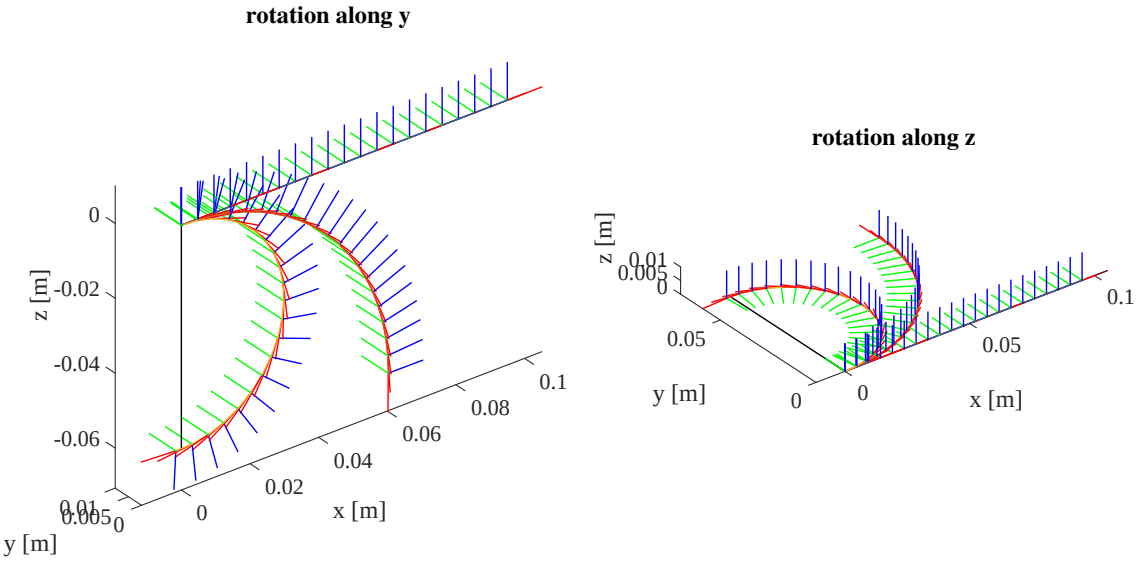

Figure A.4.: Validation of the simulation. The initial configuration of the spatial beam, the deflected configuration for $\theta_d = 90$ deg and $\theta_d = 180$ deg for the two bending directions is shown. The end configuration for $\theta_d = 180$ deg should be in line with the black, horizontal line. By inspection, only a slight mismatch can be observed.

APPENDIX B

A general setup to identify the continuum

In this section, the experimental setup will be introduced based on which the spatial model in paragraph 3.4.4 and the reduced nonlinear model of Chapter 4. First of all, the components are explained. Afterwards, the control and the pose-planning strategy of the robot manipulator are discussed.

B.1. Experimental setup

A robot manipulator (here: KUKA LWR 4+ with a JR3 force-torque-sensor (FTS) mounted at the end-effector) is connected to the top of the elastic continuum mechanism (ECM), see Fig. B.1. A marker target, which is to be detected by the camera, is fixed between the top of the ECM and the FTS to measure the associated deflection of the ECM.
The FTS is a six-DOF sensor based on foil strain gauges. In our experiment, we chose the version 100M40A3, it enables a standard force measurement range from -200 N to 200 N in y, z directions and from -400 N to 400 N in x direction, and torque measurement about all axes from -20 Nm to 20 Nm. To accurately track the target at the ECM, the K-series optical measurement systems [126] is used. The measurement system is equipped with a camera (three lenses), infrared LEDs and Space-Probe, which also has 9 LEDs. The measurement system can accurately localize the LEDs within its workspace with an accuracy of 37 μm.

B.2. Practical issues

B.2.1. Pose measurement and calibration

The poses are obtained by measuring the positions of the LEDs on the marker target and transforming them into the ECM reference frame. To eliminate unintended camera movements during the experiments compromise calibrated transforms, a second marker target is rigidly fixed near the ECM. To avoid systematic errors in the pose measurement, it is essential that the constant transformations from the marker targets to the desired ECM top frame and ECM reference frame are carefully calibrated.

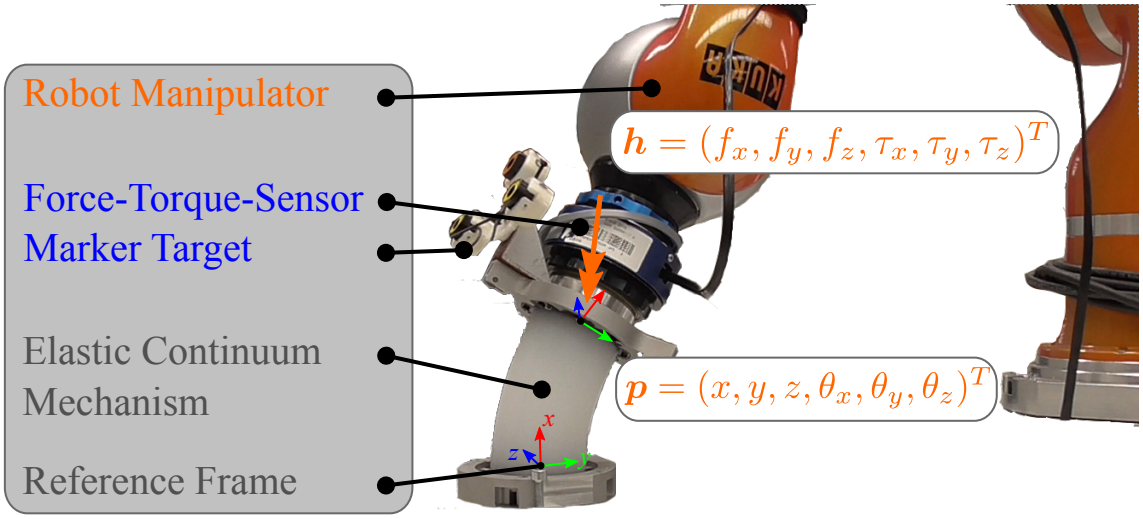

Figure B.1.: Experimental setup

B.2.2. Wrench measurement and calibration

In the simulation, the wrench data refers to the wrench exerted on the ECM top respecting the ECM reference frame, while the wrench data measured in the experiment is the one applied at the origin of the FTS frame. Thus, the measured wrenches need to be transformed using Adjoint transformations [117] based on a constant, calibrated transformation.
The FTS shows offsets in each measured direction. These offsets drift during the experiments, which is supposed to be related to the temperature of the sensor, and result in non-constant biases of the measurement. The timing characteristic of these offsets are studied and a linear compensation law is adopted between the measured offsets before and after each experiment to reduce their influence.

B.3. Implementation of the Experimental Procedure

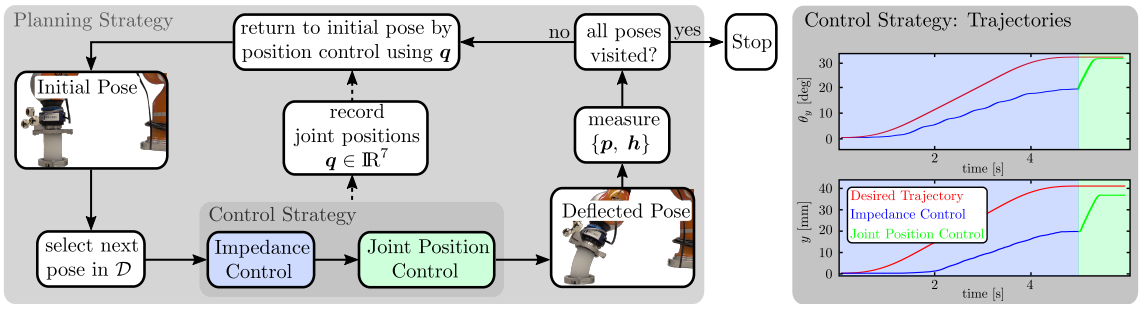

Figure B.2.: Block diagram of the implemented procedure to illustrate the subsequent steps during the experiment which can be seen in the attached video also. Right: Example of a measured pose trajectory for the position y and the angle θ_y to examine the different stages while reaching a desired pose.

As described earlier, the implementation of the pose sampling process for the experi-

ment needs to be carefully executed as configurations that may damage the mechanism or impose unwanted behaviors need to be avoided. For the implementation, the following considerations are made:

B.3.1. Comparison of Planning Strategies

One possible planning strategy is to start from the poses close to the initial configuration to those relatively far away from the initial position. After reading the wrench data in one pose the robot moves directly to the next pose. This scheme saves experimental time but it requires knowledge about the path between different configurations. Since the transition between two configurations could cause an unexpected behavior, the path between the poses needs to be designed rigorously.
Another possibility is to return to the initial configuration after each sampling. This scheme is relatively easy to implement and there is no need to concern about the transitions among the poses. Only the transitions from the initial configuration to each sample pose needs to be considered. Since the initial configuration is a pose without any deflection, the transition from it to each sample pose is easier to handle than the one among two poses.

B.3.2. Comparison of Control Strategies

One strategy is to plan a Cartesian trajectory from the initial pose to the desired pose. The joint space trajectory is calculated the robot is controlled in joint position control mode. In this case each sampled pose requires a specifically designed smooth trajectory such that the ECM can reach the desired pose without unexpected behavior.
Since deflecting the ECM is an interaction between the robot manipulator and the environment, the impedance control seems to be appropriate in this case. The robot is firstly controlled in Cartesian impedance control mode [168] and deflects the ECM towards the desired pose. Due to the controlled compliance, the resulting pose of the ECM differs from the desired pose. After the ECM is stabilized near the desired pose, the control mode therefore switches to joint position control [168], to drive the ECM from the stabilized pose to the desired pose to ensure that the all poses from $\mathcal{D}$ are reached. Since the ECM is already close to the desired pose at that moment, an unexpected motion of ECM can be excluded during the position control mode. The different trajectories in impedance control and joint position control are depicted in the right of Fig. B.2.

Based on the above considerations, the experimental procedure can be described by Fig. B.2 and the video attached to the present paper. After a pose to be sampled of $\mathcal{D}$ has been selected, the robot drives the ECM from its initial, straight pose in the impedance control mode towards this pose along the planned Cartesian trajectory [1]. After the termination of the Cartesian trajectory interpolator, the inverse kinematics is solved from the current pose to the goal and the robot is driven in joint position controlled mode to reach the desired pose. During the movement from initial pose to the goal, the joint positions of each time instance are recorded and saved in a stack. After reaching the goal the measurements of the pose and the wrench are logged and then the robot returns to the initial pose in joint position control mode in which the desired trajectory are the joint positions saved in the stack. This sequence will be repeated until every pose in $\mathcal{D}$ has been visited. To eliminate the effect of measurement noise, the logging of measurements lasts for 200 ms and the mean values of pose and wrench are taken.

[1] A simple point-to-point motion is concerned and a cubic polynomial timing law is chosen.

Bibliography

[1] V.C. Anderson and R.C. Horn. *Tensor Arm Manipulator Design*. American Society of Mechanical Engineers. American Society of Mechanical Engineers, 1967. 23, 24

[2] G. S. Chirikjian and J. W. Burdick. A hyper-redundant manipulator. *IEEE Robotics & Automation Magazine*, 1(4):22–29, 1994. 23

[3] G. Robinson, J. Davies, and Bruce C. Continuum robots-a state of the art. In *IEEE International Conference on Robotics and Automation*, volume 4, pages 2849–2854, 1999. 23

[4] M. W. Hannan and I. D. Walker. Kinematics and the implementation of an elephant's trunk manipulator and other continuum style robots. *Journal of Robotic Systems*, 20(2):45–63, 2003. 24

[5] M. W. Hannan and I. D. Walker. The'elephant trunk'manipulator, design and implementation. In *IEEE/ASME International Conference on Advanced Intelligent Mechatronics*, volume 1, pages 14–19, 2001. 24

[6] J. Burgner-Kahrs, D. C. Rucker, and H. Choset. Continuum robots for medical applications: A survey. *Transactions on Robotics*, 31(6):1261–1280, 2015. 24

[7] Mro blog. https://www.mroelectric.com/blog/kuka-robot-arm/. Accessed: 2019-05-28. 24

[8] Kuka robotics corporation debuts the lbr iiwa to north america at automate 2015. https://www.businesswire.com/news/home/20150320005018/en/KUKA-Robotics-Corporation-debuts-LBR-iiwa-North. Accessed: 2019-05-28. 24

[9] Continuum robot offers brand new possibilities. https://aeroreport.de/en/innovation/continuum-robot-offers-brand-new-possibilities. Accessed: 2019-05-28. 24

[10] L. U. Odhner, L. P. Jentoft, M. R. Claffee, N. Corson, Y. Tenzer, R. R. Ma, M. Buehler, R. Kohout, R. D. Howe, and A. M. Dollar. A compliant, underactuated hand for robust manipulation. *The International Journal of Robotics Research*, 33(5):736–752, 2014. 24, 25

[11] M. T. Leddy, J. T. Belter, K. D. Gemmell, and A. M. Dollar. Lightweight custom composite prosthetic components using an additive manufacturing-based molding technique. In *IEEE International Conference of the Engineering in Medicine and Biology Society*, pages 4797–4802, 2015. 24, 25

[12] Q. Zhao, K. Nakajima, H. Sumioka, H. Hauser, and R. Pfeifer. Spine dynamics as a computational resource in spine-driven quadruped locomotion. In *IEEE/RSJ International Conference on Intelligent Robots and Systems*, pages 1445–1451, 2013. 24, 25

[13] AG Festo and KG Co. Bionic handling assistant. *Info-brochure. Festo, Esslingen, Germany*, 2010. 24, 25

[14] A. K. Mishra, E. Del Dottore, A. Sadeghi, A. Mondini, and B. Mazzolai. Simba: Tendon-driven modular continuum arm with soft reconfigurable gripper. *Frontiers in Robotics and AI*, 4:4, 2017. 24, 25

[15] C. B. Black, J. Till, and C. D. Rucker. Parallel continuum robots: Modeling, analysis, and actuation-based force sensing. *Transactions on Robotics*, 34(1):29–47, Feb 2018. 24, 25

[16] J. Reinecke, B. Deutschmann, and D. Fehrenbach. A structurally flexible humanoid spine based on a tendon-driven elastic continuum. In *IEEE International Conference on Robotics and Automation*, pages 4714–4721, 2016. 25, 31, 33, 40, 41, 42

[17] E. Amanov, J. Granna, and J. Burgner-Kahrs. Toward improving path following motion: Hybrid continuum robot design. In *IEEE International Conference on Robotics and Automation*, pages 4666–4672, May 2017. 25

[18] Y. Guo, J. Granna, K. D. Weaver, R. J. Webster III, and J. Burgner-Kahrs. Comparison of optimization algorithms for a tubular aspiration robot for maximum coverage in intracerebral hemorrhage evacuation. In *Proc. Hamlyn Symp. Med. Robot.*, pages 11–12, 2015. 25

[19] V. Falkenhahn, A. Hildebrandt, and O. Sawodny. Trajectory optimization of pneumatically actuated, redundant continuum manipulators. In *American Control Conference (ACC)*, pages 4008–4013. IEEE, 2014. 25

[20] S. S. Antman. *Nonlinear Problems of Elasticity.* Springer New York, 2001. 26

[21] F. Renda, M. Giorelli, M. Calisti, M. Cianchetti, and C. Laschi. Dynamic model of a multibending soft robot arm driven by cables. *Transactions on Robotics*, 30(5):1109–1122, 2014. 26

[22] C. D. Rucker and R. J. Webster III. Statics and dynamics of continuum robots with general tendon routing and external loading. *Transactions on Robotics*, 27(6):1024–1030, 2011. 26

[23] J. Starke, E. Amanov, M. Chihaoui, and J. Burgner-Kahrs. On the merits of helical tendon routing in continuum robots. In *IEEE/RSJ International Conference on Intelligent Robots and Systems*, pages 6470–6476, 2017. 26

[24] F. Boyer, M. Porez, and W. Khalil. Macro-continuous computed torque algorithm for a three-dimensional eel-like robot. *Transactions on Robotics*, 22(4):763–775, 2006. 26

[25] J. Allard, S. Cotin, F. Faure, J.P. Bensoussan, F. Poyer, C. Duriez, H. Delingette, and L. Grisoni. Sofa-an open source framework for medical simulation. In *MMVR 15-Medicine Meets Virtual Reality*, volume 125, pages 13–18. IOP Press, 2007. 26, 29

[26] C. Duriez. Control of elastic soft robots based on real-time finite element method. In *IEEE International Conference on Robotics and Automation*, pages 3982–3987, 2013. 26

[27] C. D. Rucker and R. J Webster. Computing jacobians and compliance matrices for externally loaded continuum robots. In *IEEE International Conference on Robotics and Automation*, pages 945–950, 2011. 26

[28] S. Hirose. *Biologically inspired snake-like robots*. Oxford University Press, 1993. 26

[29] I. A. Gravagne and I. D. Walker. On the kinematics of remotely-actuated continuum robots. In *IEEE International Conference on Robotics and Automation*, pages 2544–2550, 2000. 26

[30] I. A. Gravagne, C. D. Rahn, and I. D. Walker. Large deflection dynamics and control for planar continuum robots. *IEEE/ASME Transactions on Mechatronics*, 8(2):299–307, 2003. 26, 30

[31] N. Simaan. Snake-like units using flexible backbones and actuation redundancy for enhanced miniaturization. In *IEEE International Conference on Robotics and Automation*, pages 3012–3017, 2005. 26

[32] P. E. Dupont, J. Lock, B. Itkowitz, and E. Butler. Design and control of concentric-tube robots. *Transactions on Robotics*, 26(2):209–225, 2010. 26

[33] D. B. Camarillo, C. F. Milne, C. R. Carlson, M. R. Zinn, and J. K. Salisbury. Mechanics modeling of tendon-driven continuum manipulators. *Transactions on Robotics*, 24(6):1262–1273, 2008. 26

[34] B. A. Jones and I. D. Walker. Practical kinematics for real-time implementation of continuum robots. *Transactions on Robotics*, 22(6):1087–1099, 2006. 26, 28

[35] I. S. Godage, D. T. Branson, E. Guglielmino, G. A. Medrano-Cerda, and D. G. Caldwell. Shape function-based kinematics and dynamics for variable length continuum robotic arms. In *IEEE International Conference on Robotics and Automation*, pages 452–457, 2011. 27

[36] V. Falkenhahn, T. Mahl, A. Hildebrandt, R. Neumann, and O. Sawodny. Dynamic modeling of bellows-actuated continuum robots using the euler–lagrange formalism. *IEEE Transactions on Robotics*, 31(6):1483–1496, 2015. 27

[37] E. Tatlicioglu, I. D. Walker, and D. M. Dawson. Dynamic modelling for planar extensible continuum robot manipulators. In *IEEE International Conference on Robotics and Automation*, pages 1357–1362, 2007. 27

[38] B. A. Jones and I. D. Walker. Kinematics for multisection continuum robots. *Transactions on Robotics*, 22(1):43–55, 2006. 27, 28

[39] T. Mahl, A. Hildebrandt, and O. Sawodny. A variable curvature continuum kinematics for kinematic control of the bionic handling assistant. *Transactions on Robotics*, 30(4):935–949, 2014. 27

[40] R. Kang, E. Guglielmino, D. T. Branson, and D. G. Caldwell. Kinematic model and inverse control for continuum manipulators. In *IEEE International Conference on Control and Automation*, pages 1615–1620, 2013. 27

[41] D. Braganza, D. M. Dawson, I. D. Walker, and N. Nath. Neural network grasping controller for continuum robots. In *45th IEEE Conference on Decision and Control*, pages 6445–6449. IEEE, 2006. 27

[42] M. Giorelli, F. Renda, M. Calisti, A. Arienti, G. Ferri, and C. Laschi. Neural Network and Jacobian Method for Solving the Inverse Statics of a Cable-Driven Soft Arm With Nonconstant Curvature. *Transactions on Robotics*, 31(4):823–834, 2015. 27

[43] M. Malekzadeh, J. Queißer, and J. J. Steil. Learning the end-effector pose from demonstration for the bionic handling assistant robot. In *Proceedings of the International Workshop on Human Human Friendly Robotics*, pages 101–107, 2016. 27

[44] A. W. Mahoney, T. L. Bruns, P. J. Swaney, and R. J. Webster. On the inseparable nature of sensor selection, sensor placement, and state estimation for continuum robots or "where to put your sensors and how to use them". In *IEEE International Conference on Robotics and Automation*, pages 4472–4478, 2016. 27

[45] C. Shi, X. Luo, P. Qi, T. Li, S. Song, Z. Najdovski, T. Fukuda, and H. Ren. Shape sensing techniques for continuum robots in minimally invasive surgery: A survey. *Transactions on Biomedical Engineering*, 64(8):1665–1678, 2017. 28

[46] V. K. Chitrakaran, A. Behal, D. M. Dawson, and I. D. Walker. Setpoint regulation of continuum robots using a fixed camera. In *IEEE American Control Conference 2004*, pages 1504–1509, 2004. 28

[47] M. Li, K. Rongjie, D. T. Branson, and J. S. Dai. Model-free control for continuum robots based on an adaptive kalman filter. *IEEE/ASME Transactions on Mechatron*, 23(1):286–297, 2018. 28, 29

[48] A. Vandini, A. Salerno, C. J. Payne, and G. Yang. Vision-based motion control of a flexible robot for surgical applications. In *IEEE International Conference on Robotics and Automation*, pages 6205–6211, 2014. 28

[49] D. B. Camarillo, C. R. Carlson, and J. K. Salisbury. Configuration tracking for continuum manipulators with coupled tendon drive. *Transactions on Robotics*, 25(4):798–808, 2009. 28

[50] V. Falkenhahn, A. Hildebrandt, R. Neumann, and O. Sawodny. Dynamic control of the bionic handling assistant. *IEEE/ASME Transactions on Mechatronics*, 22(1):6–27, 2016. 28, 30

[51] W. S. Rone and P. Ben-Tzvi. Multi-segment continuum robot shape estimation using passive cable displacement. In *IEEE International Symposium on Robotic and Sensors Environments*, pages 37–42, 2013. 28

[52] H. Liu, A. Farvardin, R. Grupp, R. J. Murphy, R. H. Taylor, I. Iordachita, and M. Armand. Shape tracking of a dexterous continuum manipulator utilizing two large deflection shape sensors. *Sensors*, 15(10):5494–5503, 2015. 28

[53] W. McMahan, B. A. Jones, and I. D. Walker. Design and implementation of a multi-section continuum robot: Air-octor. In *IEEE/RSJ International Conference on Intelligent Robots and Systems*, pages 2578–2585, 2005. 28

[54] J. Sganga and D. Camarillo. Orientation estimation of a continuum manipulator in a phantom lung. In *IEEE International Conference on Robotics and Automation*, pages 2399–2405, 2017. 28

[55] R. E. Goldman, A. Bajo, and N. Simaan. Compliant motion control for multisegment continuum robots with actuation force sensing. *Transactions on Robotics*, 30(4):890–902, 2014. 28, 30

[56] J. C. Case, J. Booth, D. S. Shah, M. C. Yuen, and R. Kramer-Bottiglio. State and stiffness estimation using robotic fabrics. In *IEEE International Conference on Soft Robotics*, pages 522–527, 2018. 28

[57] B. Kim, J. Ha, F. C. Park, and P. E. Dupont. Optimizing curvature sensor placement for fast, accurate shape sensing of continuum robots. In *IEEE International Conference on Robotics and Automation*, pages 5374–5379, 2014. 28

[58] D. Trivedi and C. D. Rahn. Model-based shape estimation for soft robotic manipulators: The planar case. *ASME Journal of Mechanisms and Robotics*, 6(2):021005–1 – 021005–11, 2014. 28

[59] R. J. Roesthuis and S. Misra. Steering of multisegment continuum manipulators using rigid-link modeling and FBG-based shape sensing. *Transactions on Robotics*, 32(2):372–382, 2016. 28

[60] K. Schmid, F. Ruess, M. Suppa, and D. Burschka. State estimation for highly dynamic flying systems using key frame odometry with varying time delays. In *IEEE/RSJ International Conference on Intelligent Robots and Systems*, pages 2997–3004, 2012. 29, 118

[61] F. Steidle, A. Tobergte, and A. Albu-Schäffer. Optical-inertial tracking of an input device for real-time robot control. In *IEEE International Conference on Robotics and Automation*, pages 742–749, 2016. 29, 105, 118

[62] R. Lampariello, H. Mishra, N. Oumer, P. Schmidt, M. De Stefano, and A. Albu-Schäffer. Tracking control for the grasping of a tumbling satellite with a free-floating robot. *Robotics and Automation Letters*, 3(4):3638–3645, 2018. 29

[63] M. Bloesch, M. Hutter, M. A. Hoepflinger, S. Leutenegger, C. Gehring, C. D. Remy, and R. Siegwart. State estimation for legged robots-consistent fusion of leg kinematics and imu. *Robotics*, 17:17–24, 2013. 29

[64] M. T. Chikhaoui and J. Burgner-Kahrs. Control of continuum robots for medical applications: State of the art. In *International Conference on New Actuators*, pages 1–11. VDE, 2018. 29

[65] A. Bajo, R. B. Pickens, S. D. Herrell, and N. Simaan. Constrained motion control of multisegment continuum robots for transurethral bladder resection and surveillance. In *IEEE International Conference on Robotics and Automation*, pages 5837–5842, 2013. 29

[66] M. C. Yip and D. B. Camarillo. Model-less feedback control of continuum manipulators in constrained environments. *Transactions on Robotics*, 30(4):880–889, 2014. 29

[67] M. C. Yip and D. B. Camarillo. Model-less hybrid position/force control: A minimalist approach for continuum manipulators in unknown, constrained environments. *IEEE Robotics and Automation Letters*, 1(2):844–851, 2016. 29

[68] J. Bosman, O. Bieze, T. Lakhal, M. Sanz, R. Merzouki, and C. Duriez. Domain decomposition approach for fem quasistatic modeling and control of continuum robots with rigid vertebras. In *IEEE International Conference on Robotics and Automation*, pages 4373–4378, 2015. 29

[69] A. Melingui, R. Merzouki, J. B. Mbede, C. Escande, and N. Benoudjit. Neural networks based approach for inverse kinematic modeling of a compact bionic handling assistant trunk. In *IEEE International Symposium on Industrial Electronics*, volume 21, pages 1239–1244, 2014. 30

[70] A. Melingui, J. J. M. Ahanda, O. Lakhal, J. B. Mbede, and R. Merzouki. Adaptive algorithms for performance improvement of a class of continuum manipulators. *Transactions on Systems, Man, and Cybernetics: Systems*, 48(9):1531–1541, 2018. 30

[71] M. Mahvash and P. E. Dupont. Stiffness control of a continuum manipulator in contact with a soft environment. In *IEEE/RSJ International Conference on Intelligent Robots and Systems*, page 863, 2010. 30

[72] L. Toscano, V. Falkenhahn, A. Hildebrandt, F. Braghin, and O. Sawodny. Configuration space impedance control for continuum manipulators. In *IEEE International Conference on Automation, Robotics and Applications*, pages 597–602, 2015. 30

[73] C. G. Frazelle, A. D. Kapadia, and I. D. Walker. A nonlinear control strategy for extensible continuum robots. In *IEEE International Conference on Robotics and Automation*, pages 7727–7734, 2018. 30

[74] A. Mousa, S. Khoo, and M. Norton. Robust control of tendon driven continuum robots. In *IEEE International Workshop on Variable Structure Systems*, pages 49–54, 2018. 30

[75] D. Braganza, D. M. Dawson, I. D. Walker, and N. Nath. A neural network controller for continuum robots. *Transactions on Robotics*, 23(6):1270–1277, 2007. 30

[76] Streichel mich sonst ersetzt ich dich. http://www.faz.net/aktuell/wirtschaft/streichel-mich-sonst-ersetz-ich-dich-14084129.html. Accessed: 2018.10.14. 31, 42

[77] B. Deutschmann, S. R. Eugster, and C. Ott. Reduced models for the static simulation of an elastic continuum mechanism. In *Proc. of the IFAC MathMOD*, 2018. 32, 34, 46, 111

[78] S. R. Eugster and B. Deutschmann. A nonlinear timoshenko beam formulation for modeling a tendon-driven compliant neck mechanism. *PAMM*, 18(1):1–2, 2018. 32, 34, 46

[79] B. Deutschmann, T. Liu, A. Dietrich, C. Ott, and D. Lee. A method to identify the nonlinear stiffness characteristics of an elastic continuum mechanism. *IEEE Robotics und Automation Letters*, 3(3):1450–1457, 2018. 32, 34, 73

[80] B. Deutschmann, A. Dietrich, T. Liu, and C. Ott. Verfahren und vorrichtung zur charakterisierung eines kontinuumgelenks, 2019. German Patent 10 2017 215 432.2, under review. 32

[81] B. Deutschmann, M. Chalon, J. Reinecke, M. Maier, and C. Ott. Six dof pose estimation for a tendon-driven continuum mechanism without a deformation model. *IEEE Robotics und Automation Letters*, (4):3425–3432, 2019. 33, 34, 103

[82] A. Shu, B. Deutschmann, A. Dietrich, C. Ott, and A. Albu-Schäffer. Robust h control of a tendon–driven elastic continuum mechanism via a systematic description of nonlinearities. *IFAC-PapersOnLine*, 51(22):386–392, 2018. 33, 34, 137, 143, 144

[83] B. Deutschmann, C. Ott, C. A. Monje, and C. Balaguer. Robust motion control of a soft robotic system using fractional order control. In *International Conference on Robotics in Alpe-Adria Danube Region*, pages 147–155, 2017. 33, 137, 160, 161

[84] B. Deutschmann, A. Dietrich, and C. Ott. Position control of an underactuated continuum mechanism using a reduced nonlinear model. In *56th IEEE Conference on Decision and Control*, pages 5223–5230, 2017. 33, 34, 137

[85] J. Reinecke, M. Chalon, W. Friedl, and M. Grebenstein. Guiding effects and friction modeling for tendon driven systems. In *IEEE International Conference on Robotics and Automation*, pages 6726–6732, 2014. 39, 40

[86] KauPo Plankenhorn. http://www.kaupo.de/produkte/silikonkautschuk-additionsvernetzend/dragon-skin-serie/, 2015. Accessed: 2018.10.14. 40, 57

[87] Erich Wintermantel and Suk-Woo Ha. *Medizintechnik: Life Science Engineering*. Springer Science & Business Media, 2009. 40

[88] Motorfamily p01-48x240. https://linmot.com/products/linear-motors/. Accessed: 2018.10.14. 41

[89] Subminiature tension or compression high accuracy load cells. http://www.omega.com/pressure/pdf/LCFD.pdf. Accessed: 2018.10.14. 41

[90] W. Friedl, C. Chalon, J. Reinecke, and M. Grebenstein. Fas a flexible antagonistic spring element for a high performance over. In *IEEE/RSJ International Conference on Intelligent Robots and Systems*, pages 1366–1372, Sept 2011. 42

[91] B. Deutschmann and C. Ott. Feasible modeling approaches for thick continuum robots. a planar experimental study. In *IEEE/RSJ International Conference on Intelligent Robots and Systems*, 2015. 45

[92] L.F. Shampine. Solving hyperbolic pdes in matlab. *Applied Numerical Analysis & Computational Mathematics*, 2(3):346–358, 2005. 46

[93] A. E. H. Love. *A treatise on the mathematical theory of elasticity.* Cambridge university press, 4 edition, 1934. 46

[94] R. J. Webster III and B. A. Jones. Design and kinematic modeling of constant curvature continuum robots: A review. *The International Journal of Robotics Research*, 29(13):1661–1683, 2010. 46, 108

[95] C. Li and C. D. Rahn. Design of continuous backbone, cable-driven robots. *Journal of Mechanical Design*, 124(2):265–271, 2002. 46

[96] S. R. Eugster. *Geometric continuum mechanics and induced beam theories*, volume 75. Springer, 2015. 46, 50

[97] J. Salençon. *Handbook of continuum mechanics: General concepts thermoelasticity.* Physics and Astronomy Online Library. Springer Science & Business Media, 2001. 50

[98] M. E. Johnson, L. M. Moore, and D. Ylvisaker. Minimax and maximin distance designs. *Journal of statistical planning and inference*, 26(2):131–148, 1990. 61, 88

[99] E. Marengo and R. Todeschini. A new algorithm for optimal, distance-based experimental design. *Chemometrics and Intelligent Laboratory Systems*, 16(1):37–44, 1992. 61, 88

[100] J. W. Strutt and B. Rayleigh. *The theory of sound.* Dover, 1945. 65, 66

[101] D. A. Belsley, E. Kuh, and R. E. Welsch. *Regression diagnostics: Identifying influential data and sources of collinearity*, volume 571. John Wiley & Sons, 2005. 80

[102] M. Shacham and N. B. Minimizing the effects of collinearity in polynomial regression. *Industrial & engineering chemistry research*, 36(10):4405–4412, 1997. 80

[103] J. Neter, M. H. Kutner, C. J. Nachtsheim, and W. Wasserman. *Applied linear statistical models*, volume 4. Irwin Chicago, 1996. 80

[104] J. Friedman, T. Hastie, and R. Tibshirani. *The elements of statistical learning*, volume 1. Springer series in statistics Springer, Berlin, 2001. 80

[105] J. Mandel. Use of the singular value decomposition in regression analysis. *The American Statistician*, 36(1):15–24, 1982. 80

[106] F. Pukelsheim. *Optimal design of experiments.* SIAM, 2006. 85, 87

[107] Y. B. Lim. D-optimal design for cubic polynomial regression on the q-simplex. *Journal of statistical planning and inference*, 25(2):141–152, 1990. 86

[108] L. Pronzato. Optimal experimental design and some related control problems. *Automatica*, 44(2):303–325, 2008. 86

[109] N. Gaffke and B. Heiligers. Algorithms for optimal design with application to multiple polynomial regression. *Metrika*, 42(1):173–190, 1995. 86

[110] B. J. Smucker. *By design: exchange algorithms to construct exact model-robust and multiresponse experimental designs.* PhD thesis, The Pennsylvania State University, 2010. 86

[111] F. Triefenbach. Design of experiments: the d-optimal approach and its implementation as a computer algorithm. *Bachelor's Thesis in Information and Communication Technology*, 2008. 87

[112] J. Klodmann, R. Konietschke, A. Albu-Schäffer, and G. Hirzinger. Static calibration of the dlr medical robot miro, a flexible lightweight robot with integrated torque sensors. In *IEEE/RSJ International Conference on Intelligent Robots and Systems*, pages 3708–3715, 2011. 87

[113] N. Gaffke and B. Heiligers. Optimal and robust invariant designs for cubic multiple regression. *Metrika*, 42(1):29–48, 1995. 87

[114] N. Gaffke and B. Heiligers. Computing optimal approximate invariant designs for cubic regression on multidimensional balls and cubes. *Journal of statistical planning and inference*, 47(3):347–376, 1995. 87

[115] N. K. Nguyen and A. J. Miller. A review of some exchange algorithms for constructing discrete d-optimal designs. *Computational Statistics & Data Analysis*, 14(4):489–498, 1992. 87

[116] C. Makkar, W. E. Dixon, W. G. Sawyer, and G. Hu. A new continuously differentiable friction model for control systems design. In *IEEE/ASME International Conference on Advanced Intelligent Mechatronics.*, pages 600–605, July 2005. 96

[117] R. M. Murray, Z. Li, and S. S. Sastry. *A mathematical introduction to robotic manipulation.* CRC press, 1994. 105, 169, 204

[118] R. Hermann and A. Krener. Nonlinear controllability and observability. *IEEE Transactions on Automatic Control*, 22(5):728–740, 1977. 106

[119] K. Madsen and H. B. Nielsen. *Introduction to Optimization and Data Fitting.* Informatics and Mathematical Modelling, Technical University of Denmark, DTU, 2010. 106, 107

[120] D. P. Bertsekas and A. Scientific. *Convex optimization algorithms.* Athena Scientific Belmont, 2015. 107

[121] A. K. Singh and J. Hahn. On the use of empirical gramians for controllability and observability analysis. In *American Control Conference*, pages 140–141, 2005. 111

[122] A. J Krener and K. Ide. Measures of unobservability. In *IEEE Conference on Decision and Control*, pages 6401–6406, 2009. 111

[123] W. Sun and Y. Yuan. *Optimization theory and methods: nonlinear programming*, volume 1. Springer Science & Business Media, 2006. 113, 169

[124] S. Thrun, W. Burgard, and D. Fox. Probabilistic robotics (intelligent robotics and autonomous agents series). *Intelligent robotics and autonomous agents, The MIT Press (August 2005)*, 2006. 119

[125] G. Ciccarella, M. Dalla Mora, and A. Germani. A luenberger-like observer for nonlinear systems. *International Journal of Control*, 57(3):537–556, 1993. 120

[126] k610 CMM Metris. http://www.metris3d.hu, 2016. Accessed: 2018.10.14. 120, 203

[127] Mark W Spong. Modeling and control of elastic joint robots. *Journal of dynamic systems, measurement, and control*, 109(4):310–318, 1987. 138

[128] H. K. Khalil and J. W. Grizzle. *Nonlinear systems*, volume 3. Prentice Hall, 2002. 138

[129] C. Ott, A. Albu-Schaffer, and G. Hirzinger. Comparison of adaptive and nonadaptive tracking control laws for a flexible joint manipulator. In *IEEE/RSJ International Conference on Intelligent Robots and Systems*, volume 2, pages 2018–2024. IEEE, 2002. 138

[130] M. W. Spong. Partial feedback linearization of underactuated mechanical systems. In *IEEE/RSJ International Conference on Intelligent Robots and Systems*, pages 314–321, 1994. 139

[131] R. Olfati-Saber. *Nonlinear Control of underactuated Systems with Application to Robotics and Aerospace Vehicles*. PhD thesis, Massachusetts Institute of Technology, 2001. 139

[132] K. Zhou, J. C. Doyle, and K. Glover. *Robust and optimal control*, volume 40. Prentice hall New Jersey, 1996. 142, 144

[133] K. J. Åström and B. Wittenmark. *Computer-controlled systems: theory and design*. Courier Corporation, 2013. 142

[134] P. Axelsson, A. Helmersson, and M. Norrlöf. H-inf-controller design methods applied to one joint of a flexible industrial manipulator. *IFAC PapersOnline*, 47(3):210 – 216, 2014. 142

[135] L. S. Mello, G. V. Raffo, and B. V. Adorno. Robust whole-body control of an unmanned aerial manipulator. In *Control Conference, European*, pages 702–707. IEEE, 2016. 142

[136] M. Djukanovic, Khammash M., and V. Vittal. Application of structured singular value theory for robust stability and control analysis in multimachine power systems. *Transactions on Power Systems*, 13(4):1317–1322, Nov 1998. 142

[137] N. Amann and F. Allgower. Mu-suboptimal design of a robustly performing controller for a chemical reactor. *International Journal of Control*, 59(3):665–687, 1994. 142, 143

[138] M. R. Katebi and Y. Zhang. H-inf ontrol analysis and design for nonlinear systems. *International Journal of Control*, 61(2):459–474, 1995. 142

[139] M. Dlapa. Algebraic approach using structured singular value: Application to a nonlinear plant. In *ECMS 2011 Proceedings*, pages 487–493. European Council for Modeling and Simulation, 2011. 142

[140] A. L. Shu. H-inf control of a tendon driven elastic continuum mechanism with high model uncertainty. Master's thesis, Technical University of Munich (TUM), 4 2018. 143

[141] G. J. Balas and J. C. Doyle. Control of lightly damped, flexible modes in the controller crossover region. *Journal of Guidance, Control, and Dynamics*, 17(2):370–377, 1994. 144

[142] A. Isidori. *Nonlinear control systems*. Springer Science & Business Media, 2013. 145, 147

[143] R. Seifried. *Dynamics of underactuated multibody systems*. Springer, 2014. 145

[144] M. Fliess, J. Lévine, P. Martin, and P. Rouchon. Flatness and defect of nonlinear systems: introductory theory and examples. *International journal of control*, 61(6):1327–1361, 1995. 146

[145] H. Sadeghian, C. Ott, G. Garofalo, and G. Cheng. Passivity-based control of underactuated biped robots within hybrid zero dynamics approach. In *IEEE International Conference on Robotics and Automation*, pages 4096–4101, 2017. 147

[146] R. Seifried. Two approaches for feedforward control and optimal design of underactuated multibody systems. *Multibody System Dynamics*, 27(1):75–93, 2012. 151, 152

[147] W. Blajer and K. Kołodziejczyk. Control of underactuated mechanical systems with servo-constraints. *Nonlinear Dynamics*, 50(4):781–791, 2007. 152

[148] Y. Chen, I. Petras, and D. Xue. Fractional order control-a tutorial. In *2009 American control conference*, pages 1397–1411. IEEE, 2009. 160

[149] C. A. Monje, Y. Chen, B. M. Vinagre, D. Xue, and V. Feliu-Batlle. *Fractional-order systems and controls: Fundamentals and applications*. Springer Science & Business Media, 2010. 160, 162

[150] I. Petras. *Handbook of Fractional Calculus with Applications: Applications in Control*, chapter 6. De Gruyter, 2019. 160

[151] C. A. Monje, F. Ramos, V. Feliu, and B.M. Vinagre. Tip position control of a lightweight flexible manipulator using a fractional order controller. *Control Theory & Applications, IET*, 1(5):1451–1460, 2007. 160, 166

[152] J. Malzahn and T. Bertram. Fractional order strain feedback for oscillation damping of a multi-elastic-link arm under gravity. In *ISR/Robotik 2014; 41st International Symposium on Robotics*, pages 1–8. VDE, 2014. 160

[153] C. A. Monje, B. M. Vinagre, V. Feliu, and Y. Chen. Tuning and auto-tuning of fractional order controllers for industry applications. *Control Engineering Practice*, 16(7):798–812, 2008. 160, 161, 166

[154] G. F. Franklin, J. D. Powell, and A. Emami-Naeini. Feedback control of dynamics systems. *Addison-Wesley, Reading, MA*, 1994. 161

[155] Y. Chen, C. Hu, and K. L. Moore. Relay feedback tuning of robust pid controllers with iso-damping property. In *42nd IEEE Conference on Decision and Control*, pages 2180–2185, 2003. 161

[156] A. van der Schaft. *L_2-Gain and Passivity Techniques in Nonlinear Control*. Springer-Verlag, 2nd edition, 2000. 162

[157] A. Ben-Israel and T. N. Greville. *Generalized inverses: theory and applications*, volume 15. Springer Science & Business Media, 2003. 169

[158] A. Dietrich, C. Ott, and A. Albu-Schäffer. An overview of null space projections for redundant, torque-controlled robots. *The International Journal of Robotics Research*, 34(11):1385–1400, 2015. 169

[159] M. Grebenstein, A. Albu-Schäffer, T. Bahls, M. Chalon, O. Eiberger, W. Friedl, R. Gruber, S. Haddadin, U. Hagn, and R. Haslinger. The dlr hand arm system. In *2011 IEEE International Conference on Robotics and Automation*, pages 3175–3182. IEEE, 2011. 175

[160] F. Loeffl, A. Werner, D. Lakatos, J. Reinecke, S. Wolf, R. Burger, T. Gumpert, F. Schmidt, C. Ott, and M. Grebenstein. The dlr c-runner: Concept, design and experiments. In *IEEE International Conference on Humanoid Robots (Humanoids)*, pages 758–765. IEEE, 2016. 175

[161] Alexander Dietrich, Thomas Wimbock, Alin Albu-Schaffer, and Gerd Hirzinger. Integration of reactive, torque-based self-collision avoidance into a task hierarchy. *IEEE Transactions on Robotics*, 28(6):1278–1293, 2012. 180

[162] Alexander Dietrich and Christian Ott. Hierarchical impedance-based tracking control of kinematically redundant robots. *IEEE Transactions on Robotics*, 36:204–221, 2020. 180

[163] Alexander Dietrich, Christian Ott, and Stefano Stramigioli. Passivation of projection-based null space compliance control via energy tanks. *IEEE Robotics and automation letters*, 1(1):184–191, 2015. 180

[164] Jens Reinecke, Bastian Deutschmann, Alexander Dietrich, and Marco Hutter. An anthropomorphic robust robotic torso for ventral/dorsal and lateral motion with weight compensation. *IEEE Robotics and automation letters*, 2020. 180

[165] Alexander Dietrich, Thomas Wimbock, Alin Albu-Schaffer, and Gerd Hirzinger. Reactive whole-body control: Dynamic mobile manipulation using a large number of actuated degrees of freedom. *IEEE Robotics & Automation Magazine*, 19(2):20–33, 2012. 181

[166] Alexander Dietrich, Kristin Bussmann, Florian Petit, Paul Kotyczka, Christian Ott, Boris Lohmann, and Alin Albu-Schäffer. Whole-body impedance control of wheeled mobile manipulators. *Autonomous Robots*, 40(3):505–517, 2016. 181

[167] A. Dietrich. Whole-body impedance control of wheeled humanoid robots. In *Springer Tracts in Advanced Robotics (STAR)*, volume 116. Springer International Publishing, 2016. 181

[168] A. Albu-Schäffer, S. Haddadin, C. Ott, A. Stemmer, T. Wimböck, and G. Hirzinger. The dlr lightweight robot: design and control concepts for robots in human environments. *Industrial Robot: An International Journal*, 34(5):376–385, 2007. 205

PERSÖNLICHE INFORMATIONEN

Bastian Deutschmann
Dipl.-Ing.
birth: 28.06.1985, Gemrany
Nationalität: deutsch
Familienstand: ledig

Adresse:
Senserstraße 20
81371 München
Tel: +49 178 2882604
Email: bastian.deutschmann@dlr.de

AUSBILDUNG

Externer Doktorrand
10/2017 – 04.2019

Leibniz Universität Hannover, Deutschland
Labor für Kontinuumsrobotik, Fakultät Maschinenbau

Dipl. -Ing. in Maschinenbau
10/2005 – 05/2011

Universität Stuttgart, Deutschland

- Dipl. -Ing. : 27 Mai 2011
- Betreuer: Prof. J. Nagel, Prof. P. Eberhard
- Dipl. -Ing. Thesis: "Modellierung eines Robotischen Instrumentes für die Minimal Invasive Chirurgie",

Schüler
09.1995 – 07.2004

Ernst-Sigle Gymnasium Kornwestheim, Deutschland

- Allgemeine Hochschulreife: 07.2004
- Vertiefungsfächer: Physik, Chemie

BERUFSERFAHRUNG

Wissenschaftlicher Mitarbeiter
02/2012 – present

Deutsches Zentrum für Luft und Raumfahrt, Deutschland
Institut für Robotik Mechatronik.

Ausstauschstudent
01/2010 – 07/2010

Universität Trondheim, Norwegen
Department of Structural Engineering
Betreuer: Prof. Bjorn Skallerud
Forschungsthema: Biomechanical assessment of bone elasticity during callotasis

Praktikant
09/2009-12/2009

Bosch GmbH, Deutschland
Vorentwicklung Brenstoffzellenantriebstechnik

Ausshilfe/Tutor
05/2008-07/2009

Universität Stuttgart, Deutschland
Institut für Experimentelle und Numerische Mechanik
Tutor für Technische Mechanik 2 und 3

Werkstudent
05/2007-12/2007

Dürr Systems GmbH, Deutschland
Abteilung für Arbeitsvorbereitung und Qualitätsicherung

Praktikant
05.2005 – 07.2005

Dürr Systems GmbH, Deutschland
Pflicht-Vorpraktikum zum Maschinenbaustudium

Zivildienstleistender	**Jakob-Sigle Heim Kornwestheim**, Deutschland
08.2004 – 04.2005	Zivildienst in der Tagespflege eines Seniorenheims

Veröffentlichungen

KONFERRENZ PROCEEDINGS (PEER-REVIEWED)

[C1] WIMMER, A., DEUTSCHMANN, B., KUEBLER, B., RINK, C., HIRZINGER, G. "Spine-kinematics with constraint guidance for robot supported MIS-instruments.", *IEEE International Conference on Robotics and Automation (ICRA)*, 5453-5460, 2013

[C2] DEUTSCHMANN B., KONIETSCHKE, R. AND ALBU-SCHÄFFER, A. "Task-specific evaluation of kinematic designs for instruments in minimally invasive robotic surgery.", *Proceeding of the IEEE/RSJ International Conference on Intelligent Robots and Systems (IROS)*, 3590-3597, 2013.

[C3] DEUTSCHMANN B., KONIETSCHKE, R. OTT C. "Kinematic Analysis of Instruments for Minimally Invasive Robotic Surgery: Generalization of the Reference Task.", *In: New Trends in Medical and Service Robotics.* Mechan. Machine Science, Vol. 38. Springer, 2016.

[C4] REINECKE J., DEUTSCHMANN B., FEHRENBACH, D. "A structurally flexible humanoid spine based on a tendon-driven elastic continuum." *IEEE International Conference on Robotics and Automation (ICRA)*, pages 4714-4721, May 2016.

[C5] DEUTSCHMANN, B., OTT, C. MONJE, C.A, BALAGUER C. "Robust motion control of a soft robotic system using fractional order control." *International Conference on Robotics in Alpe-Adria Danube Region.* Springer, Cham, 2017.

[C6] DEUTSCHMANN, B., DIETRICH, A. OTT,C. "Position control of an underactuated continuum mechanism using a reduced nonlinear model."*IEEE 56th Annual Conference on Decision and Control (CDC)*, pages 5223-5230, Dez. 2017.

[C7] DEUTSCHMANN, B., EUGSTER, S.R., OTT,C. " Reduced Models for the Static Simulation of an Elastic Continuum Mechanism." *IFAC-PapersOnLine 51(2)*, pages 403-408, Mar. 2018.

[C8] EUGSTER, S.R. AND DEUTSCHMANN, B. "A nonlinear Timoshenko beam formulation for modeling a tendon-driven compliant neck mechanism." *PAMM 18.1* 2018.

[C9] SHU, A., DEUTSCHMANN, B., DIETRICH, A., OTT, C., ALBU-SCHÄFFER, A. "Robust H-∞ control of a tendon–driven elastic continuum mechanism via a systematic description of nonlinearities." *IFAC-PapersOnLine 51(22)*, pages 386-392, Sept. 2018.

[C10] DEUTSCHMANN, B., CHALON, M., REINECKE, J., MAIER, M., OTT, C. "Six DoF pose estimation for a tendon-driven continuum mechanism without a deformation model." *IEEE Robotics and Automation Letters (4)4* presented at the *IEEE/RSJ International Conference on Robotics and Intelligent Systems (IROS)*, Nov. 2019

ARTIKEL

[J1] BAHLS, T., FROEHLICH, F.A., HELLINGS, A., DEUTSCHMANN, B., ALBU-SCHÄFFER, A. "Extending the capability of using a waterjet in surgical interventions by the use of robotics", *IEEE Transactions on Biomedical Engineering 64(2)*, pages 284-294, 2016

[J2] DEUTSCHMANN, B., LIU, T., DIETRICH, A., OTT,C., LEE, D. " A method to identify the nonlinear stiffness characteristics of an elastic continuum mechanism." *IEEE Robotics and Automation Letters (3)3* pages 1450-1457, Jan. 2018.

[J3] DEUTSCHMANN, B., CHALON, M., REINECKE, J., MAIER, M., OTT, C. "Six DoF pose estimation for a tendon-driven continuum mechanism without a deformation model." *IEEE Robotics and Automation Letters (4)4* pages 3452-3432, Jul. 2019

BÜCHER

[B1] MONJE, C.A, DEUTSCHMANN, B., OTT, C., BALAGUER C. "Control of a soft robotic link using a

fractional-order controller." *Handbook of Fractional Order Calculus with Applications.* de Gruyter, 2019.

PATENTE

[P1] DEUTSCHMANN, B., DIETRICH, A., REINECKE, R., STEIDLE, F. "Kontinuumsgelenk", Deutsche Patent Anmeldung Nr. 102017200866, genehmigt 20.01.2017.

[P2] DEUTSCHMANN, B., DIETRICH, A., LIU, T., OTT, C. "Verfahren und Vorrichtung zur Charakterisierung eines Kontinuumgelenks", Deutsche Patent Anmeldung Nr. 10 2017 215 432.2, angemeldet am 04.09.2017.